# Infrared Polarimetry and Integral Field Spectroscopy of Post-Asymptotic Giant Branch Stars

Krispian Tom Edward Lowe

A thesis submitted in partial fulfilment of the requirements of the University of Hertfordshire for the degree Doctor of Philosophy.

This programme of research was carried out in the School of Physics, Astronomy and Mathematics, Faculty of Engineering and Information Sciences, University of Hertfordshire

June 2008

Tom Lowe

*...strove with his last ounce of courage*

*to reach the unreachable star.* - Joe Darion.

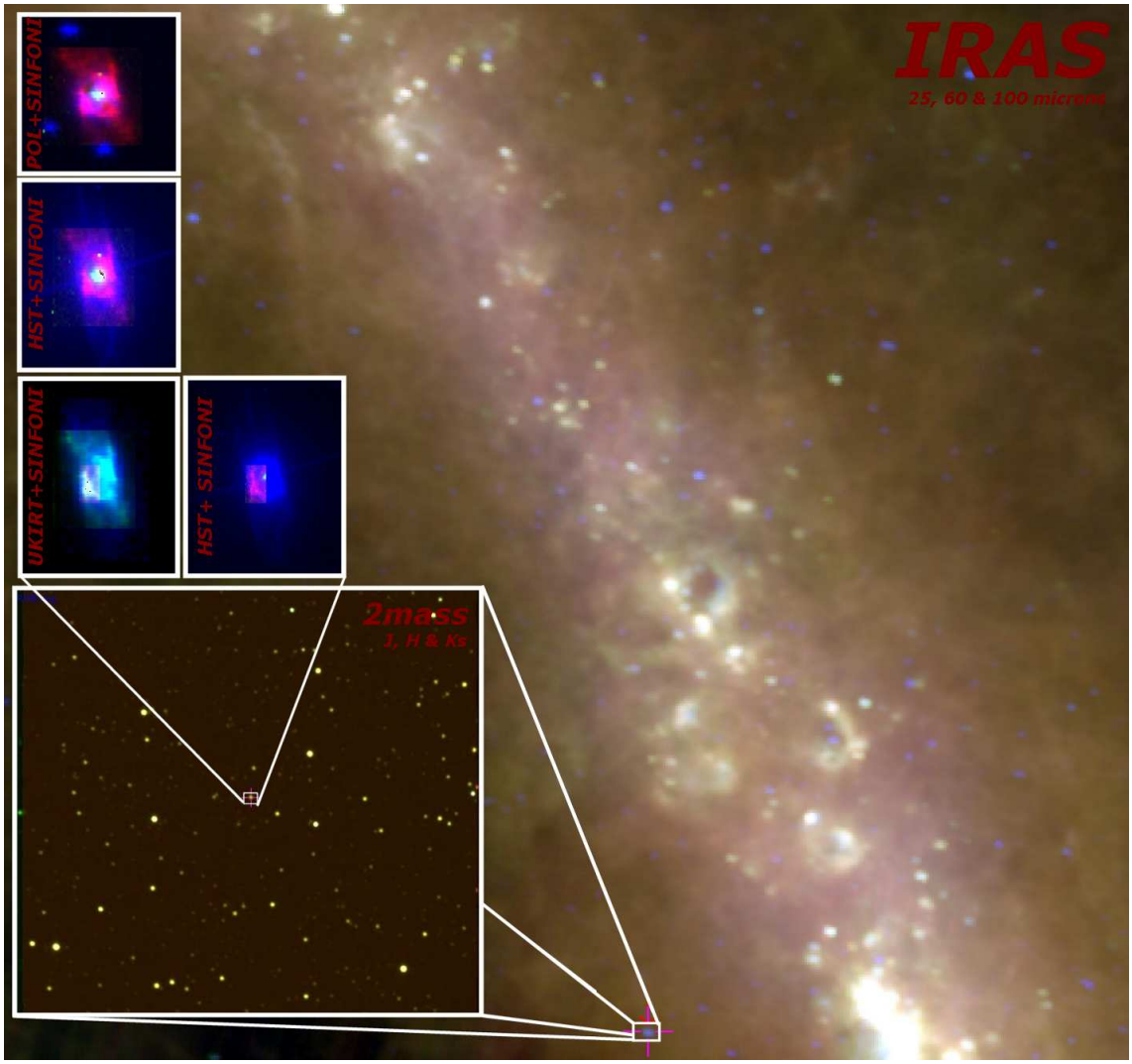


Figure 1: A collage of false colour RGB images of *IRAS*, 2mass, *HST*, SINFONI and UKIRT images indicating the location of *IRAS* 19306+1407 near to the Galactic plane and within a 2mass field. The *IRAS* image consists of 25, 60 and 100 μm as blue, green and red, respectively, displayed with log intensities. The 2mass image is comprised of J, H and $K_s$ images as blue, green and red, respectively. The blown up panels indicate combinations of polarimetry, molecular hydrogen emission, atomic emission and intensity images from UKIRT:IRPOL2, SINFONI and *HST*, which are indicated by the label within each panel. POL+SINFONI (top left): The *J*-band polarimetry (UKIRT), brackett gamma and 1-0S(1) emission (medium resolution SINFONI) represented as blue, green and red, respectively. *HST*+SINFONI (centre left): The *F606W HST* image displayed in a log-scale, brackett gamma and 1-0S(1) $H_2$ emission (Medium resolution SINFONI) represented as blue, green and red, respectively. UKIRT+SINFONI (bottom left): The 1-0S(1) emission images obtained from UKIRT:IFU, medium resolution and high resolution SINFONI images are represented as blue, green and red, respectively. HST+SINFONI (bottom right): The *F606W HST* image displayed in a log-scale, brackett gamma and 1-0S(1) $H_2$ emission (high resolution SINFONI) represented as blue, green and red, respectively.

# Abstract

Krispian Tom Edward Lowe

infrared Polarimetry and Integral Field Spectroscopy of Post-Asymptotic Giant Branch Stars

University of Hertfordshire, 2008

In this thesis, I present the properties of *IRAS* 19306+1407 central source and its surrounding circumstellar envelope (CSE), from the analysis of near-infrared (near-IR) polarimetry and integral field spectroscopy (IFS), with supporting archived *HST* images and sub-millimetre (sub-mm) photometry. This is supported by axi-symmetric light scattering (ALS), axi-symmetric radiative transfer (DART) and molecular hydrogen ($H_2$) shock models.

The polarimetric images show that *IRAS* 19306+1407 has a dusty torus, which deviates from axisymmetry and exhibits a 'twist' feature. The DART and ALS modelling shows that the CSE consists of Oxygen-rich sub-micrometre dust grains, with a range in temperature from $130 \pm 30$ to $40 \pm 20$ K at the inner and outer radius, respectively, with inner and outer radii of $1.9 \pm 0.1 \times 10^{14}$ and $2.7 \pm 0.1 \times 10^{15}$ m. The CSE detached $400 \pm 10$ years ago and the mass loss lasted $5700 \pm 160$ years, assuming a constant asymptotic giant branch (AGB) outflow speed of 15 km $s^{-1}$. The dust mass and total mass of the CSE is $8.9 \pm 5 \times 10^{-4}$ and $1.8 \pm 1.0 \times 10^{-1}$ $M_{\odot}$, assuming a gas-to-dust ratio of 200. The mass loss rate was $3.4 \pm 2.1 \times 10^{-5}$ $M_{\odot}$ $year^{-1}$. The central source is consistent with a B1I-type star with a radius of $3.8 \pm 0.6$ $R_{\odot}$, luminosity of $4500 \pm 340$ $L_{\odot}$ at a distance of $2.7 \pm 0.1$ kpc.

A purpose built IDL package (FUS) was developed and used in the SINFONI IFS data critical final reduction steps. It also produced emission line, kinematic and line

ratio images. The IFS observations show that $H_2$ is detected throughout the CSE, located in bright arcs and in the bipolar lobes. The velocity of the $H_2$ is greatest at the end of the lobes. Br$\gamma$ emission originates from, or close, to the central source – produced by a fast jump (J) shock or photo-ionised atomic gas. The 1-0 S(1)/2-1 S(1) and 1-0 S(1)/3-2 S(3) ratios were used as a diagnostic and determined that $H_2$ was excited by bow shaped shocks; however, these shock models could not wholly explain the observed rotational and vibrational temperatures. The CDR values were fitted by combining continuous (C) or J-bow shock and fluorescence models, with a contribution from the latter, observed throughout the CSE (5–77 per cent). The majority of shock can be described by a C-bow shock model with $B = 0.02$ to 1.28 mG. Shocks are predominately seen in the equatorial regions. Polarimetry and IFS highlight a 'twist' feature, which could be due to an episodic jet undergoing a recent change in the outflow direction.

The sub-arcsecond IFS observations reveal a flocculent structure in the south-east bright arc, consisting of several clumps interpreted as a fast-wind eroding an equatorial torus, possibly forming $H_2$ knots seen in (some) evolved planetary nebulae (PNe).

My analysis has effectively constrained the following: spectral type, stellar radius, luminosity and distance, chemistry, dust grain properties, geometry, age, mass loss, excitation mechanism and evolutionary state of the post-AGB star and its surrounding CSE. I conclude that *IRAS* 19306+1407 is a post-AGB object on the verge becoming a PN.

# Acknowledgements

I thank and acknowledge the following people and institutions:

My supervisors, Dr. Tim Geldhill, Dr. Antonio Chrysostomou and Prof. Jim Hough for guiding, supporting and making this PhD possible. Dr. Kim "I have a quick question" Clube for all the discussions of infrared post-AGB stars and tuition on radiative modelling. Dr. Emma Allard for advice on finer points of integral field spectroscopy and IDL, which made the FUS program possible. Dr. Emma Brannigan for offering support and helping me see the wood through the trees. Dr. Robert Priddey for stimulating conversations on sub-millimetre astronomy and the JCMT. Tom Scott for his advice on molecular hydrogen and the multiple discussions on shocks and fluorescence. Dr. Chris Davis and Dr. Michael Smith for the discussion on molecular hydrogen. I am extremely thankful for Dr. Michael Smith for providing the $H_2$ model code.

The United Kingdom Infrared Telescope is operated by the Joint Astronomy Centre on behalf of the Science and Technology Facilities Council of the U.K. The University of Hertfordshire, for providing IRPOL2 for the UKIRT. The James Clerk Maxwell Telescope is operated by The Joint Astronomy Centre on behalf of the Science and Technology Facilities Council of the United Kingdom, the Netherlands Organisation for Scientific Research, and the National Research Council of Canada (Program ID: S04BU09). Part of this thesis is based on observations made with the NASA/ESA Hubble Space Telescope, obtained from the data archive at the Space Telescope Institute. STScI is operated by the association of Universities for Research in Astronomy, Inc. under the NASA contract NAS 5-26555. Part of this thesis is based on observations made with ESO Telescopes at the La Silla or Paranal Observatories under programme ID 075.D-0429(A). All model calculations were run on the HiPerSpace Computing Facility at University College London. Bruce Hrivnak

for the private communication on *IRAS* 19306+1407. VizieR catalogue access tool and SIMBAD database, CDS, Strasbourg, France. This research has made use of NASA's Astrophysics Data System. I am amazed at the wealth of data obtained from UKIRT and VLT towards the end of the PhD, despite the initial observing run at UKIRT with MICHELLE was a failure[1] and the backup run with the JCMT with SCUBA[2] that never was observed.

My immediate family, Regan, Jacquie and Allizon Lowe, for supporting me throughout my undergraduate and postgraduate degrees and my great-grandparents and grandparents for providing opportunities, which have made all this possible. I also thank my family for buying my first telescope even though the instruction book was in Russian. Paul Ferguson for all his vital support, love and keeping me motivated throughout my PhD. My friends for their patience and support throughout my PhD, especially those who have offered encouraging[3] advice. I would thank Mrs. Charnock who first captured my interest in science and astronomy. Krispian Lowe was supported by a PPARC studentship.

[1] due to bad weather and a broken instrument

[2] My highly ranked telescope proposal was accepted, but soon after SCUBA broke for the final time.

[3] and sometimes blunt

# Contents

# List of Figures

# List of Tables

# Chapter 1

# Introduction

The post-main sequence evolution of 95 per cent of stars in the Galaxy is dominated by the mass-loss occurring on the Asymptotic Giant Branch (AGB) (Kwok 2000). The initial mass of an AGB star can range between 0.8-8 $M_{\odot}$ and its mass loss can range between $10^{-7}$-$10^{-4}$ $M_{\odot}$ year$^{-1}$ (e.g. Schönberner 1983; Vassiliadis & Wood 1994b). The mass loss drops dramatically at the end of the AGB, creating a detached circumstellar envelope (CSE) (see van Winckel 2003, for a general review), and the star enters the post-AGB stage. These dusty CSEs are visible at optical and near-infrared (near-IR) wavelengths as proto-planetary nebulae (PPNe; Kwok 1993), which contain a luminous ($10^3$-$10^4$ $L_{\odot}$) central illumination source. A seemingly ubiquitous feature of PPNe is their lack of spherical symmetry, with many having bipolar, multipolar or a point symmetric structure. A gallery of objects is presented in Figure 1.1, which show these remarkable structures. Notable and well studied examples are the Egg Nebula (AFGL 2688; Sahai et al. 1998) and the Red Rectangle (AFGL 915; Cohen et al. 2004), which are shown in Figures 1.2 and 1.3, respectively. Optical and near-IR surveys of PPNe have shown that in all cases, where a CSE is detected, it appears asymmetric in some way (e.g. Ueta, Murakawa & Meixner 2005; Gledhill et al. 2001). Possible mechanisms for shaping of PPNe usually involve

interaction of a mass-losing star with magnetic fields or with a binary companion, and these have been reviewed by Balick & Frank (2002). Past observations and models present the following questions: *How do these shapes arise? Are they shaped during the AGB or post-AGB stages? What causes such a variety of morphologies? Is there an underlying shaping mechanism common to all PPNe?* In this thesis the above questions are described and discussed.

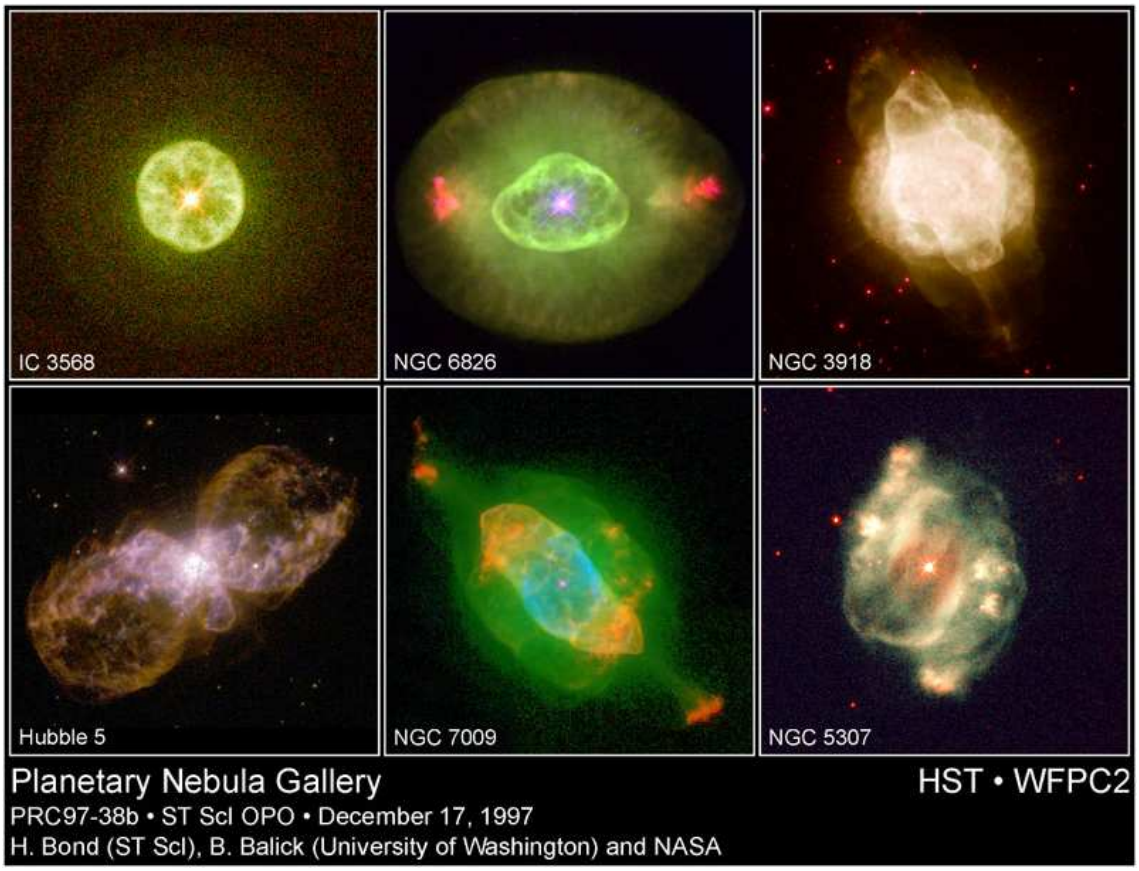


Figure 1.1: A selection of *HST* images of planetary nebulae showing round (top-left), elliptical (top-centre), bipolar (top-right, bottom-left and bottom-centre) and point symmetric (bottom-right) morphologies. Top Left Credits: Howard Bond (Space Telescope Science Institute), Robin Ciardullo (Pennsylvania State University) and NASA Top Center Credits: Bruce Balick (University of Washington), Jason Alexander (University of Washington), Arsen Hajian (U.S. Naval Observatory), Yervant Terzian (Cornell University), Mario Perinotto (University of Florence, Italy), Patrizio Patriarchi (Arcetri Observatory, Italy) and NASA Top Right Credits: Howard Bond (Space Telescope Science Institute), Robin Ciardullo (Pennsylvania State University) and NASA Bottom Left Credits: Bruce Balick (University of Washington), Vincent Icke (Leiden University, The Netherlands), Garrelt Mellema (Stockholm University), and NASA Bottom Center Credits: Bruce Balick (University of Washington), Jason Alexander (University of Washington), Arsen Hajian (U.S. Naval Observatory), Yervant Terzian (Cornell University), Mario Perinotto (University of Florence, Italy), Patrizio Patriarchi (Arcetri Observatory, Italy), NASA Bottom Right Credits: Howard Bond (Space Telescope Science Institute), Robin Ciardullo (Pennsylvania State University) and NASA.

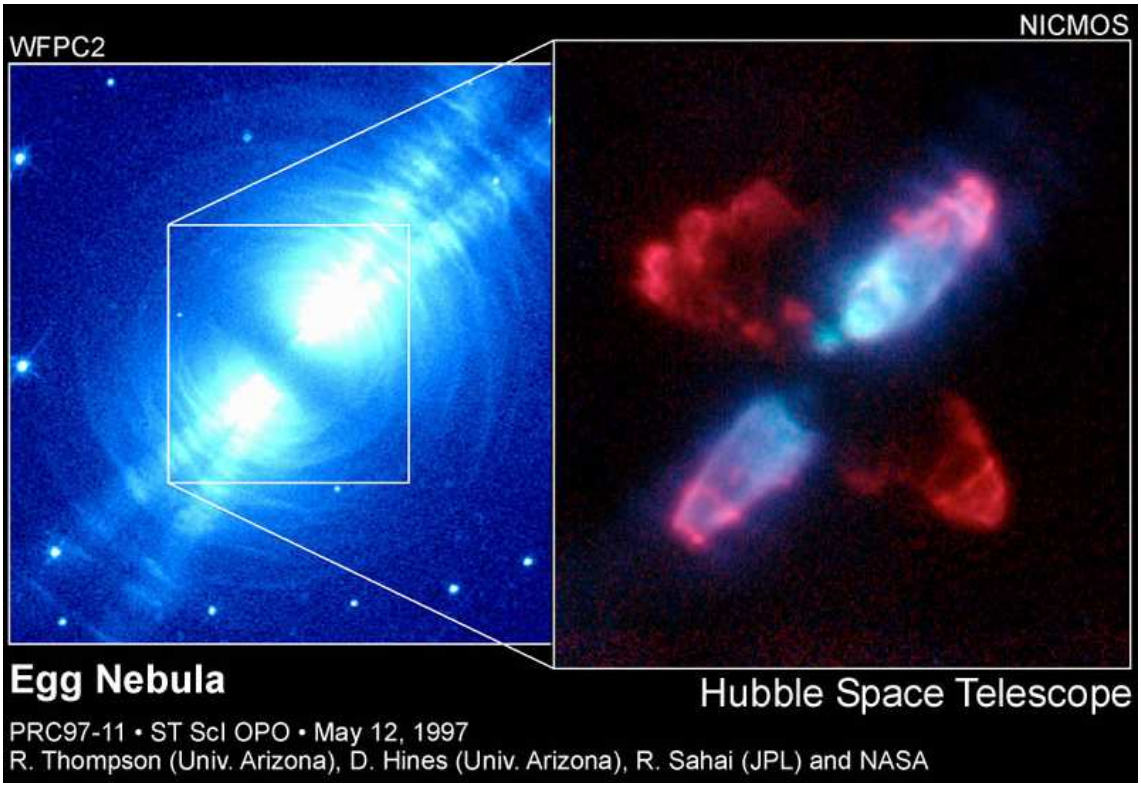


Figure 1.2: The Egg Nebula. The left hand panel is an optical image obtained with the *HST*. The central region is blown up and is displayed in the right hand panel, which shows $H_2$ emission at the ends of the bipolar lobes and the equatorial torus. Credit: Rodger Thompson, Marcia Rieke, Glenn Schneider, Dean Hines (University of Arizona); Raghvendra Sahai (Jet Propulsion Laboratory); NICMOS Instrument Definition Team, and NASA

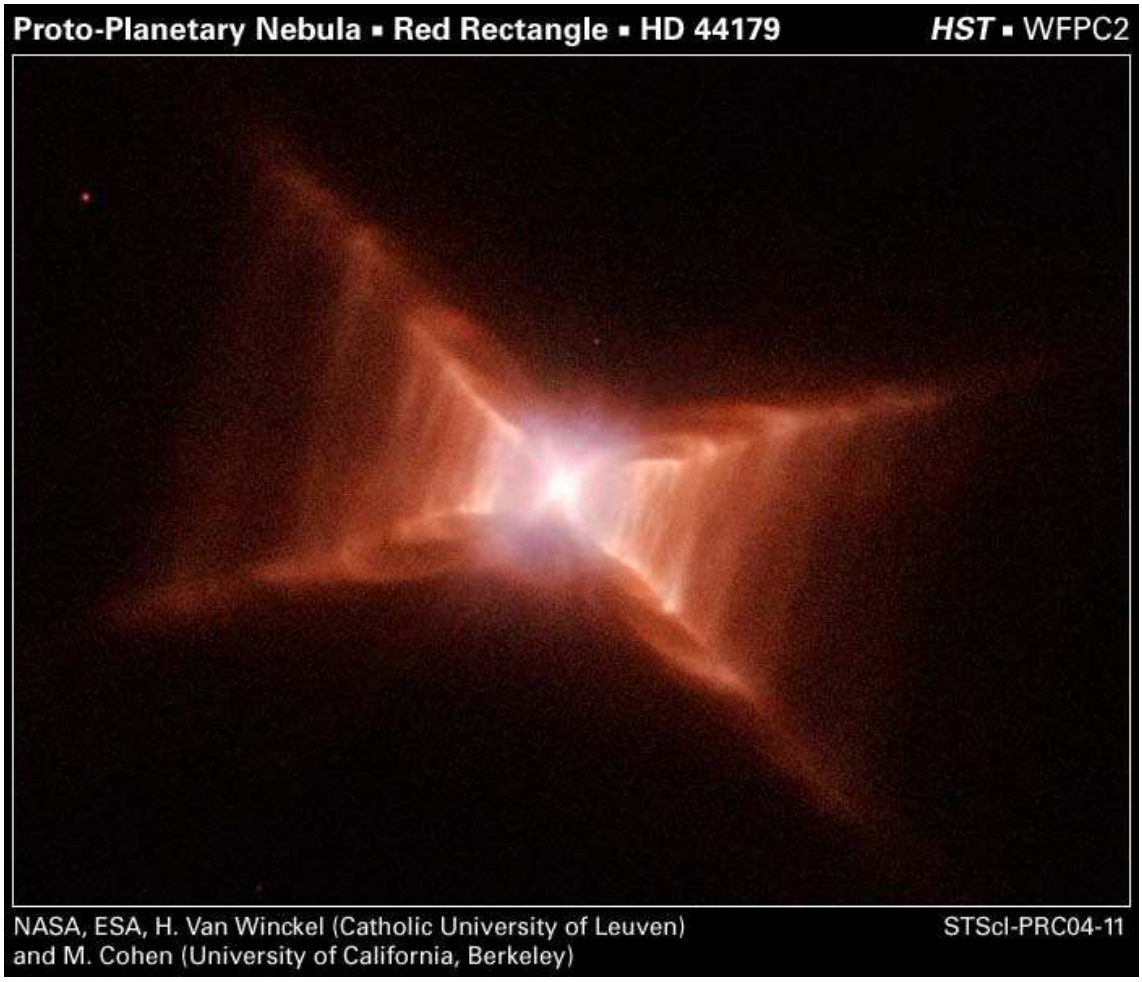


Figure 1.3: The Red Rectangle. Credit: NASA; ESA; Hans Van Winckel (Catholic University of Leuven, Belgium); and Martin Cohen (University of California, Berkeley)

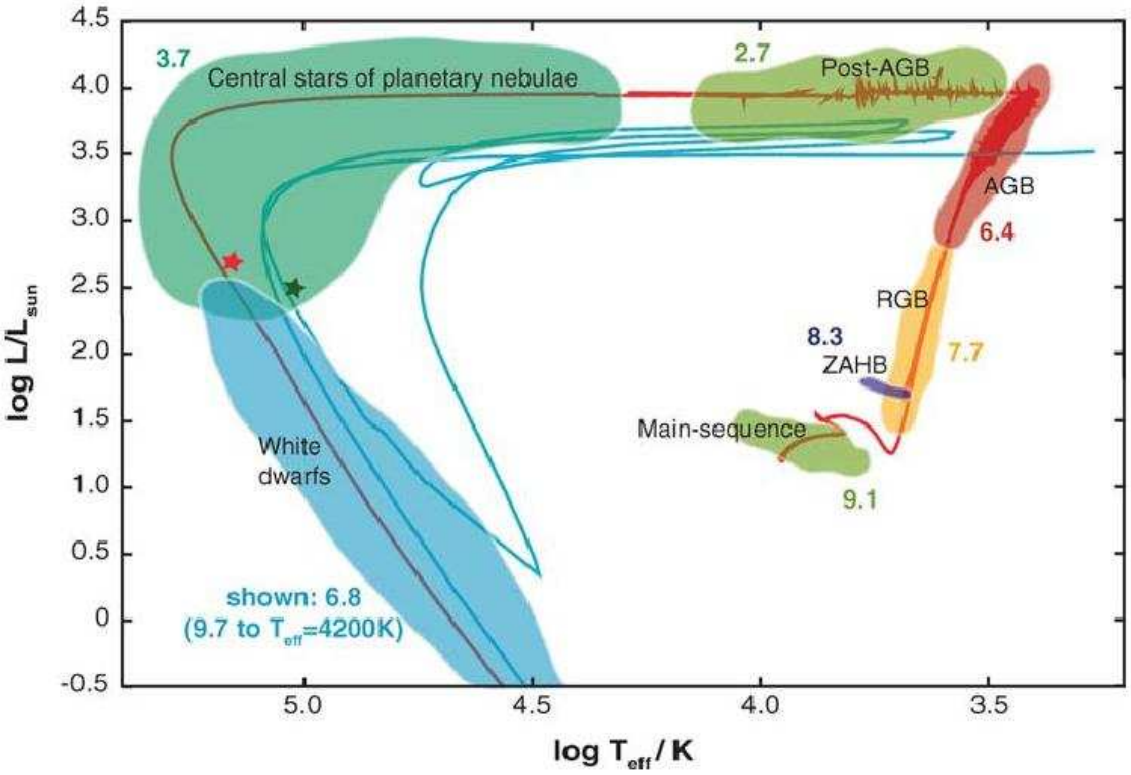


Figure 1.4: The above Hertzsprung-Russel diagram and following caption has been taken from Herwig (2005). The Hertzsprung-Russell diagram of a complete $2M_{\odot}$ evolution track for solar metallicity from the main sequence to the white dwarf evolution phase. In the cooler section of the post-AGB phase, wiggles in the track are caused by numerical convergence difficulties. The blue track shows a born-again evolution (triggered by a late thermal pulse), of the same mass, however, shifted by approximately $\Delta \log T_{\rm eff} = -0.2$ and $\Delta \log L/L_{\odot} = -0.5$ for clarity. The number labels for each evolutionary phase indicates the log of the approximate duration for a 2 $M_{\odot}$ case. Larger or smaller mass cases would have smaller or larger evolutionary timescales, respectively.

## 1.1 Evolution and shapes

A star spends the majority of its nuclear burning life on the main sequence, during which it fuses Hydrogen (H) into Helium (He), via the proton-proton chain or the CNO cycle for massive stars (see Appendix C.1 and Appendix C.3). The fusion takes place within the core of the star and energy is transported, via convection and radiation, to its surface. Very low mass stars ($M_{\star} < 0.4$ $M_{\odot}$) are fully convective, low mass stars ($0.4 < M_{\star} < 1.8$ $M_{\odot}$ ) releases energy from the radiative core into the

convective envelope, whilst intermediate and massive stars ($M_\star > 1.8$ M$_\odot$) releases energy from the convective core into the radiative envelope.

Once a low mass star, ( $0.8 < M_\star < 2.0$ M$_\odot$), has converted the majority of H in the core to He, the star will progress from the main-sequence to the Red Giant Branch (RGB; Fig. 1.4), and will start fusing H in a shell around the core, which is also known as shell burning. The stellar envelope will increase in radius and luminosity, whilst its effective temperature decreases. The He-core grows in mass, from He supplied by the H-shell burning, but continues to shrink and becomes electron-degenerate. Once the core reaches a temperature of $\sim 10^8$ K, it will experience a He-core flash, where upon the He is fused into Carbon (C), via the triple-alpha process (see Appendix C.2). The He burning core will be surrounded by a H-burning shell and the star will settle on the Horizontal Branch (HB).

The intermediate mass stars ($2.0 < M_\star < 8.0$ M$_\odot$) will ignite He-burning, without a He-core flash, since their cores are convective, and will proceed along the HB. Some C nuclei can be converted into Oxygen (O) via the fusion of an extra He nuclei. Once all fusion has ceased in the core, of the lower and higher mass stars, they will move onto the AGB.

The AGB star will consist of a C/O degenerate core surrounded by He- and H-burning shells (see Herwig 2005, for a general review). In addition, the radius of the AGB star can be several hundred solar radii, which varies due to subtle changes in the core and nuclear burning shells situated at the bottom of the large convective envelope. The chemistry of mass loss from an AGB star is characterised as C- or O-rich, depending on whether the C/O ratio is greater or less than 1, respectively. The chemistry of convective envelope can be enriched by repeated deep convective envelope mixing (dredge-up). The first and second dredge-ups occur at the end of the H- and He-core burning phases, respectively. AGB stars are initially O-rich and can become C-rich, if material from deep within the star is brought to the surface

on the third dredge-up.

The mass loss on the AGB is thought to be mostly spherically symmetric and driven by radiation pressure on the condensed dust grains (cf Habing & Blommaert 1993). The mass loss becomes axisymmetric towards the end of the AGB stage and drops dramatically at the end of the AGB stage. The CSE detaches, the central star contracts and its effective temperature increases. The central source generates a fast-wind, which impacts the slower AGB wind. The classical theory of Planetary Nebula (PN) formation is the Interacting Stellar Wind model (ISW) (Kwok, Purton & Fitzgerald 1978), where material is swept up by a fast-wind produced from the hot ionising central star, which propagates into the slowly expanding AGB envelope. The Generalised ISW (GISW) model was developed to explain the elliptical and bipolar PNe morphologies, which can be described by a density distribution by Kahn & West (1985). The basic shapes were described as round, elliptical, bipolar and irregular (Balick 1987). In addition to these basic shapes other morphologies have been observed, such as the multipolar Starfish Nebula (Sahai, Sánchez Contreras, & Morris 2005), quadrupolar NGC 6881 (Guerrero & Manchado 1998) and point-symmetric Hen 3-1475 (Sahai 2004), which cannot be described by the GISW model.

Several surveys have attempted to systematically categorise PNe/PPNe shapes. Zhang & Kwok (1998) produced 110 simulated images and compared them to existing PNe. They determined that the equator-to-pole ratio varied from 1 to 10. Ueta, Meixner & Bobrowsky (2000) conducted a *Hubble Space Telescope* (*HST*) snapshot survey of 27 PPNe and separated them into two distinct groups based on the visibility of the central star and surrounding nebulosity. These two groups are Star-Obvious Low-level-Elongated (SOLE) and DUst-Prominent Longitudinally EXtended (DUPLEX). SOLE types are very low surface brightness elongated nebulosity that surrounds extremely bright central stars. DUPLEX types are limb-brightened bipolar lobes with partially visible or obscured central stars. A large proportion of

objects are compact and have a diameter of a few arcseconds. They also suggest that DUPLEX sources are higher mass due to their proximity to the Galactic plane.

The most recent *HST* surveys of PNe/PPNe have been conducted by Sahai et al. (2007) and Siódmiak et al. (2008), of which the former found no round young PNe. Sahai et al. (2007) suggest that the primary shaping of a PN occurs at a significantly earlier time than the PN stage and develop a new morphological classification scheme. The complexity of this scheme is evident for *IRAS* 19306+1407, which is classified as 'Bo⋆(0.60),h' that translates as a bipolar nebula with lobes open at each end, central star visible at 0.6 μm with a halo. A total of four primary classifications (biploar, multipolar, elongated and irregular) and 16 additional secondary classifications are used to describe PPNe/PNe. Siódmiak et al. (2008) use their *HST* survey[1] to classify PPNe as SOLE or DUPLEX based on the infrared colours. They reinforce the suggestion by Ueta et al. (2000) that DUPLEX and SOLE sources have high and low mass progenitors, respectively.

A definition of acronyms and abbreviations used in this thesis are located in the Glossary chapter starting on page 229.

[1] which some of their targets overlap with Sahai et al. (2007)

## 1.2 Shaping

The mechanism for shaping PPNe is a matter of some debate, in which the main proposed theories are fast rotating AGB stars, magnetic fields and binary interactions. Bujarrabal et al. (2001) found that radiatively driven winds could not supply sufficient momentum, by a factor of $> 500 - 1000$, to the molecular outflows in their PPNe. Therefore, any additional momentum must be supplied by the shaping mechanism. Soker (2006b) states that a single star cannot supply the energy and momentum to develop a large scale magnetic field to shape the CSE, and he strongly suggests that the primary shaping mechanism is due to binary interaction and that magnetic fields are not dynamically important within a shaping context. However, magnetic fields have been detected around post-AGB stars and PNe such as OH17.7-2.0 (+4.6 mG at 1612 MHz; +2.5mG at 1667 MHz; Bains et al 2003), *IRAS* 20406+2953 (-3.1 mG at 1612 MHz; Bains et al. 2004) and NGC 7027, NGC 6537, NGC 6302 and CRL 2688 ($\sim$few mG at 450- and 850-$\mu$m; Sabin, Zijlstra & Greaves 2007). These have been suggested to be local fields by Soker (2006b). Moe & De Marco (2006) and Soker (2006a) provide a population synthesis study of PNe created from single and binary stars and suggest that the current population of PNe can be explained by binary progenitors.

There are various models for the binary shaping of the CSE. Mastrodemos & Morris (1998) investigate the effect of mass loss from the primary star, which produces a permanent and stable accretion disk around the companion. Gawryszczak, Mikołajewska & Różyczka (2002) found that no axisymmetric structures arose if the companion was more than 10 AU from the mass-losing star. Nordhaus & Blackman (2006) investigated the effect of low-mass binary induced outflows from AGB stars and state three possible outcomes: (1) the envelope is ejected equatorially; (2) the envelope is spun-up and could produce dynamo driven jets, and (3) the companion

is shredded to form a disc that drives a collimated wind. In a later paper, Nordhaus, Blackman & Frank (2007) pursue the dynamo outcome and determine that magnetically or thermally induced 'explosions' are possible, which in the former case can produce a bipolar outflow.

It has been shown that a collimated outflow, from magnetically driven winds, is possible (e.g. García-Segura et al. 1999; Blackman et al. 2001; Blackman, Frank & Welch 2001; Gardiner & Frank 2001; García-Segura, López & Franco 2005). The underlying mechanism for producing these magnetic fields is unknown, but there are suggestions that it can be supplied from the angular momentum transfer from a companion or a rotational differential between the AGB core and its envelope.

There is a wide ranging debate concerning the origin of the shaping mechanisms, and combined binary and magnetic field models are currently being proposed (Blackman & Nordhaus 2007). To constrain these newer and existing models observable parameters such as outflow speed, equator-to-pole ratio, central star temperature and evolutionary state of the PPN etc. are desperately needed (see Frank et al. 2007, for a framework for investigating post-AGB stars, PPNe and PNe). This thesis presents observational techniques to constrain some of these observational parameters.

## 1.3 Observing gas and dust in PPNe

The post-AGB stage is short lived and the spectral type of the central illumination source ranges from G to O/B. The equatorial dusty torus can obscure the central star and a determination of the spectral type becomes difficult. Light is scattered by dust grains within the torus and into the polar lobes. The main problems in imaging PPNe are their compact size and the bright central illumination source. In many cases the inner radius of the CSE lies within the point spread function (PSF). Polarimetry can be used as a tool to image the CSE around the post-AGB star to differentiate between the polarised and unpolarised emission. The excitation of the CSE can indicate if it is a PPN or a PN, since shocks occur in the former and ionisation occurs in the later. Molecular hydrogen ($H_2$) has been used as an evolutionary marker (e.g. Davis et al. 2003; Kelly & Hrivnak 2005). If a fast wind is shocking the slower AGB envelope, it is possible that the $H_2$ emission can trace the interaction of these winds. If the CSE is being ionised and subjected to UV photons, it will be visible in atomic Hydrogen and $H_2$ emission. The following sections describe the use of light scattered by dust grains, and becoming polarised, and $H_2$ emission as tools to uncover the properties of post-AGB stars and their surrounding CSE.

### 1.3.1 Polarimetry

Imaging polarimetry is a differential imaging technique, which is well-suited to the study of CSEs surrounding post-AGB stars. The technique discriminates between the faint but polarised scattered light from the PPN and any bright unpolarised emission from the central star. This enables the imaging of circumstellar material that would normally be lost under the wings of the stellar PSF, thereby obtaining information on the dust distribution close to the central source. Imaging polarimetric

surveys of post-AGB stars using the United Kingdom Infrared Telescope (UKIRT) have detected scattered light from PPN around 34 stars, and all of these PPN were found to be axisymmetric in some way (Gledhill et al. 2001; Gledhill 2005). Higher spatial resolution polarimetry using the *HST* has enabled more detailed studies of the morphology of PPN, as well as providing constraints on dust grain properties in these systems, and has revealed point-symmetries, jets and multilobed structures (e.g. Ueta et al. 2005; Su et al. 2003). The combined modelling of the scattered light and radiative transfer models can provide information on the equator-to-pole density ratios, spectral type, CSE chemistry, inclination angle and the mass of the CSE.

### 1.3.2 Molecular Hydrogen

The $H_2$ molecule has no dipole moment and can only emit ro-vibrational lines, with wavelengths from ultraviolet (UV) to the mid-infrared (mid-IR). In this thesis, the $H_2$ emission is used as a marker to probe the interaction between the slow and fast winds. The emission lines are caused by a change in vibrational, $v$, and rotational, $J$, quantum level of $H_2$. The quadrupole nature of $H_2$ means that the rotational quantum numbers can change by 2, 0 or -2, excluding the $v = 0 - 0$ transition, that are denoted by S, Q or O, which indicates that $J$ is less, equal or greater than the quantum number in the upper level, respectively. For example: the 1-0 S(1) (2.1218 μm) line has the same vibrational and rotational upper level quantum numbers as the 1-0 Q(3) (2.4237 μm) line. This enables a measurement of the extinction at $K$-band and an estimation of extinction at $V$, however the 1-0 Q(3) line occurs in an opaque part of the $K$-band.

The measurement of the various line ratios, 2-1 S(1) and 1-0 S(0), 3-2 S(3) and the Br$\gamma$ transition makes it possible to differentiate between the excitation mechanisms (Davis et al. 2003). The ratio of 1-0 S(0)/2-1 S(1) can be used in

principle to discriminate between fluorescence and shocking, the lower the ratio the greater the fluorescence, but this diagnostic breaks down at high densities ($10^5$ $cm^{-3}$) in photo-dissociation regions (PDRs). The higher populations ($v = 2-1$) will become filled and give ratios of 10-20, similar to shocking or gas in local thermal equilibrium (LTE), even if the gas is undergoing fluorescence. Additional higher vibrational state line ratios (e.g. 1-0 S(1)/3-2 S(3)) can be used as an additional check for fluorescence. This is described further in Chapters 3 and 6.

### 1.3.3 Previous $H_2$ observations

$H_2$ absorption and emission has been observed from the UV through the near-infrared and into the mid-infrared for PNe/PPNe (e.g. Hurwitz 1998; Kastner et al. 1996; Cox et al. 1998). Kastner et al. (1996) present an $H_2$ imaging survey at 2.122 μm for 60 PNe with 23 detections and suggest that this emission is a signature of bipolarity. They conclude that the majority of emission originates from the ring-like or equatorial waists in PNe. They state that bipolar PNe are constrained to low Galactic latitudes and conclude they have a larger progenitor mass than non-emitters of $H_2$. They suggest $H_2$ emission arising in four PNe originates from fluorescence and that the rest of their sample is excited by shocks.

García-Hernández et al. (2002) conducted an infrared spectroscopy survey of southern targets, in which they primarily looked at 1-0 S(1), 2-1 S(1), Br$\alpha$, Br$\gamma$, Pfund$\gamma$ and CO[v=2-0] transition and recombination lines. They find that the emission of $H_2$ is dependant on the excitation mechanism and not morphology. Fluorescent excitation is produced by hot and rapidly evolving central post-AGB stars, which excite the $H_2$ in their CSEs. The bipolar PPNe that emit $H_2$ are shock excited and can preserve the molecule into the PNe stage. They suggest that the correlation between bipolarity and $H_2$ emission, in previous studies, is a *"consequence of the bias"*. Their chosen diagnostic of using the 1-0 S(1)/2-1 S(1) and 1-0 S(1)/Br$\gamma$ is

shown to be a good indicator of the excitation mechanism in the PPNe. However, they were unable to determine the spatial resolution of the $H_2$ emission and therefore the subsequent locations of the fluorescence and shocks.

Davis et al. (2003) investigated 11 bright PNe and PPNe using *K*-band spectroscopy. They used a combined model of shocks and fluorescence and concluded that the excitation changes with the evolution of the PPNe/PNe. They found that fluorescence is a component in all of their observations and is needed to explain the $H_2$ emission from the higher vibrational states. They suggest that fluorescence is *"probably the major excitation mechanism for intermediate evolutionary stages"* and there may be a period of time that $H_2$ is observable in PPNe/PNe. They acknowledge that their sample is biased towards bright $H_2$ sources and further high resolution spectroscopy studies are needed to confirm the mixture of shocks and fluorescence.

Kelly & Hrivnak (2005) conducted a *K*-band spectroscopic survey of 51 objects, in which 16 objects had detected $H_2$ emission. These focused on PPNe north of -30° and a range of spectral types ranging from G to B. The earlier G, F and A spectral types have a correlation with a bipolar shape, whilst the majority of the B-type PPNe emitted $H_2$, which was stimulated by fluorescence, thermal or a mixture of both mechanisms. They also state for B spectral types that *"there does not appear to be a correlation between morphology and $H_2$ emission"* and *"show $H_2$ emission, irrespective of morphology."* Kelly & Hrivnak (2005) found that the B-types were all classified as SOLE types except *IRAS* 19306+1407, which is DUPLEX[2]. The $H_2$ emitting G-A type PPNe were close to the Galactic plane at a latitude of $3.6 \pm 1.2°$, whilst the B-types had a greater range of $8.1 \pm 2.4°$. The B-types shared a similar range to the G-A types that do not emit $H_2$. They proposed the flowing evolutionary sequence: (1) F-G type stars with an equatorial torus always develop a collimated

[2]Siódmiak et al. (2008) classify *IRAS* 19306+1407 as SOLE.

fast wind; (2) the fast-wind is focused and collimated, by the gas and dust in the torus, along the polar axis; (3) the shape of the PPNe remains bipolar throughout the post-AGB stage and into the PN stage; (4) once the central illumination source becomes a B-type star, it begins to excite the $H_2$ with UV photons in conjunction with shocks. They suggest that the $H_2$ is protected from disassociation, due to UV photons, by $H_2$ self-shielding and dust grains. The $H_2$ emission from non-bipolar B-type PPNe is excited by UV photons. The fluoresced $H_2$ emission is common to all objects, and is a short-lived transient stage, before the CSE becomes ionised

A sample of post-AGB stars from Kastner et al. (1996), García-Hernández et al. (2002) and Kelly & Hrivnak (2005) provide a basis for follow up observations at high spectral and spatial resolution. These two types of observations can be combined using Integral Field Spectroscopy (IFS) for high spatial and spectral resolution over a small Field of View (FOV). This new observing technique has been rarely used to investigate PPNe and PNe (e.g. Tsamis et al. 2008; Sharp et al. 2006; Sandin et al. 2006; Lowe & Gledhill 2006; Santander-García, Corradi, & Mampaso 2005; Exter & Christensen 2005; Monreal-Ibero et al. 2005), and this thesis presents one of the first few near-IR IFS observations of a PPN.

### 1.3.4 Summary of the main observational techniques

This thesis presents two astronomical techniques to investigate the post-AGB stage. The polarimetry is used to investigate the scattered light by dust grains within the CSE, whilst the *K*-band IFS examines the $H_2$ and Br$\gamma$ emission from the CSE and central illumination source at high spectral and spatial resolution. The majority of PPNe are compact and have a radius of a few arcseconds, which can easily fit within the FOV of an IFS instrument. Therefore it is possible to directly compare the dust and gas in PPNe using both techniques. *IRAS* 19306+1407 is used as a test case for the combination of these techniques.

### 1.3.5 Target selection

In 2003 *IRAS*, *JHK* and *V*-band photometry and *ISO* spectroscopy was the sum total of published information for *IRAS* 19306+1407 (Omont et al. 1993; Kwok, Volk & Bidelman 1997; García-Lario et al. 1997; Hrivnak, Volk & Kwok 2000). The spectral energy distribution (SED) of *IRAS* 19306+1407 is displayed in Fig. 1.5. Preliminary polarimetric observations (PI: Gledhill), taken in 2003, showed a spatially resolved CSE in polarised flux (see Chapter 5). Kelly et al. (2004) presented a single slit *K*-band spectrum, which indicated that this object showed a mixture of shock and fluorescence, and was possibly beginning to ionise its CSE. Volk, Hrivnak & Kwok (2004) presented the first image of spatially resolved $H_2$ emission in the CSE, which appeared similar to the polarimetric observations, whilst the archived *HST* image showed a different morphology.

An IFS program was created to observe *IRAS* 19306+1407 to determine the locations of the excited $H_2$ with respect to the polarised light. *IRAS* 19306+1407 is important to observe because the dusty torus and $H_2$ emission can be resolved. The $H_2$ emission could be due to shocks from the shaping process or the result of UV photons from the central source. The atomic hydrogen emission has been detected, but has not been spatially resolved.

The central illumination spectral type is loosely defined as a B-type or faint-K by Hrivnak et al. (2000) and García-Lario et al. (1997), respectively, which the former would indicate a possible transisition between post-AGB to young PN stage. If *IRAS* 19306+1407 is on the cusp of becoming a young PNe, it is important to investigate the shaping and evolution of its CSE from the PPNe to the PNe stage.

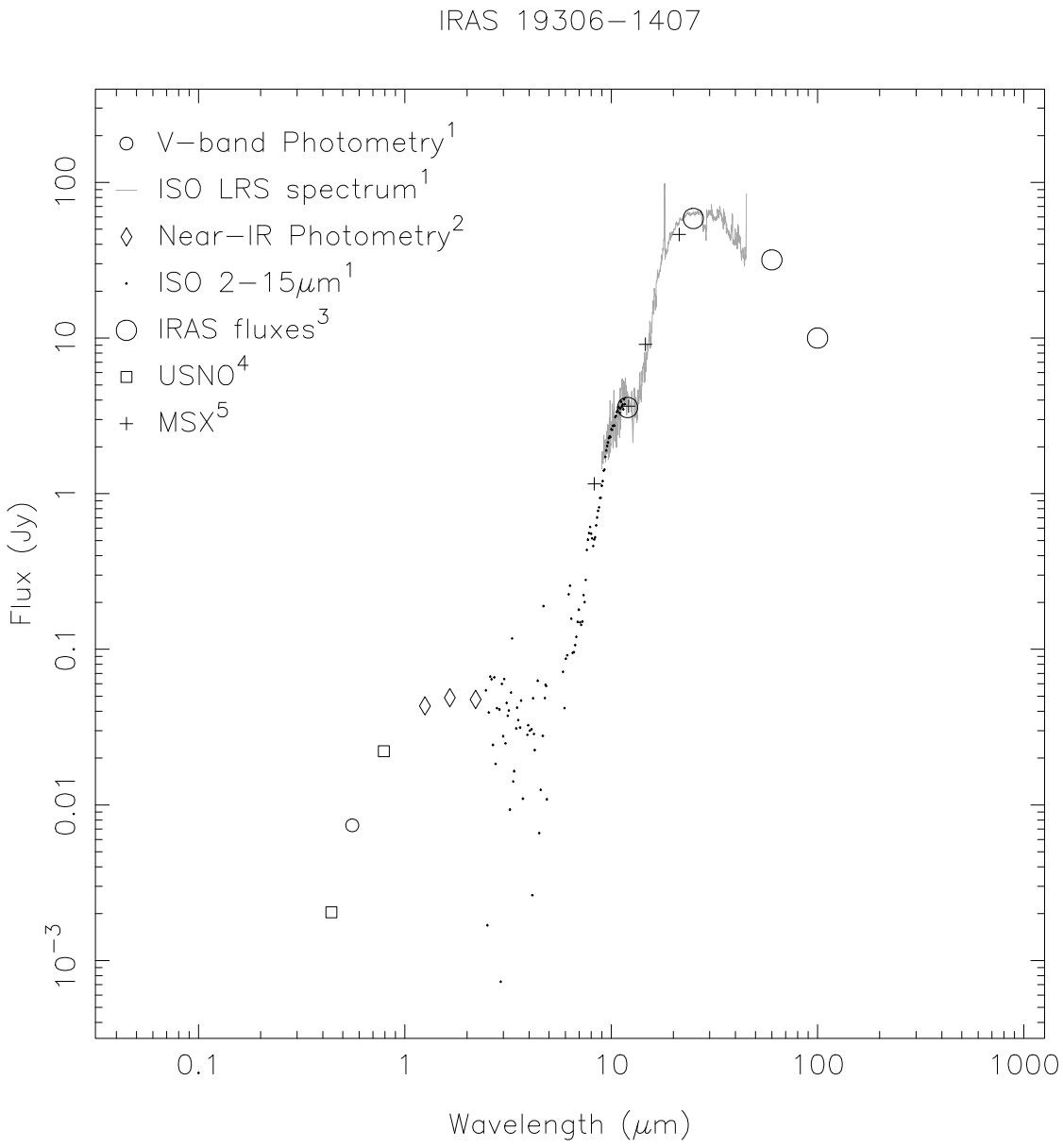


Figure 1.5: The observed SED for *IRAS* 19306+1407. References: (1) Hrivnak et al. (2000), (2) Ueta et al. (2003), (3) Joint *IRAS* Science working group (1988), (4) Monet et al. (2003) and (5) Egan et al. (2003)

## 1.4 Structure of thesis

The thesis is organised with the following structure:

**Chapter 1:** presents the background to post-AGB star evolution and shaping of the circumstellar envelope. The difficulties of observing the circumstellar envelope and the shaping mechanisms with the previous observations for imaging, imaging polarimetry and spectroscopy described.

**Chapter 2:** outlines the observational and subsequent data reduction techniques for imaging polarimetry and integral field spectroscopy that are presented in this thesis. A description of the instruments and telescopes used are also included.

**Chapter 3:** shows the mathematical treatment of the $H_2$ information, to produce an extinction correction, line ratios, column density ratio, ortho-para ratios and vibration-rotation temperatures from the integral field spectroscopy

**Chapter 4:** describes the IDL package, Fitting Utility for SINFONI (FUS), that I created to interpret, reduce and analyse the SINFONI integral field spectroscopy data.

**Chapter 5:** is the first science chapter that describes the near-IR imaging polarimetry in conjunction with *HST* images and submillmetre photometry of *IRAS* 19306+1407. This chapter also documents the modelling of the dusty circumstellar envelope with axisymmetric radiative transfer and light scattering models.

**Chapter 6:** details the integral field spectroscopy from UKIRT and VLT instruments of *IRAS* 19306+1407 and compares the results with fluorescence and shock models.

**Chapter 7:** combines the results from chapters 5 and 6 to produce an overall picture of *IRAS* 19306+1407 and is used to determine its evolutionary state.

# Chapter 2

# Near-infrared Polarimetry and Integral Field Spectroscopy

This chapter introduces the background to polarimetry and integral field spectroscopy. This will include a description of UKIRT and Very Large Telescope (VLT) with their respective instruments, which are used in this dissertation to observe post-AGB stars. These astronomical observing techniques are more involved than standard imaging and spectroscopy with a description of the data reduction processes using the STARLINK reduction suite and the European Southern Observatory (ESO) pipeline.

## 2.1 Polarimetry

Polarimetry is a differential imaging technique, which is a very powerful tool for resolving the dusty CSEs surrounding post-AGB stars (Dougados et al. 1990; Gledhill et al. 2001; Gledhill & Takami 2001; Gledhill 2005). This technique discriminates between the faint polarised scattered light from the dusty CSE and the bright unpolarised emission from the central star. Normally the imaging of CSE material

would be lost under the wings of the PSF, since the inner radius of a CSE can be less than 1 arcsec. Therefore, information can be obtained on the dusty CSE close to the central source. An excellent example of this technique is displayed in Fig. 2.1, taken from Gledhill et al. (2001), which shows that the total intensity is dominated by the PSF of the star and the polarised light shows an extended structure. Imaging at multiple wavelengths can provide additional information on the properties of post-AGB stars and their surrounding CSEs. It is possible to obtain information on the grain size distribution, dust species, extinction, equator-to-pole density contrast ratio and structure of the CSE by modelling the observations.

The equipment and resources required for polarimetry restricts its use to a few telescopes world wide. Polarimetry either requires a dedicated instrument or a modification to the telescope's light path (e.g. IRPOL2). A list of commissioned polarimetry instruments, wave-plates and their host telescopes is given in Table 2.1. The polarimetry equipment used is described in § 2.1.2.

### 2.1.1 Scattering

Light can be polarised by a variety of processes, and the polarisation that considered in this thesis is produced by light scattering due to dust grains. The size or type of the particle relative to wavelength will determine if light will be scattered in the Rayleigh, Thomson or Mie regimes. Thomson scattering is produced by light scattering off free electrons and can be detected in the coronas of hot stars; however, the electron density in the CSE of a post-AGB star is too low for this to be a significant contribution to any observed polarised flux.

When discussing light scattering by a dust particle, it is useful to consider the

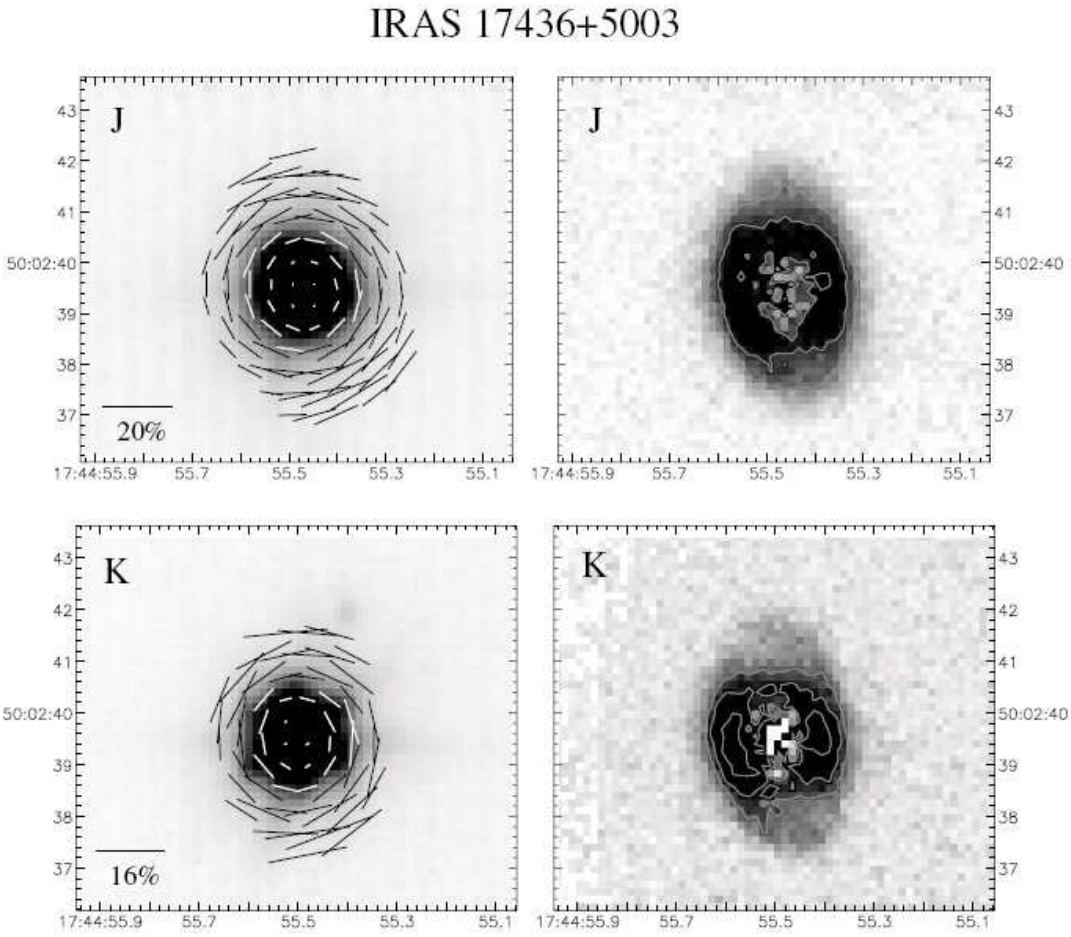


**Figure 3.** Polarimetric observations of IRAS 17436+5003 in the *J* and *K* bands. Details as for Fig. 1.

Figure 2.1: An example of imaging polarimetry taken from Gledhill et al. (2001). The left hand panels (total intensity) clearly show a point source like structure with a centro-symmetric polarisation pattern elongated north north-east and south south-west for *J*- and *K*-band, top and bottom respectively. Assuming an optically thin case, the dust shell is being illuminated isotropically by a central source. The right hand panels show the polarised flux with bright scattering arcs embedded in an extended faint halo.

Table 2.1: A list of major infrared polarimetry facilities available to UK astronomers in 2008 and ordered by telescope size, including the instrument name, telescope and location, wavelength range, polarimetry modes available, usable wave-bands, type of polariser and additional instrument configurations.

| Instrument† | Telescope† | Wavelength range [μm] | Polarimetry modes⋆ | Additional notes |
|---|---|---|---|---|
| SofI | 3.6-m NTT, La Silla, Chile. | 0.9 - 2.5 | D: ∥ Im. | Fixed polariser - instrument rotated. |
| IRPOL2 + UIST, UFTI, and CGS4. | 3.8-m UKIRT, Mauna Kea, Hawai'i. | 0.9 - 2.5, 3.5 & 4.75 | D: ◯ & ∥ Im. & Sp. | Wave-plates. *I, J, H, K, L* and *M* bands. Coronagraphic mask available. |
| MICHELLE | 8-m Gemini North, Mauna Kea, Hawai'i. | 10 & 20 | S: ∥ Im.‡ | Wire-grids and wave-plates. *N* and *Q* bands. |
| ISAAC | 8.2-m VLT (UT1), Paranal, Chile. | 0.9 - 2.5 | D: ∥ Im. | Wave-plate. *Z, J,* H and *K* bands. |
| NACO | 8.2-m VLT (UT4), Paranal, Chile. | 1.0 - 5.0 | D: ∥ Im. | Wollaston prisms and wave-plate. *J*-band not available. |

†Instrument and telescope acronyms are displayed below and in the glossary.

⋆D: - dual beam polarimeter, S: - single beam polarimeter, ◯ - circular polarimetry, ∥ - linear polarimetry, Im. - imaging polarimetry and Sp. - spectro-polarimetry offered. ‡Spectro-polarimetry mode is not commissioned.

NTT - New Technology Telescope, UKIRT - United Kingdom Infrared Telescope and VLT - Very Large Telescope.

SofI - Son of Isaac, IRPOL2 - infrared polarimetry waveplate, UFTI - UKIRT fast track imager, UIST - UKIRT 1-5 micron imager spectrometer, MICHELLE - mid-infrared echelle spectrograph, ISAAC - infrared spectrometer and array camera and NACO - NAOS CONICA, which inturn is an acronym of nasmyth adaptive optics system and coude near infrared camera.

size parameter, $x$, which is defined as

$$x = \frac{2\pi a}{\lambda}, \tag{2.1}$$

assuming a spherical particle with a radius, $a$, with an incident beam of light of wavelength, $\lambda$. If $x \ll 1$ then light is scattered in the Rayleigh regime, for which the scattering cross section is proportional to $\lambda^{-4}$. Hence at short wavelengths light is scattered more efficiently than at longer wavelengths. For example blue light is more efficiently scattered, by nitrogen and oxygen molecules in the Earth's atmosphere, than red light, hence the daytime sky is blue.

A description of scattering by particles larger than the Rayleigh limit requires a rigorous solution and, in the case of spherical particles, this is provided by Mie theory (Mie 1908; Bohren & Huffman 1983). Unlike the case of Rayleigh scattering, Mie scattering solutions are rarely analytical and have to be calculated numerically. The modelling codes used in this thesis are discussed further in Chapter 5.

### 2.1.2 Imaging Polarimetry at UKIRT

UKIRT is located on Mauna Kea in Hawai'i at an altitude of 4194 m above sea level. The site is well suited for infrared observations and UKIRT experiences a median seeing of 0.43 arcsec. The telescope consists of a 3.8 m diameter mirror and a Cassegrain suite of instruments. In polarimetric mode, the incoming light passes through a half wave-plate module, IRPOL2 (see Fig. 2.2), constructed by the University of Hertfordshire and situated underneath the primary mirror and above the dichroic and instruments. This position allows correction for the polarisation introduced by the telescope dichroic and instrument optics and enables the use of polarimetry with all Cassegrain instruments, which are the Cooled Grating Spectrometer 4 (CGS4), UKIRT Fast-Track Imager (UFTI) and the UKIRT 1-5 micron

Imager Spectrometer (UIST; Ramsay Howat et al. 1998). The near-IR wave-plate is composed of Quartz and Magnesium Fluoride, achromatic from 0.9 to 2.5 μm and is manufactured with a free aperture diameter of 95 mm, so as not to vignette the UIST field of view. The dichroic separates the visible and infrared light, with the latter directed to the Cassegrain instruments. Light entering the UIST instrument, passes through the desired infrared filter, focal plane mask and a subsequent Wollaston prism, which splits the light beam into two separate *o*- and *e*-beams. The beams have an angular separation of 20.4 and 19.9 arcsec for *J*- and *K*-filters at a pixel scale of 0.12 arcsec pixel$^{-1}$, respectively. The focal plane mask ensures that the object and sky *o*- and *e*-beams are separated on the detector. These images are projected onto the 1024×1024 pixel Indium Antimonide (InSb) array, which can be configured to observe bright sources, enabling magnitudes of $J > 6$ and $K > 5.6$ to be observed. This can be achieved by using very short exposure times, requiring the use of a 512 by 512 pixel sub-array and removal of the focal plane mask. The polarimetry data presented in this thesis was observed without the focal plane mask. However, this method produces highly polarised artefacts, which are documented further in section 2.1.3.

Polarimetry data can be reduced as normal imaging data, but with a few additional steps. To reduce the polarimetry data, three packages from the STARLINK software suite are required. These are CCDPACK, KAPPA and POLPACK. An overview of the data reduction process is shown in Fig. 2.3 and is documented in Berry & Gledhill (2003).

All images are dark subtracted, this includes the sky flats, science and standard images. This removes the dark current from the images. A bad pixel mask is applied to remove hot, cold and dead pixels. The bad pixel mask is generated using the UKIRT pipeline software, ORACDR, based on sigma clipped array test images. All sky flat images are median combined and normalised to produce a master flat field,

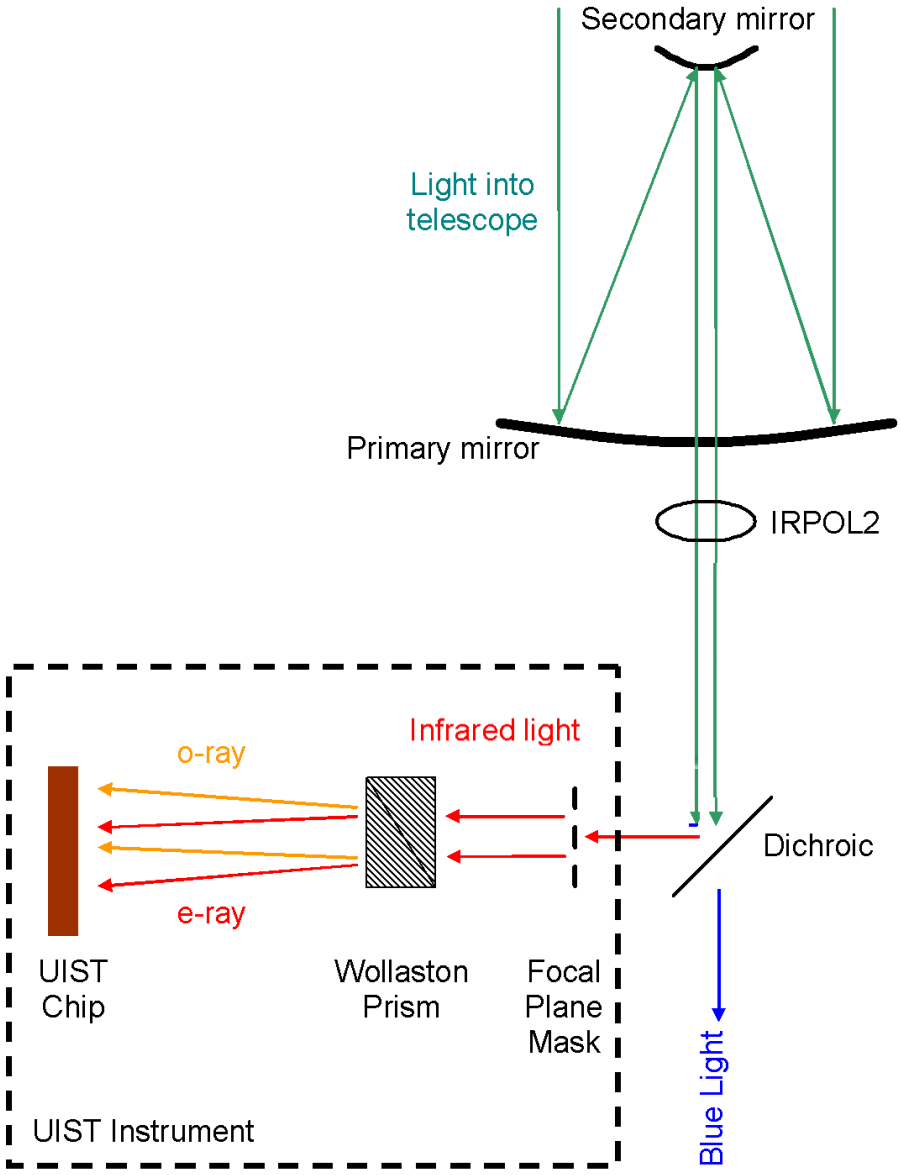


Figure 2.2: A cartoon of the light path through UKIRT in polarimetry mode with UIST. The light is reflected by the primary mirror up to the secondary mirror and passes through IRPOL2. The dichroic reflects infrared light and is transparent to blue light, which is directed towards the guider camera. The infrared light passes into UIST through a filter (not marked on diagram). The light is spilt into two components (*o*- and *e*-rays) by the Wollaston prism and focused onto the UIST chip.

which is subsequently cleaned by hand. The science and standard images are cleaned by hand to remove any remaining bad pixels and cosmic rays. The master flat field is applied to the science and standard images, to correct for any variations in the pixel to pixel sensitivity of the CCD array.

These images are now in the required format for the polarimetry reduction. The POLKA program, in the POLPACK suite, was developed for the reduction of single and dual beam polarimetry data and calculation of the Stokes parameters. The detailed use of this program is documented in Berry & Gledhill (2003) and the rest of this section details the mathematical method POLKA uses to calculate the Stokes parameters.

The Stokes parameters can be calculated from images taken at two wave-plate positions, however, additional plate positions are required to remove any instrumental effects or atmospheric variations. The first step is to subtract the sky emission from the images. The Stokes parameters are calculated using Malus' Law which is of the form,

$$I_\alpha = I_\mathrm{p} \cos^2(\alpha - \theta), \tag{2.2}$$

where $\theta$ is the angular difference between the plane of polarisation of the incident light and the reference direction, $I_\alpha$ is the transmitted intensity of the component polarised at angle $\alpha$ relative to the reference direction and $I_\mathrm{p}$ is the intensity of the incident beam. In the presence of unpolarised light, $I_\mathrm{up}$, Equation 2.2 is modified to

$$I_\alpha = I_\mathrm{p} \cos^2(\alpha - \theta) + I_\mathrm{up}. \tag{2.3}$$

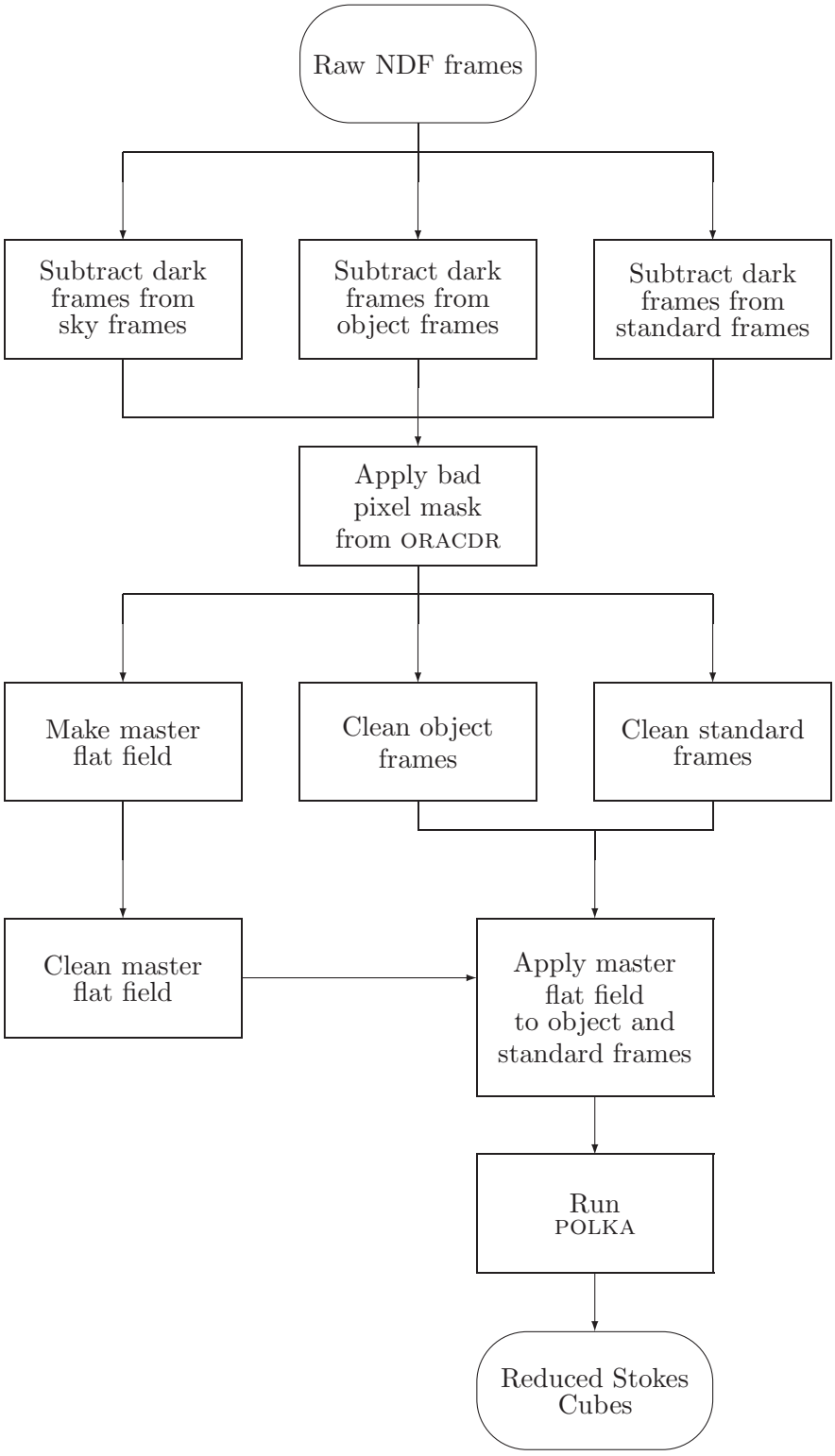


Figure 2.3: An overview of the polarimetry data reduction process, starting from the raw NDF images through the dark subtraction and bad pixel masking. The master flat field is applied independently to the object and standard images, which are processed separately by POLKA to produce the final reduced Stokes data cube.

For the 0° wave-plate position the *o*- and *e*-ray intensities are

$$I_{0^\circ} = I_{\rm p}\cos^2\theta + \frac{I_{\rm up}}{2} \quad \text{and} \tag{2.4}$$

$$I_{90^\circ} = I_{\rm p}\cos^2(90^\circ - \theta) + \frac{I_{\rm up}}{2} \tag{2.5}$$

$$= I_{\rm p}\sin^2\theta + \frac{I_{\rm up}}{2} \tag{2.6}$$

If the half wave-plate is rotated by 22.5° this modifies Equations 2.4 and 2.6 to

$$I_{45^\circ} = I_{\rm p}\cos^2(45 - \theta) + \frac{I_{\rm up}}{2} \quad \text{and} \tag{2.7}$$

$$I_{135^\circ} = I_{\rm p}\sin^2(45 - \theta) + \frac{I_{\rm up}}{2}. \tag{2.8}$$

The Stokes parameters *I, Q* and *U* can be calculated from these images and are given by

$$I = I_{0^\circ} + I_{90^\circ} \equiv I_{45^\circ} + I_{135^\circ}, \tag{2.9}$$

$$Q = I_{0^\circ} - I_{90^\circ} \equiv I_{\rm p}\cos(2\theta) \quad \text{and} \tag{2.10}$$

$$U = I_{45^\circ} - I_{135^\circ} \equiv I_{\rm p}\sin(2\theta). \tag{2.11}$$

These Stokes parameters are formed into a data cube and can be manipulated to produce linear per cent polarisation ($p$), polarised flux images ($I_{\rm pi}$) and angle of polarisation, which are given below

$$p = \frac{\sqrt{Q^2 + U^2}}{I}, \tag{2.12}$$

$$\theta = \frac{1}{2}\tan^{-1}\left(\frac{U}{Q}\right) \quad \text{and} \tag{2.13}$$

$$I_{\rm pi} = \sqrt{Q^2 + U^2}. \tag{2.14}$$

Using the definitions for $I$, $Q$ and $U$ stated in Equations 2.9, 2.10 and 2.11 the

polarised flux, per cent polarisation and angle of polarisation take the form,

$$p = \frac{\sqrt{(I_{0^\circ} - I_{90^\circ})^2 + (I_{45^\circ} - I_{135^\circ})^2}}{(I_{0^\circ} + I_{90^\circ})^2}, \tag{2.15}$$

$$\theta = \frac{1}{2}\tan^{-1}\left(\frac{I_{45^\circ} - I_{135^\circ}}{I_{0^\circ} - I_{90^\circ}}\right) \quad \text{and} \tag{2.16}$$

$$I_{\rm pi} = \sqrt{(I_{0^\circ} - I_{90^\circ})^2 + (I_{45^\circ} - I_{135^\circ})^2} \tag{2.17}$$

Additional images are observed at half wave-plate positions of 45° and 67.5° and are used to correct for instrumental bias (e.g. differences in the relative strengths of the *o*- and *e*-beams). The instrumental polarisation, for imaging polarimetry with UIST, is less than 1 per cent at *J*- and *K*-bands[1]. Once the data reduction is completed the images are presented using POLPACK and KAPPA software packages.

### 2.1.3 Reduction artefacts due to instrumental setup

To observe bright sources without the risk of saturation, the UIST chip can be configured as a 512 by 512 pixel sub-array, which enables faster readout times and exposures of less than 1 second. However, in order to use the sub-array, the focal plane polarimetry mask has to be removed. This results in the overlapping of the *o*- and *e*-beams produced by the Wollaston prism, with a final analysis area of 20 by 60 arcsec. The Wollaston prism splits each source into an *e*- and *o*-component separated by approximately 20 arcsec, so that any star in the field lying more than 10 arcsec along the prism dispersion axis from the target will only have one component in the analysis area (see Fig. 2.4). Since both *o*- and *e*-beams are required to calculate the Stokes intensities *I, Q* and *U* correctly, these offset stars appear as highly polarised artefacts in the reduced data. As the prism dispersion varies slightly with wavelength, this results in an apparent shift of the artefact stars between *J*-

[1] see `http://www.jach.hawaii.edu/UKIRT/instruments/irpol/UKIRT-pol-standards.html` for values

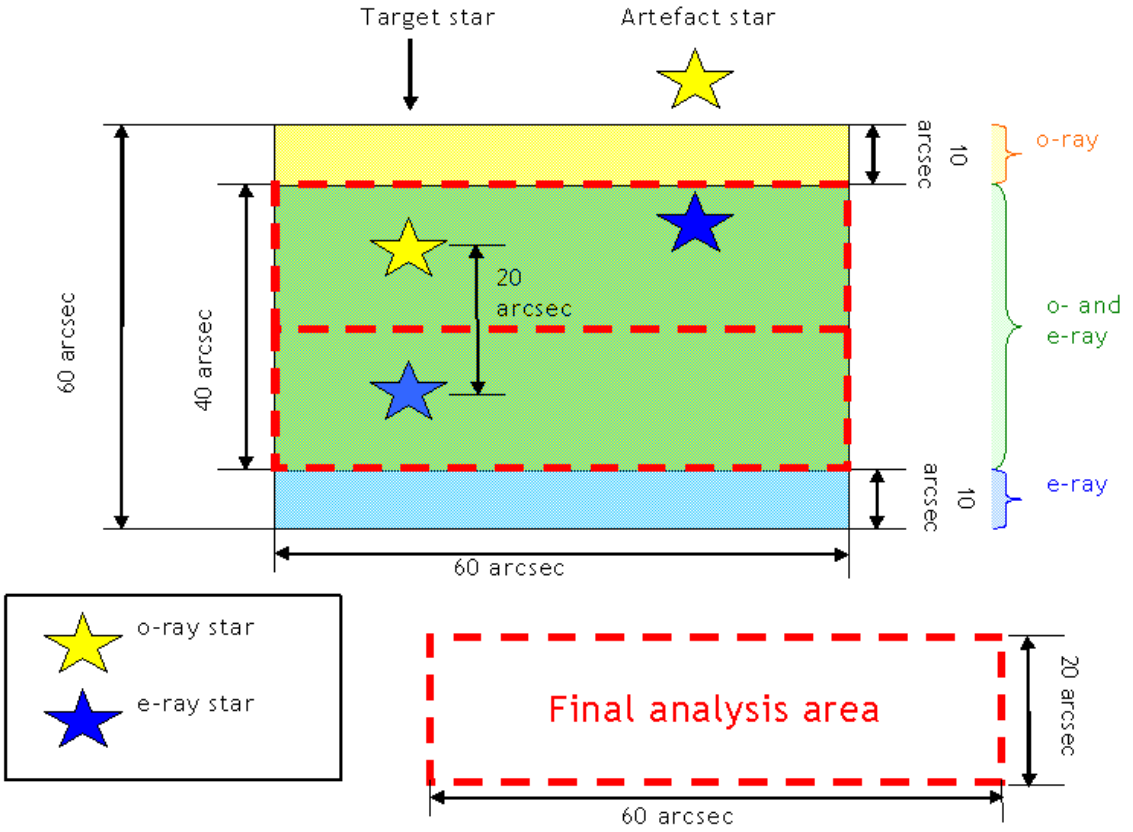


Figure 2.4: A cartoon showing how an artefact star is produced in unmasked imaging polarimetry. The o- and e-ray regions beams can be projected in areas indicated as yellow and blue, respectively, and the overlapping beams are shown as a green. The o- and e-ray stars are projected as yellow and blue, respectively. The total projected area is 60 by 60 arcsec and the overlapping beams are 40 by 60 arcsec. The o- and e-ray analysis areas are indicated by two red dotted boxes, which are combined into the 20 by 60 arcsec final analysis area. The target star (left) is projected into each e- and o-ray analysis areas, whilst the artefact star (right) is projected in one analysis area and vignetted.

and $K$- filters with respect to the science target.

## 2.2 Near-Infrared Integral Field Spectroscopy

Near-IR IFS is a relatively new observing technique in Astronomy, which can be thought of as multiple spectra observed simultaneously. It can be used to measure the emission and absorption line kinematics and relative intensities at high spatial resolution (Allard et al. 2006; Allard, Peletier & Knapen 2005). However, an integral field unit (IFU) has a limited FOV, which can be increased by sacrificing spectral or spatial resolution for a constant CCD detector size.

There are three major types of instrument configurations for IFUs. These are lenslet arrays, lenslet-fibre arrays and image slicing. An image slicer splits the FOV from the telescope into many smaller elements, which pass through a spectrograph to produce a spectrum for each sliced image. These spectra are projected onto the detector chip, which are then reduced to form a data cube with spatial and wavelength dimensions ($x \times y \times \lambda$). This can also be interpreted as a spectrum at every spatial pixel or an image at every wavelength point. The instruments described in this thesis are based on image slicing technology, which efficiently uses the CCD detector, a high throughput and information density.

IFS is commonly used to observe the extragalactic universe, since the wavelength information can be interpreted as velocity space. It can also be a useful tool to analyse kinematics and line emission/absorption in galactic sources. The added advantage of IFS is to spatially resolve the gas kinematics, but this is limited by the resolution of the spectrograph, $R = \lambda_0/\Delta\lambda$, where $\lambda_0$ is the reference wavelength and $\Delta\lambda$ is the minimum measurable change in wavelength. The velocity resolution, $\Delta v$, is equal to

$$\frac{\Delta\lambda}{\lambda} \cdot c \quad \text{or} \quad \frac{c}{R} \quad \text{, where c is the speed of light.} \tag{2.18}$$

The details of UIST and SINFONI IFS and their velocity resolution (Eisenhauer et

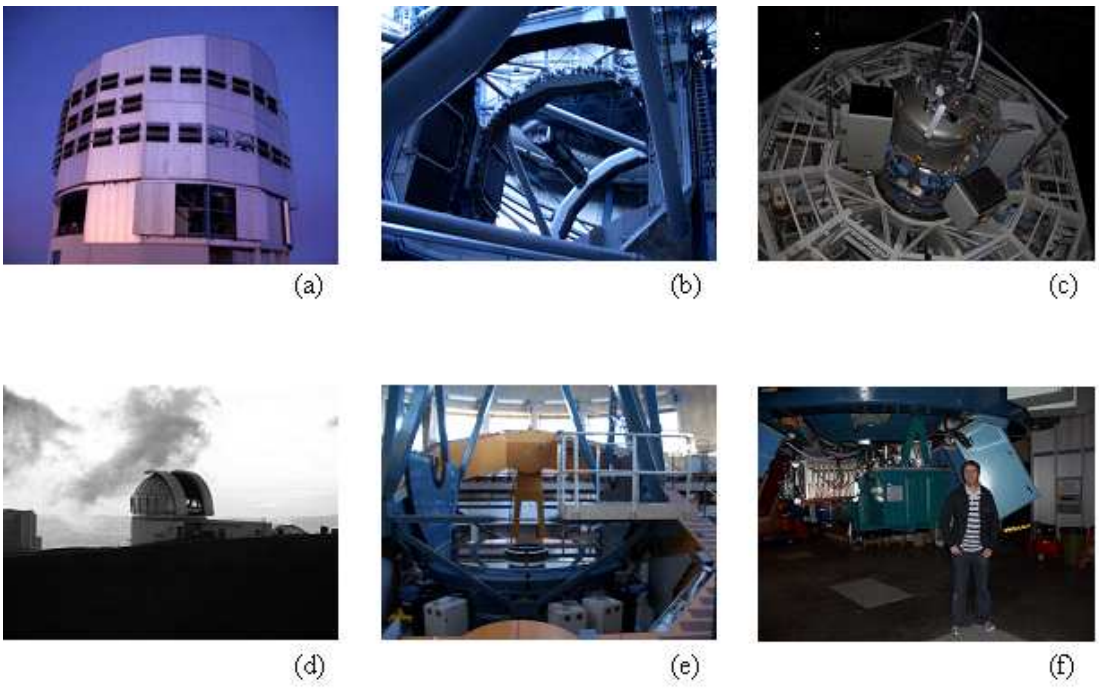


Figure 2.5: This collection of images show the various aspects of the VLT and UKIRT with the instruments SINFONI and UIST. The VLT's UT4 telescope with atmospheric vents visible (a), 8-m primary mirror with a central tertiary mirror to direct the light path to Nasmyth focus instruments (b) and the SINFONI instrument situated at the Cassegrain focus(c). The UKIRT telescope situated at Mauna Kea (d), 3.8-m primary mirror of UKIRT (e), and a picture of the author next to the UIST instrument (f).

Table 2.2: A summary of the two IFS instruments, SINFONI and UIST+IFU, used in this thesis. The details of the pixel scale, wavelength coverage, field of view, and spectral and velocity resolution are given.

| Instrument | Pixel Scale (arcsec × arcsec) | Wavelength coverage (μm) | Spectral resolving power | Velocity resolution ($kms^{-1}$) | Field of view (arcsec × arcsec) |
|---|---|---|---|---|---|
| UIST | 0.24×0.12 | ∼2.02 - ∼2.25 | 1800 | ∼166 | 3.3×6.0 |
| SINFONI | 0.05×0.1 | 1.95 - 2.45 | 5090† | ∼58.9 | 3×3 |
| SINFONI | 0.0125×0.025 | 1.95 - 2.45 | 5950† | ∼50.4 | 0.8×0.8 |

†The spectral resolution varies as a function of the pixel scale.

al. 2003; Bonnet et al. 2004; Kissler-Patig & Szeifert 2005) are given in Table 2.2. However, it is possible to obtain a greater velocity resolution by careful fitting of a Gaussian curve to an emission line. The fitting of emission lines at every spatial coordinate will give emission line maps, which can then be used to produce line intensity ratio maps. If the signal-to-noise for a particular emission line is low, it can be increased by summing the spatial component (henceforth known as 'binning up'). In addition similar regions can be combined to reduce the data generated to manageable levels.

### 2.2.1 IFS at UKIRT

The IFU is a component of UIST (described in § 2.1.2) and is 'slotted' into the light path for IFS observations. The IFU consists of 18 mirrors[2], of which 14 are usable, and gives a rotatable $3.3 \times 6.0$ arcsec$^2$ FOV of the sky. Each mirror projects a $0.24 \times 6.0$ arcsec$^2$ 'slice' onto the CCD (Fig. 2.6). The spatial resolution is $0.24 \times 0.12$ arcsec$^2$ with a spectroscopic resolution for the *short-K* band grism of $\sim 1800$. These slices are staggered to minimise cross contamination from strong emission lines; however, this reduces the overall wavelength coverage by approximately 4 per cent at either end of the spectrum, giving a wavelength coverage of ∼2.02- to ∼2.25-μm, rather than 2.01- to 2.26-μm for long slit spectroscopy. The throughput

[2]4 of which are vignetted or damaged

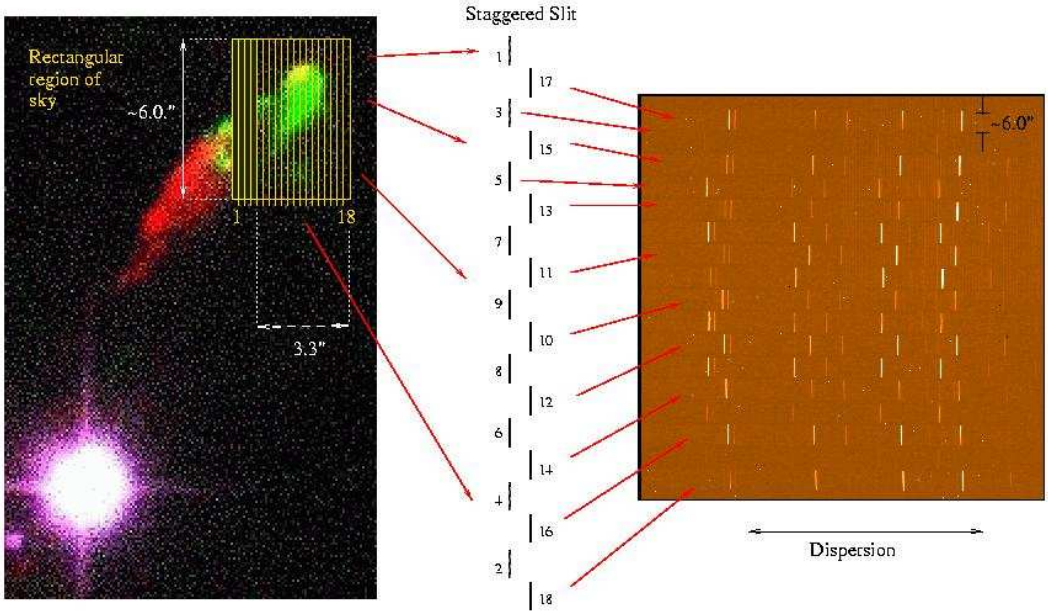


Figure 2.6: The left section of the image shows an overview for slices IFU in respect to its position on the sky. The centre of the image shows the order of the slits. The right section of the image shows how the spectra are staggered on to the UIST chip. This image was obtained from the UKIRT website.

of the IFU is approximately 60 per cent, compared to UIST used in traditional long slit spectroscopy mode. In addition to the reduced throughput, 50 per cent of the observations are on source and 50 per cent on sky, excluding overheads. The integration time has to be increased by approximately a factor of 4, when compared to long slit spectroscopy to measure an equivalent level of flux. However, the 14 spectra are obtained simultaneously as opposed to 1 single slit spectrum. UIST with the IFU can produce 700 spectra or 1024 images at different wavelengths simultaneously.

### 2.2.2 IFS at VLT

One of the IFS instruments at the VLT is the Spectrograph for INtegral Field Observations in the Near-Infrared (SINFONI), which is situated on the 8-m UT4 at

the Cassegrain focus. It was commissioned in first quarter of 2004. The instrument is optimised for observations in the infrared *J*, *H*, *HK* and *K* bands with spectroscopic resolution of 2000, 3000, 1500 and 4000, respectively. It has 3 spatial plate scales of $0.0125 \times 0.025$[3], $0.05 \times 0.1$ and $0.125 \times 0.25$ arcsec$^2$ with a FOV of $0.8 \times 0.8$, $3 \times 3$ and $8 \times 8$ arcsec$^2$, respectively. SINFONI has twice the spectroscopic resolution, up to 46 times greater spatial resolution with adaptive optics (AO) and greater wavelength coverage than UIST. The instrument consists of a 2048×2048 pixel$^2$ Hawaii 2G array with 32 image slicing mirrors. An additional AO module, which can give excellent spatial resolution, however a bright R-band star (<17 mag) is needed for this correction. An excellent correction is achieved with an *R*-band magnitude less than 11. The AO guide star needs to be either the science target or lie within 30 arcsec, ideally within 10 arcsec, of the science target. The SINFONI instrument can produce 2048[4] spectra or 2048 images at different wavelengths simultaneously (Dumas 2007).

### 2.2.3 IFS Data Reduction

The data reduction for image slicing IFS images is similar to long slit spectroscopy, but repeated many times. The data reduction process is similar between UIST and SINFONI; however SINFONI has additional data reduction steps. The UIST data is reduced using the STARLINK packages, FIGARO, KAPPA and CCDPACK, and SINFONI uses the SINFONI pipeline. A brief overview of the reduction process is given in Fig. 2.7 and 2.8 for UIST and SINFONI, respectively.

The minimum observations required for IFS reduction are a long dark, flat lamp, arc lamp, science and standard images inclusive of sky images. A long dark image is used to produce a bad pixel mask, which is applied to the flat lamp, arc,

[3]This value is approximately twice the theoretical maximum of the VLT's angular resolution: 0.057 arcsec

[4]32 imaged sliced spectra which are 64 pixels wide

science and standard images. The science and standard images are observed 50 per cent on source and 50 per cent on a relatively blank part of sky. The sky frames are subtracted from the on source frames to remove dark current, bright OH emission lines and the infrared continuum contribution from the sky.

A single exposure time for an IFS observation is generally greater than 180 seconds, and the sky will vary between observing the object and the sky. This can require a moderate amount of rescaling of the sky spectrum when performing sky subtraction, which is achieved by comparing the fluxes of the OH lines. The sky absorption can vary significantly longwards of 2.24 μm, which is the location of the Q-branch $H_2$ lines. This can affect the strength of the emission of the $H_2$ lines in that region.

All the slices are extracted from the flat, arc, science and standard images and are treated individually, since all slices are staggered. A flat lamp is used to correct for the varying spectral response of the CCD array. The lamp flat is normalised, by fitting a polynomial, and is divided into the science and standard slices. An arc image is used to wavelength calibrate the standard and science data, which are then 'scrunched' to form a linear wavelength-pixel relationship.

Each individual slice is cleaned by hand to remove any remaining hot pixels, cosmic rays before the scrunching process. The replacement pixel values are determined from the surrounding eight pixels. Any artefacts from the scrunching process are also cleaned by hand. The slices for the science target are reordered and formed into a data cube[5] (Fig. 2.9). The standard star slices are reordered into an image and the brightest spectra are extracted into an one-dimensional spectrum. The intrinsic stellar absorption and emission lines (i.e. Brackett Gamma) are removed, since G-type standards are used, the spectrum is flux calibrated and expanded into a

[5]A script to convert an IFU scrunched 2-D image to a 3-D data cube, for UIST+IFU data, has been written by the author and released to the community. It is available from the UKIRT website, `http://www.jach.hawaii.edu/UKIRT/instruments/uist/ifu/ifu_recombine.prg`.

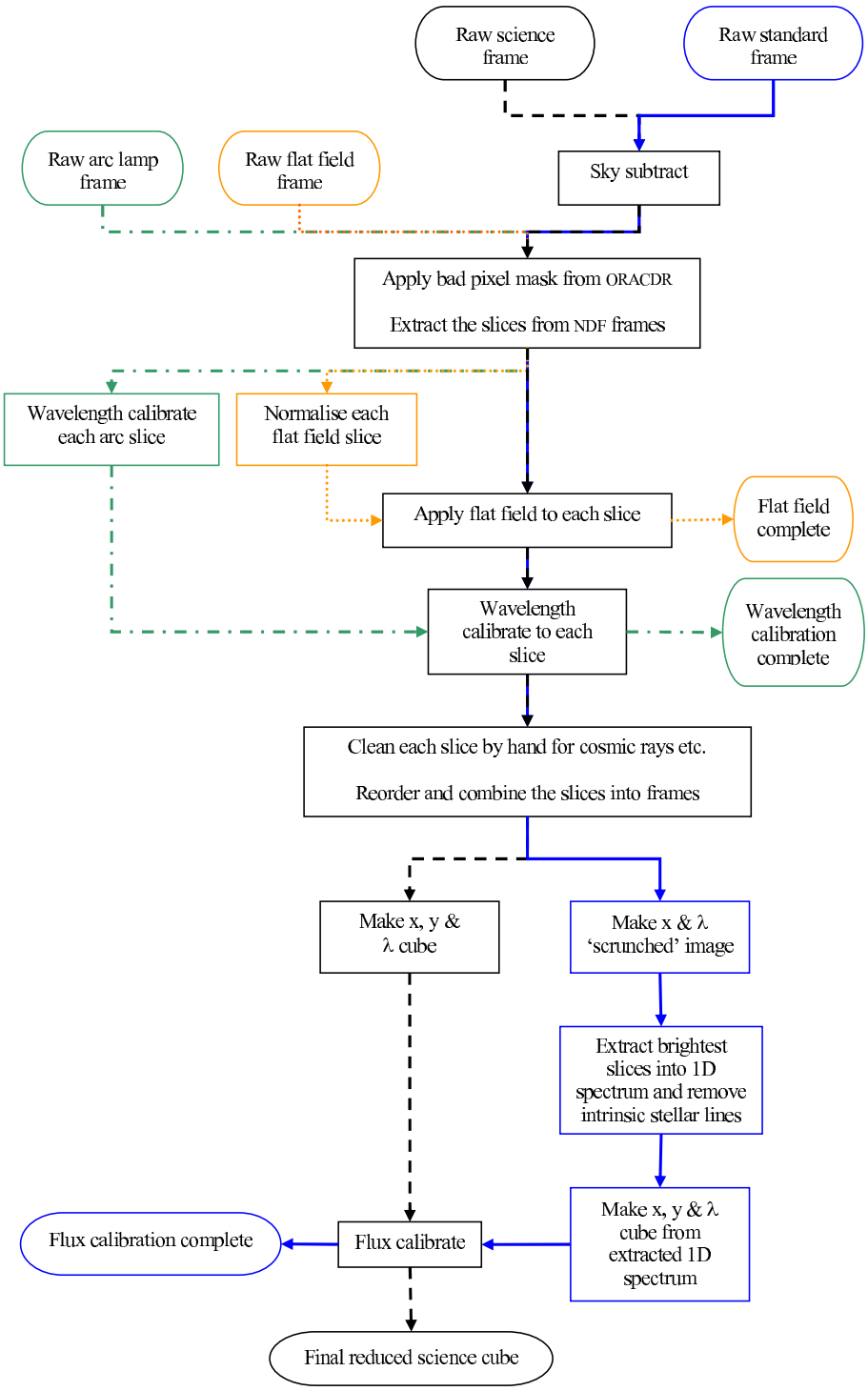


Figure 2.7: An overview of the data reduction for the UIST IFS data. The orange line shows the reduction route of the flat field to its final stage of flat field calibration. The green line tracks the process for the arc lamp to its final step of the wavelength calibration. The black and blue lines trace the reduction steps of the science and standard targets to the final reduced data cube and the flux calibration, respectively.

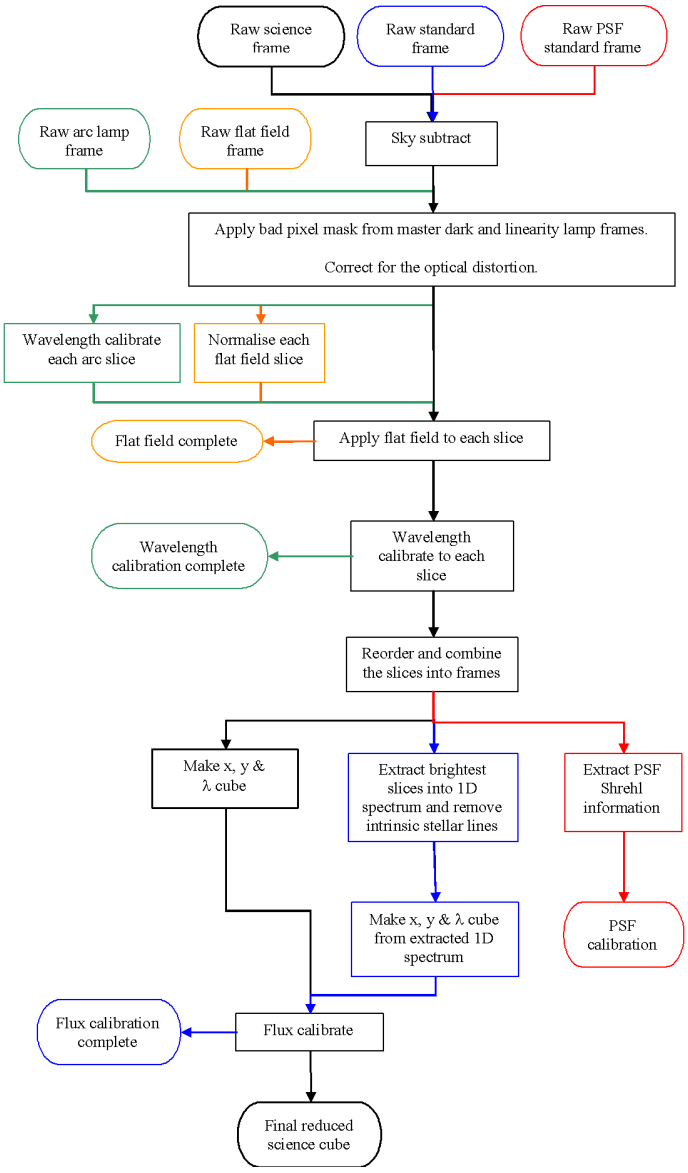


Figure 2.8: The overview of the data reduction for the VLT IFS data. The orange line shows the reduction route of the flat field to its final stage of flat field calibration. The green line tracks the process for the arc lamp to its final step of the wavelength calibration. The black and blue lines traces the reduction steps of the science and standard targets to the final reduced data cube and the flux calibration, respectively. The Red line follows the route of the PSF standard reduction.

data cube. The standard is divided into the science cube, thus removing the telluric atmospheric features, to produce the final reduced flux calibrated IFS cube.

#### 2.2.3.1 Additional SINFONI reduction

The reduction pipeline has three extra processes. These are to detect non-linear pixels, correct for the optical distortion and the reduction of the PSF standard, which measures the efficiency of the AO system. To detect the non-linear pixels, the pipeline analyses a series of lamp flat fields of increasing intensity. This process detects any cold, warm and hot pixels, which could produce artefacts in the final reduced cube.

Each spectrum projected onto the chip suffers from a curve distortion. This is produced by the optics of the telescope and the instrument. The SINFONI pipeline uses a series of fibre flats to compute a set of polynomial parameters that correct the distortion, as a function of pixel coordinate (x,y), and the equation takes the form

$$f(x,y) = C + ax + by + dxy + fx^2 + gy^2 + hx^2y + mxy^2. \qquad (2.19)$$

A PSF standard is observed at the beginning and end of the night to characterise the performance of the AO system. Additional AO analysis can be performed on the science target and standard, if they are used as the natural guide star. The resultant information is given as a strehl ratio, where 1 is the best possible correction and 0 is no correction, at specific wavelengths. A correction is considered good for any values greater that 0.3. There is a Laser guide star (LGS) facility available on UT4, however it is only offered in service mode, requires a natural guide star (R<17.5 mag) to provide a correction and was not offered in 2005.

The SINFONI pipeline produces a reduced cube; however, the pipeline does not produce a flux calibrated science cube and the curve distortion correction leaves

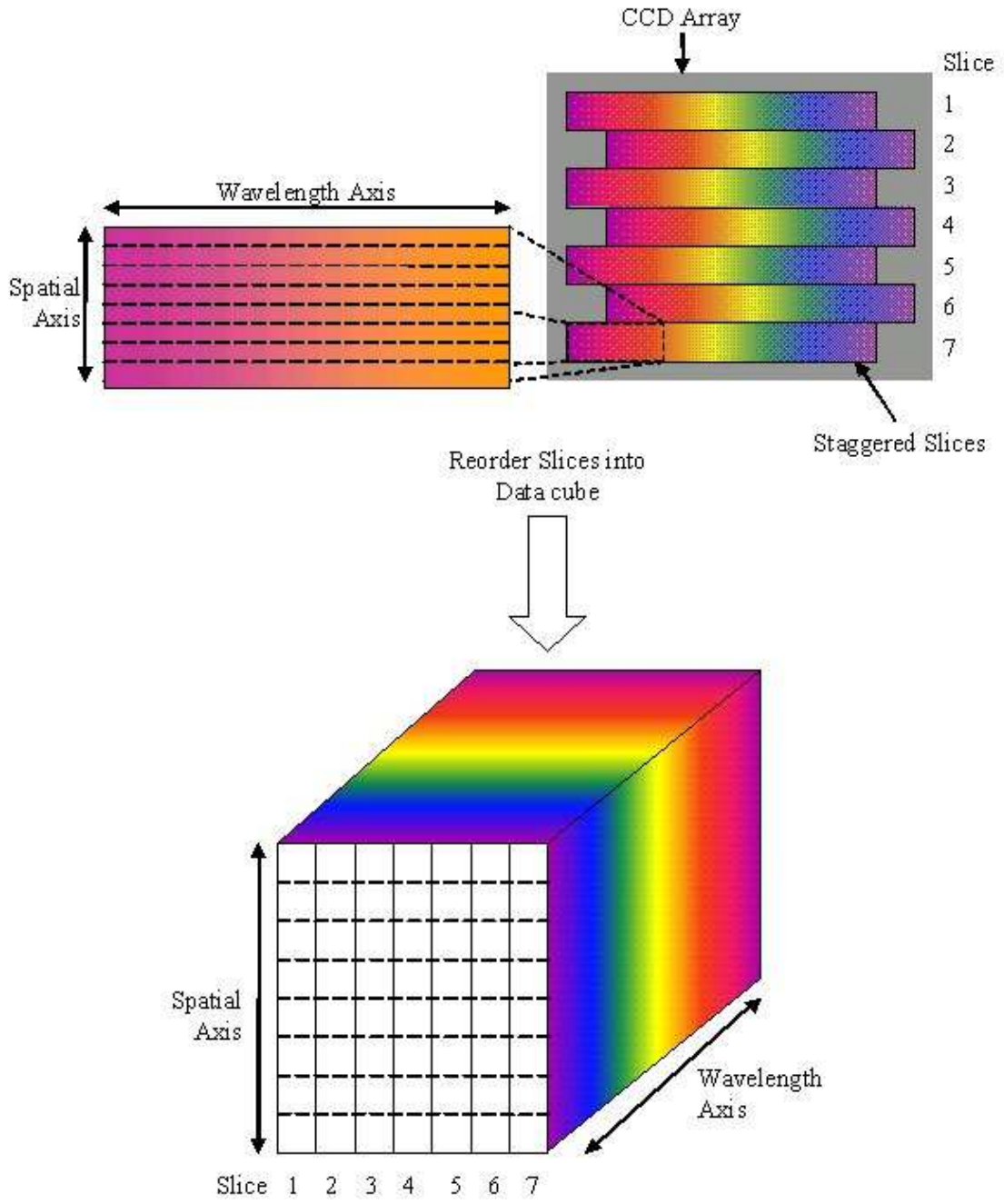


Figure 2.9: A simple cartoon of the formation of a data cube from the slices. The slices are staggered on the CCD array. The blow up section shows the spatial axis and wavelength axis. The slices are reordered and, in this case, the slices are the $x$ component and the spatial axis for each slice is the $y$ component of the data cube. The $x$ pixels are equal to the slit width.

a residue 'skew' effect, causing features to move spatially within images as a function of wavelength (ESO technical support; private communication). In addition, there is no dedicated visualisation software to display SINFONI data and to extract emission line images from a data cube. In chapter 4, the software created to complete the SINFONI data reduction, analysis and visualisation is discussed.

# Chapter 3

# Analysing Molecular Hydrogen Emission Lines

The $K$-band is host to a vast quantity of $H_2$ emission lines. The analysis of these lines can be used as a diagnostic for determining the excitation mechanisms in astrophysical environments. The simplest method to uncover the excitation mechanisms, affecting $H_2$ emission, is to compare the integrated flux of certain emission lines. An example synthetic spectrum is displayed in Fig. 3.1. As the $H_2$ molecule decays from higher populated ro-vibrational state to lower states, it emits an emission line at a specific frequency (Fig. 3.2). The ratio of lines can give an indication of whether the gas is shocked and/or fluoresced. The method of Gaussian fitting of the lines is documented in Chapter 4. This chapter details the use of $H_2$ emission to correct for extinction, emission line ratios and to generate column density ratio (CDR) plots. The latter can be used to determine if the excitation mechanisms are close to LTE. Furthermore the analysis can uncover the rotational and vibrational temperatures and ortho-para ratios.

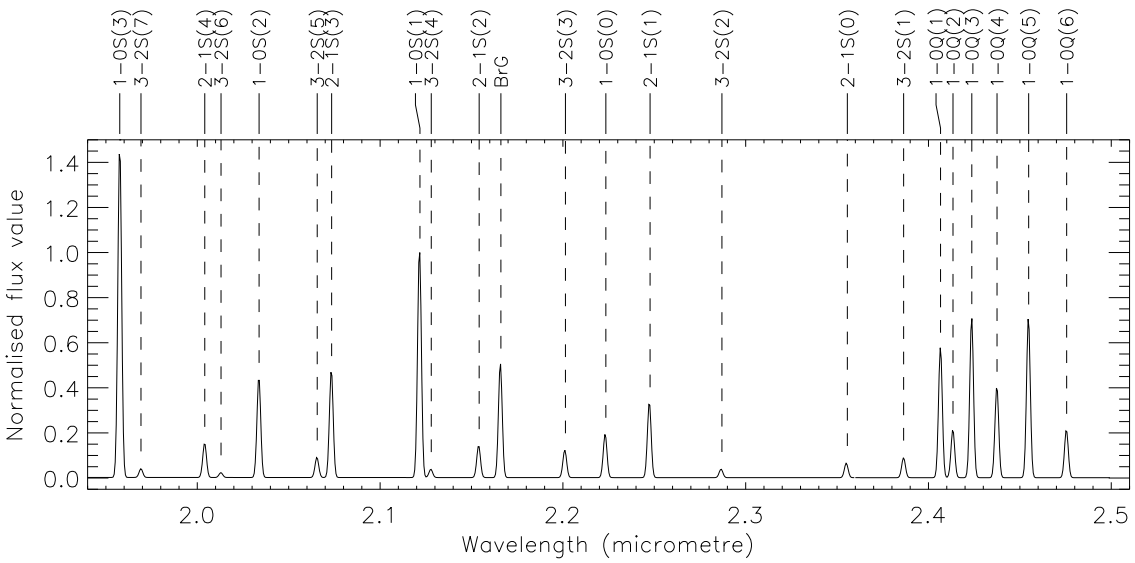


Figure 3.1: A synthetic spectrum indicating the detectable $H_2$ and brackett gamma 2.1661 μm emission lines with SINFONI for a $H_2$ gas in LTE at 4000 K. The line ratios have been obtained from Table 3.2 and are used to plot the above spectrum, using an algorithm from the Fitting Utility for SINFONI. The lines have been normalised with respect to the 1-0 S(1) 2.1218 μm emission line.

## 3.1 Extinction

The light originating from the illuminating source (a post-AGB star) is scattered and absorbed by dust in the CSE and ISM. This has the effect of attenuating and reddening the emitted light. In the near-IR, light at longer wavelengths suffers less extinction than at shorter wavelengths. If the extinction is not taken into account, then line ratios analysed with respect to the main $H_2$ line would result in an over- and under-estimation short-ward and long-ward of 2.1218 μm, respectively. This can potentially affect the conclusions regarding the emission mechanism. Thus, a correction for extinction is required.

Two pairs of emission lines are commonly used independently to correct for extinction of a spectrum. These are the HI emission, Brackett Gamma (Br$\gamma$) and Balmer Alpha (H$\alpha$) and $H_2$ ro-vibration transitions that have the same upper energy level (eg. 1-0S1 and 1-0Q3). However, there are associated problems inherent in

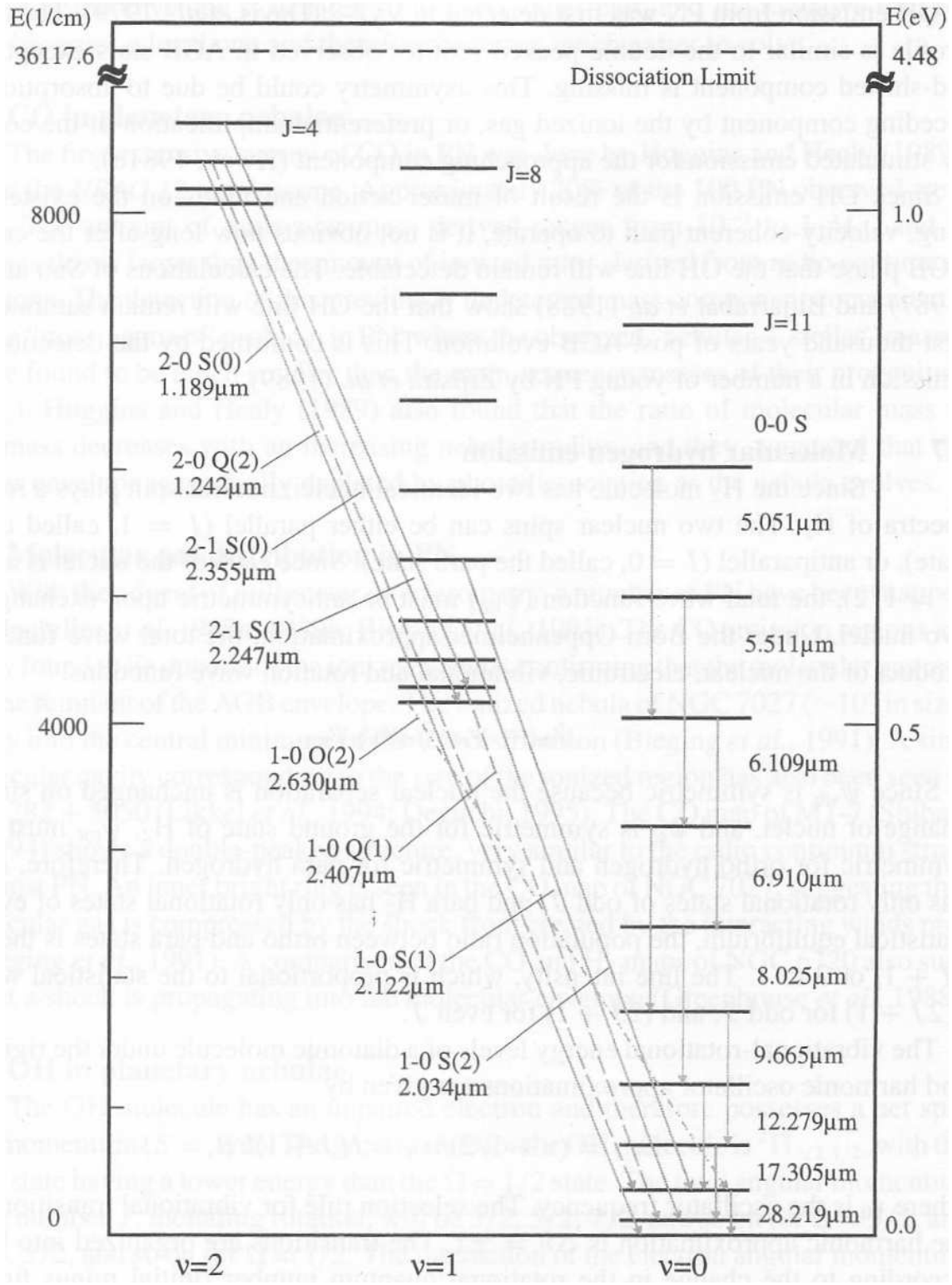


Figure 3.2: The energy diagram of molecular hydrogen with some of observed transitions marked in micrometres. The caption and image taken from Kwok 2000, pg. 62, fig. 5.4.

using these lines: the origin of the emission can be near the central source and therefore may not provide a reliable estimate of the extinction within the CSE; multiple spectra have to be taken in different band passes ($K$ band - Br$\gamma$ and $R$ band - H$\alpha$), which cannot always be technically possible; and some post-AGB stars show only weak, or no atomic hydrogen lines. The majority of $H_2$ 1-0S and 1-0Q lines lie within the $K$ band, however there is strong atmospheric absorption beyond 2.3 μm, which is the region where the Q lines are emitted. This section describes the method that can correct a spectrum or a line intensity using the 1-0S and 1-0Q line intensities, which is given in Davis et al. (2003).

The observed measured flux, $F_\lambda$, at a wavelength, $\lambda$, has an intrinsic flux, $F'_\lambda$, subjected to an extinction, $A_\lambda$, and is given by

$$F_\lambda = F'_\lambda \cdot 10^{-\frac{A_\lambda}{2.5}}. \tag{3.1}$$

The intrinsic flux is obtained by rearranging equation 3.1 to

$$F'_\lambda = F_\lambda \cdot 10^{\frac{A_\lambda}{2.5}}. \tag{3.2}$$

The intrinsic line ratio, $R'$, for Q and S lines at their respective wavelengths is equal to

$$R' = \frac{F'_{\rm Q}}{F'_{\rm S}} \tag{3.3}$$

If the Q and S lines are subject to extinction then the intrinsic line ratio is modified

$$R' = \frac{F_{\rm Q} \cdot 10^{\frac{A_{\rm Q}}{2.5}}}{F_{\rm S} \cdot 10^{\frac{A_{\rm S}}{2.5}}}, \tag{3.4}$$

where $A_{\rm Q}$ and $A_{\rm S}$ represent the extinction at wavelengths $\lambda_{\rm Q}$ and $\lambda_{\rm S}$ for an observed flux $F_{\rm Q}$ and $F_{\rm S}$, respectively. The observed line ratio is given by rearranging

equation 3.4 to

$$\frac{F_{\rm Q}}{F_{\rm S}} = R' \cdot 10^{\left(\frac{A_{\rm S}-A_{\rm Q}}{2.5}\right)}. \tag{3.5}$$

A power law relationship is assumed, which relates extinction to wavelength between 0.9- and 6-μm (He et al. 1995), for a stellar object with a colour excess, $E_{\rm c}$,

$$\frac{A_\lambda}{E_{\rm c}} \propto \lambda^{-1.75}. \tag{3.6}$$

To obtain the extinction $A_{\rm Q}$ and $A_{\rm S}$ at wavelengths $\lambda_{\rm Q}$ and $\lambda_{\rm S}$, respectively, for a known extinction, $A_\lambda$, at an arbitrary wavelength, $\lambda$, we modify equation 3.6 to

$$A_{\rm Q} = A_\lambda \left(\frac{\lambda_{\rm Q}}{\lambda}\right)^{-1.75} \quad \text{and} \quad A_{\rm S} = A_\lambda \left(\frac{\lambda_{\rm S}}{\lambda}\right)^{-1.75}. \tag{3.7}$$

Substituting equation 3.7 into equation 3.5 it now becomes

$$\frac{F_{\rm Q}}{F_{\rm S}} = R' \cdot 10^{\left\{\frac{A_\lambda}{2.5}\left[\left(\frac{\lambda_{\rm S}}{\lambda}\right)^{-1.75}-\left(\frac{\lambda_{\rm Q}}{\lambda}\right)^{-1.75}\right]\right\}}. \tag{3.8}$$

To calculate the extinction at any wavelength using the S and Q line ratio can be achieved by rearranging equation 3.8 and it now takes the form

$$A_\lambda = 2.5 \log_{10}\left(\frac{1}{R'}\frac{F_{\rm Q}}{F_{\rm S}}\right) \cdot \left[\left(\frac{\lambda_{\rm S}}{\lambda}\right)^{-1.75} - \left(\frac{\lambda_{\rm Q}}{\lambda}\right)^{-1.75}\right]^{-1}. \tag{3.9}$$

Substituting equation 3.9 into equation 3.2, gives the final equation to correct the observed spectrum or emission line for extinction using $H_2$ lines,

$$F'_\lambda = F_\lambda \left(\frac{1}{R'}\frac{F_{\rm Q}}{F_{\rm S}}\right)^{\left[\left(\frac{\lambda_{\rm S}}{\lambda}\right)^{-1.75}-\left(\frac{\lambda_{\rm Q}}{\lambda}\right)^{-1.75}\right]^{-1}}. \tag{3.10}$$

The available pairs of S and Q lines in the $K$-band are the 1-0 S(0) and 1-0 Q(2), 1-0 S(1) and 1-0 Q(3), 1-0 S(2) and 1-0 Q(4), and 1-0 S(3) and 1-0 Q(5) lines.

Table 3.1: The fixed line ratios for S and Q branch lines with the same upper energy levels, hence can be used for extinction correction.

| Line ratio | Wavelength (μm) | Upper energy level (K) | Ratio (R′) |
|---|---|---|---|
| 1-0 Q(2)/1-0 S(0) | 2.4124/2.2235 | 6471 | 1.10 |
| 1-0 Q(3)/1-0 S(1) | 2.4237/2.1218 | 6956 | 0.70 |
| 1-0 Q(4)/1-0 S(2) | 2.4375/2.0338 | 7586 | 0.56 |
| 1-0 Q(5)/1-0 S(3) | 2.4548/1.9576 | 8365 | 0.48 |

Each pair of lines have the same upper energy levels and the line ratios are given by Einstein's spontaneous decay coefficient, $A_i$, and wavelength,

$$R' \equiv \frac{F'_{\rm Q}}{F'_{\rm S}} = \frac{A_{i,{\rm Q}}\lambda_{\rm S}}{A_{i,{\rm S}}\lambda_{\rm Q}}, \tag{3.11}$$

for which the corresponding values are displayed in Table 3.1. It is possible to correct for the extinction at every wavelength and obtain the intrinsic line ratios, without knowing the colour excess of the science target. However, due to the long exposure times and variability of the atmospheric window in the Q-branch region of the $K$-band, a data cube cannot always be corrected for extinction. For example the 1-0 Q(3) line can be located on a strong time variable atmospheric absorption line and can provide an underestimation of the extinction. In addition, a 10 per cent error in the 1-0 Q(3) and 1-0 S(1) ratio can give 0.1 magnitude error at 2.2 μm. The dusty CSE preferentially scatters light at shorter wavelengths than at longer wavelengths, which can increase the strength of the 1-0 S branch lines with respect to the 1-0 Q branch lines. This will increase the ratio, $R'$, and decrease the measured extinction value. Therefore, it is important that each possible line pair is analysed and assessed for accuracy.

## 3.2 Line ratios

Line ratios of $H_2$ emission are a quick and simple method of obtaining information of the gas excitation mechanism, and are predominantly used in single slit spectroscopy or narrow band imaging (e.g. Brand et al. 1988; Richter, Graham & Wright 1995; Smith, Davis & Lioure 1997; van de Steene & van Hoof 2003; Kelly & Hrivnak 2005).

The thermalisation and shocking processes populate the $H_2$ ro-vibrational energy states, bottom-up, from the lowest, $v = 0$, to the higher, $v \geq 2$, states. When the $H_2$ gas undergoes a non-thermal process (e.g. fluorescence) the energy levels are populated, top-down, from the high, $v \geq 3$, to low, $v = 0$, states. Comparing the emission lines from high and low excitation states will uncover the underlying mechanism.

It is common for the 1-0 S(1) 2.1218 μm and the 2-1 S(1) 2.2477 μm lines to be used to probe the possible excitation mechanism. A ratio of 10 or more indicates thermalisation, which is indicative of shock excitation (Hollenbach & Shull 1977; Burton, Hollenbach & Tielens 1992); however, Hollenbach & Natta (1995) state that a ratio of 10 can be achieved for a fluoresced dense gas ($n \gtrsim 10^5$ cm$^{-3}$) with a high level of far ultraviolet (FUV) flux ($G_0 \gtrsim 10^4$) in a PDR. A fluoresced gas can populated the lower energy levels by collisional de-excitation, if the density is high enough ($\sim 10^5$ cm$^{-3}$). The interstellar FUV field is equal to 1 $G_0$, which is $1.6 \times 10^{-6}$ W m$^{-2}$ sr$^{-1}$ (Habing 1968; Burton, Hollenbach & Tielens 1990). A typically low ratio, approximately 2, implies fluorescent excitation in a low density region (Hollenbach & Natta 1995). Therefore, a low ratio indicates fluorescence in a low density gas and a high ratio indicates shock excitation in a low density gas or fluorescence in high density gas.

To break this degeneracy the 1-0 S(1) 2.1218 μm and 3-2 S(3) 2.2014 μm lines can be compared, since the ratio remains low ($\sim 8$) for a fluoresced gas with a

density ranging from $10^4$ to $10^7$ cm$^{-3}$ for FUV flux approximately $10^3 G_0$. The 1-0 S(1) and 3-2 S(3) ratio increases to values $\geq$10 with a FUV flux $\geq 10^4 G_0$ at densities $\geq 10^5$ cm$^{-3}$ (Burton et al. 1990). Therefore, combining the 1-0 S(1)/2-1 S(1) and 1-0 S(1)/3-2 S(3) ratios, it can be shown that an emitting $H_2$ gas is undergoing fluorescence or shocking unless the gas is extremely dense and with an intense FUV flux.

The ratio of the 1-0 S(1) line with respect to the Br$\gamma$ line can indicate the evolution of the central star. Davis et al. (2003) found large ratios in their least and most evolved sources. They found that the ratio does not directly coincide with post-AGB stage. However a high ratio does correspond to objects that show thermalisation and possibly shock excitation. In a survey of 51 objects by Kelly & Hrivnak (2005), with spectral types ranging from G to B, $H_2$ emission and Br$\gamma$ were detected in 16. They observed that Br$\gamma$ is in strong absorption (sometimes in emission) for F and G-type post-AGB stars, and there were no G-type post-AGB stars that emitted both $H_2$ and Br$\gamma$. However, Davis et al. (2003) did detect Br$\gamma$ in *IRAS* 17150-3224 (G-type), whilst Kelly & Hrivnak (2005) did not. The 1-0 S(1)/Br$\gamma$ will be high for F and G types due to the weak emission from Br$\gamma$. The A type stars did not emit $H_2$, therefore their ratio is 0. The majority of B-type stars in Kelly & Hrivnak (2005) and Davis et al. (2003) have $H_2$ and Br$\gamma$ emission and the ratio will be low, since the star will ionise nearby material, increasing the Br$\gamma$ intensity.

Line ratios will ascertain if a gas is undergoing fluorescence and/or shocks by comparing the 1-0 S(1)/2-1 S(1) and 1-0 S(1)/3-2 S(3) lines. A simple comparison of the 1-0 S(1) and Br$\gamma$ lines will determine if the central star is a less evolved G-type or a more evolved B-type.

## 3.3 Column Density Ratio (CDR) Plots

To analyse $H_2$ emission in a more systematic way, rather than using line ratios, we can use the CDR method, which has been used by Burton & Haas (1997), Eislöffel, Smith & Davis (2000) and Davis et al. (2003) to investigate $H_2$ excitation in young stellar objects. The CDR method can produce diagrams that can determine if a system is in LTE assuming a Boltzmann population density function with a partition function. The column depth of gas in the upper level transition, $N_i$, of the molecular gas is in LTE, with a ro-vibration line index, $i$, which is equal to,

$$N_i = \frac{N(\mathrm{H_2}) g_i \exp\left(\frac{-T_i}{T_{\mathrm{gas}}}\right)}{Z(T_{\mathrm{gas}})}, \tag{3.12}$$

where N($H_2$) is the total column depth of $H_2$, with the degeneracy factor, $g_i$, with the upper energy level temperature, $T_i$, with a gas excitation temperature, $T_{\mathrm{gas}}$, and $Z(T_{\mathrm{gas}})$ is the partition function. The above equation can be rearranged to,

$$N(\mathrm{H_2}) = \frac{Z(T_{\mathrm{gas}}) N_i}{g_i} \exp\left(\frac{T_i}{T_{\mathrm{gas}}}\right). \tag{3.13}$$

If equation 3.13 is normalised with respect to the 1-0 S(1) line, which is designated with a subscript 0, at a gas temperature of 2000K,

$$\frac{N(\mathrm{H_2})}{N(\mathrm{H_2})_{2000\mathrm{K}}} = \frac{g_0 N_i}{N_0 g_i} \exp\left(\frac{T_i - T_0}{2000\mathrm{K}}\right) \tag{3.14}$$

The intensity of an emission line, $I_i$, produced by the emitting column density of the gas is

$$I_i = hc\left(\frac{N_i A_i}{\lambda_i}\right), \tag{3.15}$$

where $h$ is Planck's constant and $c$ is the speed of light. $N_i$ is then given by,

$$N_i = \frac{I_i \lambda_i}{A_i} \frac{1}{hc}. \tag{3.16}$$

Substituting equation 3.16 into equation 3.14

$$\frac{N(\mathrm{H_2})}{N(\mathrm{H_2})_{2000\mathrm{K}}} = \frac{I_i}{I_0} \frac{\lambda_i g_0 A_0}{\lambda_0 g_i A_i} \exp\left(\frac{T_i - T_0}{2000\mathrm{K}}\right). \tag{3.17}$$

The ratio of the measured fluxes[1] subtending an equal solid angle is equal to the line intensity ratio,

$$\frac{F_1}{F_2} = \frac{I_1}{I_2}. \tag{3.18}$$

If the values for the 1-0 S(1) line from Table 3.3 are substituted then equation 3.17 becomes,

$$\mathrm{CDR} \equiv \frac{N(\mathrm{H_2})}{N(\mathrm{H_2})_{2000\mathrm{K}}} = 34.343 \times 10^{-7} \left[\mathrm{s\ \mu m^{-1}}\right] \cdot \frac{F_i}{F_0} \frac{\lambda_i}{A_i g_i} \exp\left[\frac{(T_i - 6956\mathrm{K})}{2000\mathrm{K}}\right] \tag{3.19}$$

For a gas at 2000 K, the gradient of the logarithm of the CDR, plotted against the temperature of the upper energy level, is equal to zero (Fig. 3.3 top right). A cooler gas will have a negative gradient (Fig. 3.3 top left), whilst a warmer gas will have a positive gradient (Fig. 3.3 bottom left and bottom right). An example of different CDR diagrams for the various $H_2$ excitation mechanisms are shown in figure 1 of Eislöffel et al. (2000). These include C- and J-type planar and bow shaped shocks that have one smooth continuous CDR curve for *all* vibrational groups, where as the non-LTE models show a distinct curve for *each* vibrational group.

It is possible to plot the CDR of a gas in LTE at a temperature, $T_{\mathrm{gas}}$, on the CDR diagrams. This can be achieved by substituting equation 1 from Burton et al.

[1]The line intensity, at wavelength $\lambda$, is related to line flux by $F_\lambda = I_\lambda \left(\frac{\theta^2}{4\pi}\right)$, for a fixed solid angle, $\theta^2$, assuming an isotropic optically thin radiation.

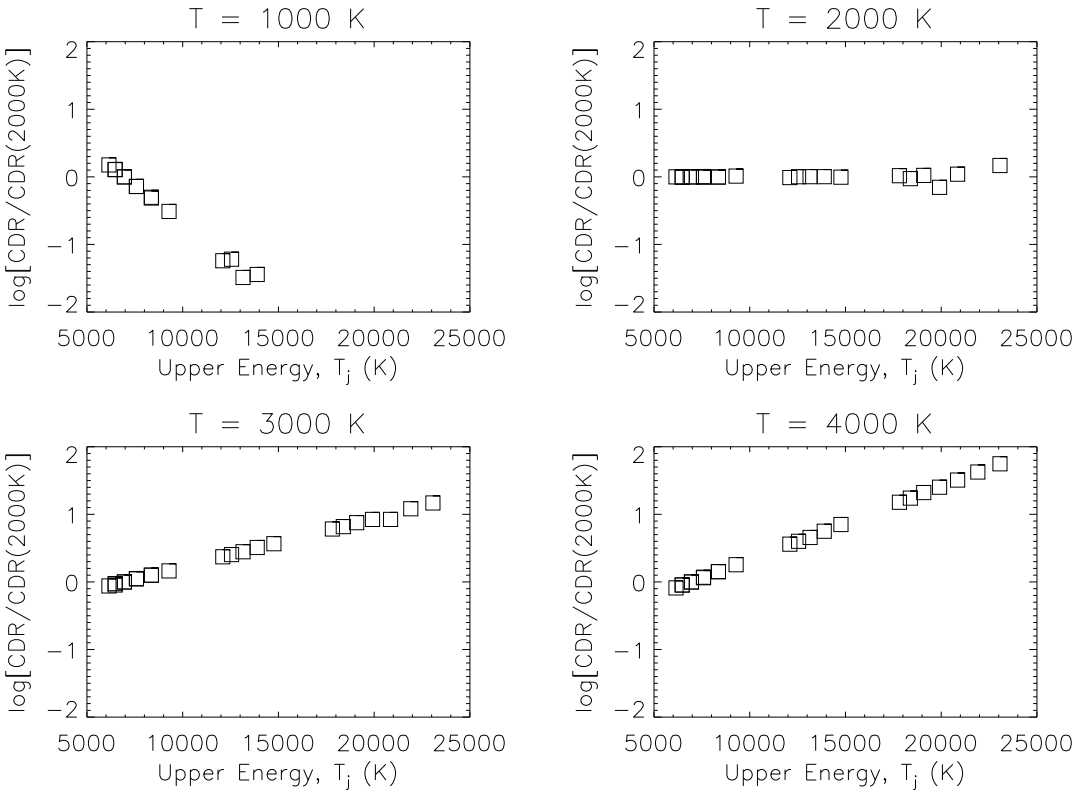


Figure 3.3: The plots of the CDR with respect to the upper energy temperature, $T_{\rm j}$,for $H_2$ in LTE, using the data stated in Table 3.2, for four characteristic temperatures, T, of 1000 K (**top left**), 2000 K (**top right**), 3000 K (**bottom left**) and 4000 K (**bottom right**).

(1989) into equation 3.17 to give:

$$\mathrm{CDR} = \exp\left[\frac{(T_0 - T_i)}{T_{\rm gas}}\right] \cdot \exp\left[\frac{(T_i - T_0)}{2000\mathrm{K}}\right], \tag{3.20}$$

where $T_0$ is the upper energy temperature for the reference ro-vibrational emission line[2] and $T_i$ is the upper energy temperature for all other ro-vibrational transitions.

[2]In the case of the 1-0 S(1) 2.1218 μm emission line $T_0 = 6956$ K.

Table 3.2: $H_2$ ro-vibrational lines with the emitted wavelength ($\lambda_i$), level degeneracy ($g_i$), temperature of the upper energy level ($T_i$), Einstein's spontaneous emission coefficient ($A_i$), and the ratio of the line w.r.t. the main 1-0 S(1) line at LTE at four temperatures. The line list has been cropped to reflect the wavelength range of UIST and SINFONI. The **bold** font denotes that a particular line is only visible to SINFONI.

| Line | $\lambda_i$ | $g_i$ | $T_i$ | $A_i$ | LTE $\frac{I_i}{I_0}$ | | | |
|---|---|---|---|---|---|---|---|---|
| | μm | | K | $10^{-7}$s | 1000 K | 2000 K | 3000 K | 4000 K |
| 1-0 S(0)$^{+}$ | 2.2235 | 5 | 6471 | 2.53 | 0.27 | 0.21 | 0.19 | 0.19 |
| 1-0 S(1)$^{\times}$ | 2.1218 | 21 | 6956 | 3.47 | 1.00 | 1.00 | 1.00 | 1.00 |
| 1-0 S(2)$^{\diamond}$ | 2.0338 | 9 | 7584 | 3.98 | 0.27 | 0.37 | 0.42 | 0.44 |
| **1-0 S(3)$^{*}$** | **1.9576** | **33** | **8365** | **4.21** | **0.51** | **1.02** | **1.29** | **1.45** |
| ..... | | | | | | | | |
| **1-0 Q(1)** | **2.4066** | **9** | **6149** | **4.29** | **1.05** | **0.70** | **0.61** | **0.57** |
| **1-0 Q(2)$^{+}$** | **2.4134** | **5** | **6471** | **3.03** | **0.30** | **0.23** | **0.22** | **0.21** |
| **1-0 Q(3)$^{\times}$** | **2.4237** | **21** | **6956** | **2.78** | **0.70** | **0.70** | **0.70** | **0.70** |
| **1-0 Q(4)$^{\diamond}$** | **2.4375** | **9** | **7586** | **2.65** | **0.15** | **0.21** | **0.23** | **0.24** |
| **1-0 Q(5)$^{*}$** | **2.4548** | **33** | **8365** | **2.55** | **0.24** | **0.49** | **0.62** | **0.70** |
| **1-0 Q(6)** | **2.4756** | **13** | **9286** | **2.45** | **0.036** | **0.12** | **0.17** | **0.21** |
| ..... | | | | | | | | |
| **2-1 S(0)** | **2.3556** | **5** | **12095** | **3.68** | **0.001** | **0.017** | **0.041** | **0.063** |
| 2-1 S(1) | 2.2477 | 21 | 12550 | 4.98 | 0.005 | 0.083 | 0.21 | 0.33 |
| 2-1 S(2) | 2.1542 | 9 | 13150 | 5.60 | 0.001 | 0.031 | 0.086 | 0.14 |
| 2-1 S(3) | 2.0735 | 33 | 13890 | 5.77 | 0.003 | 0.084 | 0.27 | 0.47 |
| **2-1 S(4)** | **2.0041** | **13** | **14764** | **5.57** | - | **0.021** | **0.078** | **0.15** |
| ..... | | | | | | | | |
| **3-2 S(1)** | **2.3864** | **21** | **17818** | **5.14** | - | **0.006** | **0.035** | **0.087** |
| **3-2 S(2)** | **2.2870** | **9** | **18386** | **5.63** | - | **0.002** | **0.014** | **0.037** |
| 3-2 S(3) | 2.2014 | 33 | 19086 | 5.63 | - | 0.006 | 0.043 | 0.12 |
| 3-2 S(4) | 2.1280 | 13 | 19912 | 5.22 | - | 0.001 | 0.012 | 0.036 |
| 3-2 S(5) | 2.0656 | 45 | 20856 | 4.50 | - | 0.003 | 0.023 | 0.088 |
| **3-2 S(6)** | **2.0130** | **17** | **21911** | **3.57** | - | - | **0.006** | **0.021** |
| **3-2 S(7)** | **1.9692** | **57** | **23069** | **2.54** | - | **0.001** | **0.010** | **0.038** |

$^{+}$, $^{\times}$, $^{\diamond}$ and $^{*}$ are lines that 'can' be used to calculate extinction.

The energy levels are derived from Dabrowski (1984) and the Einstein coefficients obtained from Turner, Kirby-Docken & Dalgarno (1977).

## 3.4 The ortho-para ratios

The determination of the ortho-para ratio (OPR) is an additional diagnostic for the excitation of the $H_2$ molecule. Molecular hydrogen can exist as ortho- or para-hydrogen. The ortho state, the higher energy state, occurs when the relative spins of the hydrogen atoms are parallel and the para state, the lower energy state, exists when the spins are anti-parallel. The degeneracy factor is equal to the rotational upper energy level quantum number $(2J+1)$ multiplied by spin degeneracy factor, $g_i^{\rm s}$. The ortho-$H_2$ are all the odd $J$ states and the para-$H_2$ are the even $J$ states. Normally the spin degeneracy, at the time of formation, is equal to $(2S+1)$; therefore ortho- and para-spins have values of 3 and 1, respectively. The OPR changes if the para- or ortho-$H_2$ are collisional excited or de-excited, respectively, or it is subjected to FUV photons. If the $H_2$ gas is in LTE, OPR can reduce to values less than 1 at temperatures less than 75 K, and reaches an OPR of 3 at temperatures greater than 300 K (Burton et al. 1992). In shock enviroments the OPR equals 3 (e.g. Smith et al. 1997) and ratio can decrease to a value of 1.8, if the $H_2$ collides with dust grains (Black & van Dishoeck 1987). In addition, the OPR can as low as $\sim$ 2 in a low density ($< 10^5$ cm$^{-3}$) PDR, but can be greater than 3 in a high density ($10^6$ cm$^{-3}$) PDR (Draine & Bertoldi 1996). The OPR can place important constraints on determining the processes that excite $H_2$.

The derivation of the OPR in this thesis is taken from Chrysostomou et al. (1993). It follows the CDR method closely, although the CDR method assumes that the OPR ratio is 3. A ratio of 1.7 is more indicative of a PDR region, whilst a ratio of 3 would indicate a shocked region. Equation 3.12 is modified to

$$N_i = \frac{N({\rm H_2})(2J+1)g_i^{\rm s}\exp\left(\frac{-T_i}{T_{\rm gas}}\right)}{Z(T_{\rm gas})}. \qquad (3.21)$$

If equation 3.21 is substituted into equation 3.15 it becomes

$$I_i = \frac{(2J+1)hcA_iN(\mathrm{H_2})g_i^{\mathrm{s}}\exp\left(\frac{-T_i}{T_{\mathrm{gas}}}\right)}{\lambda_i Z(T_{\mathrm{gas}})}. \tag{3.22}$$

Rearranging the above equation to make the spin degeneracy the subject gives

$$g_i^{\mathrm{s}} = \frac{I_i\lambda_i Z(T_{\mathrm{gas}})}{(2J+1)hcA_iN(\mathrm{H_2})\exp\left(\frac{-T_i}{T_{\mathrm{gas}}}\right)}. \tag{3.23}$$

The OPR is $g_{\mathrm{o}}^{\mathrm{s}}/g_{\mathrm{p}}^{\mathrm{s}}$ (referred henceforth as $\phi$), which is the comparison of an ortho line (subscript o) with a para-line (subscript p), and takes the form

$$\phi \equiv \frac{g_{\mathrm{o}}^{\mathrm{s}}}{g_{\mathrm{p}}^{\mathrm{s}}} = \frac{(2J_{\mathrm{p}}+1)A_{\mathrm{p}}I_{\mathrm{o}}\lambda_{\mathrm{o}}}{(2J_{\mathrm{o}}+1)A_{\mathrm{o}}I_{\mathrm{p}}\lambda_{\mathrm{p}}}\exp\left[\frac{(T_{\mathrm{o}}-T_{\mathrm{p}})}{T_{\mathrm{gas}}}\right] \tag{3.24}$$

and is cited from Chrysostomou et al. (1993). The above equation shows the OPR is related to the exponential of the inverse gas temperature. However, the temperature of the gas has to be determined. This is achieved by comparing a pair of ortho or para lines. For example if the ortho lines (subscript o and o′) are used, which are generally stronger than the para lines, the gas excitation temperature is equal to,

$$T_{\mathrm{gas}} = (T_{\mathrm{o}'} - T_{\mathrm{o}})\left\{\ln\left[\frac{(2J_{\mathrm{o}'}+1)I_{\mathrm{o}}A_{\mathrm{o}'}\lambda_{\mathrm{o}}}{(2J_{\mathrm{o}}+1)I_{\mathrm{o}'}A_{\mathrm{o}}\lambda_{\mathrm{o}'}}\right]\right\}^{-1}. \tag{3.25}$$

By substituting $T_{\mathrm{gas}}$ from equation 3.25 into the exponential term gives

$$\exp\left[\frac{(T_{\mathrm{o}}-T_{\mathrm{p}})}{T_{\mathrm{gas}}}\right] = \left[\frac{(2J_{\mathrm{o}}+1)I_{\mathrm{o}'}A_{\mathrm{o}}\lambda_{\mathrm{o}'}}{(2J_{\mathrm{o}'}+1)I_{\mathrm{o}}A_{\mathrm{o}'}\lambda_{\mathrm{o}}}\right]^{\left[\frac{T_{\mathrm{o}}-T_{\mathrm{p}}}{T_{\mathrm{o}'}-T_{\mathrm{o}}}\right]}, \tag{3.26}$$

and additionally substituting equation 3.18 gives

$$\phi = \left[\frac{(2J_{\mathrm{p}}+1)}{(2J_{\mathrm{o}}+1)}\frac{F_{\mathrm{o}}A_{\mathrm{p}}\lambda_{\mathrm{o}}}{F_{\mathrm{p}}A_{\mathrm{o}}\lambda_{\mathrm{p}}}\right]\left[\frac{(2J_{\mathrm{o}}+1)F_{\mathrm{o}'}A_{\mathrm{o}}\lambda_{\mathrm{o}'}}{(2J_{\mathrm{o}'}+1)F_{\mathrm{o}}A_{\mathrm{o}'}\lambda_{\mathrm{o}}}\right]^{\left[\frac{T_{\mathrm{o}}-T_{\mathrm{p}}}{T_{\mathrm{o}'}-T_{\mathrm{o}}}\right]}. \tag{3.27}$$

It is clear from the above equation that only three lines are need to calculate the OPR, e.g. 1-0 S(0), 1-0 S(1) and 1-0 S(2) . It is prudent to determine the mean excitation temperature using the ortho and para-lines S(0) and S(2), and S(1) and S(3); however in some cases a pair of ortho and para lines are not available.

### 3.4.1 Vibrational and rotational temperatures

In the section above the excitation temperatures are discussed briefly. The $H_2$ molecule has two characteristic temperatures, which are based on its excited vibrational and rotational states. These can be obtained by comparing two specific $H_2$ rovibrational emission lines. If equation 3.25 is modified with respect to comparing two lines with subscript $i$ and $j$ it will give,

$$T_{\rm gas} = (T_j - T_i) \left\{ \ln \left[ \frac{(2J_j+1) I_i A_j \lambda_i}{(2J_i+1) I_j A_i \lambda_j} \right] \right\}^{-1} . \tag{3.28}$$

The rotational temperatures can be obtained from comparing a pair of ortho- or para-lines with the same vibrational level. To obtain the rotational temperature for the $v = 1$ level, the 1-0 S(0) with 1-0 S(2) or 1-0 S(1) with 1-0 S(3) can be used. The derived rotational temperatures will be similar if the LTE assumption is correct. However, they can differ due to non-LTE effects, such as low density. In PDRs the vibrational and rotational temperatures cease to be meaningful measure of the characteristic temperature, since non-LTE effects dominate the excitation of the $H_2$ gas. The vibrational temperature between two levels, for example between $v = 1$ and $v = 2$, is obtained by comparing 1-0 S($x$) and 2-1 S($x$), where $x$ is the same lower rotational quantum number. It can be useful to combine, using a weighted mean, the vibrational temperatures from several line pairs.

# Chapter 4

# Fitting Utility for SINFONI.

## 4.1 Rationale

Integral field spectroscopy data requires a new approach to visualising and analysing the large amounts of data that are collected in one observation. The primary data products from the SINFONI PIPELINE (henceforth known as SPIPE) are an IFS data cube and a standard star spectrum. The data cube has spatial information in the $x$ and $y$ axes and the spectral information in the $z$ axis. Therefore, for every spatial pixel there is a corresponding spectrum. In addition to these SPIPE data products, the user is expected to flux calibrate and extract information from the data cube using custom made scripts or dedicated software programs. The only existing STARLINK program developed for IFS data was DATACUBE, however its functions were limited[1] and were not well suited to SINFONI data. In 2005 the STARLINK project, due to funding cuts, ceased and all development of IFS software stopped. It is possible to extract information from a data cube, by considering each spectrum in turn. This method only works for data cubes that have very few spatial pixels and a limited number of emission/absorption lines.

[1] Although it was undergoing further development and the results looked promising

A SINFONI data cube contains a minimum of 4096 ($64^2$) spatial pixels and each one contains a spectrum. A typical rich *K*-band spectrum, containing $H_2$ molecular lines and atomic lines, can contain approximately 15 emission lines. If each line were to be fitted by hand, using STARLINK applications, it would take approximately 43 days[2].

There is an existing program, QFITSVIEW[3], that can be used to inspect a data cube and to provide quick continuum subtracted emission line images (Ott 2005). However, it assumes that the emission line does not shift or broaden and is surrounded by a 'good' continuum. It can provide a limited flux calibration, as long as the intrinsic stellar lines have been removed from the standard, a black body normalisation has been applied and its flux has been calculated.

The **F**itting **U**tility for **S**INFONI (FUS) program was developed primarily for this thesis, with an option to release to the wider astronomy community. The current beta version is available from `http://star.herts.ac.uk/~klowe`. The primary functions that FUS has to fulfil are:

**Inspect:** Quickly inspect the SINFONI data cube in the spatial and spectral axes.

**Reduce:** To flux calibrate the data cube with respect to the standard spectrum.

**Analyse:** To extract emission line, velocity and continuum images.

The following sections detail the construction and operation of FUS.

[2]Assuming each emission line take 1 minute to fit and the astronomer does not require sleep.

[3]`http://www.mpe.mpg.de/~ott/QFitsView`

## 4.2 Displaying the IFS data cube.

FUS is written in the Interactive Data Language (IDL), which is optimised for manipulating data arrays and images. IDL can be used in two ways: (1) step by step command line interface and (2) object oriented widgets. These widgets are used to provide an user friendly interface. The entire program code is presented in Appendix A. The following sections detail the use and application of major parts of the FUS program.

The initial user interface consists of two windows (see Fig. 4.1): the main program window, which enables the user to perform a spatial inspection of the data cube; and the second window displays a spectrum when the mouse is moved over a spatial pixel. The `File` menu provides options to open an uncalibrated data cube, 1D standard spectra in `.tfits` or `.fits` format, flux calibrated cube, and to save the data cube. The other menu functions are `re-bin spatial scale`, `correct for SINFONI skew`, `analysis bench`, `line ratio maps` and `help`, and are detailed further in this chapter.

The main display window presents a cross section image of a data cube at a single wavelength (Fig. 4.1 lower). The default setting displays an image at the main $H_2$ 1-0 S(1) line for a $K$ band image. The display is initially scaled between $\overline{I} - n\sigma$ and $\overline{I} + n\sigma$, where $\overline{I}$ is the mean pixel value of the image, $n$ an arbitrary integer (1 - default) and $\sigma$ is the standard deviation from the mean. The display limits can be set manually, by stating minimum and maximum values, or by $\pm n$ times the standard deviation from the mean. The user can interactively move through the wavelength dimension of the data cube by moving the slider, at the bottom of the display window, using cursor keys or the mouse.

The wavelength information can be inspected by moving the mouse over the image in the main display window. A spectrum for a spatial pixel will be displayed

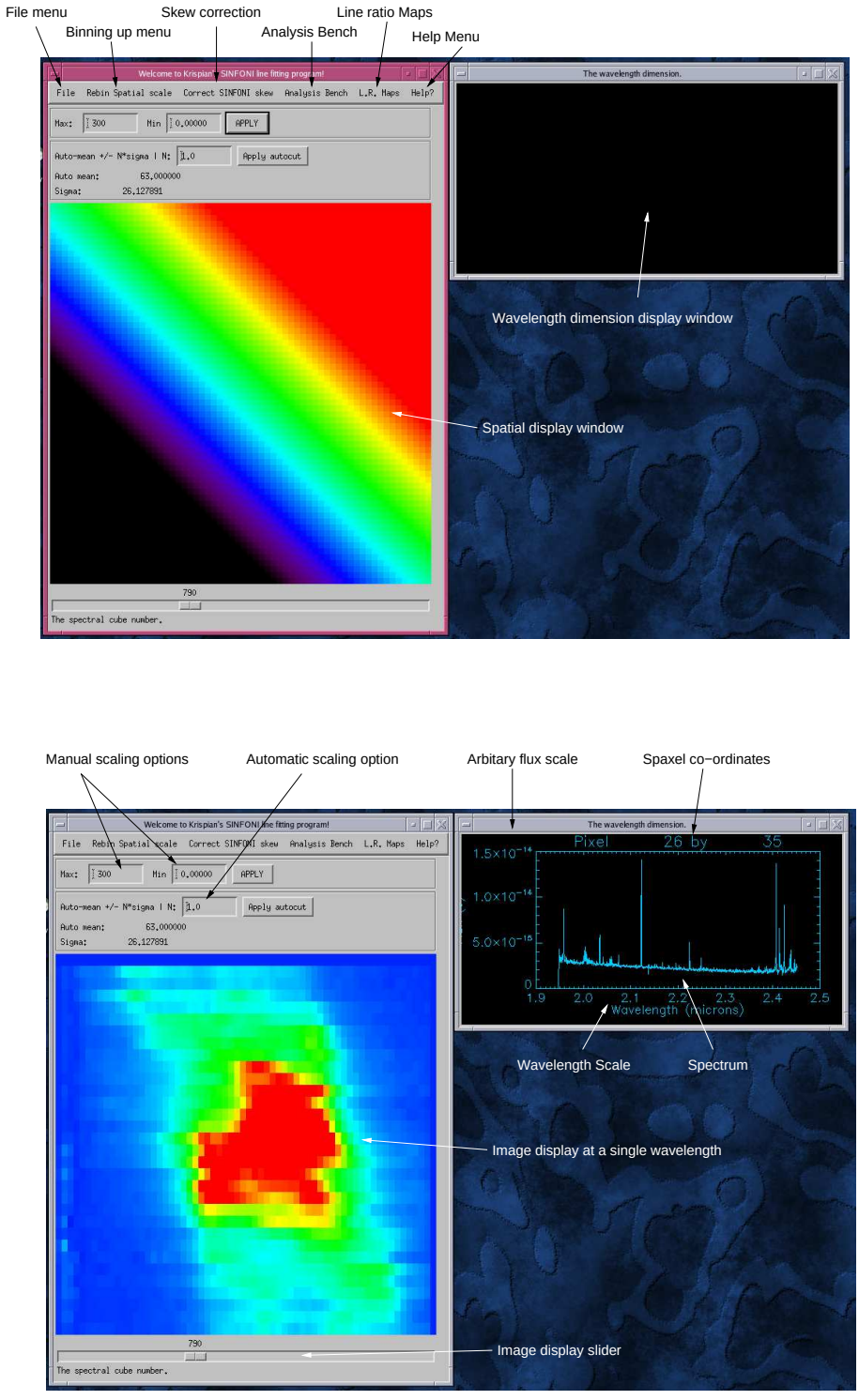


Figure 4.1: Two screen shots of the FUS program. **Top:** The initial user screen showing the various menus with the spectral and spatial wavelength display windows. **Bottom:** A data cube, of *IRAS* 19306+1407, loaded to show the functions of the FUS program with the key user options highlighted.

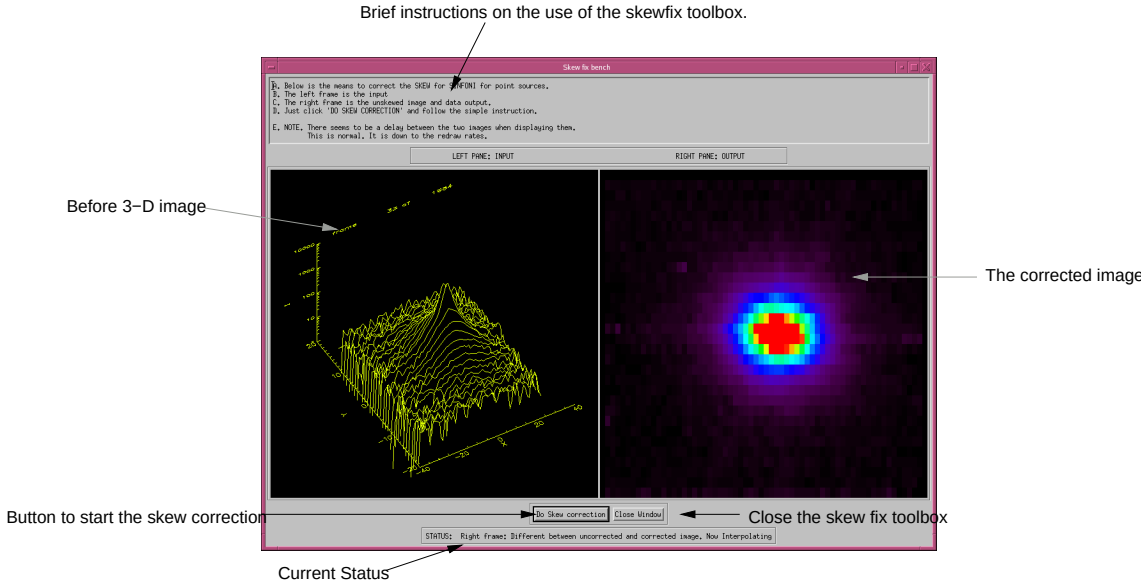


Figure 4.2: The skewfix window. The top panel contains instructions in the use of the skewfix window. The left hand panel shows the 3-D representation spatial axis ($x$ and $y$ axes) and the flux ($z$ axis) at a single wavelength bin. The right hand panel displays the corrected image. The bottom two buttons are `Do skew correction` and `close window`, which starts the skew correction procedure and closes the skewfix window. The bottom text box displays the current status of the correction.

in the wavelength dimension window. The limits are set automatically and cannot be altered by the user. These two methods of displaying 3D data enables the user to assess the quality of the data cube, look for extended structure and locations of the strongest emission lines.

## 4.3 Correcting for the skew effect.

The SINFONI instrument suffers from an optical distortion. The slitlets are not perfectly aligned to the edges of the CCD and the spectra appear slightly curved. The SPIPE provides an excellent correction, although it does not produce a complete solution. This became apparent when inspecting a data cube with the FUS program. The central peak of a point source shifts by a maximum of 1 pixel in the $x$ axis and a sub-pixel amount in the $y$ axis, over the entire wavelength range of the data cube.

This skew through the data cube is small, but is noticeable. This effect would produce a line ratio image with sharp edges. The authors of SPIPE are aware of this problem, but have not included a solution in the pipeline (private communication).

The routine `skewfix.pro`, which is available from the `correct SINFONI skew` menu option, will correct for the skew effect (Fig. 4.2). The current version only works for PSF-like sources with a bright continuum. The user is prompted to click on or close to the centre of the PSF and the centroid is determined for every spatial image at each wavelength. A polynomial is fitted to the centroid coordinates in $x$ versus wavelength and $y$ versus wavelength. A new coordinate system with respect to the calculated centroid position is applied to each and every image plane. The IDL routines `triangulate` and `trigrid` align the images to the same coordinate scheme and interpolate for the sub-pixel shifts. This provides an adequate fix for the SINFONI skew.

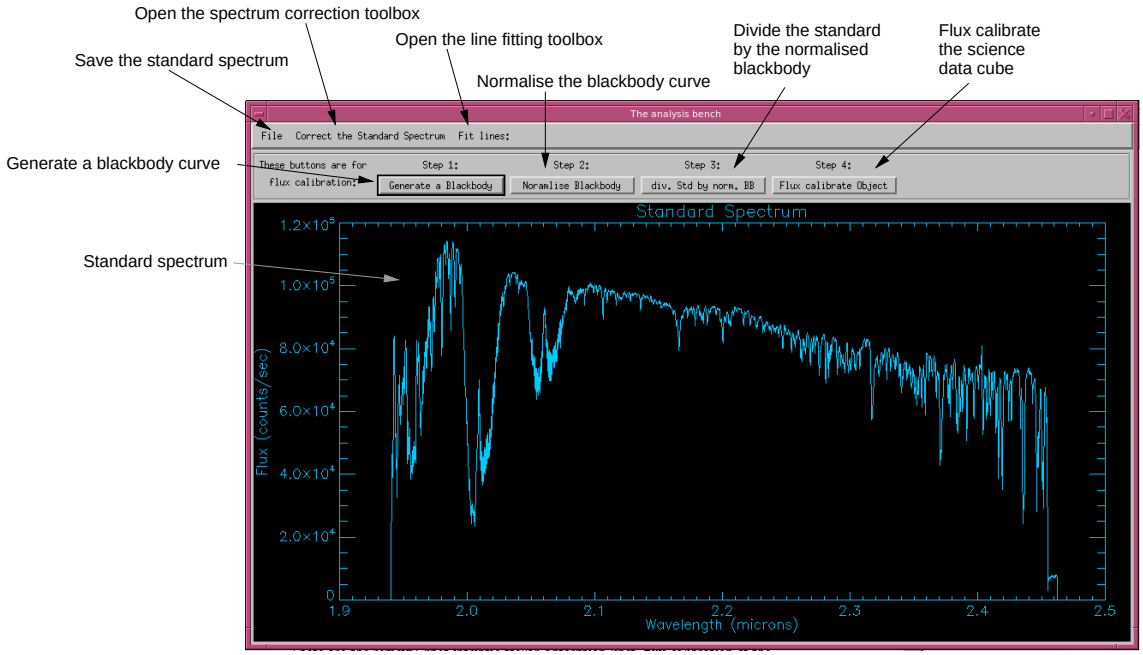


Figure 4.3: The analysis workbench. The top row shows the `file`, `correct the standard spectrum` and `fit line` menu options. The top row of buttons are used for flux calibration. The large display window currently displays a *K*-band standard star spectrum.

## 4.4 Analysis workbench

The final reduction steps are contained in the `analysis workbench` (Fig. 4.3). These are the removal of intrinsic stellar absorption lines, flux calibration of the science cube and emission line fitting.

The removal of intrinsic stellar absorption lines is very important in the flux calibration. If an intrinsic absorption line is not removed then an artefact emission line is introduced or an existing emission line is enhanced (e.g. Br$\gamma$). The FUS program includes a line correction toolbox, which enables the user to correct their standard star spectrum.

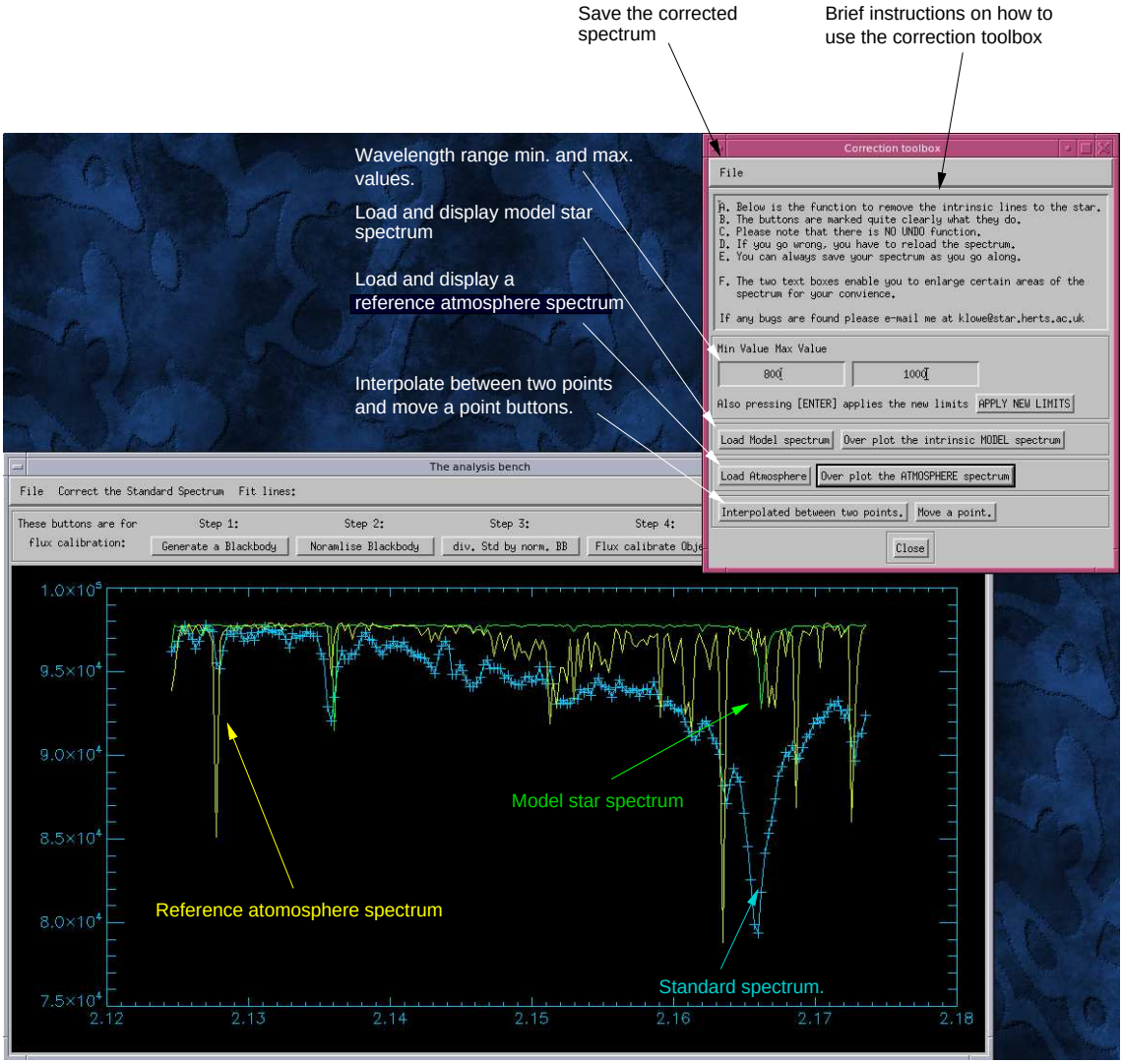


Figure 4.4: Line correction box displayed on top of the analysis workbench window. The top `file` menu option allows the user to save the current spectrum. The large text box contains the instructions for the line correction toolbox. There are two buttons to load an atmospheric and a model star spectrum, with two buttons to overplot these spectra. The bottom two buttons are to interpolate between two points or move a spectrum point.

### 4.4.1 Correct spectral standard for atmospheric and intrinsic lines.

To open the line correction tool box click on `correct the standard spectrum` > `remove intrinsic lines in STD spec` (Fig. 4.4). The correction toolbox has the following functions: brief instructions for the use of the toolbox, display sections of the standard star spectrum, load and display a model star spectrum, load and display an atmospheric spectrum, and alter the currently displayed spectrum.

The user can display the whole spectrum or a section of the spectrum, the lower and upper limits are in wavelength bin numbers, which range from 0 to 2217.

A one dimensional spectrum of the atmosphere and a model stellar atmosphere can be loaded and over-plotted on the standard star spectrum, which is displayed in the main analysis bench window. The model stellar atmosphere spectrum is read in as ASCII format file and the Earth's atmosphere is read in as a `fits` file. The comparison of these spectra enables the user to ascertain if an absorption or emission line is an intrinsic feature of the star's or Earth's atmosphere. The input spectrum must have an equal or greater spectral resolution than the standard spectrum. If the latter is true then the spectrum is convolved to match the standard star spectral resolution.

Any lines that have to be removed can be done in the following two ways, interpolating between two user indicated points or to move a single point. The user clicks on two points on the spectrum in the analysis window and then clicks the `interpolate between points`. All data between the two indicated points are interpolated with a simple linear relationship. If the user wishes to move a single point in the flux axis, they would select the desired point in the analysis bench window, click `move a point` and finally click on the final position. The correction tool box has no undo function; however, it is possible to save and reload the spectrum

at any point.

### 4.4.2 Flux calibrate science cube.

The flux calibration procedure in the FUS program is split into four steps. This enables the user to have more control and to correct mistakes easily. The first step is to generate a blackbody curve, using the `generate a Blackbody` button, between the minimum and maximum wavelength range (Fig. 4.5a). The user inputs a temperature in Kelvin with the associated error into the text fields. The resultant Blackbody is displayed in the analysis bench window. I

The second step is to normalise the blackbody, using the `Normalise Blackbody` button. The resultant spectrum is normalised at a wavelength stated by the `CRVAL3` in the FITS header. This is normally 2.2 microns for a $K$-band spectrum.

The third step is to divide the standard star spectrum by the normalised Blackbody. This is done by pressing `div. STD by norm. BB` button. It is preferable to use a blackbody than a model stellar atmosphere to normalise the standard star spectrum. This is because G-type stars have variable intrinsic absorption features that stellar atmosphere models may lack. Therefore, new absorption and emission lines could be introduced into the telluric standard spectrum and into the subsequent science IFS data cube.

The final fourth step is to flux calibrate the data cube (Fig. 4.5b). This is done by clicking the `flux calibrate object` button. An information window requires the following information to be entered: the wave band (*J, H* and *K*); plate scale in arcseconds; 2mass magnitudes (and associated error), and the integration time for the science target and standard. Once all required information has been entered press `perform flux calibration`. FUS will take a few minutes to grow the 1-D standard spectrum into a data cube, which is then divided into the science target

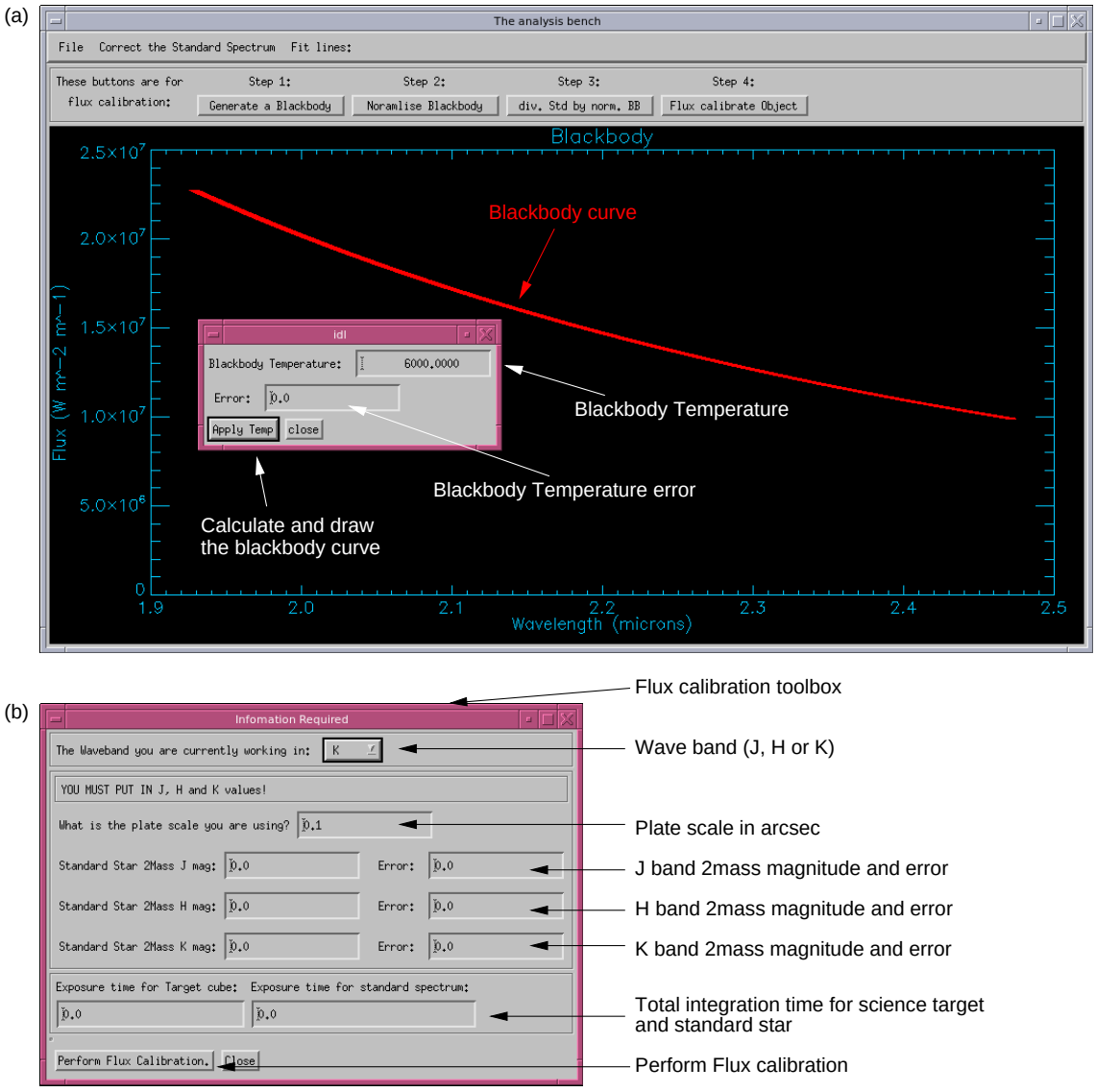


Figure 4.5: Black body and Flux calibration windows. Panel (a), shows the analysis workbench overlaid with the blackbody window, which requires a temperature and its respective error. The resultant blackbody curve is displayed in the analysis bench window. Panel (b), shows the analysis workbench with the overlaid flux calibration window. The required waveband, plate scale, infrared magnitudes and integration times are displayed in the text boxes and drop down menus. The flux calibration is initiated by the `perform flux calibration` button.

data cube. The 2mass magnitudes are converted into ESO magnitudes and then into W $m^{-2}$ $\mu m^{-1}$ $arcsec^{-2}$. The errors in the flux calibration are calculated. The final data products are a flux calibrated science cube and the corresponding calculated error data cube. These are named `<filename>.fits` and `<filename>err.fits`, respectively.

### 4.4.3 Fit emission lines and continuum for the cube.

A spectrum of a post-AGB star consists of line and continuum emission. As stated before, IFS produces a large number of spectra and each spectrum has to be analysed separately. Although the quickest method to produce continuum subtracted images is to subtract the mean flux either side of an emission line, and sum the remaining flux. This method does not take account of a blue or red shift due to line of sight velocities, line broadening, hot or cold pixels or a non-linear continuum. In addition, this method is analogous to narrow band imaging and the total line flux measure would be dependant on the chosen wavelength range. A robust method to measure the flux of an emission line, $F_j$, and the continuum is to fit a Gaussian and a polynomial, $g(\lambda)$, respectively, to a section of the spectrum, $F(\lambda)$, giving

$$F(\lambda) = P \exp\left[\frac{-(\lambda - \lambda_c)^2}{2\sigma^2}\right] + g(\lambda), \tag{4.1}$$

where $P$ is the height of the Gaussian, located at central wavelength, $\lambda_c$, with a width, $\sigma$. The polynomial is currently a hard-coded first order polynomial, which is acceptable over a small wavelength range. However, a future modification could increase $g(\lambda)$ to higher orders. The emission line flux is given by

$$F_j = \int_{\lambda_{\min}}^{\lambda_{\max}} P \exp\left[\frac{-(\lambda - \lambda_c)^2}{2\sigma^2}\right] d\lambda \tag{4.2}$$

and is evaluated numerically.

The fitting of the line is achieved with `mpfit.pro` and `mptfitexpr.pro`, which are subroutines developed by Markwardt (2006). These routines have been previously used in fitting IFS data, most notable SAURON observations of M100 (Allard et al. 2005). The routine `mptfitexpr.pro` interprets an user supplied function, in our case equation 4.1, and calls `mpfit.pro`, which finds the best fitting parameters. The procedure uses a Levenberg-Marquardt least-squared method of fitting, which finds the minimum squared difference between the function and supplied section of the spectrum. The fits are weighted with respect to the supplied errors. The errors are determined from the Poisson statistics of the science data cube and standard spectrum, and flux calibration. The input parameters for the equation are the area under the Gaussian, central wavelength, width and the height of the continuum. The best fitting values are returned with their associated errors.

The user interface for the line fitting is via the line fitting tool dialogue window, which is available from the `analysis workbench > line fitting` (Fig. 4.6). The dialogue window consists of several user input fields and a display of the total summed spectra of the data cube. The user is prompted for a wavelength range (Fig. 4.6;1), in wavelength bin numbers, and the rest wavelength in microns (Fig. 4.6;2). Once a wavelength range has been entered, the spectrum is redisplayed with labels showing the location of possible He, $H_2$ and HI emission. The user can then click on the peak of a chosen line and an initial fit is achieved (Fig. 4.6;3). This initial fit provides the routine with the initial fitting parameters.

The SINFONI instrument has an artefact which alters the emission line profiles to have broad emission wings. This is seen in the arc lines (Dumas 2007). The emission line can be fitted using three gaussian equations or a single gaussian for strong and weak lines, respectively. The artefact wings are lost in the continuum noise for the weaker emission lines.

Table 4.1: The output data from line fitting.

| Output | File name suffix | Error file name suffix | Units |
|---|---|---|---|
| A `Postscript` file of the spectrum with the best fitting profile and continuum. # indicates the number of the file. | `#.eps` | | $x$ axis - wavelength, $y$ axis - W $m^{-2}$ $\mu m^{-1}$ $arcsec^{-2}$ |
| The line intensity `fits` image file | `_fittedline.fits` | `_error.fits` | W $m^{-2}$ $arcsec^{-2}$ |
| The velocity image file. | `_vel.fits` | `_velerr.fits` | Km $s^{-1}$ |
| The continuum image file. | `_continuum.fits` | `_conterr.fits` | W $m^{-2}$ $\mu m^{-1}$ $arcsec^{-2}$ |
| The line width image file. | `_sigma.fits` | `_sigerr.fits` | $\mu$m |

A desired location and filename prefix (Fig. 4.6;4) for the resultant images has to be entered into the text box. The entire data cube can now be fitted for a chosen line, once the `fit cube` button has been pressed (Fig. 4.6;5) . The whole process takes a few minutes and the results are displayed for every spatial pixel at the bottom of the dialogue window. The output data is given in Table 4.1

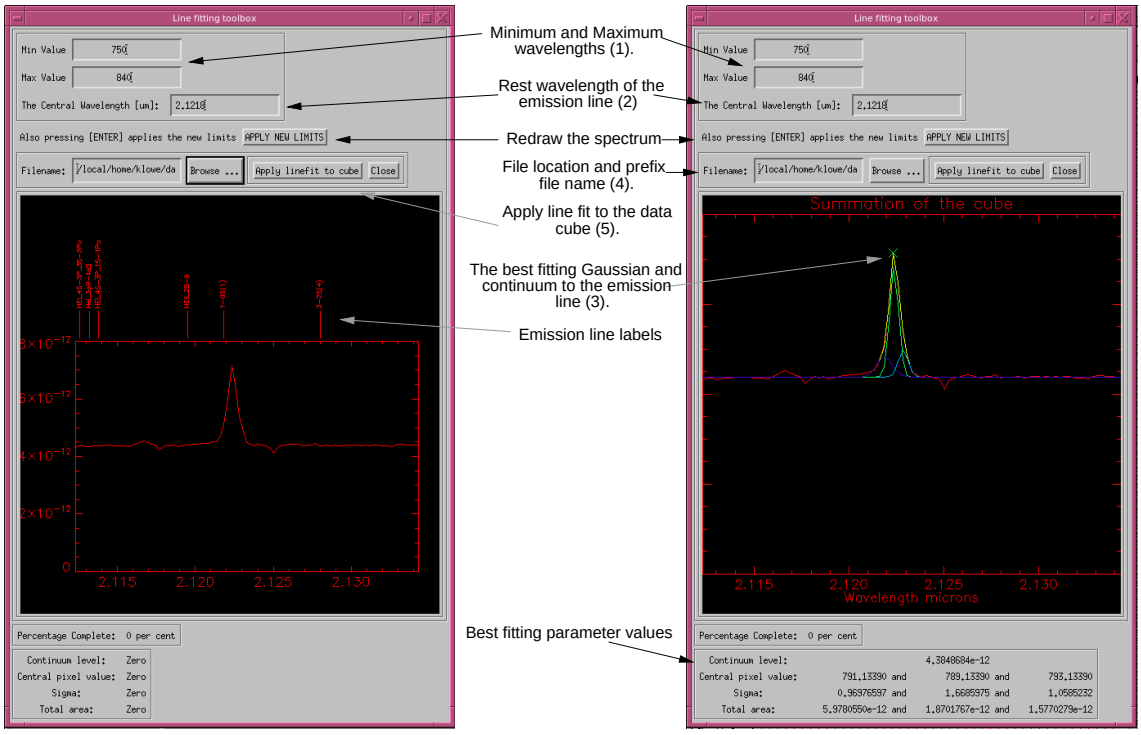


Figure 4.6: Line fitting box. The top two text boxes are the minimum and maximum wavelengths in bin number (1), to be displayed in the line fitting window. The central wavelength of the line is entered into text box in units of microns (2). The `apply new limits` button creates a new display using the user specified wavelength range. The file name text box requires a location and prefix file name(4). The main widow displays the spectrum and a fit is applied once the user has clicked in the emission peak (3). The best fitting parameters are displayed at the bottom of the window. The line fitting procedure for the entire cube is initiated by clicking `Apply line fit to cube` button (5).

## 4.5 Line ratio images.

The simplest way to ascertain physical processes or extinction is to calculate line ratios. It is possible with IFS to produce line ratio images and FUS can be used to create them. The images are loaded separated by clicking `load line maps > load image 1` and `... > load image 2`, which appear in the left and right hand panels, respectively (Fig. 4.7). The images are scaled between $\pm 1\sigma$ of the mean pixel value. The user can conduct simple arithmetic operations, addition ($+$), subtraction ($-$), multiplication ($\times$) or division ($\div$), on image 1 with respect to image 2. The resultant image is displayed in the third lower window and can be saved to a `fits` image file by selecting `File > save image`. The errors are calculated and saved to <`filename`>`_err.fits` file.

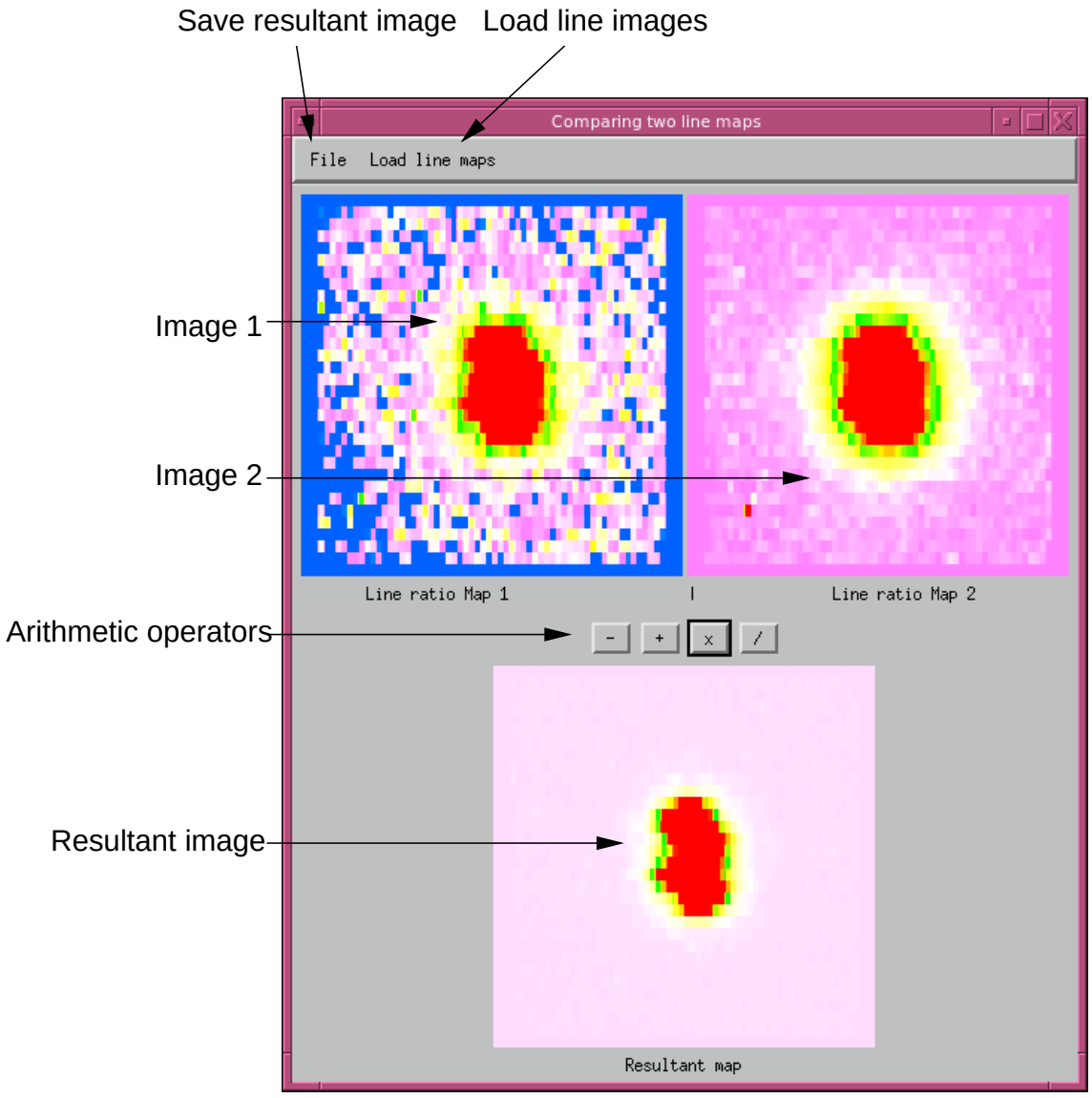


Figure 4.7: Line ratio image creation toolbox. The top menu options allow the user to save the created image (via `File`) and load the two input images. The left and right hand panels show the two loaded images. The lower panel shows the resultant image from the chosen arithmetic operator, which is situated between the top and bottom panels.

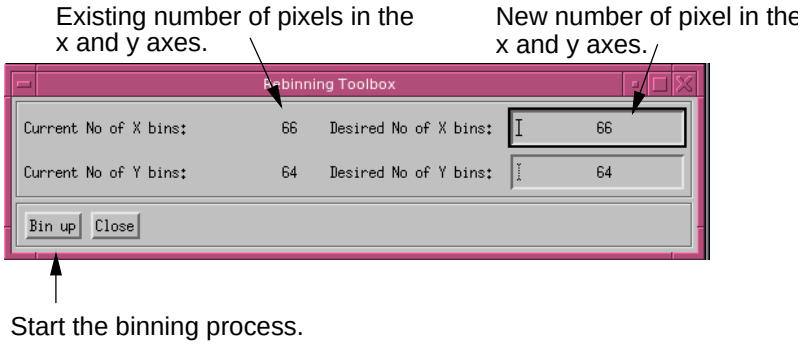


Figure 4.8: The bin up tool box, which requires the new number of pixels for the $x$ and $y$ axis.

## 4.6 Bin-up spatial components.

The integration times required for IFS observations are long, inclusive of over heads. A balance between an acceptable signal-to-noise ratio and the total integration time, for the conditions, has to be achieved. In the case of $K$-band spectroscopy, some $H_2$ molecular lines are weaker than the main 1-0 S(1) line. For example the 3-2 S(3) line, a measure of fluorescence, can be up to one thirtieth of the intensity of the main line. It can be unfeasible to observe this line for the required length of time to the required signal-to-noise, since it could require integration times far longer than the allocated observing time. The major advantage of IFS data is to 'bin up' the spatial plane to increase the signal to noise for the spectral axis. It is analogous to changing the slit width, however in our case it is done after the observations have taken place. The 'bin up' toolbox is opened from the `Rebin spatial scale` (Fig. 4.8). The new binned pixel value, $P'$, is the sum of $N$ pixels, $p_i$, and the binned pixel error, $E(P')$, which is the square root of the sum of $N$ squared pixel errors, $E(p_i)$. The binned pixel value is given by

$$P' = \sum_{i=1}^{N} p_i \quad \text{and} \quad E(P') = \sqrt{\sum_{i=1}^{N} [E(p_i)]^2} \tag{4.3}$$

If a particular spectrum has a signal-to-noise of 1 at each spatial pixel, it can be increased by binning up the data. A moderate 3×3 binning would produce a signal-to-noise of 3. The current version of FUS only allows uniform binning for a data cube.

## 4.7 Future improvements

The FUS program was developed primarily for SINFONI data and this thesis. It is a powerful tool for inspecting, reducing and analysing IFS data, for which no public software is available. There is scope to improve this program for future use. Currently the input data cube is constrained to FITS files that have specific keyword headers and the data structure is arranged in a 3-D array. For example SAURON data is arranged in a 2-D array and cannot be interpreted by `fus`. However, it can be possible to alter FUS code to interpret and rearrange the input data structure. It is also possible adapt the code to accommodate other wavelength ranges (i.e. optical to sub-mm).

The bin-up procedure can only uniformly bin the spatial component. Two possible improvements can include extracting user specified regions and adaptive binning. The former method is useful for investigating similar regions. The latter method could be used to achieve a constant signal-to-noise for a chosen emission line by implementing algorithms from Cappellari & Copin (2003).

# Chapter 5

# Polarimetry of *IRAS* 19306+1407

*This chapter is based on a refereed paper: Lowe & Gledhill (2007).*

This chapter examines *IRAS* 19306+1407 (GLMP 923), which has *IRAS* colours typical of a post-AGB star with a cold CSE (Omont et al. 1993). Radio and millimetre surveys for molecular emission have failed to detect OH or $H_2O$ masers (Likkel 1989) or CO emission (Arquilla, Leahy & Kwok 1986; Likkel et al. 1991). However, the object shows a number of dust spectral features. Hrivnak et al. (2000) present *ISO* spectroscopy showing emission features at 6.3, 7.8 and 10.7 μm, with a "probable" feature at 3.3 μm, and compare these features to the unidentified infrared (UIR) bands at 3.3, 6.2 and 7.7 μm, commonly attributed to polycyclic aromatic hydrocarbon (PAH) molecules (Allamandola, Tielens & Barker 1989). Given that the mid-infrared spectral features are similar to those seen in hot carbon-rich PN, Hrivnak et al. (2000) suggest that the object is a young PN. A further analysis of the *ISO* data by Hodge et al. (2004) confirms the presence of UIR features at 3.3, 6.2, and 7.7 μm, with the addition of the 8.6 and 11.2 μm features. These authors also mention the presence of silicate emission at 11, 19 and 23 μm, raising the possibility that *IRAS* 19306+1407 may have a mixed CSE chemistry.

Optical spectroscopy, of the central star, shows a broadened H$\alpha$ emission line with line width of ∼2300 km s$^{-1}$ indicating a fast outflow (Sahai & Contreras 2004),

as well as H$\beta$ and [NII] emission, leading Kelly & Hrivnak (2005) to suggest a spectral type of approximately B0 for the star. A number of $H_2$ emission lines are seen in the $K$-band, with line ratios suggesting a mix of radiative and shock excitation (Kelly & Hrivnak 2005). Imaging through a narrow-band $H_2$ filter, centred on the 2.122 μm line, shows that the $H_2$ emission has a ring-like structure with evidence for bipolar lobes extending perpendicular to the ring (Volk et al. 2004).

The first near-infrared polarimetric images of the dusty CSE of *IRAS* 19306+1407, showing the structure of the envelope in scattered light are presented in this chapter, with supporting sub-millimetre photometry and archived *HST* images. The observations are interpreted using 2-dimensional (axisymmetric) light scattering and radiation transport models.

## 5.1 Observations and Results

Polarimetric imaging at *J*- and *K*-band of *IRAS* 19306+1407 was obtained at the 3.8-m UKIRT on Mauna Kea, Hawai'i, using UIST in conjunction with IRPOL2. A pixel scale of 0.12 arcsec was used and observations were made on 2003 June 8 with an average seeing of 0.5 arcsec. The total integration time for each filter was 237.6 seconds, comprising 24 exposures of 9.9 seconds each (see Table 5.1). Linear polarimetry was obtained by observing at four half-waveplate angles of 0°, 22.5°, 45° and 67.5°. The data reduction was carried out using STARLINK[1] applications. A bad pixel mask was created using ORACDR and chopped to 512 by 512 pixels. The standard subtraction of dark frames and flat fielding were carried out by CCDPACK. A 3D cube consisting of the *I, Q* and *U* Stokes images, was produced using POLKA from the POLPACK suite, and this was then used to derive the per cent polarisation, polarised flux and polarisation angle. A more detailed description of dual-beam polarimetry and the data reduction techniques is given by Berry & Gledhill (2003).

Photometric standards, FS 147 (*J*) and FS 141 (*K*), were used to flux calibrate the data, giving $J$=11.18 ± 0.04 and $K$=10.29 ± 0.12. The 2mass photometric magnitudes, corrected to UKIRT magnitudes, are $11.23 \pm 0.04$ and $10.32 \pm 0.03$ for *J*- and *K*-bands, respectively. These 2mass values are similar, within errors, to the measured photometry from the UKIRT observations; however, the UKIRT values are slightly brighter. Elias 14 was used as polarimetic standards at *J*- and *K*-bands to calibrate the position angle (PA) offset and measure the level of instrumental polarisation.

For these observations the focal plane polarimetry mask was removed. This creates artefacts in the reduction process and they are marked as such on Fig. 5.1. A description of the production of these artefacts are documented in §2.1.3.

[1]Available from `www.starlink.ac.uk`

Table 5.1: Summary of photometry from *IRAS* 19306+1407 for *HST* (using Vega zero points), UKIRT and SCUBA observations, including integration time (Int.) and the extent (Size) of the semi-major and minor axes of the aperture used in photometry. The PA angle of photometry aperture is equal to 18°(E of N).

| Band | Magnitude | Flux (mJy) | Int. (s) | Size (arcsec × arcsec) |
|---|---|---|---|---|
| *F606W*[a] | $13.81 \pm 0.03$ | $9.5 \pm 0.3$ | 300 | $3.2 \times 2.0$ |
| *F814W*[b] | $12.45 \pm 0.02$ | $26.1 \pm 0.5$ | 50 | $3.2 \times 1.9$ |
| *J*[c] | $11.18 \pm 0.04$ | $51.5 \pm 0.8$ | 237.6 | $3.9 \times 2.4$ |
| *K*[d] | $10.29 \pm 0.12$ | $48.4 \pm 2.2$ | 237.6 | $3.9 \times 2.4$ |
| *450W*[e] | - | $49.9 \pm 38.7$ | 1334[†] | - |
| *850W*[f] | - | $14.1 \pm 3.7$ | 1334[†] | - |

Notes: central wavelengths at [a]0.5888μm (Broad *V*), [b]0.8115μm (Johnson *I*), [c]1.25μm, [d]2.2μm, [e]450μm and [f]850μm; and [†]inclusive of observational overheads.

### 5.1.1 Imaging polarimetry observations and results

The *J*- and *K*-band polarimetric results are shown in Fig. 5.1. The total intensity images are shown in Fig. 5.1 (a) and (c), superimposed with polarisation vectors, and show the centrally peaked nature of the source. The object is clearly extended, relative to the 0.5 arcsec seeing, with faint emission detected out to a radius of approximately 3 arcsec. The lowest contour in both filters is 3 times the sky noise and in the $I_{\rm J}$ image, shows that the faint emission is elongated in a north-northeast/south-southwest direction. Details of contour levels are given in the Figure 5.1 caption. It is possible that a similar extension is present in the $I_{\rm K}$ image, but confusion due to the presence of the artefact stars makes this uncertain.

The polarised flux, produced by light scattering from dust grains, is shown in Fig. 5.1 (b) and (d). In both filters, the central region appears elongated along a PA 136° East of North, with two bright shoulders of emission either side of the star. At *J* the polarised flux image ($\rm IP_J$) shows this structure is embedded within fainter more extended emission orientated at 18° East of North, seen in the lowest three contours (the lowest contour is at 1.5 times the sky noise). This faint extension is not as apparent in the *K*-band polarised flux image ($\rm IP_K$), which is approximately 1 mag arcsec$^{-2}$

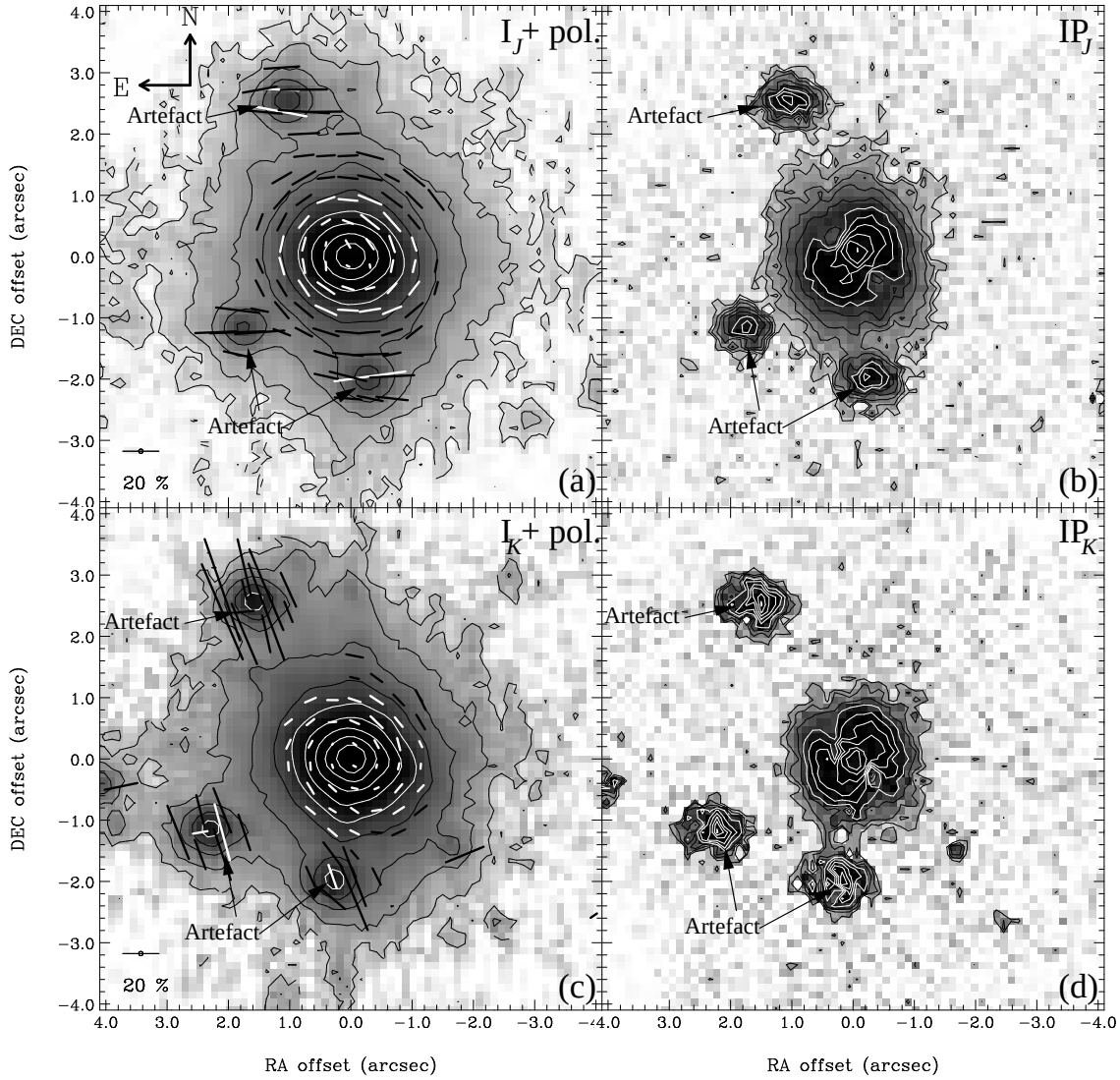


Figure 5.1: The $J$- and $K$-band observations are displayed at the top and bottom of the figure respectively. These images have been scaled logarithmically. The total intensity (I) is displayed in sub-figures (a) and (c) with overlaid polarisation vectors (pol). Sub-figures (a) and (c) are scaled between 20 and 13 mag arcsec$^{-2}$. The lowest outer contour levels are 19 and 18 mag arcsec$^{-2}$ and separated by 1 mag arcsec$^{-2}$ for (a) and (c) respectively. The polarised flux (IP) images (b) and (d) are scaled between 20 to 16 mag arcsec$^{-2}$ and 19 to 16 mag arcsec$^{-2}$ respectively. The lowest outer contours are 19 (b) and 18 (d) mag arcsec$^{-2}$ and separated by 0.5 mag arcsec$^{-2}$.

shallower than the $J$-band data. The NW shoulder is brighter than the SE shoulder, particularly apparent in the $IP_J$ image. Similar morphology has been observed in polarised flux in a number of other PPNe. Gledhill et al. (2001) found bright arc-like structures on either side of the star in *IRAS* 17436+5003 as well as shoulder-like features in *IRAS* 19500-1709 and more ring-like features in *IRAS* 22223+4327 and 22272+5435. They interpreted these structures in terms of scattering from the inner surfaces of a detached axisymmetric shell, with an equatorial density enhancement, and classified these objects as "shell-type". The arcs in *IRAS* 17436+5003 were later fully resolved in mid-infrared imaging of thermal emission from the dust (Gledhill & Yates 2003) and successfully modelled using an axisymmetric dust distribution based on that of Kahn & West (1985). Further evidence for arcs and shoulders is seen in polarised flux images of *IRAS* 06530-0213, 07430+1115 and 19374+2359 (Gledhill 2005) and was interpreted using light-scattering in a Kahn & West density distribution. Therefore the polarised flux shoulders seen around *IRAS* 19306+1407 are interpretated in the same way, and suggest that they result from increased scattering at the inner boundary of a detached shell with an equatorial dust density enhancement.

The polarisation vectors shown in Fig. 5.1 (a) and (c) are binned over 0.36 $\times$ 0.36 arcsec (3 $\times$ 3 pixels) and have a signal-to-noise threshold of 2 in per cent polarisation. The vector pattern appears approximately centro-symmetric in both filters, indicating isotropic illumination by a central source. The maximum per cent polarisation is $15 \pm 6$ and $10 \pm 4$ at $J$- and $K$-bands respectively (Table 5.2). These values are lower limits to the intrinsic polarisation, since in these observations it has not been possible to correct for dilution of the polarised flux by the unpolarised light from the central star. It is theoretically possible to obtain the intrinsic polarisation of the star by removing its total intensity PSF. This requires a bright star, with no extended emission, to be present in the FOV. In addition, if the bright PSF star is

Table 5.2: Summary of polarimetric results of *IRAS* 19306+1407 for each band, detailing the maximum polarisation, integrated polarisation and the position angle (E of N) of the major and minor axis of the nebula in polarised flux.

| Band | Max. Pol. (per cent) | Integrated Pol.† (per cent) | $PA_{major}$ (°) | $PA_{minor}$ (°) |
|---|---|---|---|---|
| *J* | $15 \pm 6$ | $1.7 \pm 0.1$ | 18 | 136 |
| *K* | $10 \pm 4$ | $1.3 \pm 0.1$ | 18 | 136 |

†- The integrated polarisation over the source with apertures of radii of 1.7- and 1.4-arcsec for *J*- and *K*-band respectively.

misaligned or the shape of the PSF is slight different, then the resultant subtraction can produce negative 'hole' in the resultant image (Gledhill & Takami 2001).

### 5.1.2 *Hubble Space Telescope* observations and results

The archive *HST* images for *IRAS* 19306+1407[2] were observed on 2003 September 8 (proposal ID: 9463). The observations were obtained with the Advanced Camera for Surveys (ACS), in conjunction with the High Resolution Channel (HRC), using *F814W*- and *F606W*-filters with pivotal wavelengths of 5888 and 8115 Å respectively. The images were reduced using the On-the-Fly Reprocessing of *HST* Data (OTFR), which produces a cosmic-ray cleaned, calibrated, geometrically corrected mosaic image. Aperture photometry was performed using GAIA, using the Vega zero points[3], and obtained magnitudes of $13.81 \pm 0.03$ and $12.45 \pm 0.02$ for *F606W* and *F814W* respectively (Table 5.1). These photometric values include the extended emission.

The reduced *F606W* and *F814W* images are shown in Fig. 5.2 (a) and (b). Fig. 5.2 (c) shows the *F606W* image superimposed with contours of *J*-band polarised flux from Fig. 5.1 (b). The object is clearly bipolar in the *F606W* image, and the curved edges of bipolar cavities, extending for 3 to 4 arcsec from the source, can be

[2]Based on observations made with the NASA/ESA Hubble Space Telescope, obtained from the data archive at the Space Telescope Institute. STScI is operated by the association of Universities for Research in Astronomy, Inc. under the NASA contract NAS 5-26555.

[3]`http://www.stsci.edu/hst/acs/analysis/zeropoints`

seen. The orientation of the bipolar axis, at PA 18 deg, is aligned with the *J*-band elongation in total and polarised intensity seen in Fig. 5.1 (a) and (b). The bipolar structure appears to be surrounded by a faint, more spherically symmetric halo, seen in both *HST* filters, and this corresponds in extent to the outer contours in Fig. 5.1 (a) and (c). The polarised flux shoulders, at PA 136 deg, are not perpendicular to the major axis of the nebula and this is clearly seen in Fig. 5.2 (c). This non-orthogonality in the two axes will be discussed further in Section 5.3.

The southern bipolar lobe appears to be the brighter of the two in both *HST* filters, which could indicate that the major axis is slightly inclined to the plane of the sky.

### 5.1.3 Sub-millimetre observations and results

Observations were made on 2005 January 8 using the Sub-millimetre Common User Bolometer Array (SCUBA) at the 15 m James Clerk Maxwell Telescope (JCMT) on Mauna Kea, Hawai'i. The SCUBA observations were made simultaneously at 450 and 850 μm in photometry mode using a jiggle pattern. The 450 and 850 μm photometry data were reduced using the SURF package within the STARLINK suite. The last JCMT sky opacity measurement was conducted several hours before the observation of *IRAS* 19306+1407 and none were conducted afterwards. The sky opacity was corrected using the Caltech Sub-millimetre Observatory (CSO) $\tau$ relationship[4]. This is a good approximation for the sky opacity, although a fixed correction without temporal variability, if the JCMT measurements are not available.

Flux calibration was performed using Mars, inclusive of a maximum ±5 per cent error due to the orientation of Mars' poles relative to the Earth and Sun. *IRAS* 19306+1407 was detected at 450- and 850-μm at $> 1\sigma$ and $> 3\sigma$ respectively

[4]Using the revised 2000 October 25 relations

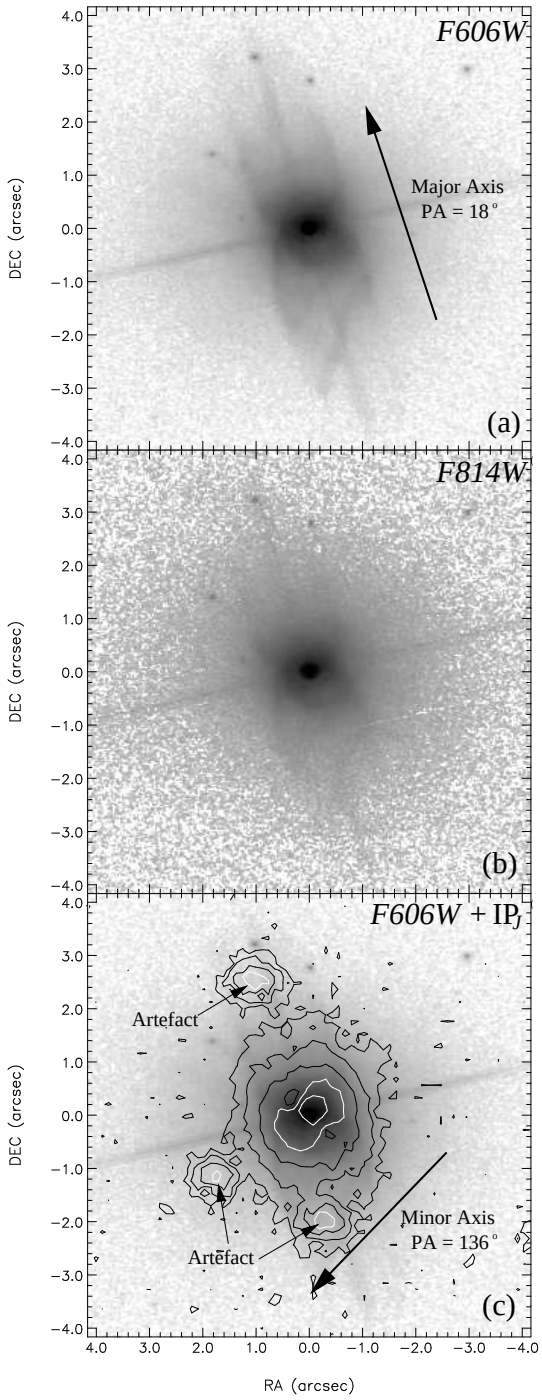


Figure 5.2: The *HST* ACS images, scaled logarithmically, of *IRAS* 19306+1407. (a) *F606W* (5888Å) scaled between 22 and 13 mag arcsec$^{-2}$ with the angle of the major axis indicated by the arrow. (b) *F814W* (8115Å) scaled between 22 and 11 mag arcsec$^{-2}$. (c) *F606W* image, scaled as above, and *J*-band polarised flux contours. The lowest contour level is 19 mag arcsec$^{-2}$ and subsequent contours are separated by 1 mag arcsec$^{-2}$.

inclusive of calibration errors. The fluxes obtained (Table 5.1) for $F_{450}$ and $F_{850}$ are $49.9 \pm 38.7$ mJy and $14.1 \pm 3.7$ mJy within a beam size of 7.5 and 14 arcsec respectively.

## 5.2 Modelling the CSE

### 5.2.1 Model details

The modified versions of the Ménard (1989) axisymmetric light scattering (ALS) code to produce Stokes *I, Q, U* images, and the axisymmetric radiative transfer (DART) code (Efstathiou & Rowan-Robinson 1990) to model the SED, are used to investigate the dusty CSE around *IRAS* 19306+1407. Both codes have previously been used to model the CSEs of post-AGB stars. Gledhill & Yates (2003) used DART to simulate multi-wavelength mid-infrared imaging observations of *IRAS* 17436+5003, in which an axisymmetric shell was resolved. To simulate the axisymmetry, the authors used a simple spatial distribution dust density formulation from Kahn & West (1985) that has been successful in reproducing all of the axisymmetric features, including the offset location of the brightness peaks seen in the data. This was found to be due to the inclination of the system to the plane of the sky. Gledhill (2005) has used the ALS code to produce generic light scattering models of PPN at varying optical depth and also finds that a Kahn & West density model provides a good representation of the observations with a minimum number of model parameters. It is important that the dust density model uses a minimum number of parameters whilst achieving an adaptable axisymmetric geometry, so that there is a better chance of each parameter being observationally well constrained. More complex dust density formulae have been used (e.g. Meixner et al. 2002), which incorporate the presence of AGB and superwind mass loss histories, but require more parameters (twice as many in the case of Meixner et al. 2002). These models result in morphologies that are qualitatively similar to the simpler models, but are unlikely to be well constrained by the observations. In both the ALS and DART models a simpler density profile from Kahn & West (1985) is used to model an axisymmetric shell, whilst it is recognised that it has a limited ability to reproduce more complex

morphologies:

$$\rho(r,\theta) = \rho_0 \left(\frac{r}{r_{\rm in}}\right)^{-\beta} (1 + \epsilon \sin^{\gamma}\theta)\,, \tag{5.1}$$

where $\rho_0$ is the density at the pole ($\theta = 0°$) at the inner radius, $r_{\rm in}$, and $\beta$ specifies the radial density distribution. The azimuthal density distribution is determined by parameters $\epsilon$ and $\gamma$, which specify the equator-to-pole density ratio $(1 + \epsilon)$ and the degree of equatorial enhancement, respectively. An increase in $\gamma$ flattens the density distribution, creating a more toroidal structure.

All parameters in Equation 5.1 are optimized in the model, apart from $\beta$, which is fixed at a value of 2 due to a limitation of the DART code, corresponding to constant mass-loss rate and expansion velocity for the AGB wind. The ALS density profile includes an extra parameter, that restricts the axisymmetry to within a radius, $r_{\rm SW}$, modifying Equation 5.1 to:

$$\rho(r,\theta) = \rho_0 \left(\frac{r}{r_{\rm in}}\right)^{-\beta} \quad \text{when} \quad r > r_{\rm SW}. \tag{5.2}$$

A power law size distribution is used with spherical grains of radius $a$, between a minimum and maximum grain size of $a_{\rm min}$ and $a_{\rm max}$ respectively, and a power-law index, $q$,:

$$n(a) \propto a^{-q} \quad \text{for} \quad a_{\rm min} \leq a \leq a_{\rm max}. \tag{5.3}$$

The inclination of the symmetry axis to the plane of the sky is not known. As mentioned in Section 5.1.2, the southern bipolar lobe appears slightly brighter than the northern one in *HST* imaging (Fig. 5.2), which could indicate a small inclination to the plane of the sky. Although the near-infrared images appear consistent with zero inclination (e.g. they are similar to edge-on axisymmetric shell models shown in Gledhill 2005), the inclination angle is considered to be a free parameter and it is varied in steps of 10 deg.

The overall chemistry of the system is uncertain. The results from Hrivnak et al. (2000) suggest a C-rich nature based on emission features consistent with C-rich PNe. Hodge et al. (2004) re-evaluated the mid-infrared spectra and classified *IRAS* 19306+1407 as "UIR features coupled with emission from crystalline silicates" suggesting a dual chemistry nature. The dust species that have been considered in the models are amorphous carbon (amC), silicon carbide (SiC) and Ossenkopf cold silicates, and the optical constants have been obtained from Preibisch et al. (1993), Pégourié (1988) and Ossenkopf, Henning & Mathis (1992) respectively.

A total of over 150 ALS and over 300 DART models have been run to create a model grid for the free physical parameters (Table 5.3). The minimum and maximum grain sizes were investigated from 0.005 to 1 μm, with a variable grain size spacing typically 0.005 to 0.02 μm. The grain size power law index was varied between 3.0 to 6.0 at increments of 0.5. The radial density fall off exponent is fixed at $\beta = 2$ and cannot not be varied. The bin widths for the CSE parameters, common to both models are 1, 2, 10° and $0.1\times10^{-2}$ for the equator-to-pole contrast ($\epsilon$), equatorial density enhancement ($\gamma$), inclination angle ($\theta$) and the ratio of the inner-to-outer radii ($r_{\rm in}/r_{\rm out}$) respectively. The stellar temperature, $T_*$, was investigated using a series of Kurucz models[5] with solar metallicities and temperatures separated by 1000 K.

The ALS code is used to determine the best-fitting envelope parameters based on the morphology, azimuthal profiles in polarised flux and radial profiles of the percentage polarisation and total intensities. The ALS code is additionally used to constrain the dust grain size by generating polarisation information. The ALS estimate of the grain size is an important input to the DART calculations, which would otherwise suffer from a degeneracy between grain size and outer CSE radius, both of which strongly influence the long-wavelength tail of the SED. The optical

[5] `http://kurucz.harvard.edu/grids.html`

Table 5.3: The CSE and dust grain parameters for the best-fitting ALS and DART models for *IRAS* 19306+1407.

| Parameter | Value | Description |
|---|---|---|
| **Dust grain parameters** | | |
| Ossenkopf | | |
| Cold Silicates[1] | 1.0 ± 0.01 | Number fraction |
| $a_{\rm min}$ (μm) | 0.10 ± 0.01 | Minimum grain radius |
| $a_{\rm max}$ (μm) | 0.40 ± 0.01 | Maximum grain radius |
| $q$ | 3.5 ± 0.5 | Grain size power law index |
| **Envelope model parameters** | | |
| $\beta^{\dagger}$ | 2 | Radial density fall off |
| $\epsilon$ | 6 ± 1 | Equator-to-pole density contrast |
| $\gamma$ | 5 ± 2 | Equatorial density enhancement |
| $\theta$ (deg) | 0 ± 10 | Inclination angle (from equator) |
| $r_{\rm in}/r_{\rm out}$ ($10^{-2}$) | 7 ± 1 | Inner-to-outer radius ratio |
| **ALS model parameters** | | |
| $\tau^{\ddagger}_{1.2}$ ($\times 10^{-1}$) | 6.78 ± 0.05 | Optical depth at 1.2 μm |
| $\tau^{\ddagger}_{2.2}$ ($\times 10^{-1}$) | 1.13 ± 0.01 | Optical depth at 2.2 μm |
| $r_{\rm SW}/r_{\rm in}$ | 2.0 ± 0.5 | Super-wind to inner radius ratio |
| **DART model parameters** | | |
| $T_{\star}$ ($10^3$ K) | 21 ± 1 | Effective Stellar Temperature |
| $r_{\star}/r_{\rm in}$ ($10^{-5}$) | 1.4 ± 0.2 | Stellar-to-inner radius ratio |
| $r_{\star}$ ($R_{\odot}$) | 3.8 ± 0.6 | Stellar radius at 2.7 ± 0.1 kpc |
| $A_V^{\rm CSE}$ (mag) | 2.0 ± 0.1 | Equatorial optical extinction |

[1]Ossenkopf et al. (1992). [†]This variable is fixed in the model code and cannot be varied. [‡]The optical depth is an output of the ALS model.

depths at 0.55, 1.2 and 2.2 μm are also derived from the ALS model and subsequently inserted into the DART model. The DART model fits to the SED are used to constrain the temperature of the central star, inner-to-outer and stellar-to-inner radii ratios. The two codes were used to iteratively produce a convergent model.

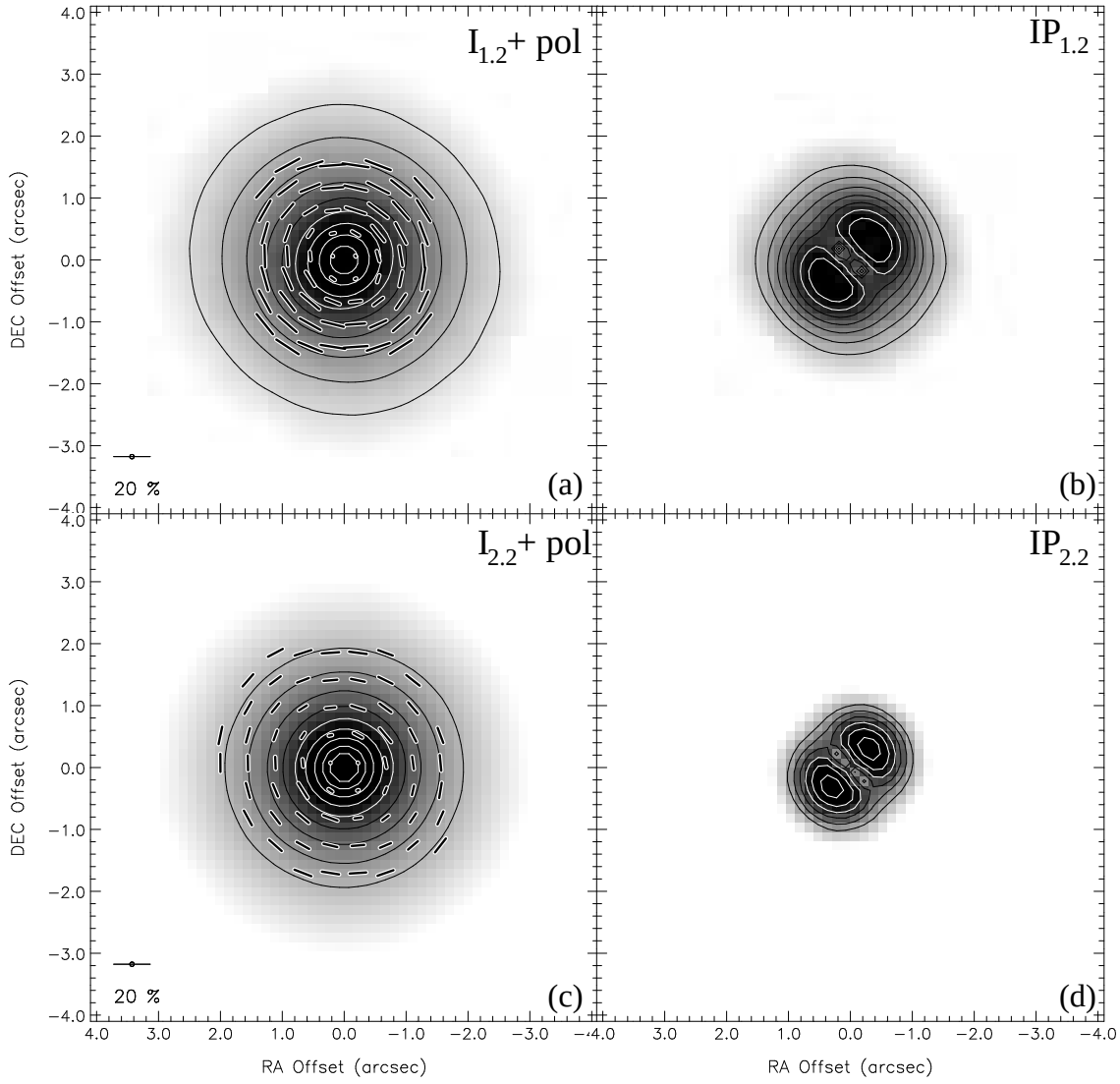


Figure 5.3: The 1.2- and 2.2-µm smoothed model images of *IRAS* 19306+1407 are displayed at the top and bottom of the figure respectively. These images are rotated to a PA of 136°to mimic the observed data. As with the observed images they have been scaled logarithmically. The total intensity (I) is displayed in sub-figures (a) and (c) with overlaid polarisation vectors (pol) and polarised flux is shown in (b) and (d). The model images have been normalised at the same levels as the observed images: (a) and (c) are scaled between 20 and 13 mag arcsec$^{-2}$ with lowest outer contour levels at 19 and 18 mag arcsec$^{-2}$, respectively, separated by 1 mag arcsec$^{-2}$; (b) and (d) are scaled between 20 to 16 mag arcsec$^{-2}$ and 19 to 16 mag arcsec$^{-2}$ respectively with lowest outer contours at 19 (b) and 18 (d) mag arcsec$^{-2}$, separated by 0.5 mag arcsec$^{-2}$.

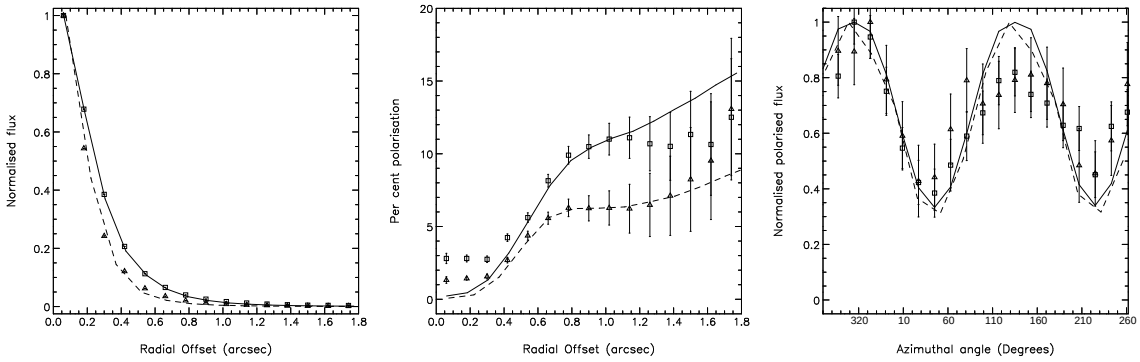


Figure 5.4: **Left:** Azimuthally averaged radial profiles of the normalised total intensity. **Centre:** Azimuthally averaged radial profiles of the per cent polarisation. The per cent polarisation within a radius of ∼0.2 arcsec is from bright central peak. **Right:** Radially averaged azimuthal profiles of the normalised polarised intensity. In all cases, the *J*- and *K*-band data are displayed as squares and triangles respectively, with $3\sigma$ error bars, and the 1.2- and 2.2-μm smoothed model data are displayed as solid and dashed curves respectively.

## 5.2.2 Model results

### 5.2.2.1 ALS model.

Before the raw model images can be compared with the polarimetric observations, they must be smoothed to mimic the effect of the atmosphere and telescope. A simple Gaussian filter is unable to reproduce the wings of the point spread function (PSF) effectively, which is essential since the PSF wings have a critical effect on the percentage polarisation in the envelope where the intensity is low, at $r > r_{\rm in}$. To obtain a more realistic fit a Moffat filter profile is adopted:

$$M(r) \propto \left[1 + \left(\frac{r}{\alpha_{\rm mof}}\right)^2\right]^{-\beta_{\rm mof}}, \tag{5.4}$$

where $r$ is radius from the source and $\alpha_{\rm mof}$ and $\beta_{\rm mof}$ are fitting parameters (Moffat 1969). The Moffat parameters were calculated by fitting to the PSF of a bright field star (Table 5.4) and their uncertainties were estimated by examining the fit to the remaining field stars. The filter was then applied to the raw (*I, Q* and *U*) model images, which were then combined to obtain polarised flux and per cent polarisation

values.

The resultant best-fitting smoothed model is shown in Fig. 5.3 and the parameters used are displayed in Table 5.3. The model reproduces the centrosymmetric polarisation pattern and the observed degrees of polarisation in the *J*- and *K*-bands. The polarised flux images show the shoulders seen in the observations, due to the enhanced scattering at the inner edges of the axisymmetric shell, where the dust density is greatest. In Fig. 5.1, the observed polarised flux images show a peak of emission at the location of the star. Any mis-alignment of the bright, centrally-peaked images during the data reduction stages will lead to a residual polarisation at this location. Since the polarised flux peak is narrower than the seeing disc size, it cannot be treated as significant. The polarised emission is not seen from the location of the star in the model images, since forward-scattered light (i.e. scattering angles close to zero) is strongly depolarised. Higher spatial resolution observations will be required to investigate the polarisation within 0.2 arcsec of the star. If there is significant polarised emission from this region then an additional dust component, close to the star, would be required in the model. Murakawa et al. (2007) detected areas of highly polarised emission close to the central illumination source in *IRAS* 19312+1950, but state it could be due to either dust close to the star or an artefact from the seeing.

The fit was assessed by comparing the full grid of ALS models to the polarimetric observations. In particular, the radial and azimuthal profiles of the smoothed model images and the observations were compared, and the profiles for the best-fitting model are shown in Fig. 5.4. The total intensity image radial profile fit (Fig. 5.4 left) provides a check on the level of smoothing, and shows an excellent fit to the observed intensity profile at both wavelengths. The fit to the radial distribution of per cent polarisation (Fig. 5.4 centre) allows us to constrain the dust grain parameters and optical depth. As the maximum degree of polarisation produced by

Table 5.4: The Moffat filter profile parameters, $\alpha_{\rm mof}$ and $\beta_{\rm mof}$, for a bright field star at $J$ & $K$.

| Band | $\alpha_{\rm mof}$ | $\beta_{\rm mof}$ |
|---|---|---|
| $J$ | $3.95 \pm 0.06$ | $2.4 \pm 0.2$ |
| $K$ | $3.03 \pm 0.02$ | $2.2 \pm 0.3$ |

the model is very sensitive to the grain size distribution, it is deemed that the grain size is well constrained. The radial distribution of per cent polarisation depends strongly on the optical depth (and hence the dust density), since this determines the surface brightness of the CSE relative to the unpolarised light from the smoothed PSF. Optical depths of 0.68 and 0.11 at $J$ and $K$, respectively, are determined, so that the CSE is optically thin in the near-infrared. The axisymmetry parameters, $\epsilon$ and $\gamma$ are determined by comparing azimuthal polarised flux profiles to the data (Fig. 5.4 right). The best fit gives an equator-to-pole density contrast of 7.

#### 5.2.2.2 DART model.

The SED of *IRAS* 19306+1407 is plotted in Fig. 5.5 using published photometry and spectroscopy from a variety of sources, including this thesis, and covering wavelengths from the $V$-band through to the sub-millimetre. The photometric values are listed in Table 5.5. The double-peaked nature of the SED is immediately evident, consisting of a reddened stellar peak around 1.6 μm and a broad thermal dust peak between 30 and 40 μm due to the CSE. Double-peaked SEDs are typical of post-AGB stars with optically thin detached CSEs (van der Veen, Habing & Geballe 1989).

The best-fitting model is shown in Fig. 5.5, both with and without correction for interstellar extinction (see below). The underlying input spectrum was created using a Kurucz stellar atmosphere model[6]. Previous attempts to model the SED us-

[6] `http://kurucz.harvard.edu/grids.html`

ing amorphous carbon dust and a cooler F/G type star, were found not to provide sufficient flux in the dust peak (Hrivnak et al. 2000). The stellar temperature is treated as a free parameter and determined a best-fitting stellar atmosphere ($T_\star$ = 21,000 K), typical of a B1I type star. This is consistent within errors with the observationally determined spectral type of B0: (Volk et al. 2004; Kelly & Hrivnak 2005), where the colon denotes an uncertainty in the 0 (Hrivnak, private communication). However, it has not been possible to fit the SED from 5 to $\sim$ 7 μm, with the best-fitting parameters (see Table 5.3). This could indicate that an extra component of warm dust is required. A C-rich CSE could not replicate the SED feature around 10 to 20 μm, whilst O-rich CSE provided a better fit. In addition, a C-rich CSE could not simultaneously fit the observed polarimetry and SED using the ALS and DART models, respectively. The CSE chemisty is discussed in further detail in §5.3.3.

An optical extinction of $A_{\rm V} = 2.0 \pm 0.1$ mag, through the CSE in the equatorial direction, was determined from the model fit. The effect of inclination of the nebula axis has been investigated and determined that the SED is consistent with a value of $0^\circ \pm 10^\circ$. The extinction through the CSE along the line of sight is, therefore, also $A_{\rm V} = 2.0$.

*IRAS* 19306+1407 lies close to the Galactic plane, $l = 50.30^\circ$ and $b = -2.48^\circ$, and the SED will be affected by interstellar extinction. The extinction through the Galaxy at this point is estimated to be $A_V = 5.1 \pm 0.2$ mag (see Fig. 5.6). This value was obtained from the *IRAS* dust reddening and extinction service[7], based on the data and technique in Schlegel, Finkbeiner & Davis (1998).

To correct the emergent model flux for interstellar extinction, a reddening model developed by Cardelli, Clayton & Mathis (1989)is applied, which gives the extinction, $A_\lambda$, at every wavelength between 0.1 and 3.3 μm for a given $A_{\rm V}$ and extinction ratio, $R_{\rm V}$. The extinction at shorter and longer wavelengths has been

[7] `http://irsa.ipac.caltech.edu/applications/DUST`

Table 5.5: Photometric values for *IRAS* 19306+1407 collated from the literature: (1) Hrivnak et al. (2000); (2) Monet et al. (2003); (3) *MSX* Bands (Egan et al. 2003), and (4) Joint *IRAS* Science working group (1988).

| Band | Central wavelength (μm) | Flux density (Jy) | Reference |
|---|---|---|---|
| *V* | 0.55 | $7.40 \times 10^{-3}$ | (1) |
| *R* | 0.44 | $2.21 \times 10^{-2}$ | (2) |
| *MSX A* | 8.28 | 1.16 | (3) |
| *IRAS* 12μm | 12.0 | 3.58 | (4) |
| *MSX C* | 12.13 | 3.65 | (3) |
| *MSX D* | 14.65 | 9.12 | (3) |
| *MSX E* | 21.34 | 46.27 | (3) |
| *IRAS* 25μm | 25.0 | 58.65 | (4) |
| *IRAS* 60μm | 60.0 | 31.83 | (4) |
| *IRAS* 100μm | 100.0 | 10.03 | (4) |

extrapolated. The DART model flux, $F_{\rm DART}$, is then modified to give the flux after correction for interstellar extinction, $F_\lambda$:

$$F_\lambda = F_{\rm DART} \times 10^{-\frac{A_\lambda}{2.5}}, \tag{5.5}$$

Assuming a standard value of $R_V$=3.1 for the ISM, then a fit to the SED shortward of 6 μm gives a value of $\rm A_V$ =4.2 ± 0.1 mag for interstellar extinction at (solid curve in Fig. 5.5). The total extinction to the star is, therefore, 6.2 ± 0.2 mag at *V*-band. This is consistent with the observed *J*-*K* colours. Assuming an reddening law ratio ($R_V$) of 3.1, and an intrinsic colour excess of $E(J-K)_0 = -0.09$ for a B1I star, gives $A_{\rm V} = 6.4 \pm 0.7$ mag. The model parameters used in DART are presented in Table 5.3.

#### 5.2.2.3 Distance estimate and derived parameters.

The interstellar extinction can be used to estimate the distance of the post-AGB star. Joshi (2005) gives an extinction per unit distance of $1.58 \pm 0.04$ mag kpc$^{-1}$ for

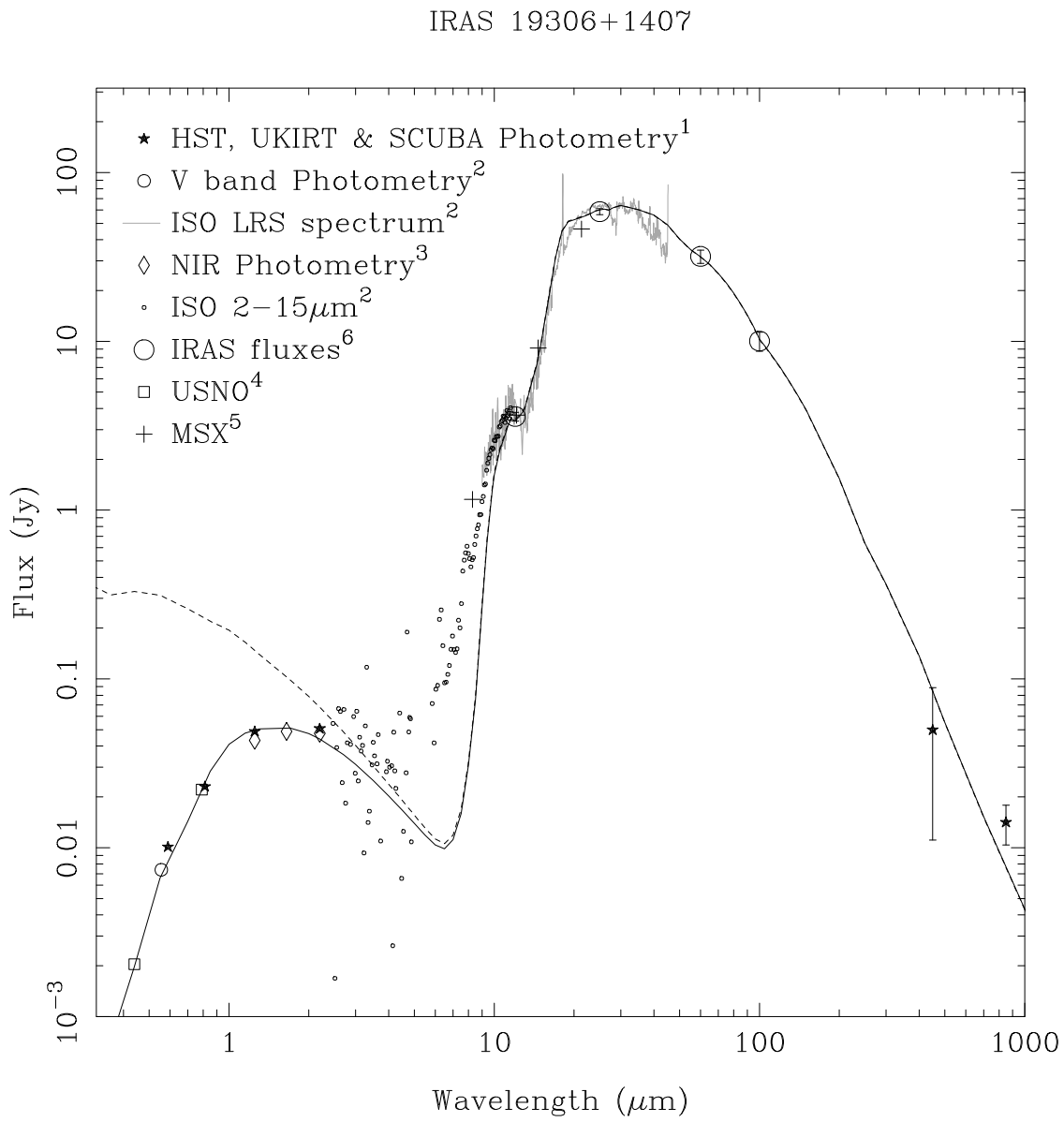


Figure 5.5: The observed SED and best model fits for *IRAS* 19306+1407. The dash line is the model fit and the solid black line is the model fit with interstellar reddening applied. References: (1) this paper, (2) Hrivnak et al. (2000), (3) Ueta et al. (2003), (4) Monet et al. (2003), (5) Egan et al. (2003) and (6) Joint *IRAS* Science working group (1988).

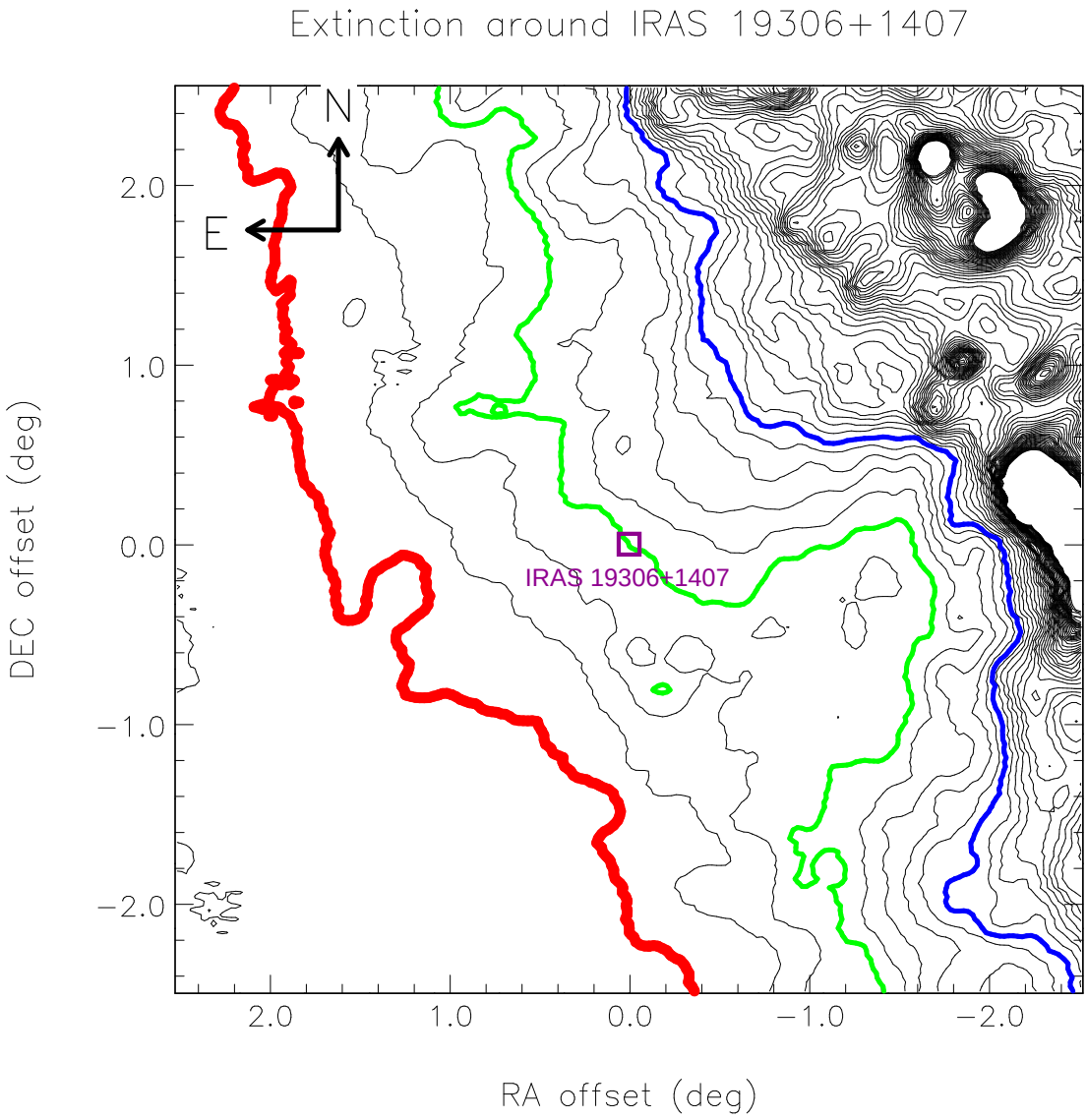


Figure 5.6: The total extinction through the galaxy around *IRAS* 19306+1407. An extinction of 2-, 5- and 10-mag is highlighted with a thick red, green and blue line respectively. The contours are separated by 1 mag and increases NW towards the Galactic plane.

a galactic coordinates ($l = 50.30$ and $b = -02.48$). An interstellar visual extinction of $4.2 \pm 0.1$ mag suggests a distance of $2.7 \pm 0.1$ kpc. This is the adopted distance from this point onwards. Using this distance estimate gives values for $r_{\rm in}$ and $r_{\rm out}$ of $1.9 \pm 0.1 \times 10^{14}$ and $2.7 \pm 0.1 \times 10^{15}$ m, respectively. Multiplying $r_{\rm in}$ by $r_\star / r_{\rm in}$ gives a stellar radius, $R_\star$, of $3.8 \pm 0.6$ $R_\odot$.

The stellar luminosity, $L_\star$, is obtained by calculating the integrated flux under the model SED, giving values of $1800 \pm 140$ and $4500 \pm 340$ $L_\odot$, with and without interstellar reddening applied respectively, for the assumed distance. Post-AGB stellar evolution models suggest a lower limit of 2500 $L_\odot$, using the lowest mass luminosity track, for the central star of a PN (Schönberner 1983), which means that *IRAS* 19306+1407 must be at least 2.0 kpc away to satisfy this criterion.

To calculate the time scales of mass loss, $r_{\rm in}$ and $r_{\rm out}$ are divided by the AGB wind speed. Only the $H_2$ and H$\alpha$ kinematic information are available for *IRAS* 19306+1407. These speeds arise from the shocks and fast winds in the post-AGB phase, and are not a true reflection of the AGB envelope expansion speed, therefore a typical speed of 15 km $s^{-1}$ from Neri et al. (1998) is assumed. The age of the CSE is then $5700 \pm 160$ years, became detached $400 \pm 10$ years ago and the mass loss lasted $5300 \pm 160$ years.

The number density of dust grains, $N_0$, at $r_{\rm in}$ is calculated from the optical depth, the extinction cross section of the dust and the CSE thickness. The optical depth at 1.2 μm is $0.678 \pm 0.005$, giving a value of $N_0 = 6.1 \pm 3.0 \times 10^{-3}$ $m^{-3}$. Using $N_0$ and integrating the dust density distribution gives the total dust mass ($M_{\rm d}$), and assuming a dust grain bulk density of $3 \times 10^3$ kg $m^{-3}$, gives a value of $8.9 \pm 5.0 \times 10^{-4}$ $M_\odot$.

The gas-to-dust ratio for this object is unknown and a value of 200 from Heras & Hony (2005), who analysed O-rich optically thin ABG stars, has been adopted. The total mass of the CSE is then $1.8 \pm 1.0 \times 10^{-1}$ $M_\odot$ with an average mass-loss

rate ($\dot{M}$) of $3.4 \pm 2.1 \times 10^{-5}$ $M_{\odot}$ year$^{-1}$. The derived parameters given in this section are summarised in Table 5.6.

## 5.3 Discussion

### 5.3.1 CSE geometry

The polarimetric observations, shown in Fig. 5.1, have been interpreted in terms of an axisymmetric shell with an equatorial density enhancement, which is optically thin in the near-infrared. The shell model successfully reproduces the observed SED from the V band to the sub-millimetre. As a further check on the validity of the model, the ALS code was run at the central wavelength of the *F606W* filter to simulate the *HST* observations shown in Fig. 5.2 (a). The results are shown in Fig. 5.7 and it is found that the bipolar structure is reproduced, inclusive of the flattened contours in the centre of the *HST* image. A single axisymmetric shell model, based on the simple Kahn & West (1985) density distribution, can account for the morphology of this object over a wide range of wavelengths. The transition from bipolar nebula in the optical to limb-brightened shell in the near-IR is due to the variation in optical depth through the envelope with wavelength. At the wavelength of the *HST* observations, the CSE is optically thick along the equatorial direction and so light is preferentially funnelled along the polar axes before scattering into the line of sight, creating the bipolar lobes. The fact that the general appearance and extent of the lobes is reproduced by the model indicates that the density structure of the shell, in particular the equator-to-pole density contrast of 7, is reasonable. At near-infrared wavelengths, where the shell is optically thin along the equator, light is mainly scattered at the inner boundary in the equatorial plane, where the dust density is greatest, creating the shoulders seen in observed polarised flux.

Since the model calculations are limited to axisymmetric geometries, one aspect of the observations that cannot be taken into account is the non-orthogonality of the polarised flux shoulders, at PA 136 deg, and the major axis of the nebula, at PA 18 deg, illustrated in Fig. 5.2. A similar 'twist' has been detected in the

mid-infrared images of *IRAS* 17456+5003, which has a curving polar axis (Gledhill & Yates 2003), and which was also modelled with an axisymmetric dust shell. A further similarity between the two objects is the unequal brightness of the polarised flux shoulders (see Gledhill et al. 2001). In the context of the model, these are due to scattering at the inner edge of the axisymmetric shell, so that the scattering optical depth is greater on one side of the shell than the other. Assuming that the dust properties are the same throughout the shell, then this suggests that there is a greater concentration of dust in the brighter shoulder. Further evidence for asymmetric dust distributions around post-AGB stars is seen in mid-infrared images of *IRAS* 07134+1005 (Dayal et al. 1998) and *IRAS* 21282+5050 (Meixner et al. 1993). Gledhill & Yates (2003) discuss possible causes for these asymmetries and conclude that they may arise due to interaction of the mass-losing star with a binary companion, although exactly how this happens is not clear.

Volk et al. (2004) imaged *IRAS* 19306+1407 using a narrowband $H_2$ filter (2.12 μm) and a narrowband $K$ continuum filter (2.26 μm), to investigate the molecular hydrogen emission. Their continuum subtracted $H_2$ image (their Fig. 2 shown in Chapter 6 as Figure 6.2) shows a broken ring with limb-brightened edges, which appears cospatial with the central dust structure, at PA 136, seen in the polarised flux images. The ring can also be seen in their 2.26 μm continuum image, so that they have resolved the dust structure that is seen in polarised flux. The similarity between the polarised flux and $H_2$ images suggests that the scattered light and molecular emission originate in the same region. Volk et al. (2004) also detect faint extended $H_2$ emission lobes, extending from the ring, corresponding to the extended bipolar structure seen in the HST images (Fig. 5.2), oriented PA 18°. It appears that the same axis twist seen in the scattered light images may be present in $H_2$ emission. Volk et al. (2004) suggest that the $H_2$ ring seen in their images collimates the $H_2$-emitting bipolar lobes.

### 5.3.2 Estimation of the dust mass from the sub-mm observations

The mass of dust in the CSE, $M_{\rm d}$, can be estimated from the *IRAS* 100 μm flux, $F_{100}$, and the SCUBA 850 μm flux. The method stated in Gledhill, Bains & Yates (2002) is used to calculate an estimate of the dust mass from the observations. The dust temperature is estimated to be 146 ± 21 K, using Wien's displacement law, with the peak dust emission at $35 \pm 5$ μm. The 850 μm flux value given in Table 5.1 and $F_{100} = 10.03 \pm 1.30$ Jy, gives an emissivity index of 1.3 ± 0.1. The assumed density for a silicate dust grain is $3{\times}10^3$ kg m$^{-3}$. The total dust mass in the CSE, using the assumed distance, is then $4.3 \pm 0.7{\times}10^{-4}$ M$_{\odot}$, which is a factor of $\sim 2$ less than the value obtained from the radiative transfer model. The difference may arise from the simple assumptions inherent in the sub-millimetre estimate, particularly that of an isothermal CSE. The bulk of dust in the envelope will be cooler than 146 K (the maximum and minimum dust temperatures in the DART model are 130 and 40 K respectively), and will radiate on the long wavelength tail of the SED. An isothermal temperature of 100 K would result in a dust mass of $7.2 \pm 1.7{\times}10^{-4}$ M$_{\odot}$. Given these approximations, the two results are comparable but that the more rigorous model calculations from DART and ALS provide a more realistic value for the dust mass in the CSE.

### 5.3.3 CSE chemistry

*IRAS* 19306+1407 has been modelled using a silicate dust model, with grain sizes between 0.1 and 0.4 μm, which reproduces the shell-like morphology in the near-infrared, the observed degrees of polarisation and the SED. However, it is found that a purely C-rich chemistry (amorphous carbon) using larger grains, typically >0.6 μm, can reproduce the observed polarisation (Lowe & Gledhill 2005) and fit

the overall shape of the SED, although this produces a poor fit at <1 μm after interstellar reddening is applied. Amorphous carbon also does not reproduce the shape of the SED between 10 and 20 μm. There is a possibility that silicon carbide could fit the 10-20 μm region, but it was found that it provides too much flux at 11-12 μm and generally a poor fit to the SED. These regions are modelled more effectively using Ossenkopf cold silicates.

As mentioned in Section 3.1, the simultaneous presence of emission from PAHs and crystalline silicates (Hrivnak et al. 2000; Hodge et al. 2004) suggests that the CSE has a mixed chemistry (both O- and C-rich). The simple investigations of mixes of carbon and silicate dust in the CSE, show that amorphous carbon significantly dominates the SED at less than 1 per cent abundance. This suggests that if the 10-20 μm fits require silicate grains, then they must be the dominant dust component. However the models do not allow us to segregate the O- and C-rich material to have, for example, a region of silicate grains close to the star with a largely C-rich outflow at larger radii. Such a configuration has been proposed to explain observations of mixed chemistry objects (Molster et al. 2002) in which the crystalline emission comes from cool silicates trapped in stable circumstellar or circumbinary discs. Matsuura et al. (2004) have shown that in the mixed chemistry post-AGB object *IRAS* 16279-4757 the carbon-rich dust, traced by PAH emission, is located in a low-density outflow, while the continuum emission is concentrated toward the centre. Although the single component model, based on silicate grains, is reasonably successful in reproducing the observations, it is almost certain that the chemistry of *IRAS* 19307+1407 involves both O- and C-rich material, perhaps spatially segregated and with more than one size distribution.

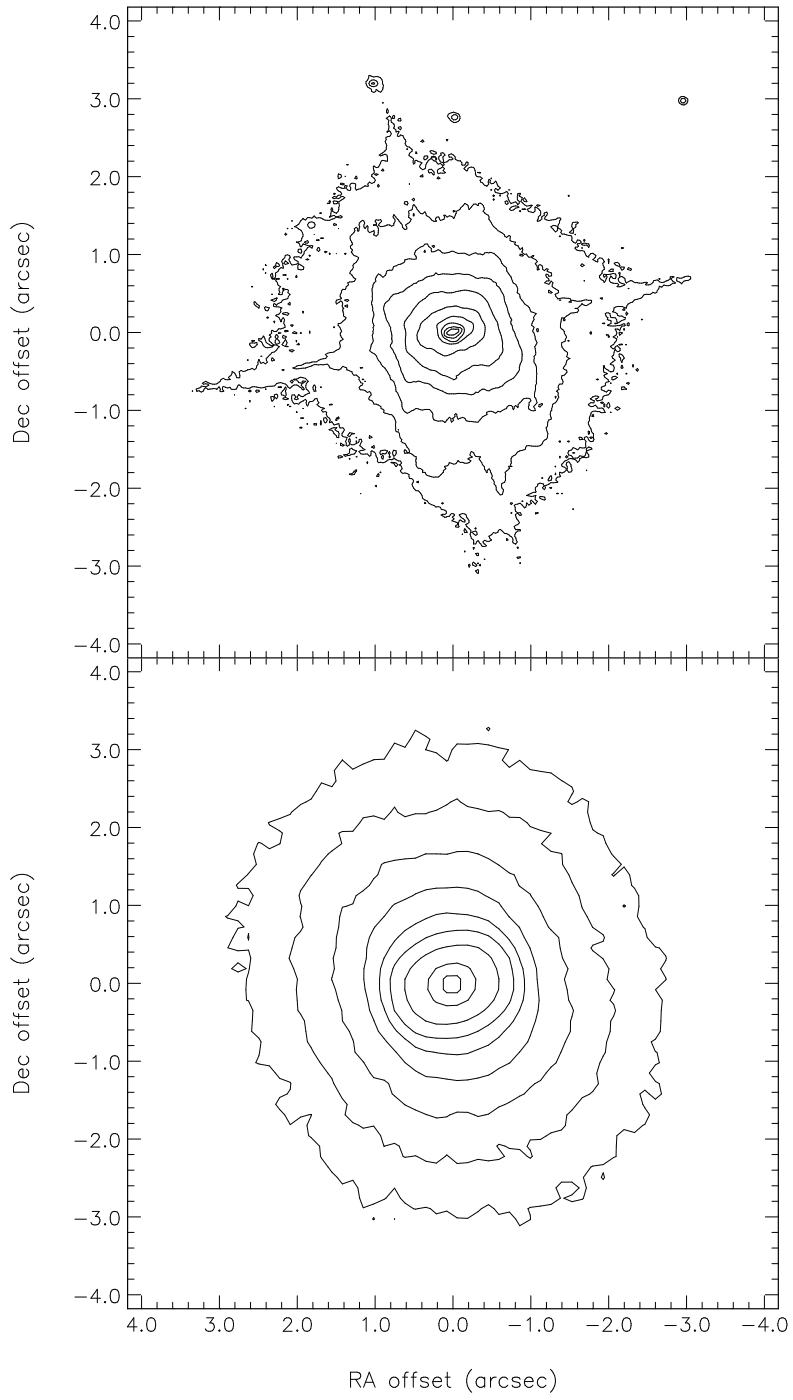


Figure 5.7: A comparison of the *F606W HST* image and the raw model image from ALS at the central wavelength of the *F606W* filter. The model image has been rotated parallel to the long axis (PA = 18°) to match the *HST* image. The contours are spaced at an interval of 1 mag arcsec$^{-2}$ from the peak value.

Table 5.6: The derived model parameters at the assumed distance of 2.7 kpc obtained from ALS[†] and DART[‡] models.

| Parameter | Value | Units | Description |
|---|---|---|---|
| $R_\star$ | 3.8 ± 0.6 | $R_\odot$ | Stellar Radius[‡] |
| $r_{\rm in}$ | 1.9 ± 0.1 | $(10^{14})$ m | Inner Radius[†‡] |
| $r_{\rm SW}$ | 3.8 ± 1.0 | $(10^{14})$ m | Super-wind Radius[†] |
| $r_{\rm out}$ | 2.7 ± 0.1 | $(10^{15})$ m | Outer Radius[†‡] |
| $L_\star^\diamond$ | 4500 ± 340 | $L_\odot$ | Stellar Luminosity[‡] |
| $N_0$ | 6.1 ± 3.0 | $(10^{-3})$ m$^{-3}$ | Number density of dust grains at $r_{\rm in}^\dagger$ |
| $M_{\rm d}$ | 8.9 ± 5.0 | $(10^{-4})$ $M_\odot$ | Total mass of Dust[†] |
| $A_{\rm V}$ | 4.2 ± 0.1 | mag | Interstellar extinction[‡] |
| $T_{\rm max}$ | 130 ± 30 | K | Temperature at $r_{\rm in}^\ddagger$ |
| $T_{\rm min}$ | 40 ± 20 | K | Temperature at $r_{\rm out}^\ddagger$ |

[◇]The apparent luminosity of the star, with applied interstellar reddening, is 1800 ± 140 $L_\odot$.

## 5.4 Conclusion

This chapter presents near-infrared polarimetric images of the dusty CSE of *IRAS* 19306+1407, in conjunction with new submillimetre photometry and archived *HST* images. The polarisation vectors show a centrosymmetric structure with a maximum polarisation of 15 ± 6 and 10 ± 4 per cent for *J*- and *K*-band respectively. The polarised flux shows a very faint elongated distribution at PA 18° with two bright scattering shoulders at PA 136°. The object is clearly bipolar in archived *HST* images, with the bipolar axis also at PA 18°

The polarimetric data was modelled using an axisymmetric light scattering code and a dust model based on sub-micron sized silicate grains. The observed polarisation features are well described by a simple axisymmetric shell geometry, with an equator-to-pole density contrast of 7. The same shell model is used to fit the SED of *IRAS* 19306+1407 from optical to sub-millimetre wavelengths using an axisymmetric radiation transport code, to constrain the stellar temperature and radius, the optical depth of the CSE and the mass of dust in the CSE. It was found that a B1I-type stellar spectrum, with an effective temperature of 21,000 K, best

describes the SED, confirming previous suggestions that the object is a post-AGB object.

The models give a value for the CSE and interstellar extinction of $2.0 \pm 0.1$ mag and $4.2 \pm 0.1$ mag respectively. The estimated distance, from the interstellar extinction, is equal to $2.7 \pm 0.1$ kpc and this value is used to derive parameters from the models.

The polarimetric imaging shows deviations from axisymmetry that are beyond the scope of the model calculations. There appears to be a greater concentration of dust on one side of the star than the other, plus the axisymmetric shell is not aligned with the larger-scale bipolar axis, clearly seen in archive *HST* images. Similar asymmetric features are seen in other post-AGB objects, such as *IRAS* 17150-3224 (Su et al. 2003), *IRAS* 17441-2411 (Su et al. 2003) and *IRAS* 07134+1005 (Ueta et al. 2005). The process that creates a point symmetric structure is unknown, but it may result from interaction of the mass-losing star with a binary companion or magnetic fields (see Balick & Frank 2002, for an overview of models).

# Chapter 6

# Integral Field Spectroscopy of *IRAS* 19306+1407

This chapter details the $K$-band integral field spectroscopy of *IRAS* 19306+1407 using instrumentation at the UKIRT and the VLT. The $H_2$ and Br$\gamma$ lines are used as diagnostics to uncover the boundaries of the fast- and slow-winds, and thermal and non-thermal heating. Previous studies that have focused on $H_2$ emission have primarily used single slit spectroscopy or narrow band imaging (e.g. Latter et al. 1995; García-Hernández et al. 2002; Davis et al. 2003; Kelly & Hrivnak 2005). In contrast, near-IR IFS has seldom been used to investigate post-AGB stars and PNe (e.g. Matsuura et al. 2007; Santander-García et al. 2007). Post-AGB stars are compact objects and in most cases their outflows are only a few arcseconds across. These will fit easily within the FoV of an IFU. *IRAS* 19306+1407 has a diameter of 3.9 by 2.4 arcsec for the long and short axis, respectively, and is comparable to the FoV of UIST and SINFONI (see Table 2.2, see Fig. 6.1).

*IRAS* 19306+1407 has a bipolar structure at optical wavelengths. It has bright arcs in near-IR polarised flux, either side of the central illuminating source, (Chapter 5; Lowe & Gledhill 2007).

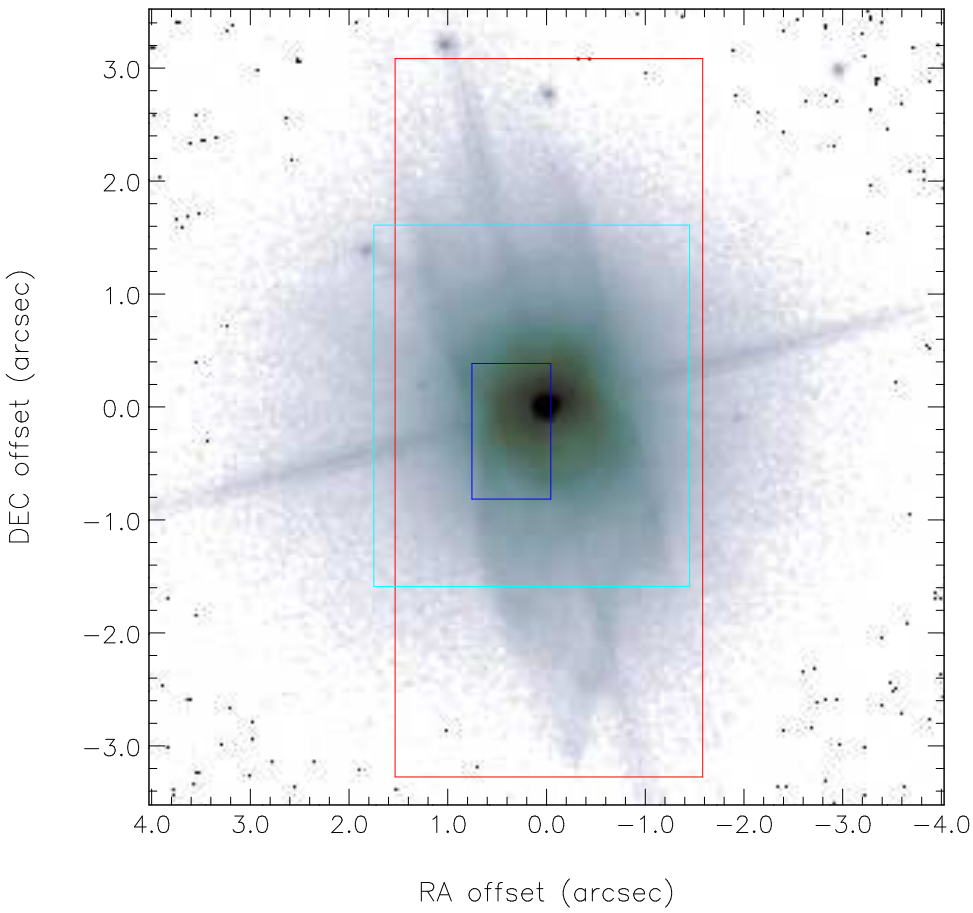


Figure 6.1: A *HST* ACS *F606W* image of *IRAS* 19306+1407 scaled between 21- and 12-mag arcsec$^{-2}$. The red, cyan and blue contours show the FoV of UKIRT's UIST IFU, the medium and sub-arcsecond FoV for SINFONI IFU.

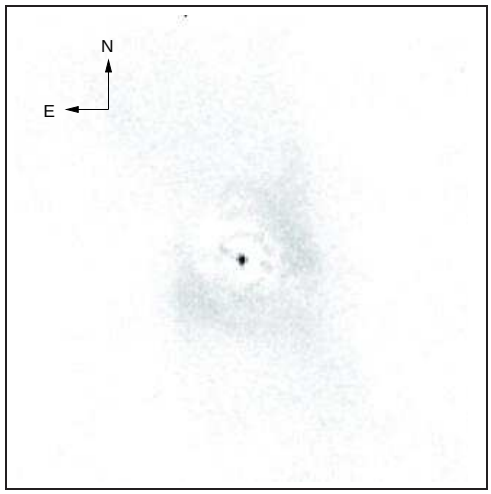


Figure 6.2: The $H_2$ image from Volk et al. (2004). The image width and height is 3.2- by 3.2- arcsec.

$H_2$ emission in *IRAS* 19306+1407 has been previously observed by Volk et al. (2004) and Kelly & Hrivnak (2005). Volk et al. (2004) used narrow-band imaging with the Quick Infrared Camera (QUIRC) at the 8-m Gemini telescope. Two images were obtained, at 2.12 μm and 2.26 μm, with a total integration time of 40 minutes[1]. The 1-0 S(1) line emission was extracted by scaling and subtracting the 2.26 μm continuum image from the 2.12 μm image. However, the 2.26 μm image contained a contribution from the 2-1 S(1) and 1-0 S(0) lines and would decrease the extracted 1-0 S(1) line emission. They uncovered an incomplete ring extending south and around to the northwest, with the brightest regions interpreted as limb-brightened edges of the ring (Fig. 6.2). There is a 'suggestion' of two limb-brightened lobes extending north-northeast and south-southwest. Ultimately *IRAS* 19306+1407 is characterised as a bipolar nebula with an equatorial ring.

Kelly & Hrivnak (2005) obtained long-slit spectroscopy with the Near Infra-Red Camera and Multi-Object Spectrometer 3 (NICMOS3) at the 2.3-m Steward observatory. The spectral resolution was $R \sim 2600$. The slit was 2.4 arcsec wide and 86 arcsec long and aligned east-west centred on the bright continuum emission

[1] 20 minutes each

peak. A total of three observations were required to cover the 2.1 μm to 2.32 μm spectral range, with a total integration time of 54 minutes. It was found that *IRAS* 19306+1407 has a rich $H_2$ spectrum, containing 1-0 S(0), 1-0 S(1), 2-1 S(1), 2-1 S(2), 3-2 S(3) and Br$\gamma$ emission lines. The 1-0 S(1) line was extended roughly 2 arcsec along the slit. In addition, two MgII recombination lines were detected; however, Kelly & Hrivnak suspected that these lines arise from absorption lines in the telluric standard star spectrum, which was used to correct for the atmosphere.

A total integration time of 94 minutes was required for these two separate observations at different telescopes using different instruments. Volk et al. (2004) spatially resolved the 1-0 S(1) emission and Kelly & Hrivnak (2005) detected $H_2$ and Br$\gamma$ emission lines in their *K*-band spectrum. IFS observations will obtain multiple spectra and emission line images, over a greater wavelength range and at higher spatial resolution, in one observation for an equivalent integration time.

As previously mentioned in Chapter 5, the spectral type of the central illumination source is estimated as B0**:** (Kelly & Hrivnak 2005) or B1 (Lowe & Gledhill 2007, Chapter 5). Hrivnak et al. (2000) suggest that *IRAS* 19306+1407 is a young PN, based on its near- to mid-IR spectra. Kelly & Hrivnak (2005) state that the majority of the $H_2$ excitation is collisionally excited (70 per cent) and Volk et al. (2004) state, based on single slit spectroscopy, that the wind is impacting on the dense torus around the star and emerging in the bipolar lobes.

The IFS observations will be able investigate the evolutionary state of this object, which could confirm that it is a post-AGB object or young PN, depending on its level of thermal and non-thermal heating, which is discussed further in Chapter 7. It is possible to produce continuum subtracted images that show only line emission, by fitting a Gaussian to the emission line. The careful fitting of emission peaks will give information on the line of sight (LoS) velocity, which coupled with the excitation information will enable us to characterise the CSE and therefore the post-AGB star.

## 6.1 Observations at UKIRT with UIST

The integral field spectra were obtained at the UKIRT using UIST in conjunction with the IFU. The *short-K* filter was used, which has a wavelength range of 2.017 μm to 2.25 μm, with fourteen 0.24 arcsec wide slitlets (PA= 0°), and the plate scale of 0.12 arcsec per pixel in the spatial direction. When combined into an IFS data cube it covers an area of approximately 3.3 by 6.0 arcsec with a plate scale of 0.24 arcsec east-west and 0.12 arcsec north-south. These observations were conducted on 2004 July 23, via the UKIRT queue system, and there was an average seeing of <0.3 arcsec. A total integration time of 4800 seconds (80 minutes) was used, with 50 per cent on the source and 50 per cent on sky, comprising of 20 exposures of 240 seconds each. The object frames are sky subtracted. Cosmic rays and bad pixels are removed by hand. The arc, flat and standard star (BS 7569; G0V; $K_{2mass}$=4.58 mag) were taken prior to this observation and are used to wavelength calibrate, flat field and flux calibrate these data, respectively. The intrinsic absorption lines of the standard star were identified (e.g. Br$\gamma$), using the templates of Pickles (1998), and removed. The units of flux are in W m$^{-2}$ arcsec$^{-2}$ and flux density W m$^{-2}$ μm$^{-1}$ arcsec$^{-2}$ are displayed as $F^x$ and $F^x_\lambda$, respectively, with $x$ denoting the order of magnitude of the units[2]. The data reduction was carried out using the STARLINK suite (see Chapter 2) and the emission line information was extracted using custom IDL fitting routines (see Chapter 4 for an overview and Appendix A.1 for the code).

### 6.1.1 Molecular hydrogen emission

The integral field cube can be collapsed into a one dimensional spectrum, which shows a range of molecular emission lines. The detected lines are shown in Fig. 6.3.

[2]For example $2 \times 10^{-12}$ W m$^{-2}$ arcsec$^{-2}$ and $2 \times 10^{-12}$ W m$^{-2}$ μm$^{-1}$ arcsec$^{-2}$ are displayed as $F^{-12}$ and $F^{-12}_\lambda$, respectively

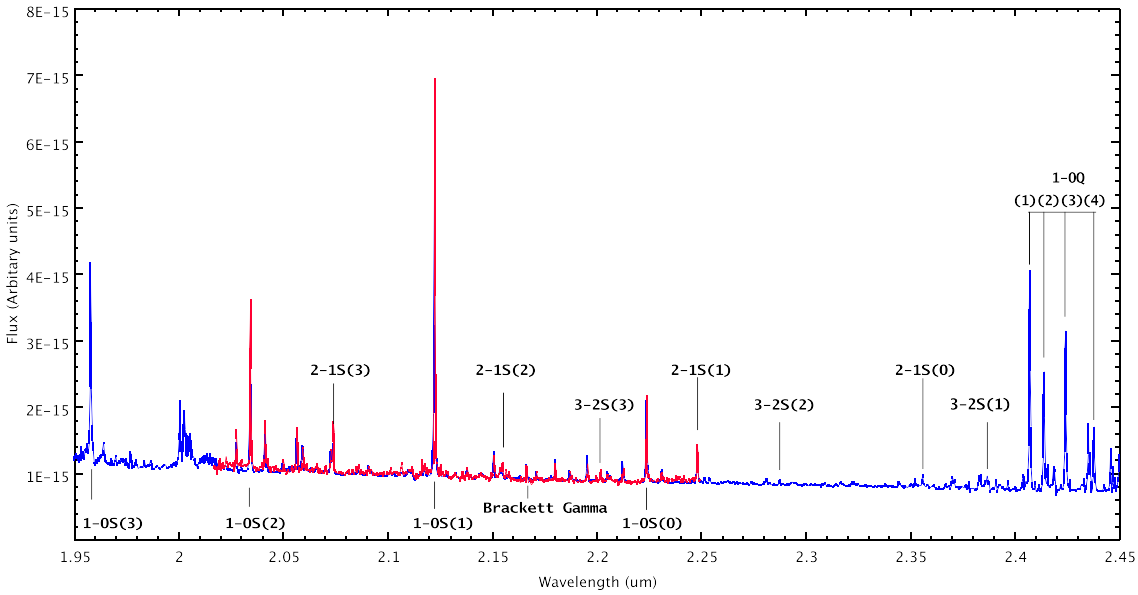


Figure 6.3: The collapsed spectra from the UIST (red) and SINFONI (blue) data cubes. The ro-vibrational 1-0 S, 2-1 S, 3-2 S and 1-0 Q lines are indicated on the plot. In addition, the Brackett Gamma (Br$\gamma$) is indicated at 2.1661µm.

In these observations there was sufficent signal-to-noise to spatially resolve three $H_2$ lines. These are the 1-0 S(0), 1-0 S(1) and 1-0 S(2), shown in Fig. 6.4a, 6.4b and 6.4c, respectively. The underlying continuum for each line is unresolved, with no detected extended emission (Fig. 6.4d, 6.4e and 6.4f). The strongest emission line is the 1-0 S(1), with the 1-0 S(0) and 1-0 S(2) showing weaker emission. All three lines show extended emission to the north-northeast and to the south-southwest.

#### 6.1.1.1 1-0 S(1) emission

The 1-0 S(1) emission line image consists of three main morphological features. These are a larger bipolar nebula with an apparent twist and two peaks of emission. The larger bipolar nebula is extended north-northwest to south-southeast, highlighted by the lowest black contours, which mostly fit within the FoV. The outer contours indicate that the dimensions of the bipolar nebula are 4.9 arcsec and 2.3 arcsec along the long axis and short axis, respectively. The long axis is aligned with a PA of $\sim$18°(east of north; Fig. 6.7b). The solid white contours show an apparent

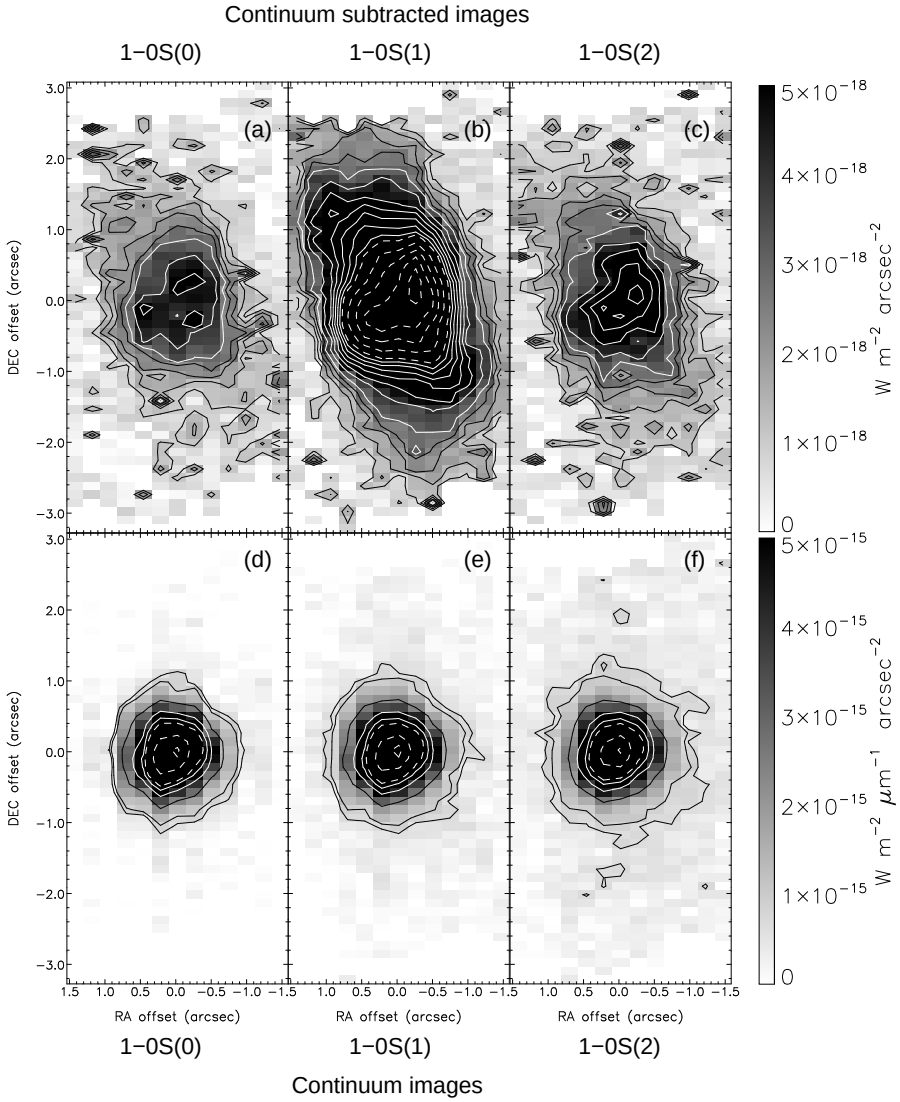


Figure 6.4: The extracted emission line and continuum images from the UKIRT UIST integral field cube. The images are aligned north and east to the top and left of the images, respectively. The co-ordinates are offset from the bright emission peak from the white light image (see Fig. 6.5). The images are scaled between limits indicated on the vertical grey scale bar on the right of the panels. **Top:** The extracted emission line images for the 1-0 S(0) 2.2235 μm **(a)**, 1-0 S(1) 2.1218 μm **(b)** and 1-0 S(2) 2.0338 μm **(c)** lines. The extracted images are in units of $F^{-18} = 10^{-18}$ W m$^{-2}$ arcsec$^{-2}$. The black contours range between 1.0- to 2.5-$F^{-18}$, separated by 0.5-$F^{-18}$. The solid white contours range between 3.0-$F^{-18}$ to a maximum of 9.0-$F^{-18}$ with separations of 1.0-$F^{-18}$. The dashed white contours range between 10.0-$F^{-18}$ to a maximum of 20.0-$F^{-18}$ with separations of 2.5-$F^{-18}$. **Bottom:** The underlying continuum images for the 1-0 S(0) **(d)**, 1-0 S(1) **(e)** and 1-0 S(2) **(f)** lines. The extracted images are in units of $F_\lambda^{-15} = 10^{-15}$W m$^{-2}$ μm$^{-1}$ arcsec$^{-2}$. The outer black contour levels are 0.75-,1.0- and 2.5-$F_\lambda^{-15}$. The solid white contour levels are 5.0- and 7.5-$F_\lambda^{-15}$. The dashed white contour levels are 10.0-, 20.0- and 30.0-$F_\lambda^{-15}$.

'twist' in the bipolar axis, giving a PA of ∼28°. The difference between the bipolar and 'twist' PA is ∼10°. The elongation is aligned northwest to southeast and possibly indicates a new outflow of material highlighted by the molecular hydrogen emission or a change in the axis orientation of an existing outflow. The inner dashed white contours show a change from a bipolar morphology to a bright round emission core, with a bright central emission bar aligned SE to northwest (PA ∼135°). A bright peak of emission is located in the northwest within the 20.0 $F^{-18}$ contour, whilst a hint of a second peak is seen in the SE between the 17.5- and 20.0 $F^{-18}$ contours. These areas could represent regions of gas excitation, via fluorescence or shocks, or areas of high $H_2$ concentration.

#### 6.1.1.2 Additional $H_2$ emission.

The 1-0 S(0) and 1-0 S(2) lines are weaker than the 1-0 S(1), but they show extended emission to the northeast and the southwest (Fig. 6.4a and Fig. 6.4c). A bright emission core, within the white contours, is elongated to the northwest and the southeast. There is brighter emission in the northwest. These features are similar to the 1-0 S(1) emission; however, the 1-0 S(0) and 1-0 S(2) images do not exhibit the faint bipolar emission, oriented at a PA of ∼28°, which is within the outer black contours in Fig. 6.4b. In addition, the 1-0 S(0) line shows a bright peak in the south west. This could be attributed to the lower signal-to-noise. The higher vibrational lines $v \geq 2$ were not spatially resolved, however with modest spatial binning it is possible to compare and contrast different regions.

#### 6.1.1.3 'White light' and Brackett Gamma images.

An IFU cube can be collapsed along the wavelength axis to create a 'white light' spatial image (Fig. 6.5c). This image is equivalent to a *short-K* filter image. The image only shows a point source structure, which indicates that the majority of the

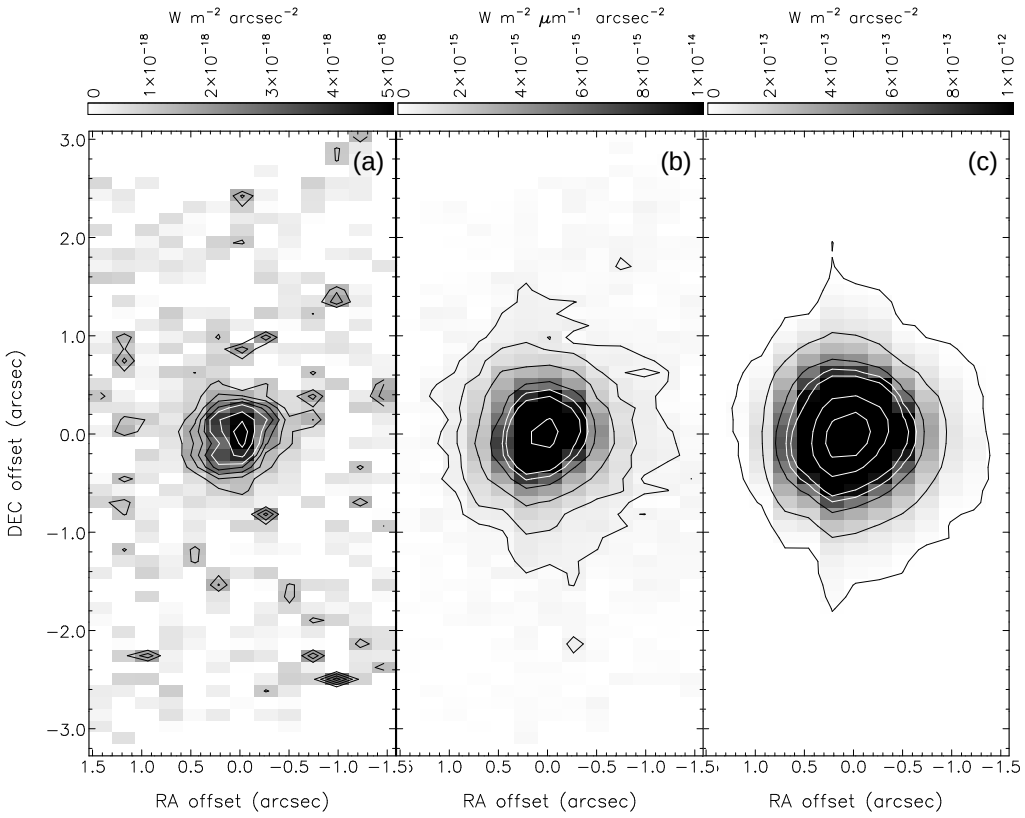


Figure 6.5: The extracted Br$\gamma$ 2.1661 µm emission line **(a)**, underlying continuum **(b)** and the 'white light' **(c)** images. The images are aligned north and east to the top and left of the images, respectively. The co-ordinates are offset from the bright emission peak from the white light image. The images are scaled between limits indicated on the horizontal grey scale bar at the top of the panels. Panel (**a**) shows the extracted emission line image for the Br$\gamma$ 2.1661 µm line. The extracted images are in units of $F^{-18} = 10^{-18}$ W m$^{-2}$ arcsec$^{-2}$. The black contours range between 1.0- to 2.5-$F^{-18}$, separated by 0.5-$F^{-18}$. The solid white contours range between 3.0-$F^{-18}$ to a maximum of 4.0-$F^{-18}$ with separations of 1.0-$F^{-18}$. Panel (**b**) shows the underlying continuum image for the Br$\gamma$ line. The extracted images are in units of $F_{\lambda}^{-15} = 10^{-15}$W m$^{-2}$ µm$^{-1}$ arcsec$^{-2}$. The outer black contour levels are 0.5-, 1.0-, 2.25- and 5.0-$F_{\lambda}^{-15}$. The solid white contour levels are 7.5, 10.0- and 25.0-$F_{\lambda}^{-15}$. Panel (**c**) shows the collapsed IFS cube, along the spectral axis, represented as a 'white light' image, which is the total of the observed flux in the *short-K* filter. The image units are $F^{-13} = 10^{-13}$ W m$^{-2}$ arcsec$^{-2}$. The black contours are 1.0-, 2.25- and 5.0-$F^{-13}$. The solid white contours are 7.5-, 10.0-, 25.0- and 50.0-$F^{-13}$.

emission is dominated by the central illumination source. The position of the peak of the white light image is used as the origin for the arcsec offset co-ordinates in Fig. 6.4 and Fig. 6.5.

The Br$\gamma$ emission is unresolved and is weaker than the 1-0 S(1) emission (Fig. 6.5a). The emission lies within a circle of radius less than 0.5 arcsec and is unresolved. The central peak of the emission is located at the same position as the white light's peak and the underlying continuum (Fig. 6.5). No kinematic information was detected in the Br$\gamma$ line. This leads us to an interpretation that the emission is originating close to or from the central source. The underlying continuum to the Br$\gamma$ line also exhibits a point source nature (Fig. 6.5b).

#### 6.1.1.4 Summary

These IFS UKIRT observations, of *IRAS* 19306+1407, have uncovered a rich range of $H_2$ and Br$\gamma$ emission, whilst the 'white light' image is unresolved. The extracted emission line images, by carefully fitting the continuum and the emission line, uncovered an extended structure in the molecular hydrogen emission. The follow up observations at the VLT focus on the inner region of CSE, using adaptive optics, greater spatial resolution, greater wavelength coverage and higher spectral resolution.

## 6.2 Observations at VLT with SINFONI

*IRAS* 19306+1407 was observed with SINFONI in conjunction with the AO system at the VLT, which is mounted at the Cassegrain focus on the 8-m UT4 telescope. The SINFONI instrument and the subsequent data reduction is described in Chapter 3. The *K*-band grating with a wavelength range of 1.95 μm to 2.5 μm was used. A FOV of $3 \times 3$ arcsec$^2$ was selected and centred on the bright continuum peak of the science target. The PA was set at 0°. The selected FOV has a spatial scale of 0.1 arcsec pixel$^{-1}$. The spectra were taken on 2005 July 28 comprising of 16 exposures of 300 s each, giving a total integration time of 4800 s (80 minutes). A total of 50 per cent of the observations were on source and 50 per cent on sky. The conditions were clear with the average seeing of $\sim$ 1 arcsec. The natural AO guide star (NGS) used the science target with a R-band magnitude of 13.9 mag. The Strehl ratio for the PSF and telluric standards, and science target is 30, 22 and 10 per cent at 2.2 μm, respectively. The resultant full width half maximum (FWHM) for the science target was 0.18 arcsec. A telluric standard star HIP 109821 (G5V) was observed immediately after science observations. The PSF standard is taken at the beginning of the night, with an exposure time of 10 seconds, to ensure that the AO system is functioning and is selected by the ESO telescope operating staff. These data were reduced using the SINFONI pipeline, formed into a data cube of dimensions of $x$, $y$ and $\lambda$ and the spatial scale was rescaled to 0.05 and 0.1 arcsec pixel$^{-1}$. Additional reduction steps, including correcting for atmospheric absorption and flux calibrating, were completed by the FUS data reduction package (see Chapter 4). The emission line intensity and kinematic images were extracted using the FUS line fitting tool[3].

[3] Available from http://star.herts.ac.uk/∼klowe

### 6.2.1 1-0 S(1) line emission

The 1-0 S(1) 2.1218 μm line is the strongest line detected in *IRAS* 19306+1407 (Fig. 6.6a) with areas of interest marked in Fig. 6.7a. A bright broken ring of emission occurs at a radius 0.3 to 0.4 arcsec from the PSF peak, with two bright distinct and separate arcs situated southeast and northwest, with the latter arc appearing brighter. These arcs can be interpreted as the limb brightened edges of an equatorial torus of molecular hydrogen, that is undergoing shocking and/or fluorescence, which will be discussed in later sections. To the southwest a bright knot is located at a similar radial distance as the bright arcs (Fig. 6.7a). This could be a bright knot connecting the bright arcs. The 'twist' feature, previously identified in the UKIRT polarimetry data, is clearly seen and is aligned northeast to southwest (Fig. 6.7b & 6.7c). The ring structure is embedded within a larger bipolar halo, aligned north-northeast and south-southwest (Fig. 6.7c). The bipolar lobes are seen to extend north-northeast and south southwest and extend outside the FoV. Two knots of emission are situated at both ends of the twist feature (Fig. 6.7a & 6.6a). These could be areas of an outflow impacting the bipolar cavity wall or a beam illuminating the cavity wall. Two tail features above the northwest arc and below the southeast arc, indicated in Fig. 6.7a & Fig. 6.7c, appear to trace the edge of the cavity wall. However, there does not seem to be a corresponding feature below or above the northwest and southeast arcs, respectively.

### 6.2.2 1-0 S and 1-0 Q emission lines

A dusty environment will attenuate the emission from the CSE as a function of wavelength. This can alter the observed structure at different wavelengths and could create confusion effects. In this section, the 1-0 S branch images, 1.9576-, 2.0338-, 2.1218- and 2.2235-μm, are compared with the 1-0 Q branch images, 2.4066-, 2.4134-, 2.4237- and 2.4375-μm, to ascertain if extinction dramatically changes the observed

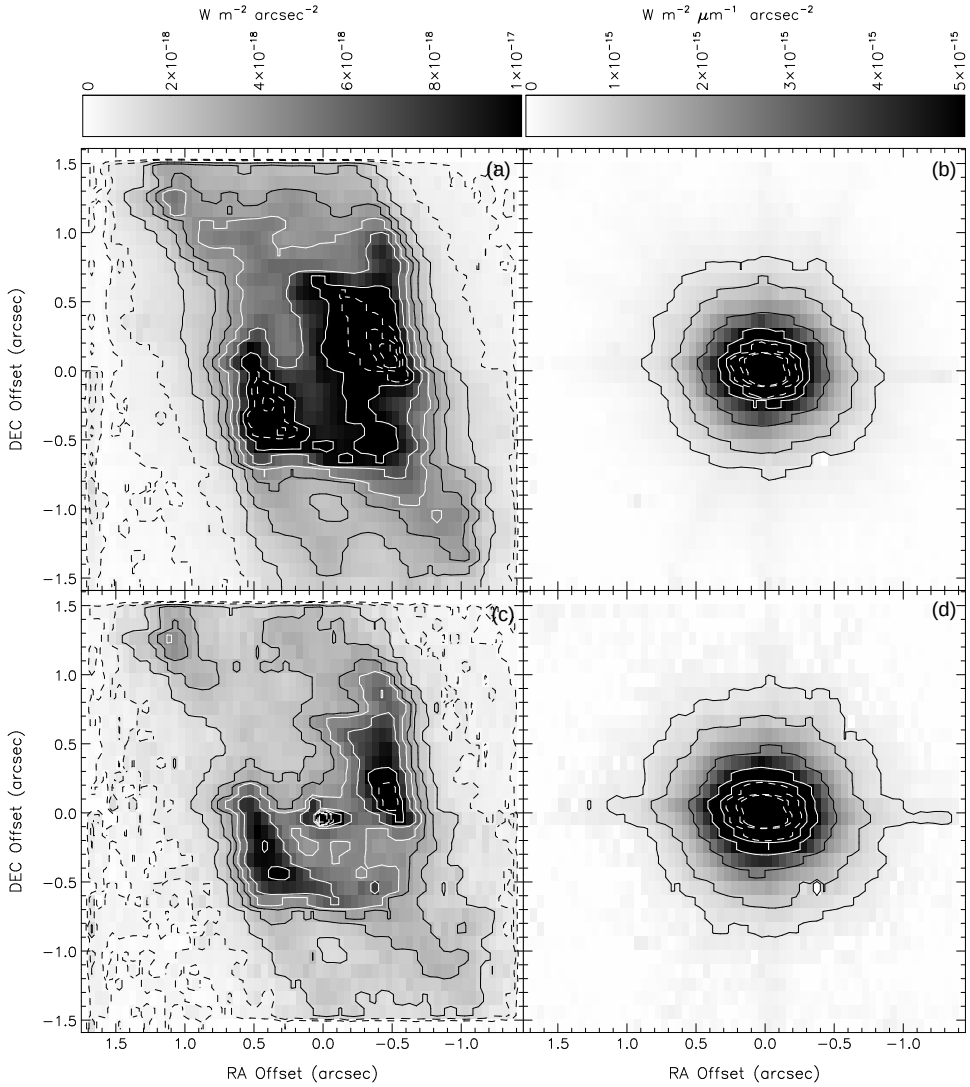


Figure 6.6: The extracted 1-0 S(1) 2.1218 μm and 1-0 S(3) 1.9576 μm emission lines, (**a**) and (**c**), and continuum images, (**b**) and (**d**), from the VLT SINFONI integral field cube. The images are aligned north and east to the top and left of the images, respectively. The co-ordinates are offset from the bright emission peak from the continuum light image. The images are scaled between limits indicated on the horizontal grey scale bar at the top of the panels. The panels (**a**) and (**c**) show the extracted emission line images for the 1-0 S(1) and 1-0 S(3) lines, respectively. The extracted line emission images are in units of $F^{-18} = 10^{-18}$ W m$^{-2}$ arcsec$^{-2}$. The black dashed contours are 0.3- and 0.7-$F^{-18}$. The black contours range between 1.5- to 3.5-$F^{-18}$, separated by 1.0-$F^{-18}$. The solid white contours are 4.5, 6.5 and 10.-$F^{-18}$. The dashed white contours range between 12.5-$F^{-18}$ to a maximum of 20.0-$F^{-18}$ with separations of 2.5-$F^{-18}$. The panels (**b**) and (**d**) show the underlying continuum images for the 1-0 S(1) and 1-0 S(3) lines, respectively. The extracted images are in units of $F_{\lambda}^{-15} = 10^{-15}$W m$^{-2}$ μm$^{-1}$ arcsec$^{-2}$. The outer black contour levels are 0.5-, 1.0- and 2.5-$F_{\lambda}^{-15}$. The solid white contour levels are 5.0- and 7.5-$F_{\lambda}^{-15}$. The dashed white contour levels are 10.0-, 20.0- and 30.0-$F_{\lambda}^{-15}$.

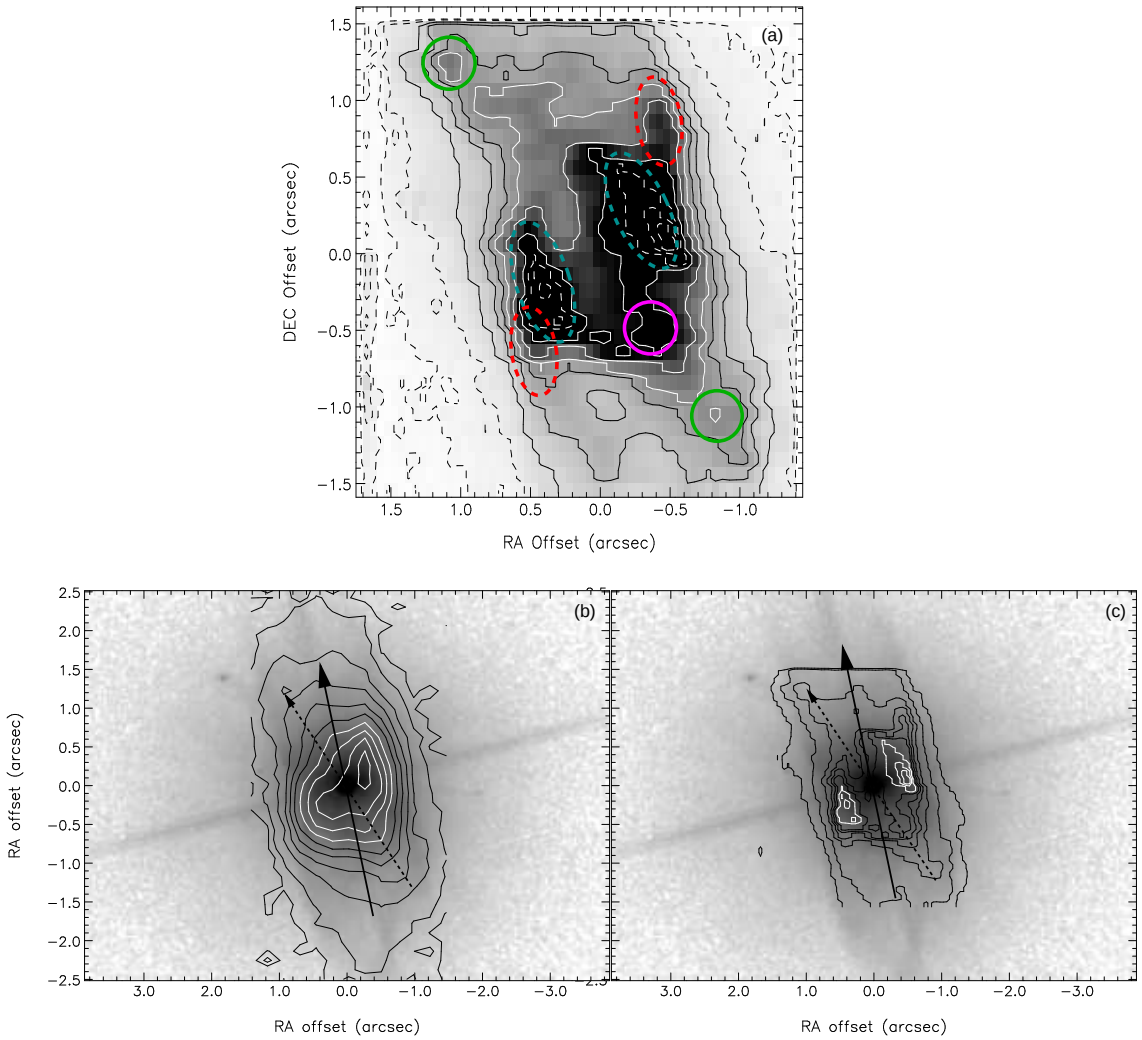


Figure 6.7: The extracted 1-0 S(1) 2.1218 μm line image overlaid with annotated symbols that indicate certain features in panel **(a)**. Panel **(a)** is displayed at the same levels as Fig. 6.6a. The annotated symbols indicate the following: dashed turquoise ellipses mark the arc features; solid green circles mark the knot features; dashed red ellipses indicated the position of the tails, and the solid magenta circle marks an additional bright knot at a similar radius as the arcs. The panels **(b)** and **(c)** show the *HST F606W* image with 1-0 S(1) line contours overlaid from UIST and SINFONI, respectively. The *HST* image is displayed between 22 and 13 mag arcsec$^{-2}$. The black contours are displayed at 1.0-$F^{-18}$ and between 2.0- to 10.0-$F^{-18}$, separated by 2.0-$F^{-18}$. The white contours are displayed from 12.5-$F^{-18}$ to 20.0-$F^{-18}$, separated by 2.5-$F^{-18}$. The PA of the bipolar lobes clearly seen in the HST image, Fig. 6.7(b) & 6.7(c), and is marked by the solid black line with a PA of 18°. The bipolar 'twist' is indicated by the dotted black line with a PA of 28°.

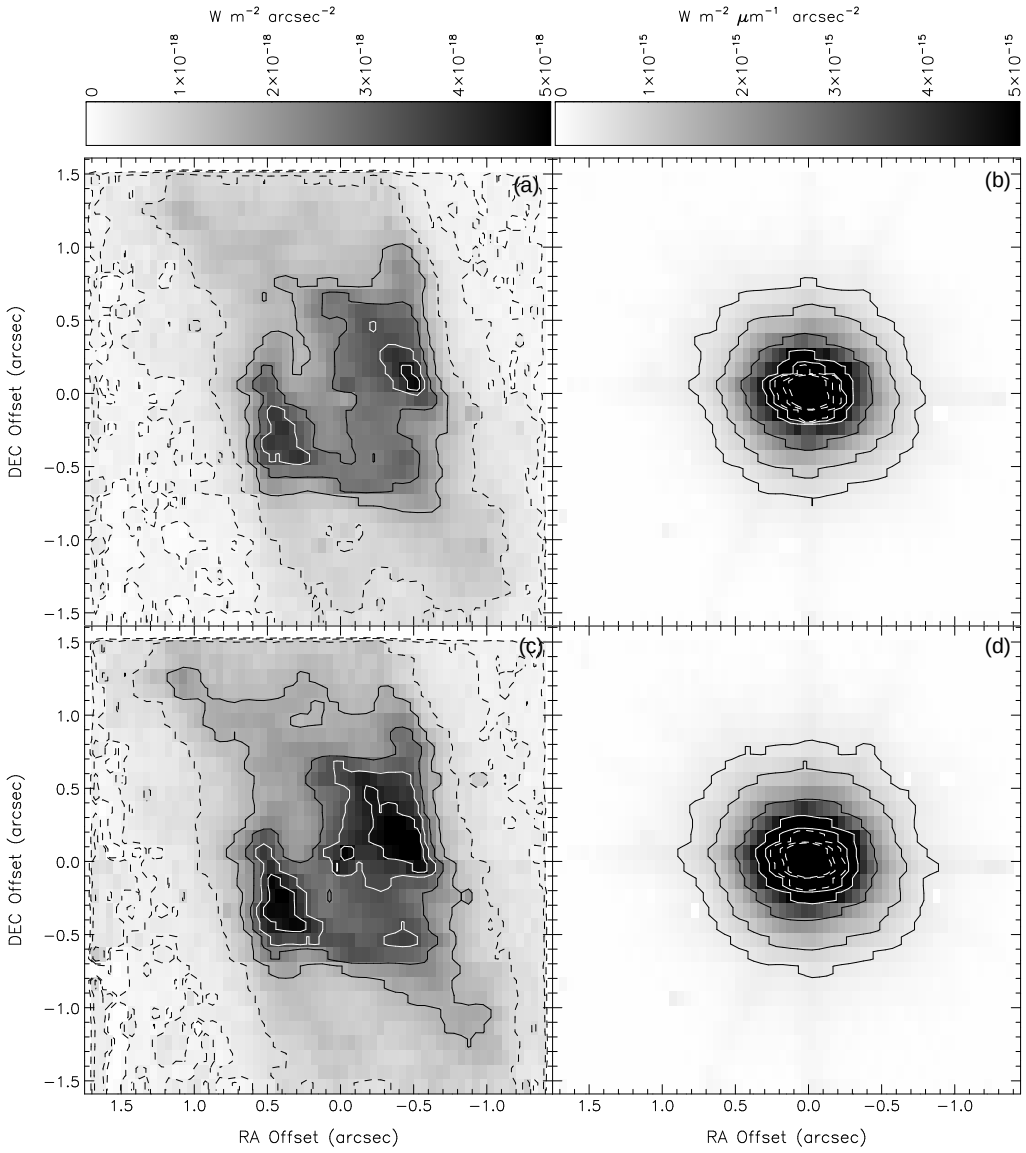


Figure 6.8: The extracted 1-0 S(0) 2.2235 μm and 1-0 S(2) 2.0338 μm emission lines, (**a**) and (**c**), and continuum images, (**b**) and (**d**), from the VLT SINFONI integral field cube. The images are aligned north and east to the top and left of the images, respectively. The co-ordinates are offset from the bright emission peak from the continuum light image. The images are scaled between limits indicated on the horizontal grey scale bar at the top of the panels. The panels (**a**) and (**c**) show extracted emission line images for the 1-0 S(0) and 1-0 S(2) lines, respectively. The extracted line emission images are in units of $F^{-18} = 10^{-18}$ W m$^{-2}$ arcsec$^{-2}$. The black dashed contours are 0.15-, 0.30- and 0.7-$F^{-18}$. The black contours range between 9.0-, 1.5- and 2.5-$F^{-18}$. The solid white contours are 3.5-, 4.5-, 6.5- and 10.-$F^{-18}$. The dashed white contours range between 12.5-$F^{-18}$ to a maximum of 20.0-$F^{-18}$ with separations of 2.5-$F^{-18}$. The panels (**b**) and (**d**) show the underlying continuum images for the 1-0 S(0) and 1-0 S(2) lines, respectively. The image scale and contour levels are identical to Fig. 6.6.

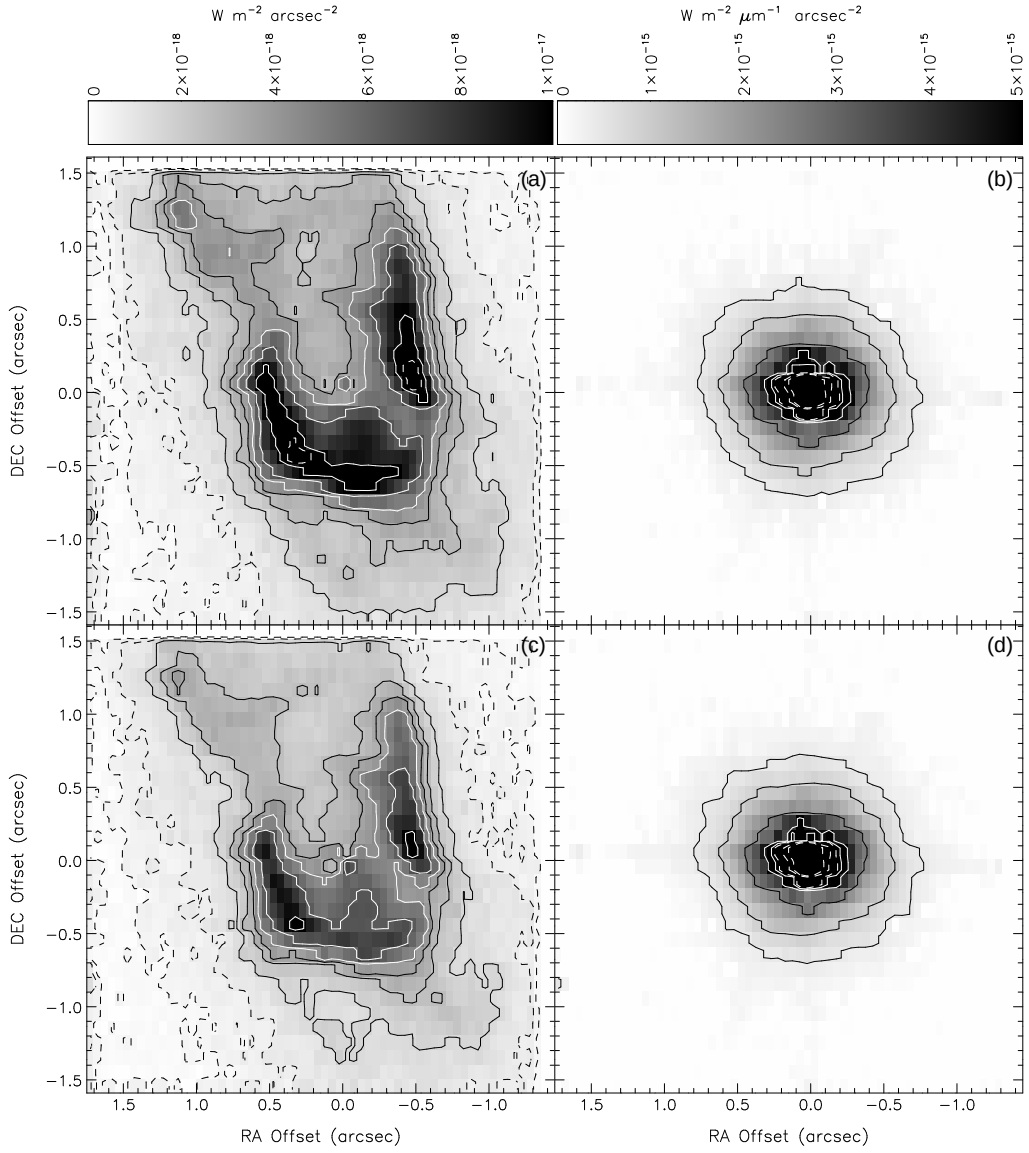


Figure 6.9: The extracted 1-0 Q(1) 2.4066 μm and 1-0 Q(3) 2.4237 μm emission lines, (**a**) and (**c**), and continuum images, (**b**) and (**d**), left and right panels respectively, from the VLT SINFONI integral field cube. The images are aligned north and east to the top and left of the images, respectively. The co-ordinates are offset from the bright emission peak from the continuum light image. The images are scaled between limits indicated on the horizontal grey scale bar at the top of the panels. The panels (**a**) and (**c**) show the extracted emission line images for the 1-0 Q(1) and 1-0 Q(3) lines, respectively. The extracted line emission images are in units of $F^{-18} = 10^{-18}$ W m$^{-2}$ arcsec$^{-2}$. The black dashed contours are 0.3- and 0.7-$F^{-18}$. The black contours range between 1.5- to 3.5-$F^{-18}$, separated by 1.0-$F^{-18}$. The solid white contours are 4.5, 6.5 and 10.-$F^{-18}$. The dashed white contours range between 12.5-$F^{-18}$ to a maximum of 20.0-$F^{-18}$ with separations of 2.5-$F^{-18}$. The panels (**b**) and (**d**) shows the underlying continuum images for the 1-0 Q(1) and 1-0 Q(3) lines. The image scale and contour levels are identical to Fig. 6.6.

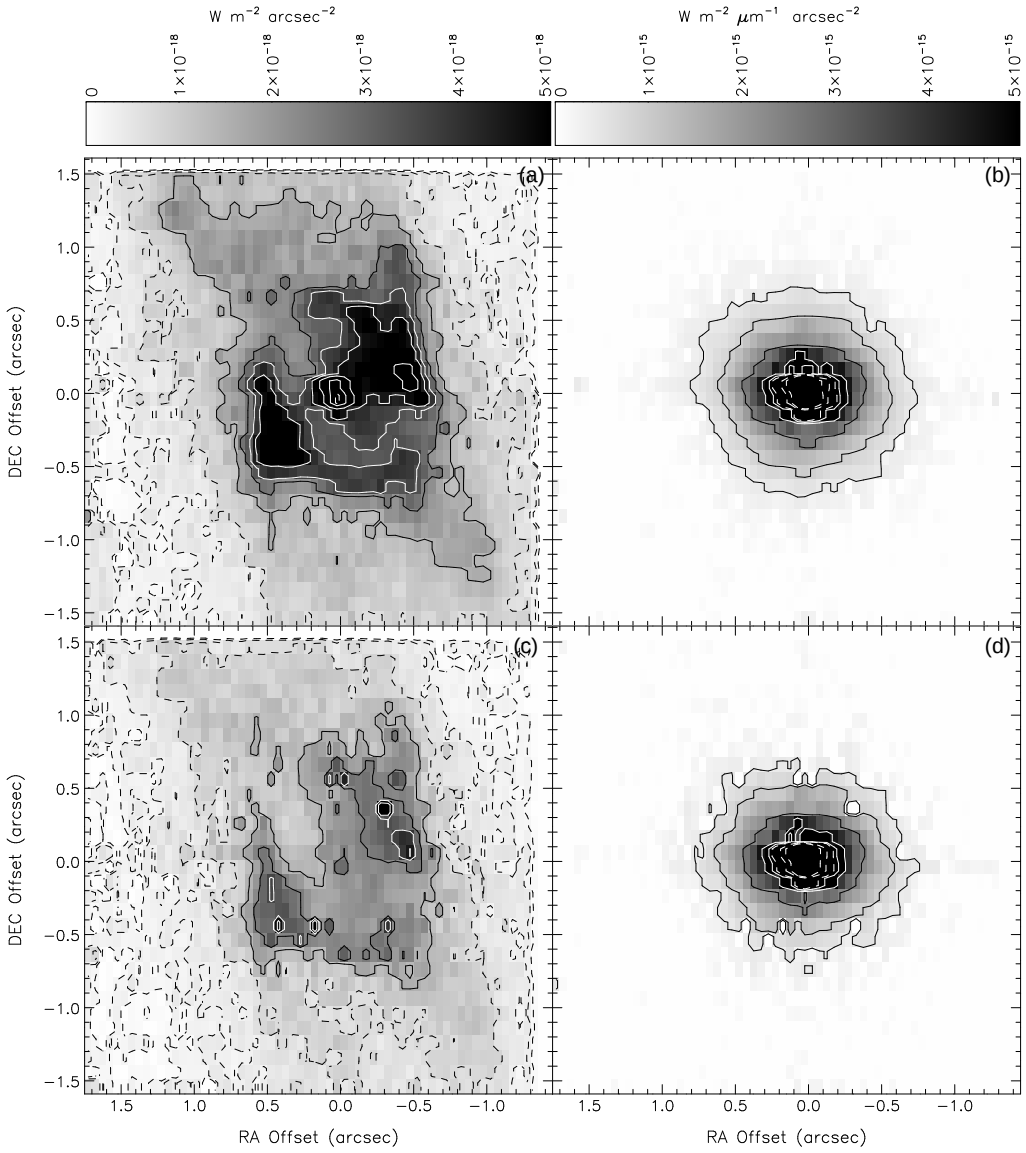


Figure 6.10: The extracted 1-0 Q(2) 2.4134 μm and 1-0 Q(4) 2.4375 μm emission lines, (**a**) and (**c**), and continuum images, (**b**) and (**d**), from the VLT SINFONI integral field cube. The images are aligned north and east to the top and left of the images, respectively. The co-ordinates are offset from the bright emission peak from the continuum light image. The images are scaled between limits indicated on the horizontal grey scale bar at the top of the panels. The panels (**a**) and (**c**) show the extracted emission line images for the 1-0 Q(2) and 1-0 Q(4) lines. The extracted line emission images are in units of $F^{-18} = 10^{-18}$ W m$^{-2}$ arcsec$^{-2}$. The black dashed contours are 0.15-, 0.30- and 0.7-$F^{-18}$. The black contours range between 0.9-, 1.5- and 2.5-$F^{-18}$. The solid white contours are 3.5-, 4.5-, 6.5- and 10.-$F^{-18}$. The dashed white contours range between 12.5-$F^{-18}$ to a maximum of 20.0-$F^{-18}$ with separations of 2.5-$F^{-18}$. The panels (**b**) and (**d**) show the underlying continuum images for the 1-0 Q(2) and 1-0 Q(4) lines. The image scale and contour levels are identical to Fig. 6.6.

structure.

The 1-0 S(3) 1.9576 μm image shows two clearly separated bright arcs northwest and southeast (Fig. 6.6c). The knots in the northeast and southwest are clearly visible. The northeast knot seems relatively brighter with respect to the southwest knot in the 1-0 S(3) line emission than in the 1-0 S(1). The central bright region is deemed to be an artefact of the line fitting, since its diameter is of the order of a few pixels. The 1-0 S(2) and 1-0 S(0) emission shows the northwest and southeast arcs (Fig 6.8a and 6.8c). These lines are similar to the 1-0 S(1) line and do not exhibit significant difference in morphology.

The Q-branch emission at 2.4066 to 2.4375 μm is similar to the 1-0 S emission at 1.9576 to 2.2235 μm (Fig. 6.9 and Fig. 6.10). The 1-0 Q(1) and 1-0 Q(3) appear to have sharper resolved arcs and prominent tails. The southeast arc seems connected to the southwest bright knot and could indicate that these morphological features could be physically linked. The northeast knot is brighter than the southwest knot. The 1-0 Q(2) and 1-0 Q(4) lines show the prominent arcs, knots and tails, but are observed at a lower signal-to-noise.

There is no significant difference in the observed structure of *IRAS* 19306+1407 between the 1-0 S and 1-0 Q branch emission. The minor differences are indicated in the relative brightness in the tails and the northeast/southwest knots. It is concluded that extinction is not significantly attenuating the near-infrared $H_2$ images.

### 6.2.3 2-1 S and 3-2 S $H_2$ emission lines

The signal-to-noise was sufficient to spatially resolve the higher 2-1 S and 3-2 S rovibrational states (Fig. 6.11 and Fig. 6.12). These lines are produced from exciting the higher energy levels. The 3-2 S vibration states are more indicative of fluorescence, since these levels can be populated easily by UV photons, although they

can be excited through shocks. The strongest emission is from the 2-1 S(1) 2.2477 μm and 3-2 S(3) 2.2014 μm lines, and the observations were sufficiently sensitive to resolve these lines without binning. The 2-1 S(1) emission shows a bipolar lobes extending north northeast and south-south west, with two bright arcs of emission located either side of the central source southeast and northwest. The 3-2 S(3) emission has lower signal-to-noise, although the bipolar lobes can be seen with two marginally brighter arcs.

It is clear that the morphology of the 2-1 S(1) and 3-2 S(3) molecular hydrogen emission follows that of the main 1-0 S(1) line closely, although the relative strengths of these lines, with respect to 1-0 S(1), will be determined by the excitation mechanisms involved.

### 6.2.4 Br$\gamma$ emission line

The Br$\gamma$ 2.1661 μm recombination line is present in the observations. The emission is unresolved and it seems that it originates close to the central source (Fig. 6.13). This can be interpreted as the volume around the star becoming ionised by a hotter faster wind or arising from photo-ionisation. Kelly & Hrivnak (2005) detected a P-Cygni profile, but in these SINFONI and UKIRT observations it was not detected, even with SINFONI's greater spectroscopic resolution. Previous observations of H$\alpha$ emission have detected P-Cygni profiles (Sánchez Contreras, private communication), this suggests that the atomic emission is variable. Sánchez Contreras does not state the location of the P-Cygni profile. It is possible that the P-Cygni profile in the Br$\gamma$ emission is variable.

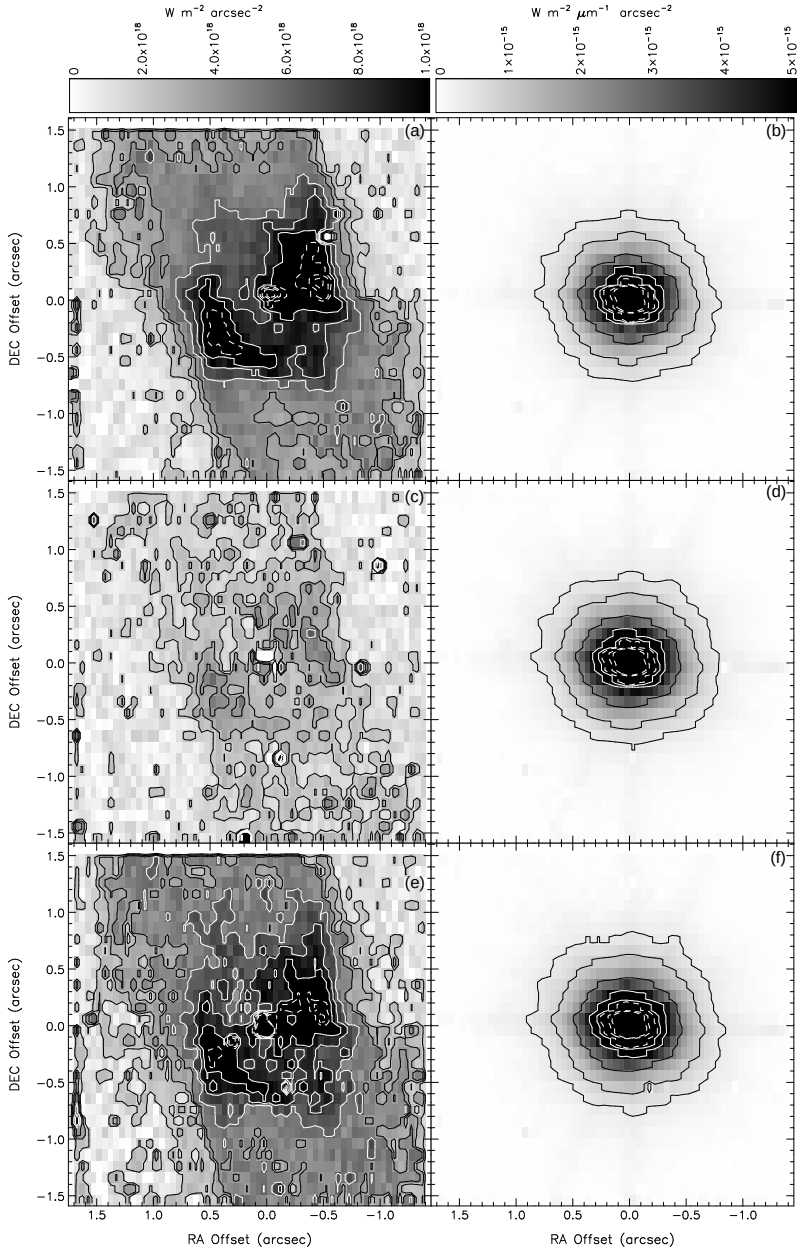


Figure 6.11: The extracted 2-1 S(1) 2.2477 μm, 2-1 S(2) 2.1542 μm, and 2-1 S(3) 2.0735 μm emission lines, (**a**), (**c**) and (**e**), and continuum images, (**b**), (**d**) and (**f**), from the VLT SINFONI integral field cube. The images are aligned north and east to the top and left of the images, respectively. The co-ordinates are offset from the bright emission peak from the continuum light image. The images are scaled between limits indicated on the horizontal grey scale bar at the top of the panels. The panels (**a**), (**c**) and (**e**) show the extracted emission line images for the 2-1 S(1), 2-1 S(2), and 2-1 S(3) lines. The extracted line emission images are in units of $F^{-18} = 10^{-18}$ W m$^{-2}$ arcsec$^{-2}$. The black contours range between 0.2-, 0.3- and 0.4-$F^{-18}$. The solid white contours are 0.6-, 0.8- and 1.0-$F^{-18}$. The dashed white contours range between 1.25-$F^{-18}$ to a maximum of 2.0-$F^{-18}$ with separations of 0.25-$F^{-18}$. The panels (**b**), (**d**) and (**f**) The underlying continuum images for the 2-1 S(1), 2-1 S(2) and 2-1 S(3) lines. The image scale and contour levels are identical to Fig. 6.6.

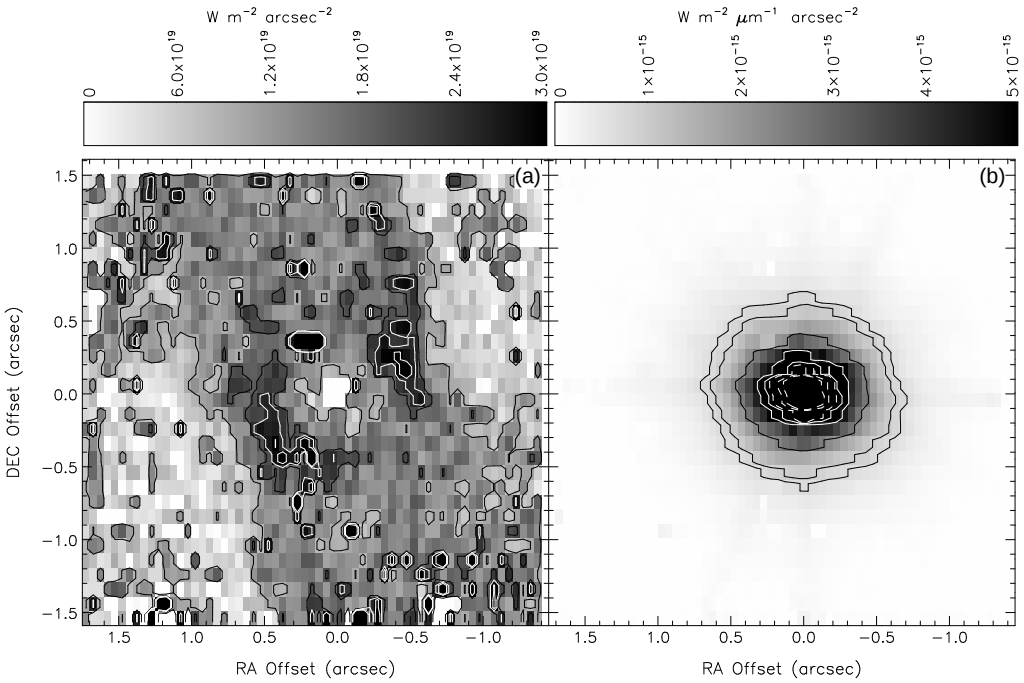


Figure 6.12: The extracted 3-2 S(3) 2.2014 μm emission line, (**a**), and continuum image, (**b**), from the VLT SINFONI integral field cube. The images are aligned north and east to the top and left of the images, respectively. The co-ordinates are offset from the bright emission peak from the continuum light image. The images are scaled between limits indicated on the horizontal grey scale bar at the top of the panels. The panel (**a**) shows the extracted emission line image for the 3-2 S(3) line. The extracted line emission images are in units of $F^{-19} = 10^{-19}$ W m$^{-2}$ arcsec$^{-2}$. The black contours range are 1.0- and 2.0-$F^{-19}$. The solid white contours are 2.5 and 3.0-$F^{-19}$. The panel (**b**) show the underlying continuum images for the 3-2 S(3) line. The image scale and contour levels are identical to Fig. 6.6.

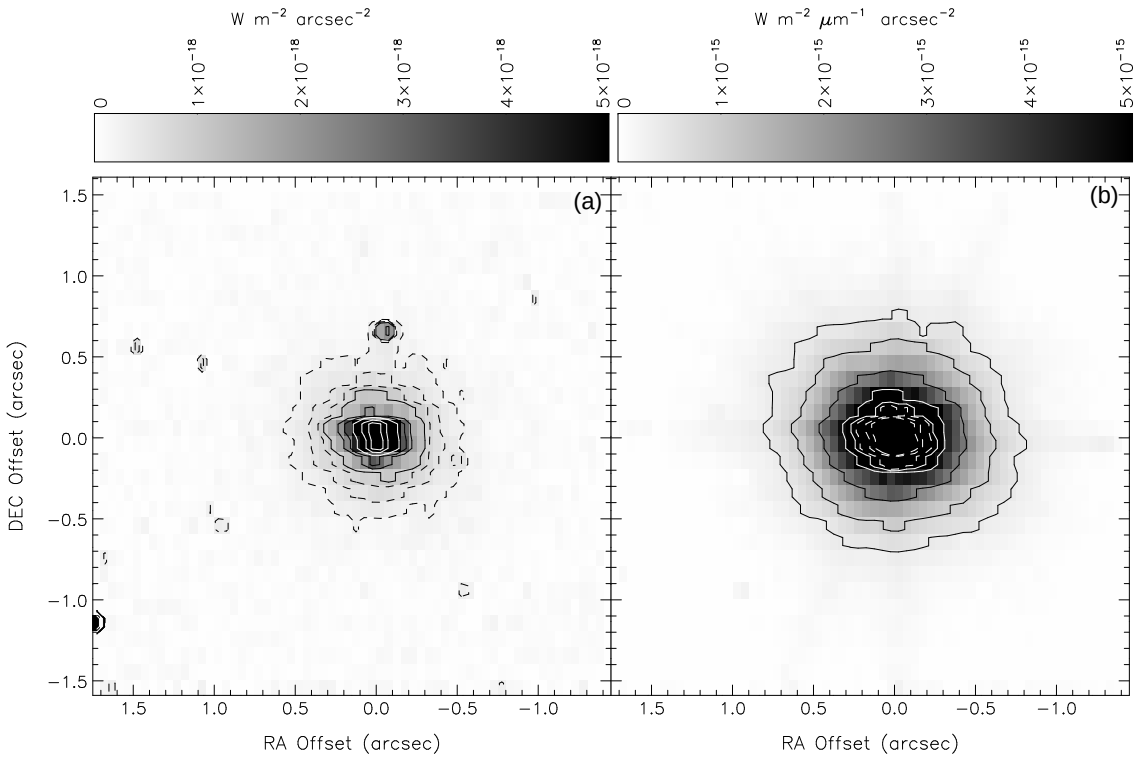


Figure 6.13: The extracted Br$\gamma$ 2.1661 μm emission line, (**a**), and continuum images, (**b**), from the VLT SINFONI integral field cube. The images are aligned north and east to the top and left of the images, respectively. The co-ordinates are offset from the bright emission peak from the continuum light image. The images are scaled between limits indicated on the horizontal grey scale bar at the top of the panels. The panel (**a**) shows the extracted emission line image for the Br$\gamma$ line and is in units of $F^{-18} = 10^{-18}$ W m$^{-2}$ arcsec$^{-2}$. The black dashed contours are 0.25-, 0.5- and 0.75-$F^{-18}$. The black contours range between 1.0-, 2.0- and 3.0-$F^{-18}$. The solid white contours are 5.0-, 10.0- and 15.0-$F^{-18}$. Panel (**b**) shows the underlying continuum image. The image scale and contour levels are identical to Fig. 6.6.

### 6.2.5 Sub-arcsecond imaging

The previous SINFONI observations of *IRAS* 19306+1407 were followed up with the instrument's sub-arcsecond mode. The same observation method was used, which is described in section 6.2. Two separate observations focused on the southeast arc and both fields of view were centred 0.4 arcsec east of the central illumination source. The first observation was positioned at the same declination as the central illumination source, whilst the second was offset by 0.4 arcsec in declination. The two fields of view, displayed as one dark blue box in Fig. 6.1, have been co-added using the SINFONI pipeline and each has a spatial scale of 0.0125 arcsec pixel$^{-1}$. The spectra were taken on 2005 July 29 with a total integration time of 4800 s (80 minutes) comprising 16 exposures of 300 s. A total of 50 per cent of the observations were on source and 50 per cent on sky. The conditions were clear with an average seeing of 0.6 to 0.7 arcsec for the first offset position and 0.6 to 0.8 arcsec for the second position. The natural AO guide star (NGS) used the science target with a $R$-band magnitude of 13.9 mag. The Strehl ratio for the PSF and telluric standards, and the science target is 71, 50 and 73 per cent at 2.2 μm, respectively. The resultant FWHM for the science target was 0.0875 arcsec. A telluric standard star HIP 103773 (G3V) was observed immediately after science observations. The data were reduced using the SPIPE, formed into a data cube of dimensions of $x$, $y$ and $\lambda$ and the spatial scale was resized to 0.025 by 0.0125 arcsec pixel$^{-1}$. Additional reduction steps, including correcting for atmospheric absorption and flux calibrating, were completed by the FUS data reduction package (see chapter 4). The emission line intensity and kinematic images were extracted using the FUS line fitting tool.

The offset positions were chosen to investigate the southeast arc of bright emission in the 1-0 S(1) line, which is shown in Fig. 6.14. The overall structure has an arc like appearance as in Fig. 6.6. However, there are four defined clumps of $H_2$ emission of which three are aligned with the curve of the arc. The fourth bright

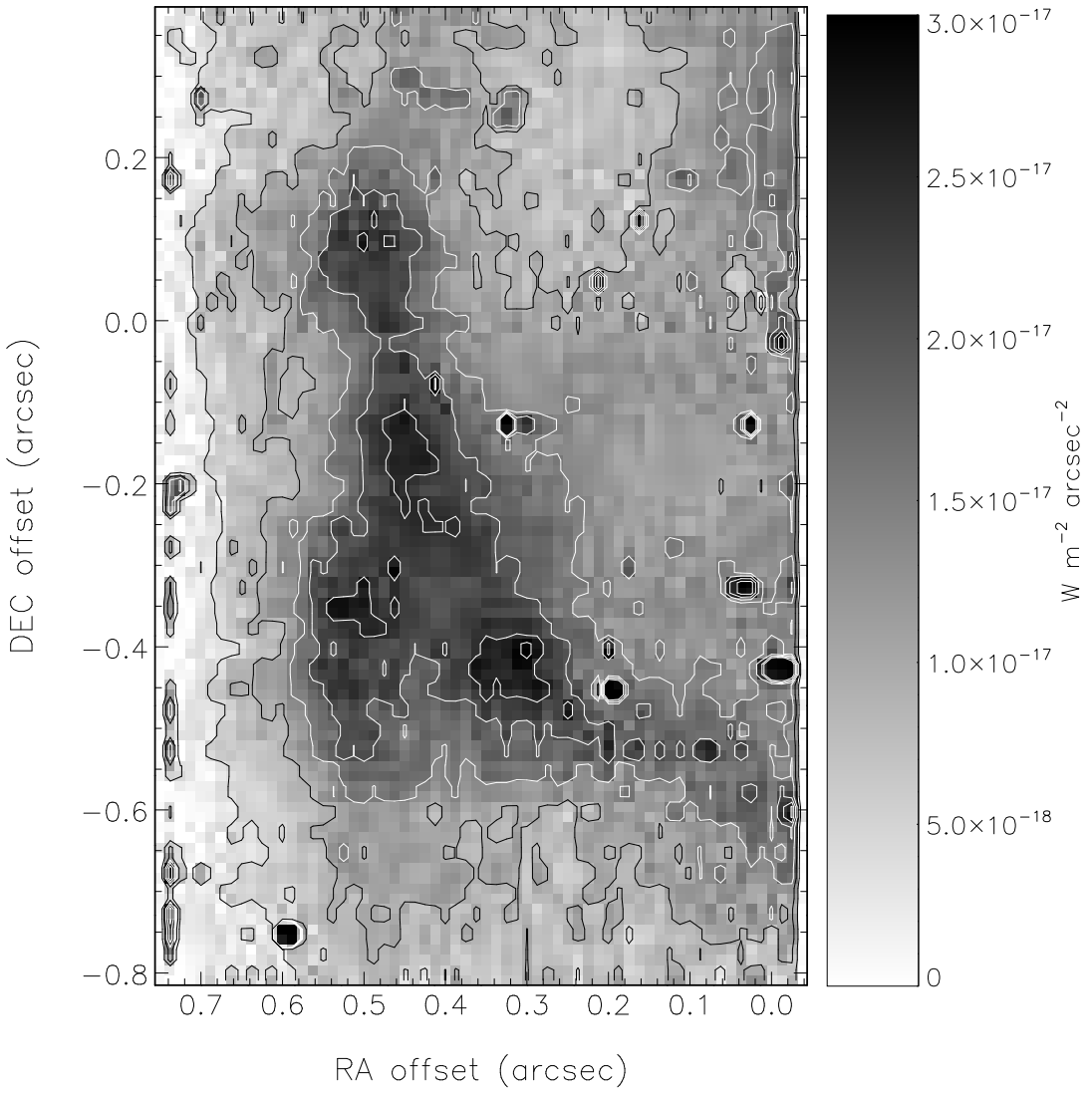


Figure 6.14: The extracted 1-0 S(1) 2.1218 μm line emission from two SINFONI integral field cubes, which have been combined. The image is scaled between limits indicated on the horizontal grey scale bar at the top of the panel. The black contours are displayed at 5.0-$F^{-18}$ and 10.0-F$^{-18}$. The white contours are displayed at 15.0-, 20.0-, 25.0- and 30.0-$F^{-18}$

peak is located at the same position of the bright tail. These bright areas can be interpreted as regions of greater $H_2$ density or areas of shocks. It is possible that the arc is fragmenting due to the fast wind interaction.

Due to the relative weakness of the 2-1 S(1) and 3-2 S(3) lines at this high spatial resolution, it is not possible to resolve these emission lines. Nevertheless by extracting regions, it is possible to increase the signal-to-noise of the weaker lines.

## 6.3 Kinematics (UIST and SINFONI)

There are no published results of the kinematic motion of *IRAS* 19306+1407, with respect to the local standard of rest (LSR). In these observations the Br$\gamma$ line is used to calibrate the difference between the LSR and *IRAS* 19306+1407. The UIST observation gives a velocity of approximately 85 $\pm$ 7 km s$^{-1}$, whilst the SINFONI observations give a value of 87 $\pm$ 5 km s$^{-1}$. These values are used as the systemic velocity. Using Brand & Blitz (1993) it can be possible to estimate the distance of an object based on its radial velocity, with respect to the local standard of rest, and galactic coordinates. This assumes that the object moves with a circular velocity around the galactic centre. The combination of the radial velocity from the Br$\gamma$ observations gives a circular velocity and a galactic centric radius of 223 km s$^{-1}$ and 5.7 kpc, respectively. This derived galactic centric radius is less than the minimum galactic centric radius, based on the galactic coordinates, predicted by equation 2 in Brand & Blitz (1993). Therefore, it is *not* possible to estimate a distance for *IRAS* 19306+1407 using the method detailed in Brand & Blitz (1993). It is possible that *IRAS* 19306+1407 motion within the galaxy is non-circular.

The larger FoV of the UIST IFU shows large red-shifted and blue-shifted components in the bipolar lobes (Fig. 6.15 left). The northern part of the nebula is red shifted and the southern part is blue shifted, with a velocity difference of $\sim$50 km s$^{-1}$. The uncertainty in the velocity is $\sim$7 km s$^{-1}$. This implies that the bipolar lobes are inclined, assuming an axial outflow, with the southern lobe pointing towards the observer. There is a small difference in velocity between the two bright peaks of emission. The SW peak is red shifted and the northwest is blue shifted with a difference of approximately 10 km s$^{-1}$.

The medium resolution SINFONI velocity map of the 1-0 S(1) line (Fig. 6.15 centre), agrees with the UIST IFU observations that the northern section of the bipo-

lar nebula is red shifted with respect to the systemic velocity and therefore inclined away from the observer, whilst the southern section is blue shifted and therefore inclined towards the observer. The velocity map is complex in the southeast and northwest bright emission arcs. The bulk of the southeast arc is receding from the observer, at $\sim 5$ km s$^{-1}$. The northwest arc appears to be blue shifted towards the observer at $\sim -7$ km s$^{-1}$. The tails attached to southeast and northwest arcs are blue and red shifted at $\sim -6$ and $\sim 5$ km s$^{-1}$, respectively.

The high resolution SINFONI images focus on the southeast arc (Fig. 6.15 right). Although the uncertainty in the velocity is approximately $\pm 5$ km s$^{-1}$, the bright arc appears to spilt into three distinct areas. The northern and southern tips of the arc are red-shifted at 5 km s$^{-1}$ and the central region is blue-shifted by approximately -5 km s$^{-1}$.

In PPNe the kinematics are measured using molecular emission, such as $H_2$ and CO, and atomic hydrogen emission, in which the latter can be spatially unresolved (e.g. IRAS 22036+5306; Sahai et al 2006). These molecules trace the emergence of collimated fast wind. In PNe the kinematics are measured using atomic and forbidden transitions, such as H$\alpha$ and [NII]. In PNe shaping is characterised by interacting winds. An object that is transiting between the PPN to PN stage might show molecular emission with similar kinematics to a PNe. Dobrinčić et al. (2008), in their H$\alpha$ study, found that their bipolar PNe expand 3-16 km s$^{-1}$ equatorially and 18-100 km s$^{-1}$ in the polar direction, which agree with the $H_2$ observations, assuming that the $H_2$ emission from the bipolar lobes arises from an axial flow and the arcs are expanding equatorially.

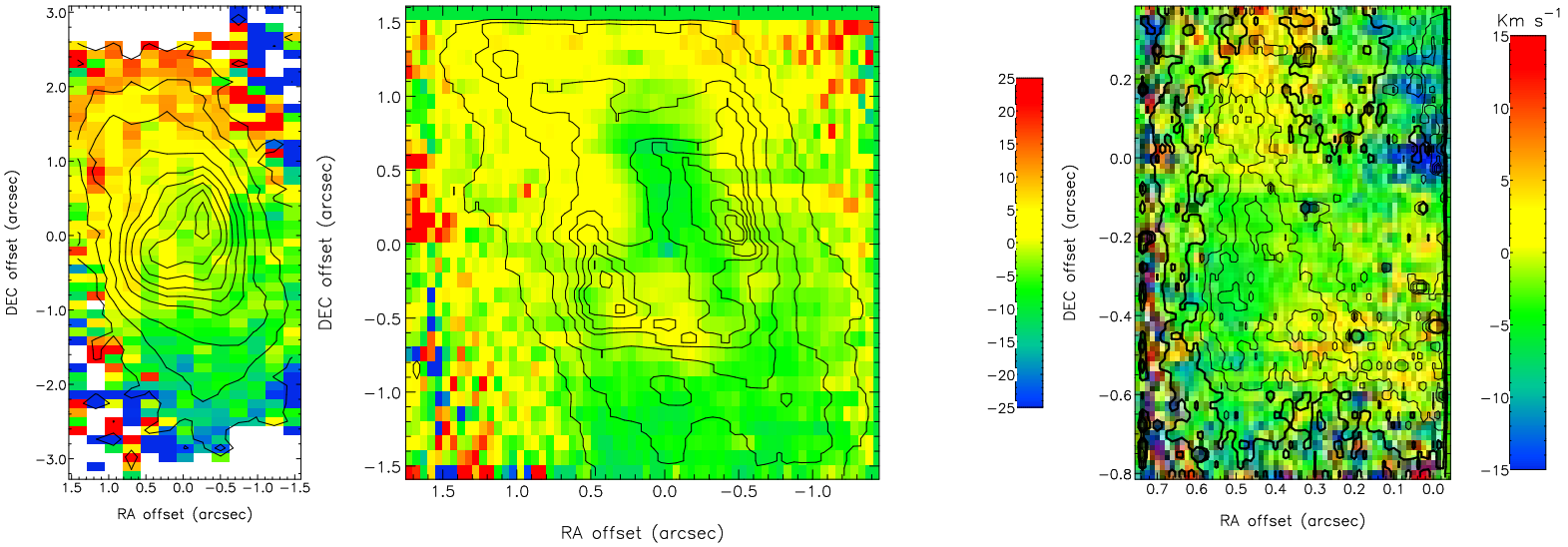


Figure 6.15: The velocity of the $H_2$ 1-0 S(1) line with respect to the mean velocity (87 $\pm$ 5 km s$^{-1}$). The left panel is the UIST IFU observations. Centre and right are the SINFONI observations from the medium to high resolution images, respectively. All panels are overlaid with contours of the line emission intensity. The left and centre velocity ranges from -25 to +25 km s$^{-1}$, with negative velocity material moving towards the observer. The right hand panel velocity ranges from -15 to +15 km s$^{-1}$

## 6.4 Line, column density and ortho-para ratios

### 6.4.1 Extinction correction

*IRAS* 19306+1407 is situated close to the galactic plane and will suffer from extinction from the interstellar medium and from its own CSE. This extinction will attenuate emission at shorter wavelengths compared to emission at longer wavelengths and artificially decrease estimates of the rotation excitation temperature and the ortho-para ratio, and increase estimates of the level of fluorescence. The level of extinction varies for each spectral pixel or binned region, and therefore has to be calculated for each spectral pixel or region. The wavelength range and spectroscopic resolution of SINFONI gives three potential line ratios to estimate the extinction. However, the required Q-branch lines are in an opaque part of the spectrum, in which the atmospheric absorption lines are variable over a short timescale. These variations are of the order of seconds and the SINFONI observations are hundreds of seconds in length, therefore calculating extinction using the 1-0 Q and 1-0 S ratios should be taken with some caution.

The use of a telluric standard star has introduced extra ambiguities into the atmospheric correction of wavelengths greater than 2.4 μm. For example the 1-0 Q(3) 2.4237 μm line lies close to an absorption line belonging to the telluric star and the correction has increased its flux. The measured 1-0 Q(3) 2.4237 μm /1-0 S(1) 2.1218 μm line ratio is less than 0.7, which gives negative values for the extinction. All attempts to compensate for the standard star's absorption feature located near to the 1-0 Q(3) line introduce a large uncertainty.

The scattering models presented in Chapter 5 and Lowe & Gledhill (2007) have a maximum extinction, at 2.2 μm, of $0.240 \pm 0.001$ mag in the CSE; in addition, the extinction due to the ISM, at 2.2 μm, is $0.48 \pm 0.01$ mag. The total extinction of $0.72 \pm 0.01$ at 2.2 μm is used as an upper limit for the line ratios, the ortho-

para ratio (OPR), temperatures and CDR, which are displayed with and without an extinction correction. The extracted regions are displayed in Figure 6.19.

The effect of extinction, assuming a simple $\lambda^{-1.7}$ power-law, on an emitting gas in LTE at a temperature of 2000 K is shown in Fig. 6.16. In the absence of extinction the 1-0 S(1) 2.1218 μm /2-1 S(1) 2.2477 μm and 1-0 S(1) 2.1218 μm /3-2 S(3) 2.2014 μm ratios are 12 and 166, respectively. The 1-0 S(1)/2-1 S(1) and 1-0 S(1)/3-2 S(3) ratios will be henceforth known as $r_{21}$ and $r_{32}$, respectively. The ratios decrease as the extinction increases, but do not reach the fluorescent ratio of $\sim 2$ and $\sim 8$, respectively. The line ratio images have *n*ot been corrected for extinction.

## 6.4.2 Line ratios

### 6.4.2.1 Line ratio images

It was possible to obtain line ratio images of $r_{21}$ and $r_{32}$ without spatial binning. The $r_{21}$ ratio image shows a complex structure, with ratios ranging from 6 to 15 (Fig. 6.17). The inner most region has low values, that can be attributed to bright emission in the 2-1 S(1) line, caused by an artefact of emission line fitting. High ratios are located in bright arcs either side of the star and in the bright knot of emission to the southwest (Fig. 6.7, solid magenta circle). The highest ratios, 13+, occur in the northern tip of the northwest arc and the southwest knot of emission. The bright arcs have ratios ranging from 10 to 12; however, the southeast arc has lower ratio values than the northwest arc. The northwest tail shows a ratio of 10, but the southeast tail has low values from 6 to 8. The bipolar lobes have low ratios, which range from 6 to 8.

The $r_{32}$ ratio image (Fig. 6.18) shows a defined structure. It has been possible to resolve the arc-like structures to the southeast and the northwest. The southeast arc has ratios between 50 and 60, whilst the northwest arc shows ratios ranging

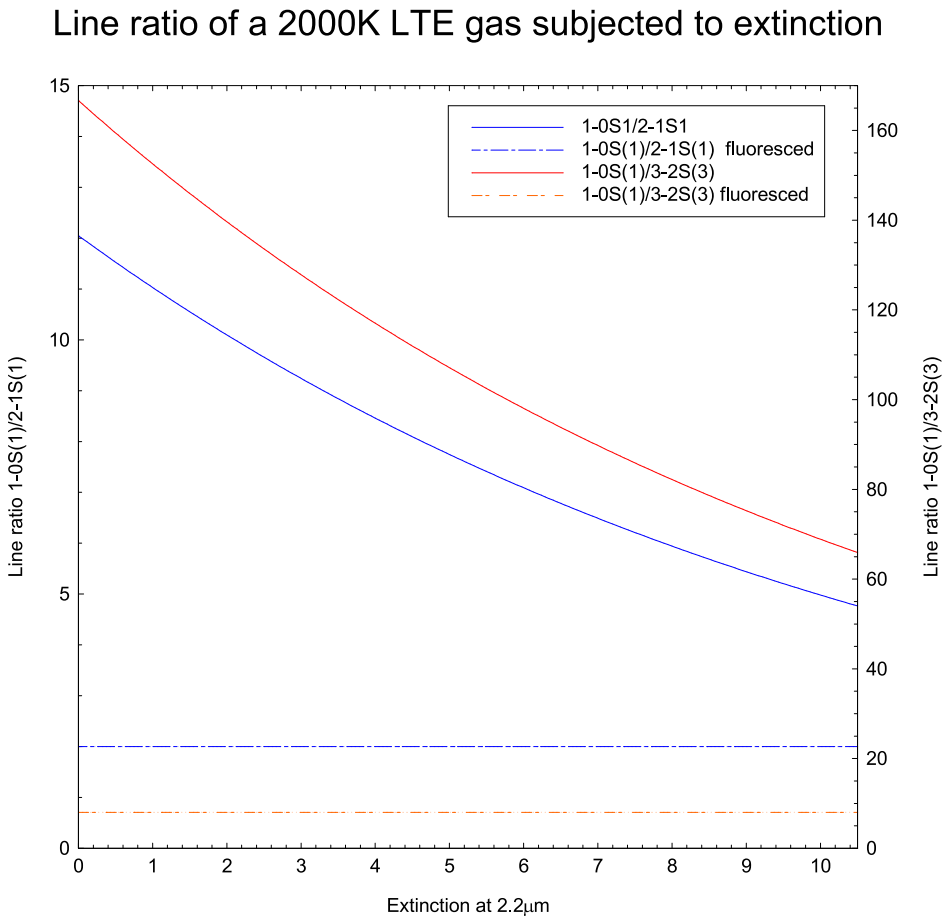


Figure 6.16: The effect of extinction on $r_{21}$ and $r_{32}$ line ratios, which are marked as blue and red solid lines, respectively. The values for $r_{21}$ and $r_{32}$ line ratios are given on the left and right $y-$axis, respectively. The line ratios for a 2000 K LTE gas are obtained from Table 3.2 in chapter 3. The fluorescent values for the $r_{21}$ and $r_{32}$ ratios are obtained from Burton et al. (1990) and are marked are blue and red dash-dot lines, respectively. The extinction at 2.2 μm, calculated using a power-law (modified from equation 3.8), is stated on the $x-$axis.

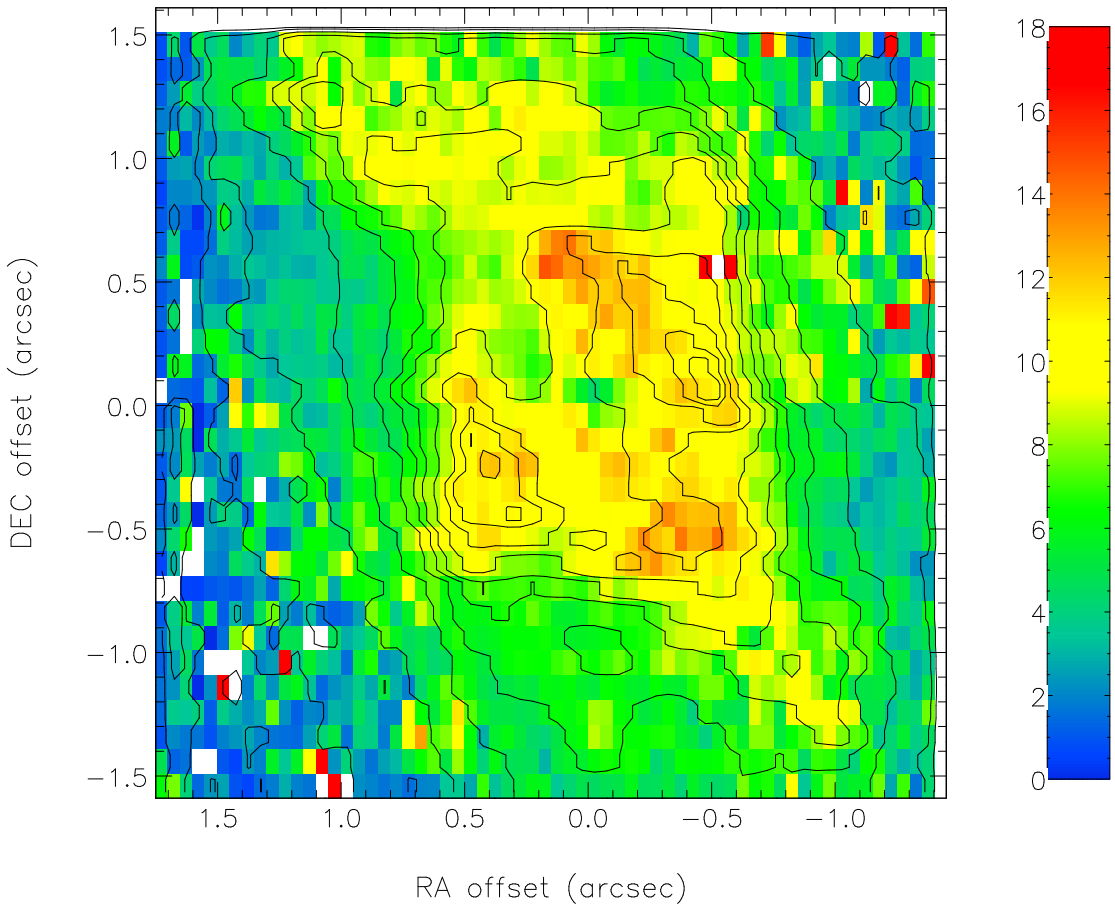


Figure 6.17: The image of the $r_{21}$ line ratio. The image scale is present on the right with the ratio number, ranging from 0 to 18. The overlaid contours are identical to those in Fig. 6.6.

Table 6.1: The 2-1 S(1) and 3-2 S(3) line ratios, from the medium resolution SINFONI observations, with respect to 1-0 S(1), which are uncorrected and corrected for extinction, for the 17 extracted regions. The extinction is $0.72 \pm 0.01$ magnitudes at 2.2 μm.

| | Line ratios | | | | | | | | | | | |
|---|---|---|---|---|---|---|---|---|---|---|---|---|
| Region | Uncorrected for extinction | | | | | | Corrected for extinction | | | | | |
| Number | $r_{21}$ | | | $r_{32}$ | | | $r_{21}$ | | | $r_{32}$ | | |
| 1 | 11.9 | ± | 0.2 | 59 | ± | 4 | 12.7 | ± | 0.5 | 62 | ± | 5 |
| 2 | 10.9 | ± | 0.3 | 57 | ± | 6 | 11.7 | ± | 0.5 | 60 | ± | 7 |
| 3 | 10.7 | ± | 0.2 | 53 | ± | 3 | 11.5 | ± | 0.4 | 55 | ± | 4 |
| 4 | 10.3 | ± | 0.2 | 45 | ± | 3 | 11.1 | ± | 0.4 | 47 | ± | 4 |
| 5 | 9.2 | ± | 0.7 | 47 | ± | 12 | 9.9 | ± | 0.8 | 49 | ± | 12 |
| 6 | 9.1 | ± | 0.1 | 36 | ± | 2 | 9.7 | ± | 0.4 | 37 | ± | 2 |
| 7 | 8.1 | ± | 0.2 | 34 | ± | 2 | 8.7 | ± | 0.3 | 35 | ± | 3 |
| 8 | 9.0 | ± | 0.2 | 15 | ± | 1 | 9.6 | ± | 0.4 | 15 | ± | 1 |
| 9 | 7.9 | ± | 0.1 | 20 | ± | 0.4 | 8.5 | ± | 0.3 | 21 | ± | 1 |
| 10 | 8.2 | ± | 0.1 | 23.3 | ± | 1 | 8.8 | ± | 0.3 | 24 | ± | 1 |
| 11 | 6.1 | ± | 0.1 | 16.7 | ± | 0.5 | 6.5 | ± | 0.2 | 17 | ± | 1 |
| 12 | 8.6 | ± | 0.1 | 27 | ± | 1 | 9.2 | ± | 0.3 | 28 | ± | 1 |
| 13 | 4.9 | ± | 0.1 | 18 | ± | 1 | 5.2 | ± | 0.2 | 19 | ± | 1 |
| 14 | 5.8 | ± | 0.1 | 20 | ± | 1 | 6.2 | ± | 0.2 | 21 | ± | 1 |
| 15 | 4.9 | ± | 0.1 | 13 | ± | 1 | 5.3 | ± | 0.2 | 14 | ± | 1 |
| 16 | 4.5 | ± | 0.1 | 8.2 | ± | 0.3 | 4.9 | ± | 0.2 | 8.5 | ± | 0.4 |
| 17 | 10.1 | ± | 0.1 | 41 | ± | 1 | 10.8 | ± | 0.4 | 42 | ± | 2 |

between 50 and 70. The southwest knot has ratios greater than 60. The inner region has a low signal-to-noise and thus the ratios are probably spurious. This is indicated by the thick grey line, which has a value equal to 2. The line ratios in the bipolar lobes decrease to values of approximately 30.

#### 6.4.2.2 Extracted regions from the medium resolution SINFONI observations

A total of 17 regions (Fig. 6.19) have been extracted and spatially binned to increase the signal-to-noise and the resultant line ratios are displayed in Table 6.1 (both uncorrected and corrected for the extinction). The following section discusses the uncorrected and corrected ratios, with the former given in square brackets.

Regions 1 and 8 are situated axially on diametrically opposite sides, southwest

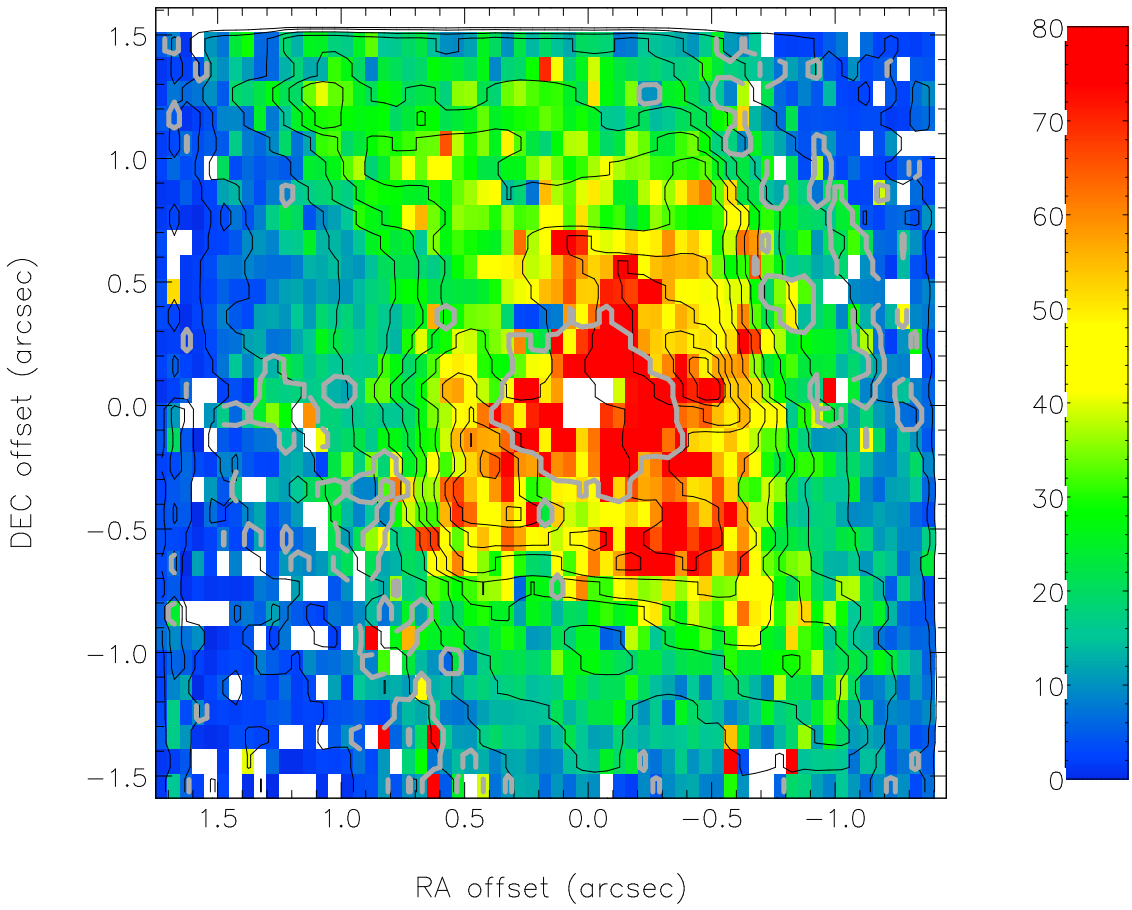


Figure 6.18: The image of $r_{32}$ line ratio. The image scale is present on the right with the ratio number, ranging from 0 to 80. The overlaid black contours are identical to those in Fig. 6.6. The thick grey line represents a signal to noise value of 2.

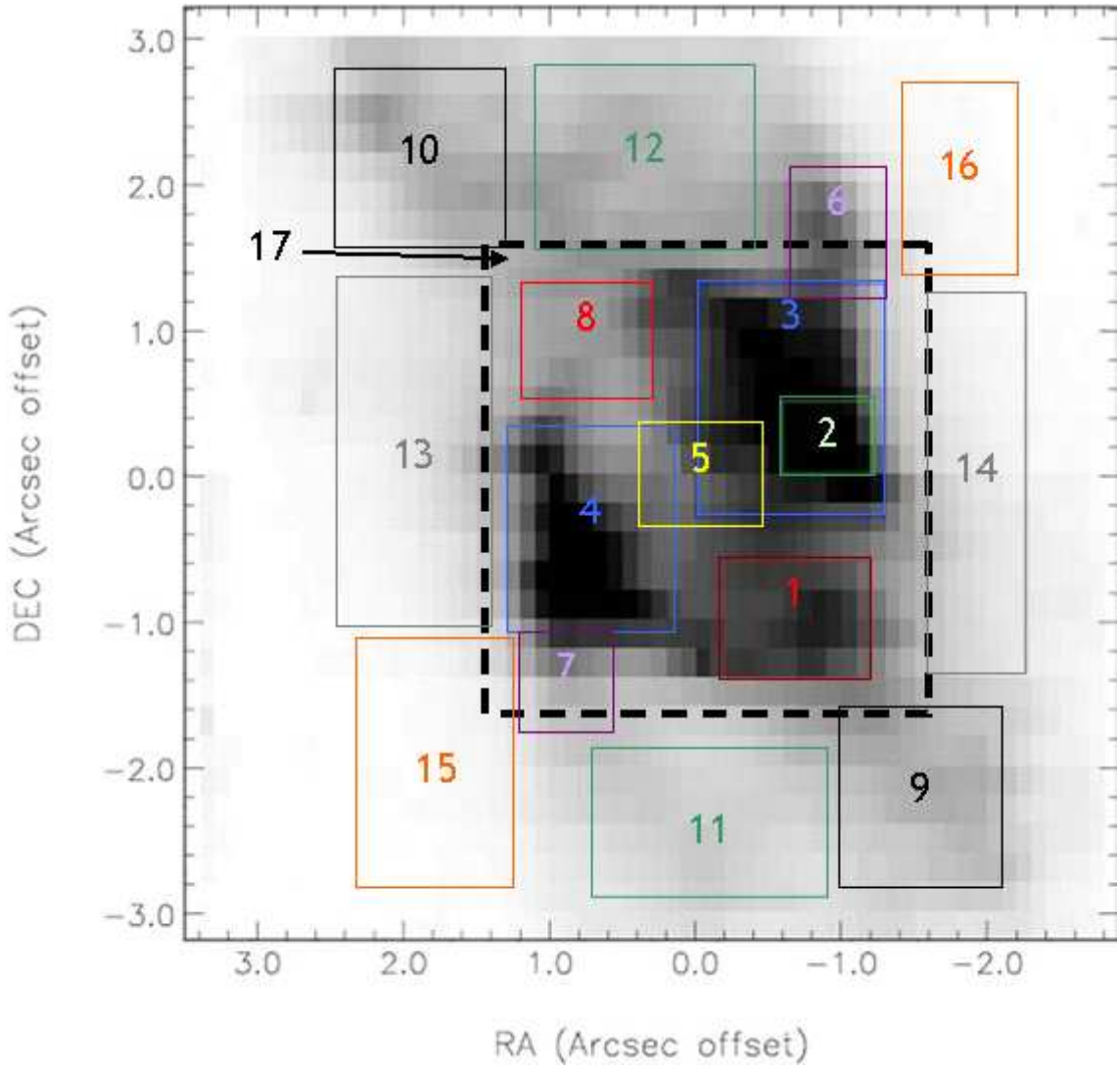


Figure 6.19: The 1-0 S(1) emission line map overlaid with the the locations of the extracted regions 1 through to 17, which are marked. Region 17 is highlighted by the black dashed lines.

and northeast, of the central illuminating source and are at equal radii. Region 1 is centred on the southwest bright knot, whilst 8 is in a region that has no bright emission. These two regions have similar values for the $r_{21}$ ratios, 12.7±0.5 [11.9±0.2] and $9.6 \pm 0.4$ [$9.0 \pm 0.2$] respectively, and the $r_{32}$ ratios are $62 \pm 5$ [$59 \pm 4$] and $15 \pm 1$ [$15 \pm 1$], respectively. Regions 3 and 4 are positioned on the equatorial bright southeast and northwest arcs, respectively. The $r_{21}$ and $r_{32}$ ratios for these two regions are similar, with values of $\sim 11$ and $\sim 50$, respectively within errors. This suggests that the excitation mechanism in both bright areas is due to shocks or high density fluoresced gas. Region 2 is located in the brightest section of the northwest arc, and gives values of $11.7 \pm 0.5$ [$10.9 \pm 0.3$] and $60 \pm 7$ [$57 \pm 6$] for the $r_{21}$ and $r_{32}$ ratios, respectively, indicating either shocks or a fluoresced dense gas. The centre of Region 5 is located on the central illumination source. The ratios are $9.9 \pm 0.8$ [$9.2 \pm 0.7$] and $49 \pm 12$ [$17 \pm 12$] for the $r_{21}$ and $r_{32}$ ratios, respectively, indicating a shock or a fluoresced dense gas. Regions 6 and 7 are situated over the northwest and southeast tails and regions 9 through to 12 are located within the bipolar lobes, in which regions 9 and 10 are extracted over the southwest and northeast knots, respectively. The tail regions show that they are either shocked or a fluoresced dense gas, whilst the lobe and knot regions show lower ratios and indicate a contribution from a low density fluoresced gas. Regions 13 through to 16 highlight areas outside the bright $H_2$ emission and their ratios indicate a component of low density fluoresced gas. Region 17 covers the central $H_2$ features and ratios are $10.8 \pm 0.4$ [$10.1 \pm 0.1$] and $42 \pm 2$ [$41 \pm 1$] for the $r_{21}$ and $r_{32}$ ratios, respectively.

The line ratios indicate that the equatorial, central and tail regions are experiencing shocks or are areas of a dense fluoresced gas, whilst the axial, lobe and outer areas show a greater contribution from a low density fluoresced gas.

#### 6.4.2.3 Extracted regions from the sub-arcsecond SINFONI observations

A total of nine regions were extracted from the high spatial resolution data cube and are displayed in Fig. 6.20. Regions 1, 2 and 4 are situated on the northern to southern knots in the bright arc. The tail feature has two extracted regions, numbered 3 and 6. The former is overplotted on the brighter part of the tail and the latter region is situated to the south. Region 5 is located south of the central source and along the ring of emission that links the bright arc to the southwest knot (Fig. 6.7). Two regions have been selected that are not located with any bright 1-0 S(1) emission, which are Regions 7 and 8. Region 7 is located between the bright arc of emission and the central source and Region 8 is located north of the central source. Region 9 encompasses regions 1 through 8. Due to the advantage of IFS it is possible to subtract Regions 1 through 8 from Region 9 to give information on the fainter material around the bright arc. The line emission has been extracted from these regions and the line ratios are displayed in Table 6.2.

Overall the corrected line ratios range from 5 to 14 and 27 to 75 for the $r_{21}$ and $r_{32}$ ratios, respectively. The majority of $r_{21}$ ratio values are $\sim 10$. The smallest $r_{21}$ ratio is $5 \pm 1$ in Region 8, where the corresponding $r_{32}$ ratio is $35 \pm 30$, whilst the greatest $r_{21}$ ratio is $14 \pm 1$ in Region 2 and the $r_{32}$ ratio is $47 \pm 7$.

The knots within the bright arc, Regions 1, 2 and 4, show $r_{21}$ ratios from 11 to 14 and $r_{32}$ ratio ranges from 47 to 75. The tail feature, Regions 3 and 6, show $r_{21}$ ratios of $11 \pm 1$ and $10 \pm 1$, respectively, in addition, the $r_{32}$ values are $58 \pm 12$ and $61 \pm 17$, respectively. Region 5 has $r_{21}$ and $r_{32}$ values of $11 \pm 1$ and $27 \pm 5$, respectively. Regions 7 and 8 are not associated with the brightest areas of $H_2$ emission and have the greatest uncertainty in the $r_{32}$ ratio. These values are $75 \pm 61$ and $35 \pm 30$. In addition, the $r_{21}$ ratios are $13 \pm 3$ and $5 \pm 1$ respectively. In these two regions Br$\gamma$

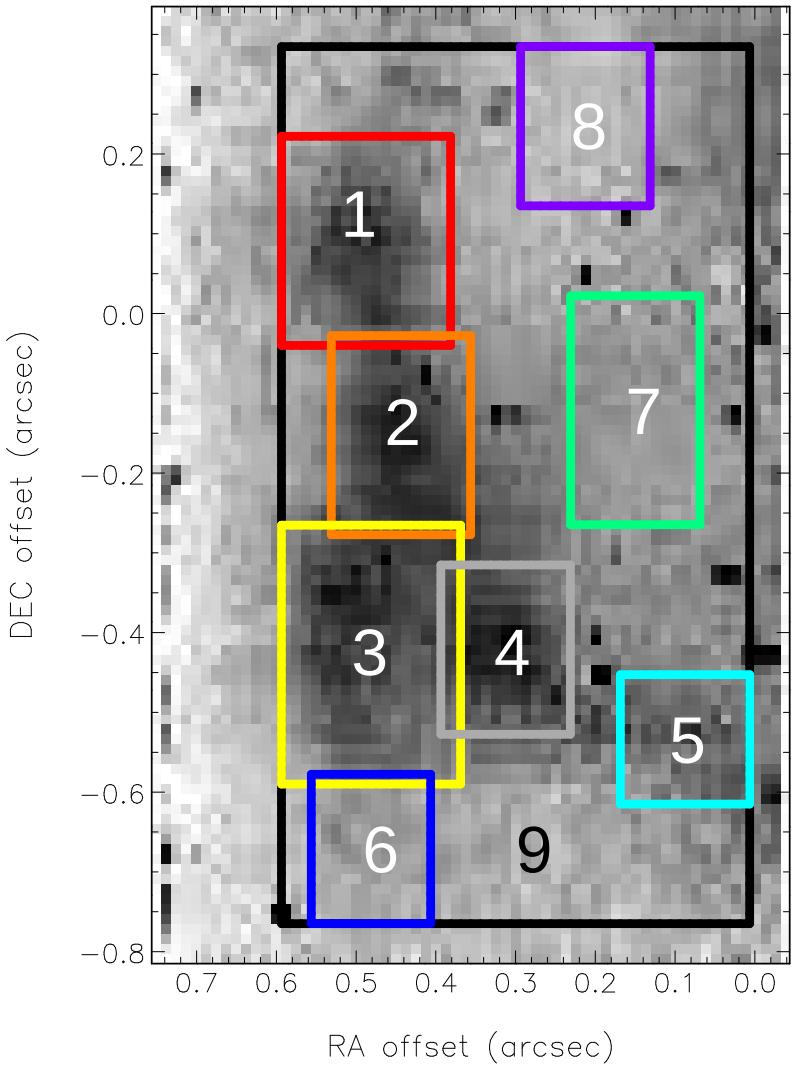


Figure 6.20: The 1-0 S(1) emission line image overlaid with the the locations of the extracted regions 1 through to 9, which are marked.

Table 6.2: The line ratios of the $r_{21}$ and $r_{32}$ are displayed below (with and without the extinction correction) for the sub-arcsecond SINFONI observations. The extinction is $0.72 \pm 0.01$ magnitudes at 2.2 μm.

| Region | $r_{21}$ ratio | | | $r_{32}$ ratio | | | $r_{21}$ ratio | | | $r_{32}$ ratio | | |
|---|---|---|---|---|---|---|---|---|---|---|---|---|
| | Uncorrected for extinction | | | | | | Corrected for extinction | | | | | |
| 1 | 9.3 | ± | 0.3 | 67 | ± | 15 | 11 | ± | 1 | 75 | ± | 18 |
| 2 | 11.8 | ± | 0.5 | 42 | ± | 6 | 14 | ± | 1 | 47 | ± | 7 |
| 3 | 10.3 | ± | 0.3 | 56 | ± | 11 | 11 | ± | 1 | 58 | ± | 12 |
| 4 | 10.9 | ± | 0.4 | 61 | ± | 13 | 13 | ± | 1 | 67 | ± | 15 |
| 5 | 9.5 | ± | 0.6 | 25 | ± | 4 | 11 | ± | 1 | 27 | ± | 5 |
| 6 | 9.9 | ± | 0.5 | 61 | ± | 15 | 10 | ± | 1 | 61 | ± | 17 |
| 7† | 11 | ± | 1 | 68 | ± | 54 | 13 | ± | 3 | 75 | ± | 61 |
| 8† | 4.6 | ± | 0.4 | 34 | ± | 29 | 5 | ± | 1 | 35 | ± | 30 |
| 9† | 10.2 | ± | 0.2 | 44 | ± | 5 | 11.4 | ± | 0.4 | 47 | ± | 6 |
| 9 - (1 to 8)†‡ | 11 | ± | 1 | 37 | ± | 11 | 12 | ± | 1 | 40 | ± | 12 |

† - denotes Br$\gamma$ was detected in this region.

‡ - The smaller regions, 1 through 8, have been subtracted from the line fluxes measured in region 9.

emission was detected, which was due to overlapping with the stellar PSF. Region 9 $r_{21}$ and $r_{32}$ ratios are $11.4 \pm 0.4$ and $47 \pm 6$, respectively. When Regions 1 through 8 are subtracted from Region 9 the ratios of $12 \pm 1$ and $40 \pm 12$ for the $r_{21}$ and $r_{32}$ ratios are obtained, respectively.

All extracted regions show ratios which are consistent with shocks or high density fluoresced gas; however, regions 7 and 8 have large errors in the $r_{32}$ ratio and could indicate a fluoresced or shocked gas.

### 6.4.3 Rotational and vibrational temperatures

The vibrational and rotational temperatures were calculated using Equation 3.28 in Chapter 3. The vibrational temperatures were calculated using the 1-0 S(1), 2-1 S(1) and 3-2 S(1) lines between the $v = 1$ to $v = 2$ and $v = 1$ to $v = 3$ vibrational transitions, and are displayed in Table 6.3. The rotational temperatures for the 1-0 S, 2-1 S and 3-2 S transitions were calculated using the 1-0 S(0) and 1-0 S(2), 2-1

S(0) and 2-1 S(2), and 3-2 S(1) and 3-2 S(3) lines, respectively, and are displayed in Table 6.4. The rotational lines for the Q-branch transitions have not been used due to the opaque nature of the atmosphere beyond 2.4 μm.

The effect of extinction on these temperatures is noticeable, but small. In Table 6.3 and Table 6.4 the corrected and uncorrected lines are directly compared. The majority of vibrational temperatures decrease as they are corrected for extinction and the rotational temperatures increase. The following explicitly discusses temperatures derived from emission lines corrected for extinction in the extracted regions (Fig. 6.19).

In all regions the vibrational temperatures from $v = 1$ to $v = 3$ are greater than $v = 1$ to $v = 2$. The vibrational temperatures for $v = 1$ to $v = 2$ range from $1966 \pm 26$ K (Region 1) to $2970 \pm 69$ K (Region 16). The inner $H_2$ morphological features, Regions 1 through 8, show vibrational temperatures ranging from $1966 \pm 26$ K to $2267 \pm 36$ K, while Region 17 has a vibrational temperature of $2083 \pm 26$ K. In the outer regions, 9 throgh 16, vibrational temperatures are higher. They start from $2219 \pm 31$ K to $2970 \pm 69$ K.

The $v = 1$ to $v = 3$ vibrational temperatures range from $2757 \pm 37$ K (Region 1) to a maximum $6504 \pm 138$ K (Region 15). The inner regions, 1 through 8, show values from $2757 \pm 37$ K to a maximum of $3520 \pm 50$ K. The outer regions, 9 through 16, have temperatures from $3808 \pm 46$ K to $6504 \pm 138$ K. It is clear that the inner regions have a lower vibrational temperature than the outer part of the nebula for the $v = 1$ to $v = 2$ and $v = 1$ to $v = 3$ transitions.

The rotational temperatures can be obtained for the 1-0 S, 2-1 S and 3-2 S transitions. In the majority of regions the highest rotational temperatures are in the 1-0 S transitions, where the temperatures range from $1032 \pm 35$ K (Region 11) to $2176 \pm 234$ K (region 5). The 2-1 S rotational temperatures are similar to the 3-2 S temperatures. The 2-1 S temperatures range from $485 \pm 46$ K (Region 5) to

1278±162 K region (Region 2) and 3-2 S from 681±24 K (Region 15) to 2602±335 K (Region 8).

When a gas is excited by fluorescence, the higher vibrational states are over populated and the vibrational temperature is greater than the rotational temperature (Rudy et al. 2001, $T_{\rm rot} \ll T_{\rm vib}$). Black & van Dishoeck (1987) compared the emission lines of a fluorescent gas to a thermal gas in the 2 - 2.5 μm region ($K$-band). They found that $T_{\rm vib}$ was approximately 6000 to 9000 K for levels $v \geq 2$ and the $T_{\rm rot}$, for $v = 1$ ranged from 400 to 1000 K. In shocks the vibrational and rotational temperatures are similar ($T_{\rm rot} \sim T_{\rm vib}$). Smith et al. (1997) state that shock theory predicts vibrational temperatures are greater than rotational temperatures in a bow shock. Overall, $T_{\rm rot} < T_{\rm vib}$, with the highest vibrational temperatures in the axial, lobe and tail regions. This suggests fluorescence is a significant component in the excitation mechanism. The temperatures in the equatorial regions indicate shocks are a significant component in the excitation mechanism.

### 6.4.4 Ortho-para ratio

The OPR is another diagnostic tool for uncovering the excitation mechanisms in $H_2$. Molecular Hydrogen is made of two identical atoms, the nuclei of which can have a parallel or anti-parallel spin. If the component nuclei have anti-parallel spins then the hydrogen molecule is in the para state. If the nuclei have parallel spins, then the hydrogen molecule is in the ortho state. The ortho state is a higher energy state than the para state. If a gas is shocked, the OPR will reach the equilibrium value of three. A PDR, where $H_2$ is fluoresced, can exhibit an OPR range of 1.3-2.3 (Chrysostomou 1993; Chrysostomou et al. 1993). In the case of *IRAS* 1930+1407 all regions have an OPR close to the value of 3 for the 1-0 S transitions. Region 16 has the lowest OPR value of $2.4 \pm 0.1$ and Region 8 has the highest value of $3.1 \pm 0.1$. The 2-1 S and the 3-2 S values are lower than the 1-0 S OPR values in all regions.

Table 6.3: The gas vibrational temperatures, $T_{\rm vib}$, between the $v = 1$ to $v = 2$ and $v = 1$ to $v = 3$ vibrational levels, calculated from 1-0 S(1) & 2-1 S(1) and 1-0 S(1) and 3-2 S(1) lines, respectively, with $1\sigma$ errors displayed, which are uncorrected and corrected for extinction.

| Region | Uncorrected for extinction | | | | | | Corrected for extinction | | | | | |
|---|---|---|---|---|---|---|---|---|---|---|---|---|
| Number | v = 1 to v = 2 | | | v =1 to v = 3 | | | v = 1 to v = 2 | | | v =1 to v = 3 | | |
| 1 | 2014 | ± | 12 | 2853 | ± | 31 | 1966 | ± | 26 | 2757 | ± | 37 |
| 2 | 2078 | ± | 18 | 2886 | ± | 48 | 2027 | ± | 30 | 2788 | ± | 50 |
| 3 | 2090 | ± | 14 | 3067 | ± | 29 | 2038 | ± | 28 | 2957 | ± | 37 |
| 4 | 2119 | ± | 16 | 3009 | ± | 36 | 2066 | ± | 29 | 2903 | ± | 41 |
| 5 | 2216 | ± | 68 | 3591 | ± | 115 | 2158 | ± | 70 | 3442 | ± | 111 |
| 6 | 2227 | ± | 14 | 3457 | ± | 25 | 2168 | ± | 31 | 3319 | ± | 40 |
| 7 | 2331 | ± | 21 | 3676 | ± | 37 | 2267 | ± | 36 | 3520 | ± | 50 |
| 8 | 2237 | ± | 23 | 3603 | ± | 47 | 2178 | ± | 35 | 3452 | ± | 56 |
| 9 | 2358 | ± | 11 | 4166 | ± | 18 | 2293 | ± | 33 | 3966 | ± | 49 |
| 10 | 2321 | ± | 12 | 4153 | ± | 21 | 2257 | ± | 32 | 3955 | ± | 49 |
| 11 | 2652 | ± | 17 | 4976 | ± | 28 | 2569 | ± | 42 | 4694 | ± | 69 |
| 12 | 2280 | ± | 11 | 3992 | ± | 19 | 2219 | ± | 31 | 3808 | ± | 46 |
| 13 | 2956 | ± | 26 | 5277 | ± | 47 | 2854 | ± | 54 | 4961 | ± | 83 |
| 14 | 2722 | ± | 20 | 5056 | ± | 40 | 2635 | ± | 45 | 4765 | ± | 75 |
| 15 | 2947 | ± | 38 | 7059 | ± | 74 | 2846 | ± | 59 | 6504 | ± | 138 |
| 16 | 3081 | ± | 48 | 6690 | ± | 87 | 2970 | ± | 69 | 6189 | ± | 134 |
| 17 | 2137 | ± | 7 | 3158 | ± | 14 | 2083 | ± | 26 | 3041 | ± | 30 |

Region 17 shows that the 1-0 S, 2-1 S and 3-2 S OPR values are $2.9 \pm 0.1$, $2.3 \pm 0.1$ and $2.9 \pm 0.1$, respectively. The OPRs suggest that equatorial regions are shocked, whilst the axial regions show a mixture of shocks and fluorescence, and the outer regions show fluorescence.

Table 6.4: A summary of the determined properties from each extracted region, which includes: the ro-vibrational emission branch; gas rotational excitation temperatures, $T_{rot}$, for each measurable branch, and the ortho-para ratio, o-p, uncorrected and corrected for extinction.

| Region | Branch | $T_{rot}$ Uncorrected for extinction (K) | o-p ratio Uncorrected for extinction | $T_{rot}$ Corrected for extinction (K) | o-p ratio Corrected for extinction |
|---|---|---|---|---|---|
| 1 | 1-0 S | 1177 ± 11 | 2.91 ± 0.02 | 1331 ± 57 | 2.9 ± 0.1 |
| | 2-1 S | 966 ± 55 | 2.5 ± 0.2 | 1063 ± 74 | 2.5 ± 0.2 |
| | 3-2 S | 1081 ± 73 | 2.4 ± 0.2 | 1168 ± 92 | 2.4 ± 0.3 |
| 2 | 1-0 S | 1308 ± 20 | 2.90 ± 0.03 | 1502 ± 75 | 2.9 ± 0.1 |
| | 2-1 S | 1116 ± 124 | 2.8 ± 0.3 | 1248 ± 162 | 2.9 ± 0.3 |
| | 3-2 S | 1076 ± 114 | 3.3 ± 0.6 | 1162 ± 137 | 3.2 ± 0.6 |
| 3 | 1-0 S | 1349 ± 13 | 2.89 ± 0.02 | 1556 ± 78 | 2.9 ± 0.1 |
| | 2-1 S | 902 ± 47 | 2.5 ± 0.1 | 986 ± 63 | 2.5 ± 0.2 |
| | 3-2 S | 958 ± 53 | 3.7 ± 0.4 | 1026 ± 66 | 3.7 ± 0.4 |
| 4 | 1-0 S | 1256 ± 14 | 2.87 ± 0.02 | 1433 ± 67 | 2.9 ± 0.1 |
| | 2-1 S | 895 ± 53 | 2.3 ± 0.2 | 977 ± 70 | 2.3 ± 0.2 |
| | 3-2 S | 1155 ± 84 | 2.5 ± 0.2 | 1255 ± 106 | 2.4 ± 0.2 |
| 5 | 1-0 S | 1791 ± 123 | 2.9 ± 0.1 | 2176 ± 234 | 3.0 ± 0.2 |
| | 2-1 S | 463 ± 41 | 1.4 ± 0.3 | 485 ± 46 | 1.5 ± 0.3 |
| | 3-2 S | 739 ± 114 | 6 ± 2 | 779 ± 128 | 6 ± 2 |
| 6 | 1-0 S | 1254 ± 16 | 2.85 ± 0.03 | 1432 ± 67 | 2.9 ± 0.1 |
| | 2-1 S | 995 ± 44 | 2.11 ± 0.10 | 1098 ± 65 | 2.1 ± 0.1 |
| | 3-2 S | 955 ± 38 | 2.31 ± 0.15 | 1022 ± 50 | 2.3 ± 0.2 |
| 7 | 1-0 S | 1154 ± 18 | 2.77 ± 0.04 | 1302 ± 58 | 2.8 ± 0.1 |
| | 2-1 S | 914 ± 50 | 2.07 ± 0.13 | 1000 ± 67 | 2.1 ± 0.2 |
| | 3-2 S | 869 ± 45 | 2.15 ± 0.19 | 925 ± 55 | 2.1 ± 0.2 |
| 8 | 1-0 S | 1185 ± 19 | 2.83 ± 0.04 | 1343 ± 61 | 2.8 ± 0.1 |
| | 2-1 S | 1109 ± 110 | 2.4 ± 0.2 | 1239 ± 145 | 2.4 ± 0.2 |
| | 3-2 S | 2207 ± 211 | 4.0 ± 0.5 | 2602 ± 335 | 4.0 ± 0.5 |
| 9 | 1-0 S | 989 ± 8 | 3.04 ± 0.03 | 1097 ± 39 | 3.1 ± 0.1 |
| | 2-1 S | 976 ± 21 | 1.63 ± 0.04 | 1075 ± 43 | 1.6 ± 0.1 |
| | 3-2 S | 968 ± 17 | 1.79 ± 0.04 | 1037 ± 33 | 1.8 ± 0.1 |

Continued on next page

**Table 6.4 – continued from previous page**

| Region | Branch | $T_{rot}$ Uncorrected for extinction (K) | o-p ratio Uncorrected for extinction | $T_{rot}$ Corrected for extinction (K) | o-p ratio Corrected for extinction |
|---|---|---|---|---|---|
| 10 | 1-0 S | 1062 ± 10 | 2.95 ± 0.03 | 1187 ± 46 | 3.0 ± 0.1 |
| | 2-1 S | 748 ± 15 | 1.51 ± 0.05 | 805 ± 26 | 1.5 ± 0.1 |
| | 3-2 S | 885 ± 19 | 1.90 ± 0.06 | 943 ± 30 | 1.9 ± 0.1 |
| 11 | 1-0 S | 937 ± 10 | 2.92 ± 0.04 | 1032 ± 35 | 2.9 ± 0.1 |
| | 2-1 S | 848 ± 19 | 1.45 ± 0.04 | 922 ± 34 | 1.5 ± 0.1 |
| | 3-2 S | 829 ± 16 | 1.87 ± 0.06 | 879 ± 26 | 1.9 ± 0.1 |
| 12 | 1-0 S | 1113 ± 10 | 2.94 ± 0.02 | 1250 ± 50 | 3.0 ± 0.1 |
| | 2-1 S | 808 ± 17 | 1.61 ± 0.05 | 875 ± 30 | 1.6 ± 0.1 |
| | 3-2 S | 871 ± 19 | 2.5 ± 0.1 | 926 ± 30 | 2.5 ± 0.2 |
| 13 | 1-0 S | 1013 ± 12 | 2.56 ± 0.03 | 1125 ± 42 | 2.6 ± 0.1 |
| | 2-1 S | 749 ± 17 | 1.50 ± 0.05 | 806 ± 28 | 1.5 ± 0.1 |
| | 3-2 S | 739 ± 18 | 1.93 ± 0.08 | 779 ± 25 | 1.9 ± 0.1 |
| 14 | 1-0 S | 1111 ± 15 | 2.67 ± 0.03 | 1249 ± 52 | 2.7 ± 0.1 |
| | 2-1 S | 782 ± 18 | 1.31 ± 0.05 | 844 ± 30 | 1.3 ± 0.1 |
| | 3-2 S | 722 ± 19 | 2.2 ± 0.1 | 760 ± 25 | 2.1 ± 0.1 |
| 15 | 1-0 S | 1042 ± 21 | 2.45 ± 0.05 | 1161 ± 50 | 2.5 ± 0.1 |
| | 2-1 S | 698 ± 16 | 0.87 ± 0.04 | 747 ± 25 | 0.88 ± 0.05 |
| | 3-2 S | 650 ± 19 | 1.28 ± 0.05 | 681 ± 24 | 1.3 ± 0.1 |
| 16 | 1-0 S | 961 ± 24 | 2.4 ± 0.1 | 1062 ± 46 | 2.4 ± 0.1 |
| | 2-1 S | 831 ± 23 | 0.82 ± 0.04 | 902 ± 36 | 0.83 ± 0.05 |
| | 3-2 S | 923 ± 28 | 1.21 ± 0.04 | 986 ± 39 | 1.2 ± 0.1 |
| 17 | 1-0 S | 1265 ± 6 | 2.86 ± 0.01 | 1446 ± 66 | 2.9 ± 0.1 |
| | 2-1 S | 901 ± 22 | 2.30 ± 0.06 | 985 ± 39 | 2.3 ± 0.1 |
| | 3-2 S | 1089 ± 27 | 2.9 ± 0.1 | 1177 ± 46 | 2.9 ± 0.1 |

## 6.5 Discussion

The two mechanisms that are considered to excite $H_2$ in the CSE of post-AGB stars are either shocks or fluorescence (e.g. Kelly & Hrivnak 2005; Davis et al. 2003; Burton et al. 1992, and references within). Cox et al. (1997) present an example of using $H_2$ to discern between shocks and fluorescence in two post-AGB objects: AFGL 2688 and NGC 7027. However, Davis et al. (2003) show that some post-AGB/PNe show a mixture of both excitation mechanisms. Therefore it is expected that *IRAS* 19306+1407 will show a mixture of both mechanisms.

$H_2$ molecules can be fluoresced by UV photons between 6 eV to 13.6 eV (912 - 2068 Å), which are commonly emitted from OB stars and hot white dwarfs. The measured UV flux, $G_0$, is given in multiples of the value observed in the interstellar medium (ISM), where $G_0 = 1$ is equivalent to $1.6 \times 10^{-6}$ W m$^{-2}$ sr$^{-1}$ (Habing 1968). Typically, fluorescence populates the higher ro-vibrational transitions ($v \geq 2$) before populating the lower transitions ($v \leq 1$).

A shock can be categorised as either a jump shock (J-shock) or a continuous shock (C-shock). The key difference between these types lies in their hydrodynamical properties. A J-shock will show a significant change in temperature, gas particle speed and density etc over a distance, which is comparable to the mean free path (MFP) of a gas particle. Typically J-shocks disassociate $H_2$ at speeds greater than 25 to 30 km s$^{-1}$ and partially disassociate $H_2$ below those speeds (Burton et al. 1992). A C-shock is the collision of charged and neutral particles, which is affected by the associated magnetic field ($B$-field) strength. Draine (1980) shows in his figure 1, a simple schematic of the difference between a C-shock and J-Shock as a function of particle velocity with respect to its position within the shock. C- and J-shocks populate the lower ro-vibrational transitions ($v \leq 1$) before populating the higher transitions ($v \geq 2$).

### 6.5.1 Models

There has been extensive work on models for the excitation of $H_2$ in star formation regions and PDRs, which are divided between shocks or fluorescence models. The fluorescence models considered in this chapter are taken from Black & van Dishoeck (1987, model 14) and Burton et al. (1990). Black & van Dishoeck (1987) investigate the effect of UV photons on interstellar clouds of low density and found that the line intensities depend *"primarily on the density in the cloud and the strength of the incident ultraviolet radiation."* The calculated line ratios, for lines from 28- to 0.7-μm, are stated in their table 3 and have been used in Kelly & Hrivnak (2005), Davis et al. (2003), Cox et al. (1997) and Fernandes, Brand & Burton (1997). The model has a number density[4] of $3 \times 10^3$ cm$^{-3}$ and a UV flux of $10^3$ $G_0$. Burton et al. (1990) only state ratios for 1-0 S(1)/2-1 S(1) (their figure 10) and model intensities for the 1-0 S(1), 2-1 S(1), 3-2 S(3) and 4-3 S(3) $H_2$ ro-vibrational lines[5]. They have extended the PDR model from Burton, Hollenbach & Tielens (1989) to include a more detailed treatment of the CO and $H_2$ molecules and explored densities of $10^3$-$10^7$ cm$^{-3}$ in UV fields of $10^3$-$10^5$ $G_0$.

Various shock models have attempted to account for $H_2$ lines seen in astrophysical systems and are typically classified into C- and J-shocks. These types of shocks can be treated as planar shocks (Le Bourlot et al. 2002; Wilgenbus et al. 2000; Draine, Roberge & Dalgarno 1983) or bow-shaped shocks (e.g. Smith & Brand 1990a,b,c). The models of Le Bourlot et al. (2002) and Wilgenbus et al. (2000) explore velocities of 10 to 40 km s$^{-1}$ for C-shocks and 5 to 25 km s$^{-1}$ for J-shocks; densities of $10^3$ to $10^7$ cm$^{-3}$, and OPRs of 0.01, 1, 2 and 3. The C- and J-bow shock code of Smith & Brand (1990c, and later papers) has been used to model the emission lines detected by SINFONI.

[4]Any reference to the number density of hydrogen molecules is henceforth referred to as density.
[5]These are used to calculate line ratios

It has not been possible to resolve a shocked region and therefore the bow geometry is fixed as a symmetric parabola and it is assumed that the $B$-field is parallel to the bow axis. A bow shock can be described by radius of the bow, $R$, from the apex and length, $z$, along the bow in cylindrical coordinates,

$$z \propto \frac{R^{b_{\rm s}}}{b_{\rm s}}, \tag{6.1}$$

where the shape of the bow shock is characterised by an exponent, $b_{\rm s}$, where values are greater than 1. A 'blunt' shock is characterised by $b_{\rm s}$ ranging from 1 up to 2, whilst narrow shocks are greater numbers. Smith (1994) states that the $B$-field, $B_0$, can determined by the Alfvén speed, $v_{\rm a}$, number density of gas particles, $n$, and is given by,

$$B_0 = 0.542 \times 10^{-3} \cdot \left(\frac{n}{\rm cm^{-3}}\right)^{1/2} \left(\frac{v_{\rm a}}{\rm kms^{-1}}\right) {\rm mG}. \tag{6.2}$$

It was found that the C-bow shocks were more sensitive to the Alfvén speed than the bow shock shape; conversely, J-bow shocks were more sensitive to the bow shape than the Alfvén speed. A range of density and velocity parameter space has been explored and the model grid is displayed in Table 6.5.

Table 6.5: The model grids for Smith's C- and J-bow shock are displayed in table (a) and (b), respectively. Each model name is a group of models, defined for Alfvén speed (C) or bow shape (J), for which a range of velocities are considered for every density, giving a total number of 700 models.

(a) The model grid for C-bow shocks for Alfvén speeds of 1 to 4 km $s^{-1}$ for densities ranging from $10^3$ to $10^7$, and shock velocities of 10 to 40 km $s^{-1}$ with the separation in velocity given in the parentheses. The magnetic field, in units of milli-Gauss (mG), is calculated for Alfvén speed and density. The bow shape is fixed at a value of 2.

| Model name | $v_a$ (km $s^{-1}$) | Density ($cm^{-3}$) | Velocity (km $s^{-1}$) | $B$-field (mG) | Number of models |
|---|---|---|---|---|---|
| C1 | 1 | $10^3$, $10^4$, $10^5$, $10^6$, $10^7$ | 10-35 [1], 40 | 0.02, 0.06, 0.2, 0.64, 2.03 | 135 |
| C2 | 2 | $10^3$, $10^4$, $10^5$, $10^6$, $10^7$ | 10-35 [1], 40 | 0.04, 0.13, 0.41, 1.28, 4.06 | 135 |
| C3 | 3 | $10^3$, $10^4$, $10^5$, $10^6$, $10^7$ | 10-35 [1], 40 | 0.06, 0.19, 0.61, 1.92, 6.08 | 135 |
| C4 | 4 | $10^3$, $10^4$, $10^5$, $10^6$, $10^7$ | 10-35 [1], 40 | 0.08, 0.26, 0.81, 2.57, 8.11 | 135 |
| | | | | Total number of models | 540 |

(b) The model grid for J-bow shocks for shapes of 1.5 to 4 for densities ranging from $10^3$ to $10^7$, and shock velocities of 10 to 40 km $s^{-1}$ with the separation in velocity given in the parentheses. The Alfvén speed is fixed at 2 km $s^{-1}$.

| Model name | $b_s$ | Density ($cm^{-3}$) | Velocity (km $s^{-1}$) | Number of models |
|---|---|---|---|---|
| J1 | 1.5 | $10^3$, $10^4$, $10^5$, $10^6$, $10^7$ | 5, 10-15 [1], 20-30 [5], 40-60 [10] | 65 |
| J2 | 2 | $10^3$, $10^4$, $10^5$, $10^6$, $10^7$ | 5, 10-15 [1], 20-30 [5], 40-60 [10] | 65 |
| J3 | 3 | $10^3$, $10^4$, $10^5$, $10^6$, $10^7$ | 5, 10-15 [1], 20-30 [5], 40-60 [10] | 65 |
| J4 | 4 | $10^3$, $10^4$, $10^5$, $10^6$, $10^7$ | 5, 10-15 [1], 20-30 [5], 40-60 [10] | 65 |
| | | | Total number of models | 260 |

### 6.5.2 $H_2$ velocity

The measured line of sight velocity ($v_{\rm los}$) can be used to measure the expansion of the CSE or used in the estimation of shock front speeds. Shock speeds are defined, within this thesis, as pre-shock velocities. If the $H_2$ emission originates from an axial bipolar flow, it is possible to estimate the outflow velocity, $v_{\rm out}$, as a function of $v_{\rm los}$ and the inclination of the system, $i$,

$$v_{\rm out} = \frac{v_{\rm los}}{\sin(i)} \tag{6.3}$$

In the bipolar lobes the $v_{\rm los}$ ranges from +10 to -15 km s$^{-1}$ (Fig. 6.17 left) and the maximum inclination of the system was estimated to be 10° (Chapter 5). This gives a lower limit to the outflow velocity of +58 to -86 km s$^{-1}$. The inner part of the CSE shows a more complex kinematic structure (Fig. 6.17 centre & right). The $v_{\rm los}$ ranges from +5 to -5 km s$^{-1}$, which cannot be corrected using the inclination of the system.

### 6.5.3 The central star

*IRAS* 19306+1407 has a bright central source that is visible in the optical through to the near infrared (Sahai et al. 2007; Lowe & Gledhill 2005, Chapter 5), with a spectral type approximating to B1, 21000 ± 1000K (Lowe & Gledhill 2005, Chapter 5). Utilizing the parameters and the Kurucz profile for the central illumination source in Chapter 5, it is possible to estimate the factor of $G_0$ at the inner radius of the CSE. The UV flux from the Kurucz model, integrated between 912 - 2068 Å, is equal to $4.54 \pm 0.04 \times 10^7$ W m$^{-2}$. The estimated UV flux at the inner radius, $1.9 \pm 0.1 \times 10^{14}$ m, emitted by a star of radius, 3.8±0.6 R$_\odot$, is equal to $8.7 \pm 1.5 \times 10^{-3}$ W m$^{-2}$, which is equivalent to $5.4 \pm 0.9 \times 10^3$ G$_0$. This method assumes that there is no attenuating medium between the star and the inner radius, which can decrease

the UV flux to $\sim 2 \times 10^3$ $G_0$ for an $A_V = 1$ mag, using the reddening relationship from Cardelli et al. (1989).

The Br$\gamma$ emission is coincident with the continuum emission peak (Fig. 6.13) with no detected emission from the $H_2$ features (i.e. the bright arcs). This line is not as attenuated by extinction as the stronger H$\alpha$ line; however, the Br$\gamma$ emission can be two orders of magnitude fainter than the H$\alpha$ emission. Sahai & Contreras (2004) detected broadened H$\alpha$ with wide emission wings and suggested an outflow velocity of $\sim 2300$ km s$^{-1}$. There has been no published photometry or flux measurement of the H$\alpha$ line. The SINFONI spectra shows wings to the Br$\gamma$ emission line; however, upon inspection of the arc lines and the SINFONI manual (Dumas 2007), it is likely that these wings are an artefact of the SINFONI instrument.

There are two possible mechanisms for stimulating the photo-ionisation emission, these being a fast dissociating shock or ionisation of the material by the star. The measured Br$\gamma$ flux within the inner radius ($\sim 0.5$ arcsec) is $\sim 2.4 \times 10^{-16}$ W m$^{-2}$. Using the J-shock results from Hollenbach & McKee (1989), a gas density of $10^6$ and $10^7$ cm$^{-3}$ with pre-shock velocities of 100 and 60 km s$^{-1}$, respectively, are required to reproduce the observed flux. These velocities are significantly lower than those indicated by the H$\alpha$ emission.

Kwok (2000, p30) specifies that the observed Br$\gamma$ intensity, $I_{B\gamma}$, within an optically thin post-AGB shell with a radius, $R$, at a distance, $D$, with an electron and proton number density, $n_e$ and $n_p$, respectively, and a filling factor of order unity, $\epsilon$, is given by

$$I_{B\gamma} = E_{H\beta} f_{Br\gamma} n_e n_p \left( \frac{R^3 \epsilon}{3D^2} \right) \text{erg cm}^{-2} \text{ s}^{-1}. \tag{6.4}$$

The power in the $H_\beta$ transition, $E_{H\beta}$, and the relative energy factor for the Br$\gamma$ transition, $f_{Br\gamma}$, have been taken from Hummer & Storey (1987, table 8). Assuming

that $n_{\rm e} \sim n_{\rm p}$ and a radius of 0.5 arcsec at a distance of 2.7 kpc, gives a number density of protons and electrons $\sim 10^4$ cm$^{-3}$ with an electron temperature of $\sim 10^4$ K.

The upper limit of the total number of ionising photons can be estimated from Kurucz model atmospheres, which are scaled with respect to the radius of the star and its distance, by integrating the flux short-ward of 912.2 Å and dividing by the energy of an 13.6 eV ionising photon. A B1I and B0I star of radius 3.8 $R_{\odot}$ and at a distance of 2.7 kpc give values of $\sim 4.5 \times 10^3$ and $\sim 2.5 \times 10^5$ photons m$^{-2}$ s$^{-1}$, respectively. These values do not include the effects of CSE or ISM extinction. A total of $\sim 2.6 \times 10^3$ photons m$^{-2}$ s$^{-1}$ is measured from the Br$\gamma$ emission, which is comparable to the number of ionising photons from a B1I star. However, a B0I star is more likely than a B1I star to produce sufficient ionising photons, which can account for of the Br$\gamma$ recombination emission. Nevertheless, a B0I illumination source cannot replicate the SED, when used as an input spectrum in the DART modelling (see Chapter 5). Therefore, some of the Br$\gamma$ photons could originate from a B1I star with additional energy supplied from an another excitation mechanism, such as shocks, alternatively the required ionising photons could be produced by an illumination source between B1I and B0I.

It is not possible to differentiate between the two mechanisms generating the Br$\gamma$ emission with the SINFONI and UIST IFS observations. An optical spectrum, higher spatial and spectral resolution observations of the H$\alpha$, and other atomic hydrogen recombination lines, are required to independently confirm the spectral type of *IRAS* 19306+1407, and the excitation mechanism that is responsible for the photo-ionisation.

### 6.5.4 Line ratios

The comparison of different $H_2$ ro-vibrational lines can uncover the excitation mechanism (See Chapter 3). The most commonly used line pairs are the $r_{21}$ and the $r_{32}$[6]. In a low density gas and low FUV environments, low ratios of $\sim 2$ and $\sim 8$ for the $r_{21}$ and $r_{32}$ ratios, respectively, indicate that the gas is undergoing fluorescence (Black & van Dishoeck 1987). The higher ratios of $\gtrsim 10$ and $\sim 10 - 100$ for the $r_{21}$ and $r_{32}$ ratios, respectively, indicate shocks. However, at high densities and higher levels of UV radiation, the fluorescent ratios increase as lower energy levels are populated. Burton et al. (1990) state that $r_{21}$ and $r_{32}$ remain around 2 and 8, respectively, for $G_0 = 10^3$ with densities up to $n = 10^7$ cm$^{-3}$. The $r_{21}$ ratio reaches values of $\sim$8 and $\sim 10$ for $G_0 = 10^4$ and densities $10^6$ and $10^7$ cm$^{-3}$, respectively. The maximum value is approximately 18 for $G_0 = 10^5$ at a density of $10^6$ cm$^{-3}$, which drops to a value of 11 at $10^7$ cm$^{-3}$. The $r_{32}$ has a value around 20 for $G_0 = 10^5$ at a density of $10^5$ cm$^{-3}$ and increases to a value $\sim 40$ at densities $10^6$ to $10^7$ cm$^{-3}$. In an intense UV field of $G_0 = 10^5$, the $r_{32}$ value reaches a maximum of 130 and drops to 60 for densities of $10^6$ to $10^7$ cm$^{-3}$, respectively. Therefore, a dense gas subjected to an intense UV field can produce line ratios that mimic shock values. Hollenbach & Natta (1995) show the $r_{21}$ ratio can change over time as the UV excites the CSE.

The likelihood of fluorescence and shocks as excitation mechanisms, ascertained using the $r_{21}$ ratio calculated from Burton et al. (1992) and Burton et al. (1990), are considered below:

- **Fluorescence:** A dense $H_2$ gas, $n_0 = 10^7$ cm$^{-3}$, subjected to UV field of $G_0 = 10^3$ and $10^4$ yields a $r_{21}$ value of $\sim$1.7 and $\sim$7.8, respectively. Higher ratios are possible with an intense UV field of $10^5$ $G_0$, but this does not correspond

[6]The ratio convention varies from paper to paper. For example Davis et al. (2003); Fernandes et al. (1997); Burton et al. (1990) use the 1-0 S(1) as the numerator and Hollenbach & Natta (1995) use 1-0 S(1) as a denominator.

to the calculated UV field of $5.4 \pm 0.9 \times 10^3$ $G_0$ at the inner radius. The values of $r_{21}$ in Fig. 6.17 are greater than those predicted for a UV field of $10^3$ $G_0$. The green areas could correspond to a dense region, $10^7$ cm$^{-3}$, and a high UV field of $10^4$ $G_0$, whilst red/orange colours and yellow areas are above the fluorescence value. The extinction corrected $r_{21}$ values extracted from the Regions, stated in Table 6.1, show that Regions 11 and 13 to 16 are within fluorescence values for $n_0 = 10^7$ cm$^{-3}$ and $G_0 = 10^4$. The only sub-arcsecond extracted region that shows a fluorescence value is Region 8 (Burton et al. 1990, 1992).

- *Slow* **J-shock:** The $r_{21}$ ratio will reach a value of $\sim 2$ for shock velocities greater than 20 km s$^{-1}$ at densities of $10^4$ and $10^6$ cm$^{-3}$. Larger ratios of 11 and 4 are achieved with lower velocities $\leq 12$ km s$^{-1}$ at densities of $10^4$ and $10^6$ cm$^{-3}$, respectively (Burton et al. 1992). These velocities are lower than the minimum speed required for dissociating shocks .

- *Fast* **C-shock:** For a density of $10^4$ cm$^{-3}$ it is possible to achieve ratios of $\sim 11$ to $\sim 18$ for velocities ranging from 45 to 35 km s$^{-1}$, respectively. In Figure 6.17 the yellow areas would relate to a shock velocity of 45 km s$^{-1}$ and the orange/red areas to a velocity of 40 to 35 km s$^{-1}$. For a density of $10^6$ cm$^{-3}$ the ratios are very sensitive to shock velocity over a small dynamic range. The ratios range between $\sim 17.5$ to $\sim 10$ for shock velocities of 30 to 33 km s$^{-1}$, respectively. For greater velocities the C-shock would become a J-shock (Burton et al. 1992).

Using only the $r_{21}$ value and the estimate for the UV field suggest that fluorescence within the bright scattering arcs, even if the density is high, is *not* the dominant excitation mechanism. In the axial and outer parts of the nebula, fluorescence is a possible $H_2$ excitation mechanism, but a dense gas is required. The J- and C-

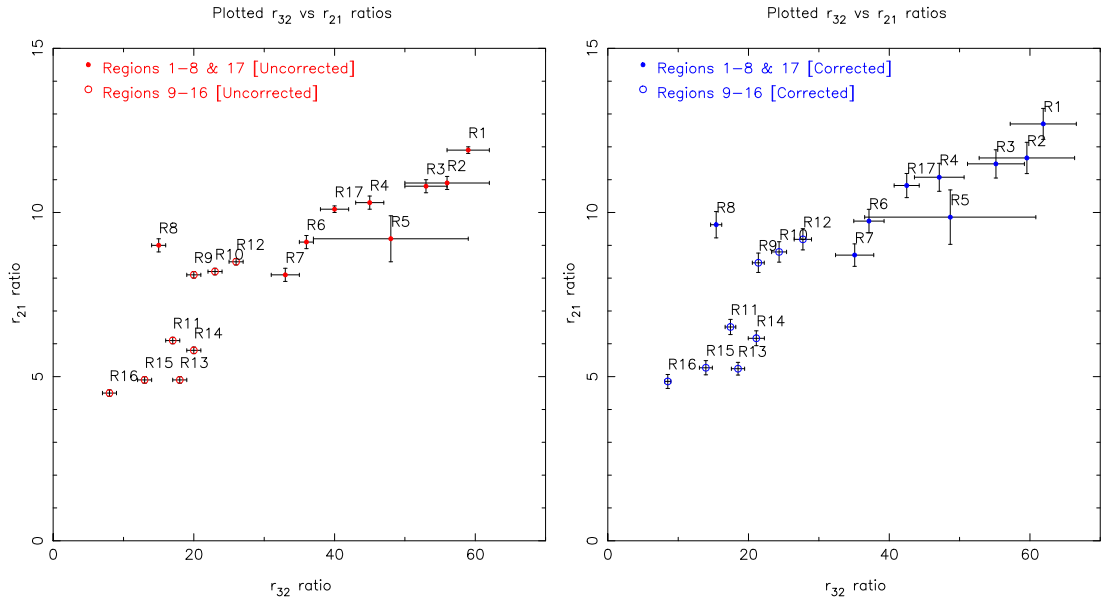


(a) Ratio values for regions uncorrected for extinction

(b) Ratio values for regions corrected for extinction

Figure 6.21: The $r_{21}$ and $r_{32}$ ratios for each region when uncorrected (a) and corrected (b) for extinction. Each point is annotated with Region number, prefixed with the letter R, right and up from the point. The uncorrected values are marked by red points and the corrected values with blue points. Regions 1 through to 8 and including 17 are marked by filled circles and the regions 9 to 16 are marked with open circles. The error bars are displayed at $1\sigma$ values.

shock velocities predicted by the line ratio are high compared to the measured $v_{\rm los}$ in Fig. 6.15; however, if the outflow velocity is angled close to the plane of the sky, then $v_{\rm los}$ will be low.

The $r_{21}$ ratio cannot discern between J- and C-shocks and the determined densities can vary by at least 2 orders of magnitude. A new diagnostic method is presented in this chapter, which directly compares the $r_{21}$ against the $r_{32}$ (Fig. 6.21). The fluorescent values from Burton et al. (1990) are plotted in Fig. 6.22. The squares, triangles and diamonds indicate FUV fields of $10^3$, $10^4$ and $10^5$ $G_0$, respectively. A polynomial can be fitted to the values and takes the form

$$r_{21} = -7.01 \times 10^{-4} \cdot r_{32}^2 + 0.226 \cdot r_{32}. \qquad (6.5)$$

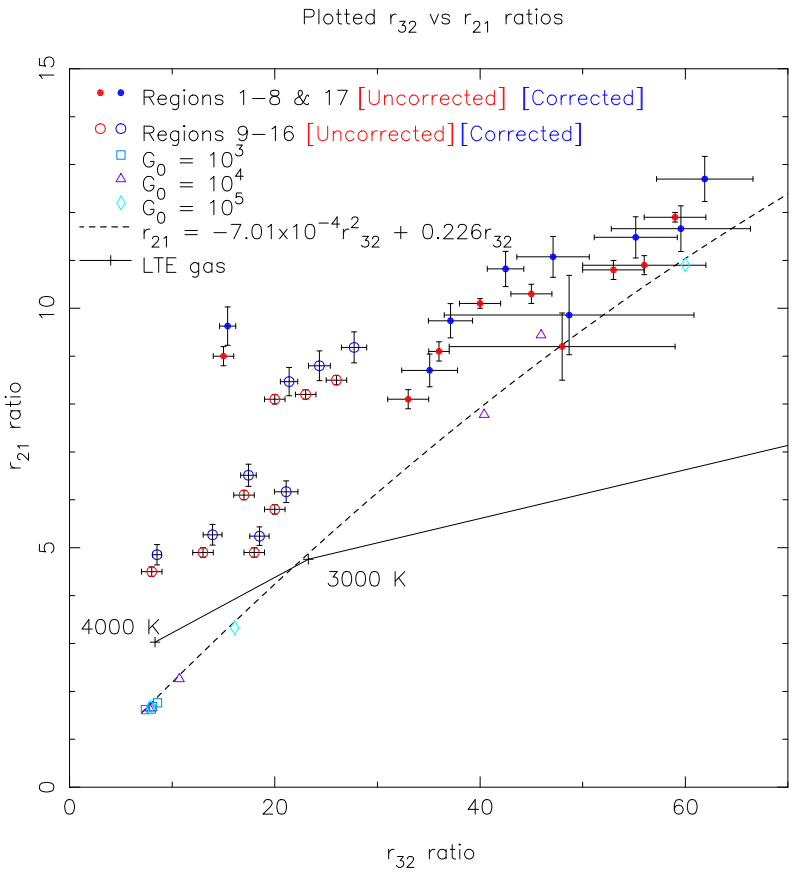


Figure 6.22: The $r_{21}$ and $r_{32}$ ratios for each region, using the same convention as in Fig. 6.21, overplotted with fluorescent ratios for FUV field $10^3$ (light blue squares), $10^4$ (purple triangles) and $10^5$ $G_0$ (cyan diamonds) for densities ranging from $10^3$ through to $10^7$ cm$^{-3}$. The best-fitting polynomial connecting the fluorescent ratios is a thick dashed black line. The ratios for a LTE gas are indicated by a thin solid black line with the temperatures annotated.

The observed points, corrected and uncorrected for extinction, are not situated on the best-fitting fluorescence line, except region 5, which has large associated errors. This strongly rules against fluorescence of a low or high density $H_2$ gas.

The shock models are plotted in Figures 6.23 & 6.24 for densities $10^3$, $10^4$, $10^5$, $10^6$ and $10^7$ cm$^{-3}$. The planar shocks from Wilgenbus et al. (2000) and Le Bourlot et al. (2002) explore velocities 5-25 km s$^{-1}$ and 10-80 km s$^{-1}$, respectively (Fig. 6.23). The C- and J-bow shocks investigate a range of velocities of 10-40 km s$^{-1}$ and 5-60 km s$^{-1}$, respectively (Fig. 6.24). In addition, the shape of bow is investigated for $b_s$ = 1.5 and 2.0 for C-shocks and $b_s$ = 1.5, 2.0, 3.0 and 4.0 for

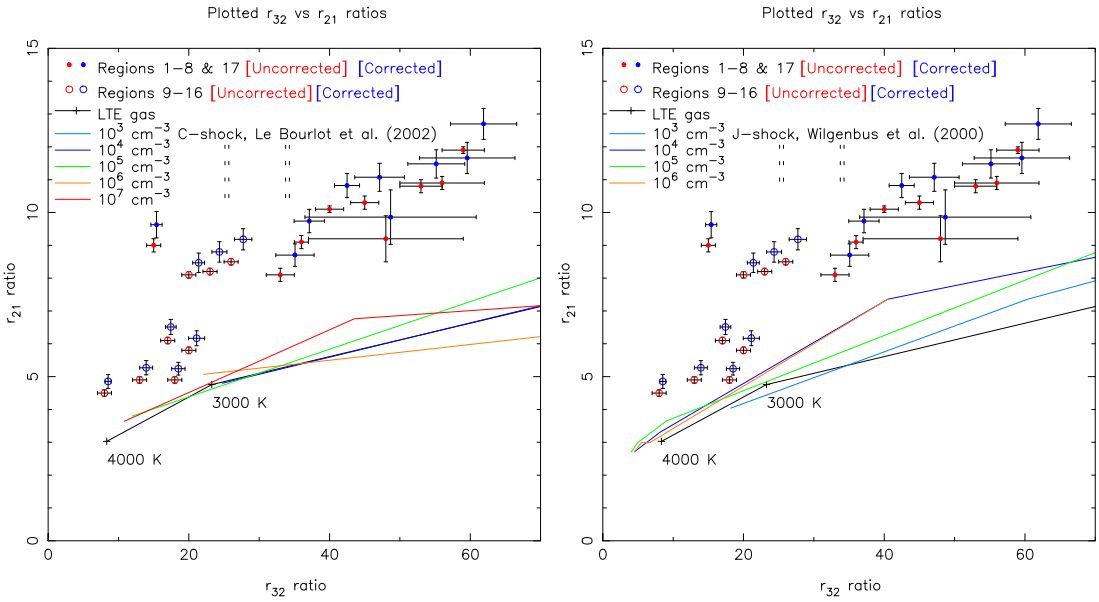


Figure 6.23: The comparison of the J- and C-planar shocks from Le Bourlot et al. (2002) and Wilgenbus et al. (2000), left and right respectively, which are over-plotted with the ratios obtained from the extracted regions. The regions' ratio values are displayed as in Fig. 6.21, with the C-shock and J-shocks as solid lines. The densities $10^3$, $10^4$, $10^5$, $10^6$ and $10^7$ cm$^{-3}$ are displayed as light blue, dark blue, green, orange and red lines, respectively. The ratios for a LTE gas are indicated by a thin solid black line with the temperatures annotated.

J-shocks. The $r_{21}$ and $r_{32}$ ratios decrease as the shock velocity increases, which is caused by a greater proportion of the $H_2$ molecules disassociating. This reduces the ability of the gas to cool the shock and therefore the gas temperature increases, populating the upper energy levels. At larger shock velocities the line ratios become fixed, since the majority of the gas disassociates and higher energy levels are more abundantly populated.

The planar shock models do not fit the observed $r_{21}$ and $r_{32}$ ratios and are similar to the ratios for $H_2$ in LTE. The bow shock models provide better fits to the extracted regions. The best fitting C- and J-bow shocks are situated in the top and bottom panels in Figure 6.24, respectively, with the model parameters displayed in Table 6.5. The regions that have been corrected for extinction are compared to the C- and J-bow shock models in the following paragraphs.

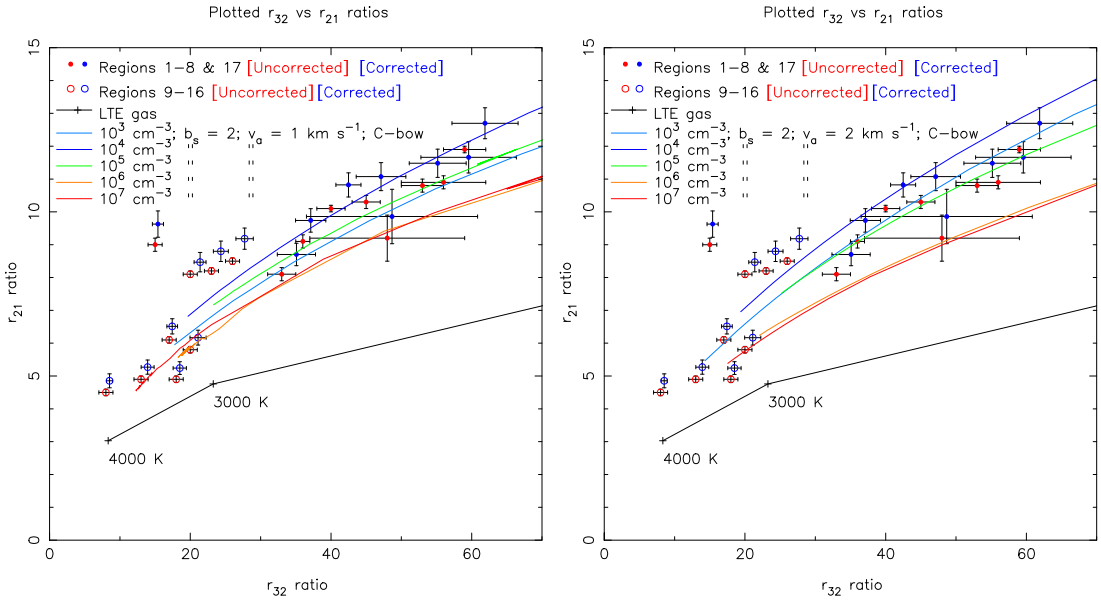


(a) Model C1 (left) and C2 (right)

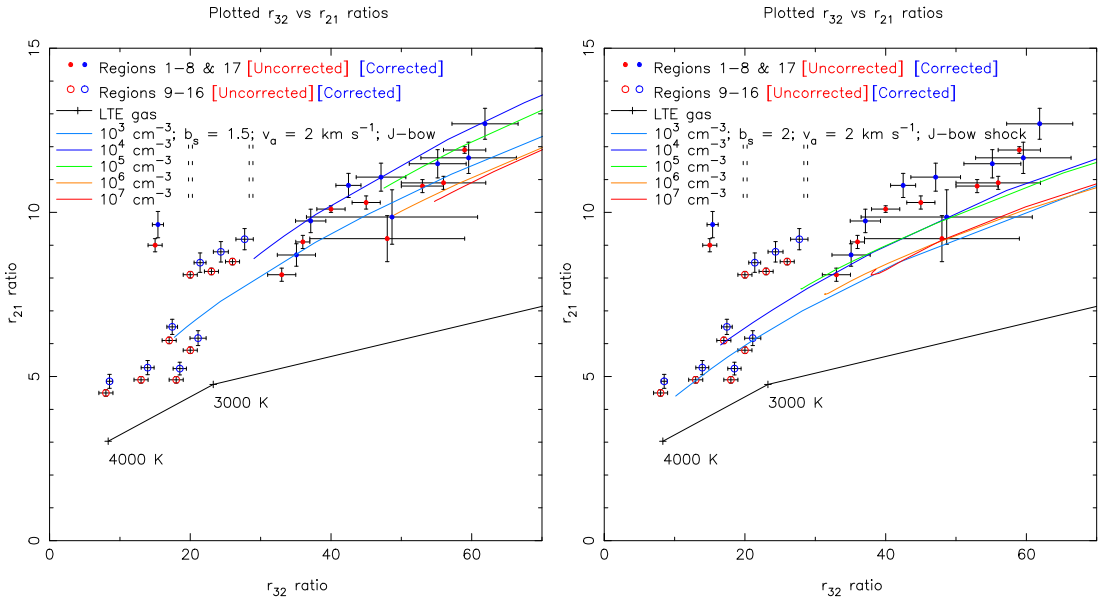


(b) Model J1 (left) and J2 (right)

Figure 6.24: The comparison of bow shock fronts for C- and J-types, top and bottom, respectively, over-plotted with the ratios obtained from the extracted regions. Smith's C-bow and J-bow shocks are displayed top and bottom, respectively. The C-shocks have Alfvén speeds of 1 and 2 km $s^{-1}$ situated on the left and right, respectively. The J-shocks have bow geometry parameters of $b_s = 2$ and 1.5 for left and right panels, respectively. The regions ratio values are displayed the same as in Fig. 6.21, with the C-shock and J-shock as solid lines. The densities $10^3$, $10^4$, $10^5$, $10^6$ and $10^7$ $cm^{-3}$ are displayed as light blue, dark blue, green, orange and red lines, respectively. The ratios for a LTE gas is indicated by a thin solid black line with the temperatures annotated. The $v_a$ in the J-bow shock models is equivalent to the sound speed.

Overall the majority of regions can be fitted with a shock density ranging from $10^3$ to $10^5$ cm$^{-3}$. However, some points have large errors and can fit a large range of densities. The majority of the points cannot be fitted with a high density gas of $10^6$ and $10^7$ cm$^{-3}$, since the points sit above these tracks.

The equatorial and tail regions can be fitted by C- or J-bow shocks with densities ranging from $10^3$ to $10^5$ cm$^{-3}$. The axial regions 8, 9, 10 and 12 cannot be fitted with any of the shock models; however, C- and J-bow shocks with a density of $10^4$ cm$^{-3}$ provided the closest tracks. The central region 5 has very large associated errors and can be fitted by bow shock or fluorescent models. Regions 11 and 13 through to 16 can be fitted by C- and J-bow shocks with densities of $10^6$ and $10^7$ cm$^{-3}$. Region 17 can be fitted with C- and J-bow shocks of a density of $10^4$ and $10^3$ cm$^{-3}$, respectively.

It is clear that this $r_{21}$ versus $r_{32}$ diagnostic rules out $H_2$ emission from dense fluorescing gas and planar C- and J- shocks, in *IRAS* 19306+1407. The equatorial and tail regions are consistent with C- and J-bow shocks. The curved shocks can replicate a greater range of $H_2$ temperatues along the shock front than planar shocks. The emission in axial regions cannot be fitted with *just* C- or J-bow shocks and suggests a possible additional fluorescent component. The outer regions can be fitted with a high density C-bow shock. It is likely that within each extracted region, there is a range of densities and velocities. Unfortunately it is not possible to differentiate between the two types of bow shocks using the $r_{21}$ and $r_{32}$ ratios and to resolve the shock surfaces in *IRAS* 19306+1407. However, the model fits strongly suggest the need for a curved shock surface to explain the observed line ratios. The sub-arcsecond 1-0 S(1) image shows a clumpy or flocculent structure that could indicate unresolved shock fronts associated with the clumps (Fig. 6.14), which might evolve into molecular hydrogen knots such as those seen in the Helix nebula (e.g. Meixner et al. 2005; Hora et al. 2006; Matsuura et al. 2007).

### 6.5.5 $H_2$ excitation temperature and ortho-para ratio

The rotational and vibrational temperatures, $T_{\rm rot}$ and $T_{\rm vib}$, are used as extra diagnostics for excitation mechanism of a $H_2$ gas. A gas that is excited by collisions will equally populate the rotational states within the same vibrational state $T_{\rm rot} = T_{\rm vib}$. This describes a gas in thermal equilibrium. The outer regions 9 through 16 show larger vibrational temperatures that are close to the fluorescent temperatures. It is possible that there is a mix of fluorescence and shocks in these regions.

The bow shocks reach a maximum vibrational and rotational temperature once the $H_2$ molecule starts disassociating. In figures 6.25, 6.26, 6.27 and 6.28 these maximum temperatures are stated for models C1, C2, J1 and J2, respectively.

The vibrational temperatures for the $v = 1$ to $v = 2$ and $v = 1$ to $v = 3$, and the rotational temperatures for the 1-0 S, 2-1 S and 3-2 S transitions can be used to determine the shock velocities. Typically the associated velocities for the observed temperatures are higher for the $v = 1$ to $v = 3$ than the $v = 1$ to $v = 2$ transitions. However, the observed rotational temperatures for 3-2 S and 2-1 S yield lower shock velocities than for the 1-0 S.

The best-fitting C- and J-bow shock models, based on rotational and vibrational temperatures, are given in Table 6.6. The C-bow shocks require greater velocities than for J-bow shocks to replicate the observed rotational and vibrational temperatures, with densities ranging from $10^3$ to $10^4$ cm$^{-3}$. The equatorial regions, southwest bright knot and tails are consistent with C- and J-bow shocks. The vibrational temperatures for the axial, lobe and outer regions are inconsistent with a pure C- or J-bow shock model, so the closest model has been estimated from the rotational temperatures. In the lobes and outer regions the vibrational temperatures are greater than those produced by the bow shock models.

The $r_{21}$ and $r_{32}$ ratios cannot be fitted using C- or J-planar shock models from

Wilgenbus et al. (2000) and Le Bourlot et al. (2002), respectively. The best-fitting results are from the bow shock models, however, it is not possible to differentiate between J and C-shocks. Bains et al. (2004) and Bains et al (2003) have detected a magnetic field of order milli-Gauss (mG) at $\sim 3\times10^{13}$ to $2\times10^{14}$ m from the central star in *IRAS* 18276-1431 and *IRAS* 20406+2953. Sabin et al. (2007) detected magnetic fields around their sample of post-AGB stars of order mG at $\sim 5\times10^{14}$ m. A young-PN (YPN), NGC 7027, shows emission of $H_2$ surrounded by an equatorial $B$-field (Sabin et al. 2007, figure 2). The $H_2$ emission in NGC 7027 is similar to *IRAS* 19306+1407, with two bright arcs either side of the central source, with a bipolar outflow. However, NGC 7027 is more evolved than *IRAS* 19306+1407 because the central star has a temperature of $\sim 200,000$ K and is ionising its surrounding nebula (Latter et al. 2000). It is not possible to rule out the presence of C-bow shocks in *IRAS* 19306+1407, since the required magnetic field strength and the inner radius distance of *IRAS* 19306+1407 are comparable with observations of other evolved objects. The combination of line ratios, OPRs and vibrational and rotational temperatures indicates that the equatorial regions, tails and southwest bright knot are largely in agreement with a fast C- or slow J-bow shock. The rotational temperatures for the axial, lobe and outer regions are consistent with bow shock models, but the vibrational temperatures exceed those generated by these models. This indicates that a fluorescent component exists and is exciting the vibrational populations. The following section employs the CDR method in determining the fraction of fluorescence and the most likely bow shock type.

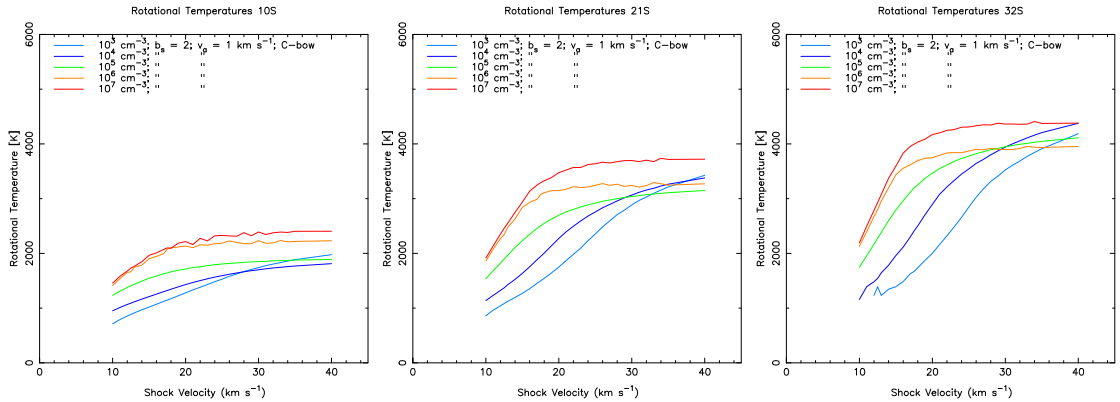


(a) The rotational temperature as a function of shock velocity for the investigated densities.

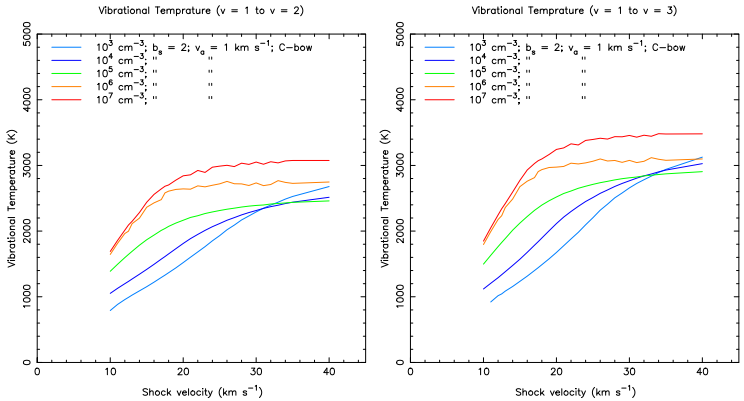


(b) The vibrational temperature as a function of shock velocity for the investigated densities.

Figure 6.25: The rotational (a) and the vibrational (b) temperatures with respect to the shock velocity for the densities $10^3$ (cyan), $10^4$ (blue), $10^5$ (green), $10^6$ (orange) and $10^7$ (red) for the C-bow shock model C1. The rotational temperatures for the 1-0 S, 2-1 S and 3-2 S transitions are displayed top-left, top-centre and top-right, respectively. The vibrational temperatures for the $v = 1$ to $v = 2$ and $v = 1$ to $v = 3$ are displayed bottom-left and bottom-right, respectively. The model parameters are indicated in each panel.

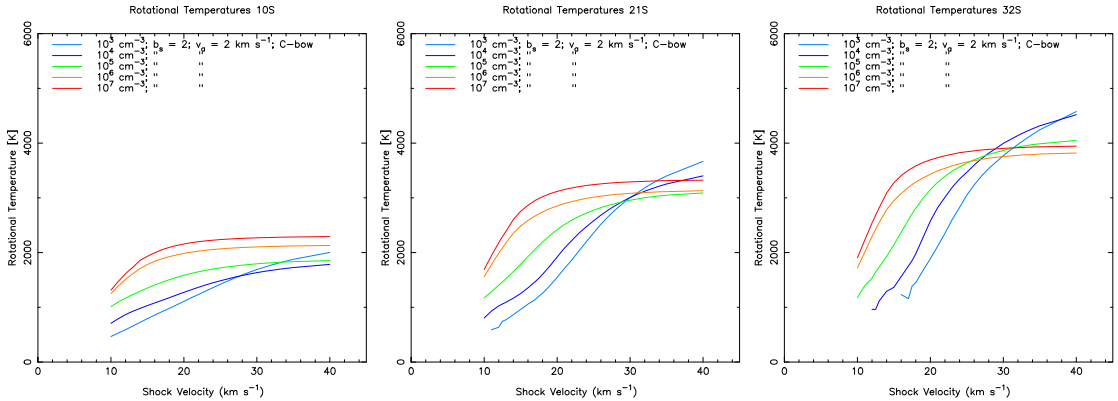


(a) The rotational temperature as a function of shock velocity for the investigated densities.

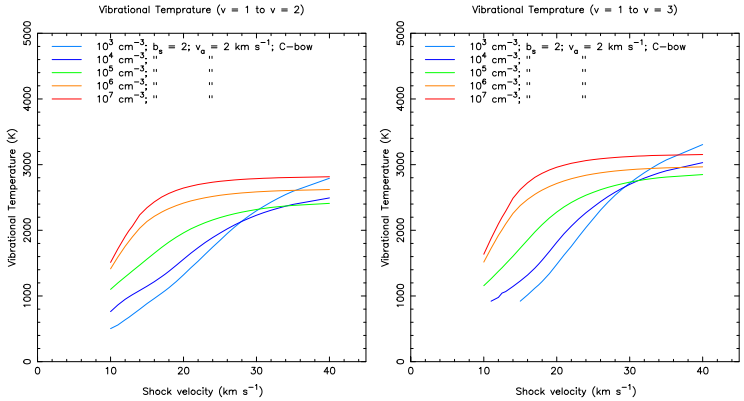


(b) The vibrational temperature as a function of shock velocity for the investigated densities.

Figure 6.26: The rotational (a) and the vibrational (b) temperatures with respect to the shock velocity for the densities $10^3$ (cyan), $10^4$ (blue), $10^5$ (green), $10^6$ (orange) and $10^7$ (red) for the C-bow shock model C2. The rotational temperatures for the 1-0 S, 2-1 S and 3-2 S transitions are displayed top-left, top-centre and top-right, respectively. The vibrational temperatures for the $v = 1$ to $v = 2$ and $v = 1$ to $v = 3$ are displayed bottom-left and bottom-right, respectively. The model parameters are indicated in each panel.

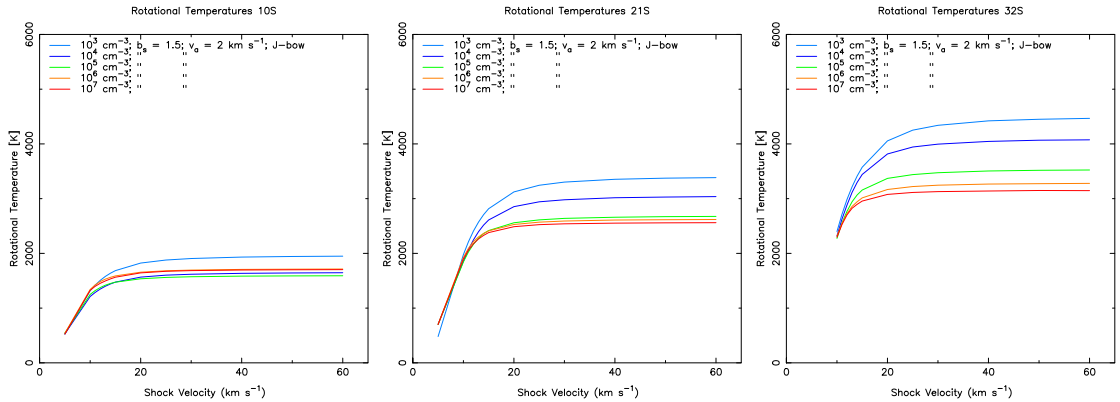


(a) The rotational temperature as a function of shock velocity for the investigated densities.

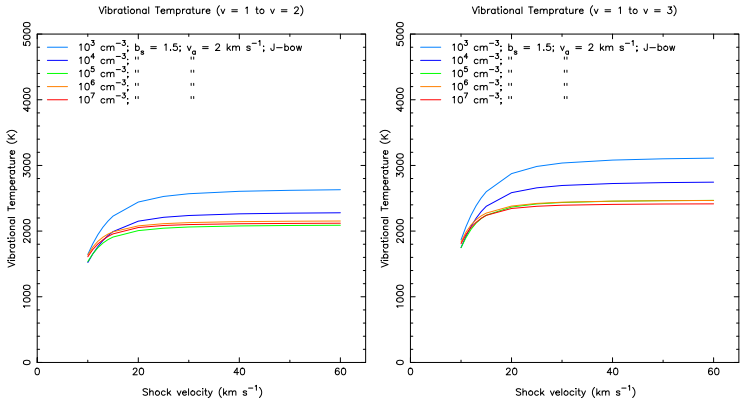


(b) The vibrational temperature as a function of shock velocity for the investigated densities.

Figure 6.27: The rotational (a) and the vibrational (b) temperatures with respect to the shock velocity for the densities $10^3$ (cyan), $10^4$ (blue), $10^5$ (green), $10^6$ (orange) and $10^7$ (red) for the J-bow shock model J1. The rotational temperatures for the 1-0 S, 2-1 S and 3-2 S transitions are displayed top-left, top-centre and top-right, respectively. The vibrational temperatures for the $v = 1$ to $v = 2$ and $v = 1$ to $v = 3$ are displayed bottom-left and bottom-right, respectively. The model parameters are indicated in each panel.

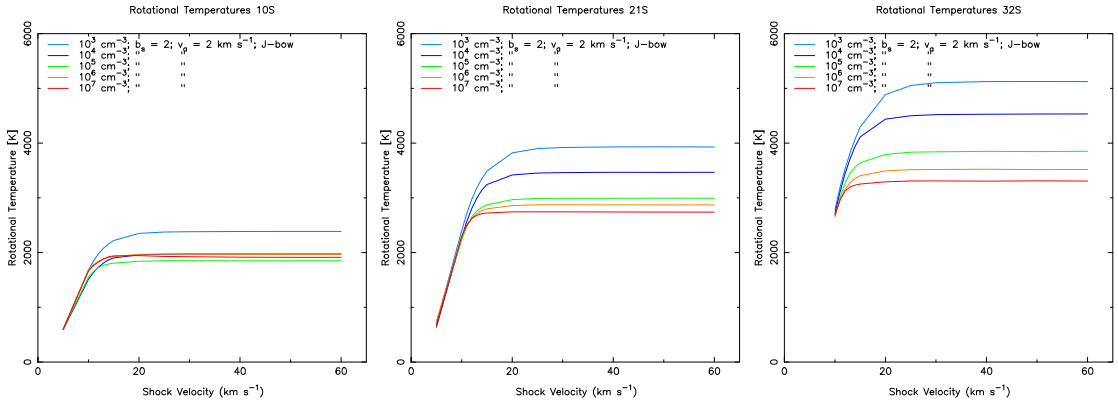


(a) The rotational temperature as a function of shock velocity for the investigated densities.

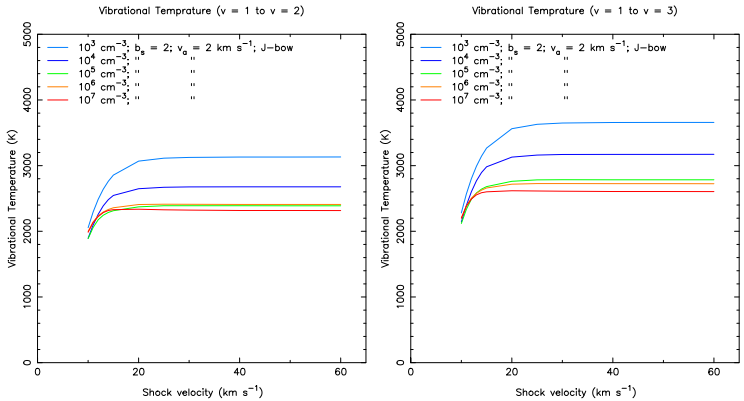


(b) The vibrational temperature as a function of shock velocity for the investigated densities.

Figure 6.28: The rotational (a) and the vibrational (b) temperatures with respect to the shock velocity for the densities $10^3$ (cyan), $10^4$ (blue), $10^5$ (green), $10^6$ (orange) and $10^7$ (red) for the J-bow shock model J2. The rotational temperatures for the 1-0 S, 2-1 S and 3-2 S transitions are displayed top-left, top-centre and top-right, respectively. The vibrational temperatures for the $v = 1$ to $v = 2$ and $v = 1$ to $v = 3$ are displayed bottom-left and bottom-right, respectively. The model parameters are indicated in each panel.

Table 6.6: The best-suited C-bow and J-bow shock models for regions 1 to 16 based on the vibrational and rotational temperatures.

| Region Number | C-bow shocks | | | | J-bow shocks | | | |
|---|---|---|---|---|---|---|---|---|
| | C1 | | C2 | | J1 | | J2 | |
| | Density $cm^{-3}$ | Velocity km $s^{-1}$ | Density $cm^{-3}$ | Velocity km $s^{-1}$ | Density $cm^{-3}$ | Velocity km $s^{-1}$ | Density $cm^{-3}$ | Velocity km $s^{-1}$ |
| 1 | $10^3$ | 21–27 | $10^3 - 10^4$ | 21–27 | $10^3$ | 10–13 | $10^3 - 10^4$ | 10–11 |
| 2 | $10^3$ | 24–27 | $10^3 - 10^5$ | 18–27 | $10^3$ | 12–13 | $10^3 - 10^5$ | 10–13 |
| 3 | $10^3$ | 26–27 | $10^3 - 10^4$ | 25–28 | $10^3$ | 13–14 | $10^3 - 10^4$ | 10–11 |
| 4 | $10^3$ | 23–28 | $10^3 - 10^4$ | 23–28 | $10^3$ | 11–15 | $10^3 - 10^4$ | 10–12 |
| 5$^+$ | $10^3$ | 31–36 | $10^3 - 10^4$ | 31–36 | $10^3$ | 17–19 | $10^3 - 10^4$ | 11–13 |
| 6 | – | – | $10^3$ | 25–30 | – | – | $10^3$ | 10–11 |
| 7 | – | – | $10^3$ | 23–33 | – | – | $10^3$ | 10–14 |
| 8$^‡$ | – | – | – | – | – | – | $10^3$ | 5–10 |
| 9$^†$ | $10^3 - 10^4$ | 13–17 | $10^3 - 10^4$ | 16–20 | $10^4$ | 5–10 | $10^4$ | 5–10 |
| 10$^†$ | $10^3 - 10^4$ | 14–18 | $10^3 - 10^4$ | 18–21 | $10^4$ | 5–10 | $10^4$ | 5–10 |
| 11$^†$ | $10^3 - 10^4$ | 11–15 | $10^3 - 10^4$ | 15–19 | $10^4$ | 5–10 | $10^4$ | 5–10 |
| 12$^‡$ | – | – | – | – | – | – | $10^3$ | 5–10 |
| 13$^†$ | $10^3 - 10^4$ | 13–17 | $10^3 - 10^4$ | 17–20 | $10^3 - 10^4$ | 5–10 | $10^3 - 10^4$ | 5–10 |
| 14$^†$ | $10^3 - 10^4$ | 15–19 | $10^3 - 10^4$ | 19–22 | $10^4$ | 5–10 | $10^4$ | 5–10 |
| 15$^†$ | $10^3 - 10^4$ | 14–18 | $10^3 - 10^4$ | 18–21 | $10^3 - 10^4$ | 5–10 | $10^3 - 10^4$ | 5–10 |
| 16$^†$ | $10^3 - 10^4$ | 11-16 | $10^3 - 10^4$ | 16–19 | $10^3 - 10^4$ | 5–10 | $10^3 - 10^4$ | 5–10 |

$^+$The rotational temperatures are inconsistent with the bow-shock models and the vibrational temperatures are used for fitting.

$^†$Fitted using the rotational temperatures.

$^‡$The observed $v = 1$ to $v = 3$ vibrational temperatures are greater than those generated by the models.

### 6.5.6 Excitation mechanisms

The CDR plots are used as a diagnostic tool for $H_2$ gases. The method of calculating the CDR is outlined in Chapter 3. The column depth for each line is calculated with respect to a gas in LTE at a temperature of 2000 K. A 2000 K $H_2$ gas will be a straight line parallel to the $x$-axis, when plotted on a CDR diagram. Therefore a gas that has a range of temperatures will exhibit a curved line, which is observed in shocks. A fluorescent mechanism introduces scatter, due to a non-LTE excitation mechanism, into the points on a CDR diagram. A pure C- and J-bow shock model can be fitted to the CDR values; however, it does not account for the scatter within each vibration group. A pure fluorescence model, taken from Black & van Dishoeck (1987, model 14), does reproduce non-LTE elements in the CDR values. The column depths from the shock and fluorescence models can be combined using

$$N(H_2)_{\rm total} = f_1 N(H_2)_{\rm fluorescence} + f_2 N(H_2)_{\rm shock}, \tag{6.6}$$

where $f_1$ and $f_2$[7] are the fractions of contribution to the fluorescence and shock column depths, respectively. A similar method has been used previously by Davis et al. (2003) and Fernandes et al. (1997) to investigate the excitation of pPNe/PNe and star formation areas. The fractions of fluorescence and shock model are determined by using a weighted-least squares minimisation method.

The CDR diagrams have been plotted for the extracted regions from the medium resolution SINFONI observations and are shown in Figure 6.29 after correcting for extinction. The Q-branch and S-branch transitions are displayed as red diamonds and orange triangles, respectively. The CDR values for the LTE gas and a shock+fluorescence model are fitted using a weighted least squares minimisation technique, in which the Q-branch lines are excluded (the 1-0 Q points have a greater

[7] $f_2 = 1 - f_1$

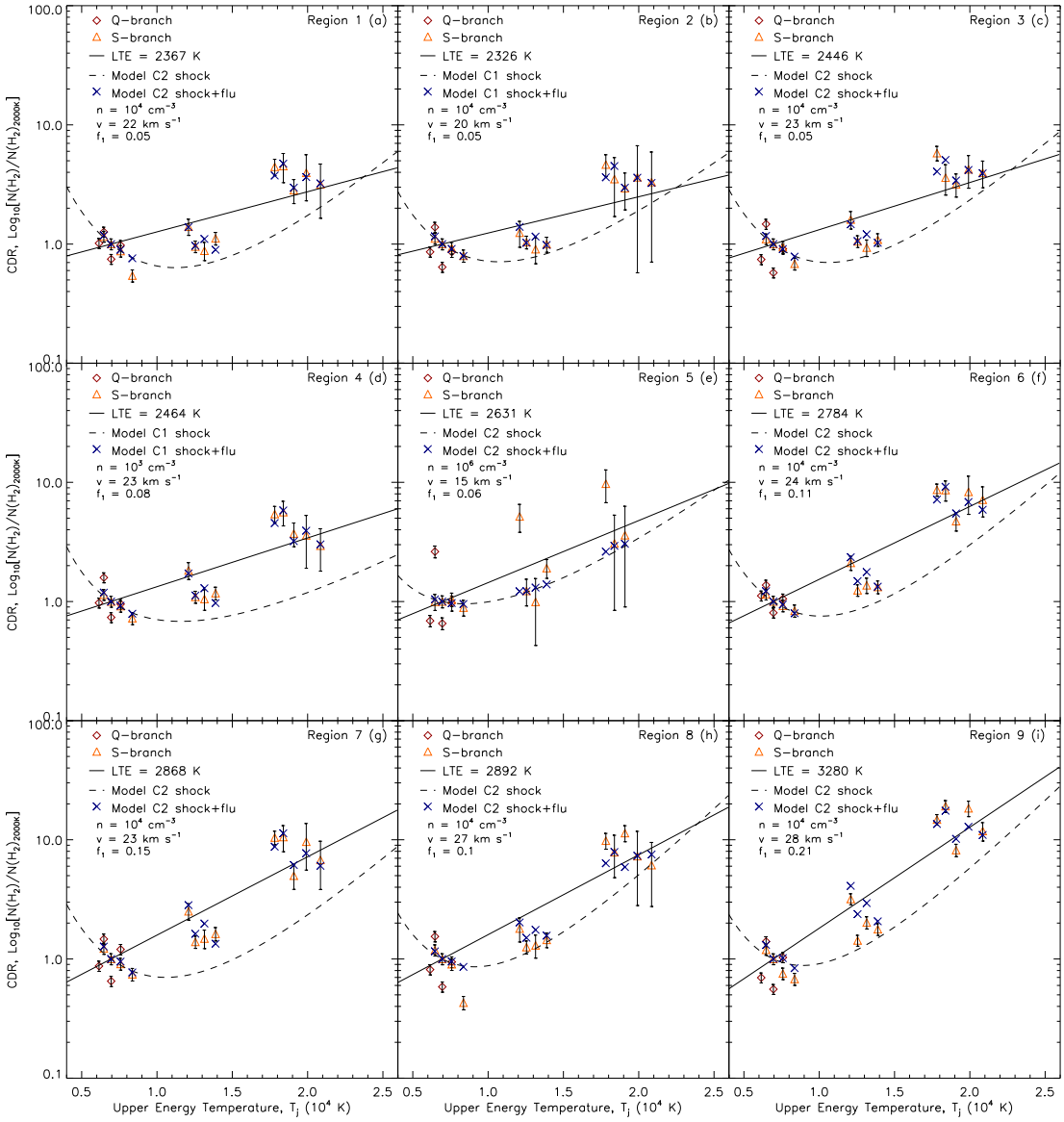


Figure 6.29: The Column density ratio (CDR) diagrams for the extracted regions 1 through 9, denoted (a) through to (i). The Q branch and S-branch transitions are marked with red diamonds and orange triangles, respectively. The errors associated with each data point are displayed as bars at $3\sigma$ values. The best-fitting LTE gas is marked as a solid black line, with the temperature marked in Kelvin in the legend. The combined CDR shock and fluorescent model are displayed as blue crosses, with the corresponding shock marked as a dashed line. The model type, denoted as either C1, C2, J1 and J2, model density, velocity and fraction of fluorescence are annotated in the legend.

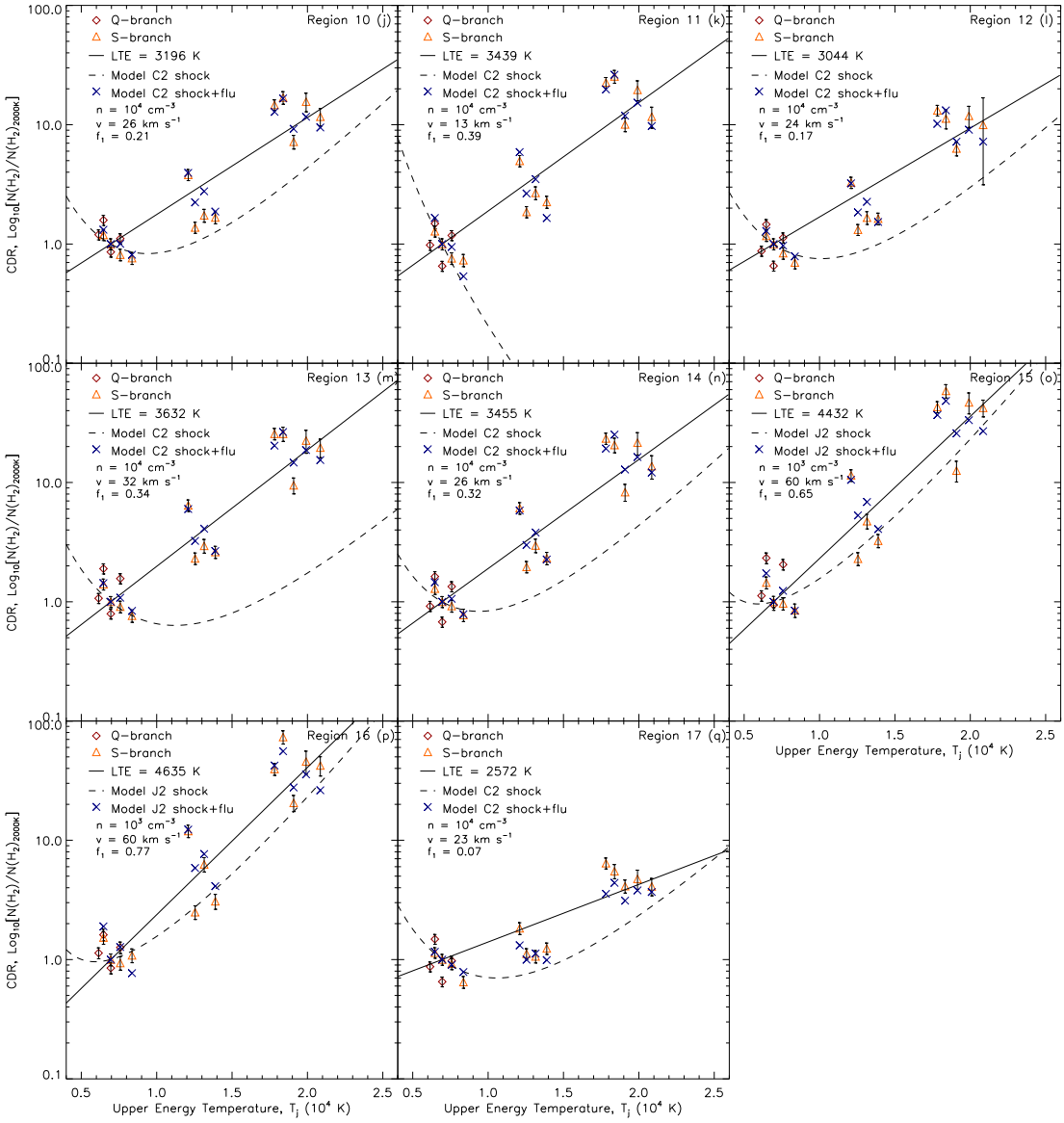


Figure 6.29: — **continued**. The Column density ratio (CDR) diagrams for the extracted regions 10 through 17, denoted (j) through to (q). The Q branch and S-branch transitions are marked with red diamonds and orange triangles, respectively. The errors associated with each data point are displayed as bars at $3\sigma$ values. The best-fitting LTE gas is marked as a solid black line, with the temperature marked in Kelvin in the legend. The combined CDR shock and fluorescent model are displayed as blue crosses, with the corresponding shock marked as a dashed line. The model type, denoted as either C1, C2, J1 and J2, model density, velocity and fraction of fluorescence are annotated in the legend.

amount of scatter than the 1-0 S points and would skew the data fit). As previously stated the atmospheric window is poor at wavelengths greater than 2.4 μm. Therefore the scatter in the 1-0 Q points is attributed to the atmosphere and the subsequent telluric correction. The 3-2 S points trace the higher ro-vibrational energy levels and have large error bars. The majority of regions show that the 2-1 S and 3-2 S points are below and above the fitted LTE line, respectively. The inner regions, 1 through 8, show LTE gas temperatures ranging from 2326 to 2890 K and in the outer regions, 9 through 16, temperatures range from 3044 to a maximum of 4635 K.

Each shock model was considered over the range of densities and velocities (Table 6.5). The CDR diagrams indicate that fluorescence is present in every extracted region ranging from 5 to 77 per cent. The error in the fluorescence fraction is approximately 0.01 (1 per cent). The bright arcs (Fig. 6.29b, c & d) and southwest knot (Fig. 6.29a) show relatively low levels of fluorescence $\sim$ 5 per cent and the tail features (Fig. 6.29f & g) have a higher percentage of 11 to 15 per cent. These areas are consistent with C-bow shocks of velocities 20 to 24 km $s^{-1}$ with densities ranging from $10^3$ $cm^{-3}$ in the southeast arc and $10^4$ $cm^{-3}$ in the other bright arc, tail and bright knot. The area diametrically opposite to the southwest knot has a fluorescent component of 10 per cent (Fig. 6.29h) with an underlying C-bow shock. The region over the central source shows a low level of fluorescence of 6 per cent (Fig. 6.29e) and a C-bow shock with a pre-shock density and velocity of $10^6$ $cm^{-3}$ and 15 km $s^{-1}$, respectively. The predicted C-bow shock velocity is lower than J-shock velocity predicted by the Br$\gamma$ emission. It is possible that the $H_2$ emission is arising from a different location than the atomic emission, i.e. $H_2$ at a similar radius to the bright arcs. The $H_2$ emission in this region has a low signal-to-noise due to the bright continuum emission from the central illumination source. The two knots in the southwest and northeast are equally fluoresced at 21 per cent and in

contrast the bipolar lobes show ratios of 17 and 39 per cent for the northern and southern lobe indicated by Figures 6.29k & l. The outer most regions (Fig. 6.29m to p) show the greatest proportion of fluorescence from 32 to 77 per cent with a fast J-bow shock.

The line ratios, vibrational and rotational temperatures and ortho-para ratios suggest that a mechanism other than shocks is exciting the higher $H_2$ transitions in *IRAS* 19306+1407. The CDR method was used in conjunction with linear combination of shock and fluorescent models, to show that the overall level of fluorescence is lowest in the equatorial regions and the southwest bright knot, whilst the axial, tails, lobes and outer regions show increasing levels of fluorescence, which dominates in the outer regions 15 and 16. Kelly & Hrivnak (2005) calculate a fluorescence fraction of 30 per cent, which is greater than the equatorial, axial and lobes, and is less than the outer regions determined in this chapter. Their method uses the $r_{21}$ ratio in combination with a 2000 K thermal model (Sternberg & Dalgarno 1989) and fluorescent model (Black & van Dishoeck 1987). The combination of bow shocks and fluorescent models, used in this thesis, has been applied to observations from Kelly & Hrivnak (2005). Using the $r_{21}$ value from Kelly & Hrivnak (2005), the best-fitting model is C-bow shock model (C2) with density of $10^3$ cm$^{-3}$, a velocity of 24 km s$^{-1}$, an associated $B$-field strength of 0.04 mG, and a 24 per cent contribution from fluorescence. However, using all emission line fluxes[8] described in Kelly & Hrivnak (2005) for *IRAS* 19306+1407, gives a C-bow shock model (C1) with a density of $10^4$ cm$^{-3}$, a velocity of 29 km s$^{-1}$, an associated $B$-field strength of 0.06 mG and a 3 per cent contribution from fluorescence. Kelly & Hrivnak (2005) observations consist of a single slit, 2.4 arcsec wide, situated east to west across the bright continuum, which would include the equatorial and axial regions, but omit the lobes and some of the outer regions. They do not correct their line fluxes for CSE or ISM

[8] 1-0 S(1), 1-0 S(0), 2-1 S(1), 2-1 S(2) and 3-2 S(3)

extinction. The combination of these factors and only considering the $r_{21}$ values can lead to an over estimation of the level of fluorescence from their observations.

The magnetic field required ranges through 0.02 to 1.28 mG. The majority of the regions require a C-shock (C2) with a pre-shock velocity of ∼20-30 km $s^{-1}$ and density of $10^4$ $cm^{-3}$, which has a B-field of 0.13 mG. These values for the magnetic field are less than or equivalent to those suggested by Bains et al (2003), Bains et al. (2004) and Sabin et al. (2007) for other nebulae.

## 6.6 Conclusion

This chapter presented the $K$-band integral field spectroscopy for *IRAS* 19306+1407 using UKIRT and VLT. The largest field of view of 3.3- by 6-arcsec, was observed at UKIRT with the UIST+IFU instrument. These observations were followed up at the VLT with SINFONI, with greater spectroscopic and spatial resolution in conjunction with AO, utilising two fields of view of 3- by 3-arcsec and 0.8- by 0.8-arcsec. The $H_2$ emission was discovered, from carefully fitting the emission lines and underlying continuum, to be extended, whilst the atomic and continuum emissions were unresolved. The UKIRT observations uncovered a bipolar nebula, a 'twist' feature and two peaks of emission aligned $\sim 18°$, $\sim 28°$ and $135°$, respectively. The detected line of sight velocity is greatest at the end of the lobes and the southern lobe is inclined towards the observer. The SINFONI observations resolved the two bright arcs in a multitude of $H_2$ emission lines ranging from the $v = 1$ to $v = 3$ states. It was also possible to uncover knots and tail features, which have not previously been detected in $H_2$. The high resolution mode for SINFONI uncovered the flocculent structure of the bright southeast arc. The Br$\gamma$ and continuum emission remained unresolved.

The central illumination source is beginning to ionise material in its immediate vicinity by photo-ionisation or fast J-shocks. It was found that the UV field is not sufficient to fluoresce all of the $H_2$ in the CSE, based on the determined spectral type from Chapter 5. The shock excitation is better categorised by a curved shock surface than planar shocks, which was confirmed by the observed $r_{21}$ and $r_{32}$ line ratios. The majority of the $H_2$ in the CSE is excited by shocks determined by using line ratios, gas excitation temperatures and the OPR as diagnostics, although these diagnostics could not account for the high vibrational temperatures, which suggested that fluorescence must be playing a role. It was not possible to differentiate between

C- or J-bow shocks using line ratios and their corresponding temperatures. Using CDR diagrams it is possible to determine that the majority of extracted regions can be accounted for by fitting a C-bow shock model with a contribution from fluorescence. The C-shocks require a magnetic field between 0.02 and 1.28 mG and shock velocities of 20 to 30 km $s^{-1}$ for densities $10^3$ and $10^4$ $cm^{-3}$. Two regions, 15 and 16, are dominated by fluorescence, $> 60$ per cent, and require J-bow shocks at a density of $10^3$ $cm^{-3}$ at velocities greater than 60 km $s^{-1}$. These shock velocities are less than the fast-wind velocity detected in H$\alpha$ emission wings, and greater than the line of sight velocities detected in the medium resolution SINFONI observation. In conclusion, *IRAS* 19306+1407 is a post-AGB object that is ionising material in its immediate location and the older AGB outflow is undergoing a shock from a fast-wind originating from (or close to) the central source.

# Chapter 7

# Discussion and Conclusions

This thesis presents near-IR polarimetry and integral field spectroscopy of *IRAS* 19306+1407, in conjunction with the creation of FUS to analyse the IFS observations. This IDL program can provide a quick inspection of the data cube, correction for instrumental artefacts, perform flux calibration and extract emission line images (see Chapter 4). The polarimetric observations were modelled by using axi-symmetric light scattering and radiative transfer models. The additional SCUBA photometry at 450- and 850-μm provided a constraint for the outer radius of the CSE. The CSE can be characterised by an equatorially enhanced dust shell consisting of O-rich sub-micrometre dust grains. The central illumination source can be represented by a B-type star that has an effective temperature of 21,000 K (see Chapter 5). It is estimated that this post-AGB star left the AGB approximately 400 years ago, assuming a constant envelope expansion speed. The polarised flux images were compared to the *HST* images and showed a near-IR dust torus offset 118° (E of N) to the long axis of the optical bipolar nebula. These images highlighted a 'twist' in the axial symmetry, leading to the conclusion that this feature signifies a recent change in the direction of the outflow axis.

The IFS observations indicated that the molecular emission is extensive and

covers an area of several arcseconds (see Chapter 6). The UKIRT $H_2$ observations showed a bipolar nebula with the southern lobe having a blue-shifted radial velocity component indicating that it is inclined towards the observer. There are also two bright peaks either side of the central illumination source. The Br$\gamma$ emission was unresolved. These observations were followed up with the SINFONI instrument at the VLT. It was discovered, with the use of adaptive optics, that the $H_2$ emission was brightest in the two arcs either side of the central source. Additional morphological features, such as knots and tails, were discovered. Using sub-arcsecond imaging of the southeast bright arc revealed that it consisted of a flocculent structure. The two resolution modes of SINFONI showed that the Br$\gamma$ emission is unresolved and originates from, or close to, the stellar photosphere (Fig. 7.1 left, centre and right). The derived line ratios and vibrational and rotational temperatures show that shocks are the dominant excitation mechanism in the arcs, lobes, tails and knots. It is apparent that a curved shocked surface is needed to reproduce the observed line ratios. The column density ratios for each line were calculated with respect to the 1-0 S(1) line and normalised to a LTE gas at a temperature of 2000 K. The C- and J-bow shock models from Smith, Brand & Moorhouse (1991) were combined with a fluorescent model from Black & van Dishoeck (1987) to fit measured CDRs. C-bow shocks produced the best fit for the bright arcs, knots, tails and lobes with increased levels of fluorescence in the lobes and tails. Fluorescence dominates in regions outside of these morphological features. In this chapter the $H_2$ emission is compared with the polarimetric observations and *HST* images.

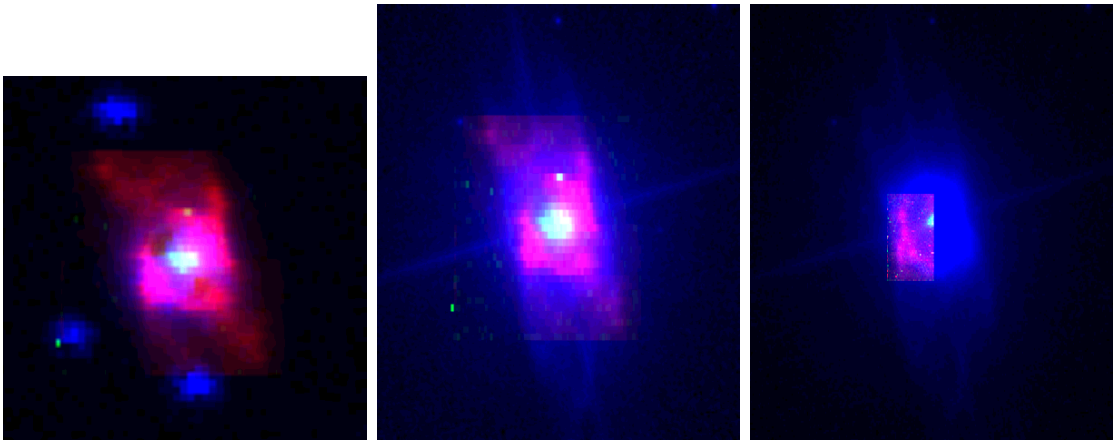

Figure 7.1: False colour images of *IRAS* 19306+1407. Left: The blue, green and red colours highlight the UKIRT *J*-band polarised flux, Br$\gamma$ emission and 1-0 S(1) emission (SINFONI medium resolution), respectively. The artefact stars are blue in colour and result from the instrument set-up and data reduction. Centre: The blue, green and red colours highlight the *HST F606W* image, Br$\gamma$ emission and 1-0 S(1) emission (SINFONI medium resolution), respectively. Right: The blue, green and red colours highlight the *HST F606W* image, Br$\gamma$ emission and 1-0 S(1) emission (SINFONI high resolution), respectively.

## 7.1 Comparisons to previous observations

The $IP_J$ and *HST F606W* images can be compared with the 1-0 S(1) images, which have been observed at three spatial scales (6 by 3.3 arcsec, 3 by 3 arcsec and 0.8 by 0.8 arcsec). The $IP_J$ flux shows the scattering of light by dust grains in the equatorial region, whereas the *HST* observations highlight the bipolar cavities, caused by light scattering from the cavity walls. The inter-comparison of these observations will show if the $H_2$ emission is co-incident with the cavity walls and the light scattered by dust grains. False colour images, displayed in Figure 7.1, combine the $IP_J$, 1-0 S(1), Br$\gamma$ and *F606W* images and highlight the extent and locations of the emission.

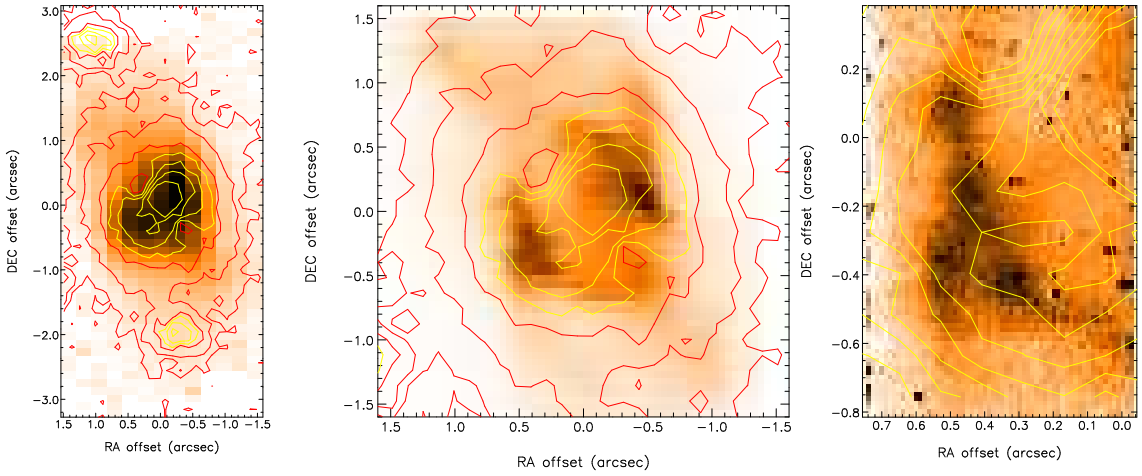


Figure 7.2: The comparison of the $H_2$ emission with the J-band polarimetry. The left, centre and right images are the extracted 1-0 S(1) emission line from the UIST+IFU, medium resolution and high resolution SINFONI observations, respectively. The J-band polarised flux image is overlaid as contours. The left image shows artefact stars, in contours, which arise from the instrument setup and the data reduction. The left and centre 1-0 S(1) images are displayed between the ranges of 20-$F^{-18}$ and 0.01-$F^{-18}$, where $F^{-18}$ is equal to $10^{-18}$ W m$^{-2}$ arcsec$^{-2}$. The images are overlaid with red contours displayed at 15, 15.5, 16 and 16.5 mag arcsec$^{-2}$ and the yellow contours at 17, 18 and 19 mag arcsec$^{-2}$. The right hand image is displayed between the ranges of 30-$F^{-18}$ and 0.01-$F^{-18}$ with the overlaid yellow contours range from 15- to 17-mag arcsec$^{-2}$ separated by 0.25 mag arcsec$^{-2}$.

### 7.1.1 *J*-band polarimetry and 1-0 S(1)

The *J*-band polarimetry was obtained at UKIRT using UIST in conjunction with IRPOL2. A full description of the observations is documented in Chapter 5. The polarised flux images show the detected light that is scattered by dust grains. The $IP_J$ image has been chosen since it is more extended than the *K*-band polarised flux image. The 1-0 S(1) emission images have been taken with UIST+IFU and SINFONI instruments; they are displayed in Fig. 7.2 with overlaid $IP_J$ flux contours. The UIST+IFU image shows that the polarised flux and 1-0 S(1) emission are co-incident (Fig. 7.2 left). The three stars associated with the polarised flux image are artefacts from the instrument's configuration and the subsequent data reduction, which is explained further in chapter 5. The two bright shoulders of polarised emission match locations of the bright $H_2$ arcs; in addition, the northwest shoulder/arc is brighter in $IP_J$ and $H_2$ than the southwest shoulder/arc. The $IP_J$ is extended north-northeast and south-southwest and aligned with the $H_2$ lobes. The medium resolution SINFONI image (Fig. 7.2 centre) shows that the 1-0 S(1) emission and the scattered light are morphologically similar, although the central bright scattered light peak does not have a counterpart in the 1-0 S(1) emission. However, the bright peak is attributed to either an artefact of the data reduction or polarised emission close to the central source. A bright knot of 1-0 S(1) emission to the southwest, does not show any associated polarised emission. The high resolution SINFONI image (Fig. 7.2 right) shows that the scattered light is co-incident with the 1-0 S(1) emission. It is not possible to resolve the clumps in the polarised flux, due to the coarser pixel scale and the seeing-limited resolution. Higher spatial resolution imaging polarimetry is required to investigate at the spatial scales that SINFONI can reach.

### 7.1.2 *HST F606W* and 1-0 S(1) images

The *HST F606W* image in conjunction with the 1-0 S(1) emission, over-plotted as contours, from UIST+IFU, medium and high resolution SINFONI images are displayed in Fig. 7.3(a), 7.3(b) and 7.3(c), respectively. To aid clarity, the images are arranged with the *HST* image in the left hand panel and the *HST* image over-plotted with 1-0 S(1) emission contours in the right hand panel. The UIST+IFU $H_2$ emission inner contours show two bright peaks of emission either side of the star and located close to the waist of the bipolar nebula (Fig. 7.3a right). The outermost contour traces the bipolar lobes with a PA of 18°, however the inner contours twist to 28° east of north.

The medium resolution SINFONI contours show two distinct arcs either side of the star (Fig. 7.3b). The location of the brightest parts of these arcs below a line passing through the star may indicate that the shell is inclined towards the observer, which is analogous to the mid-IR images and models of *IRAS* 17436+5003 (Gledhill & Yates 2003). The offset in the mid-IR arcs in *IRAS* 17436+5003 is caused by optical depth effects of a tilted equatorially enhanced shell. However, the line of sight velocity indicates that the northern bipolar lobe is tilted away from the observer. This could indicate that the arcs are created in a non-spherically symmetric outflow with an axis tilted with respect to the bipolar axis. The high resolution SINFONI contours show that the brightest knots of emission lie close to the inner edges of the bipolar lobes (Fig. 7.3c right). There are three bright knots of emission contained within the arc structure. A fourth knot, that is coincident with the tail feature, lies close to the wall of the southern bipolar lobe.

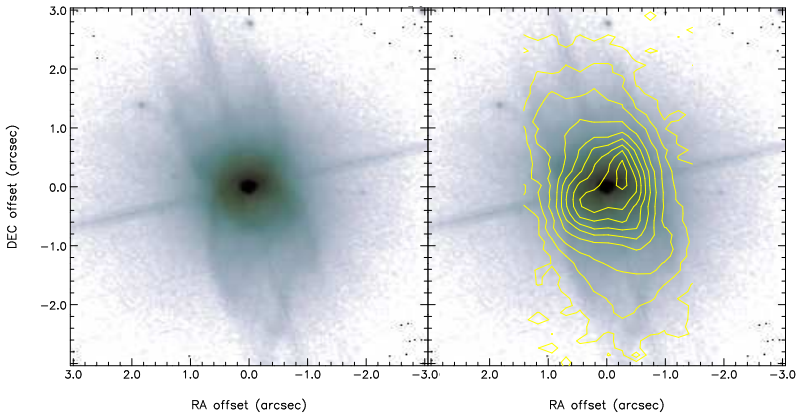


(a) The comparison of the HST image and the 1-0 S(1) emission observed with UIST+IFU.

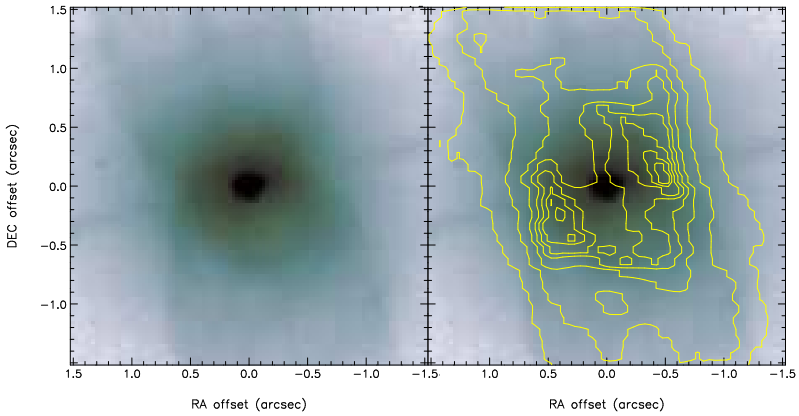


(b) The comparison of the HST image and the 1-0 S(1) emission observed with SINFONI at medium resolution.

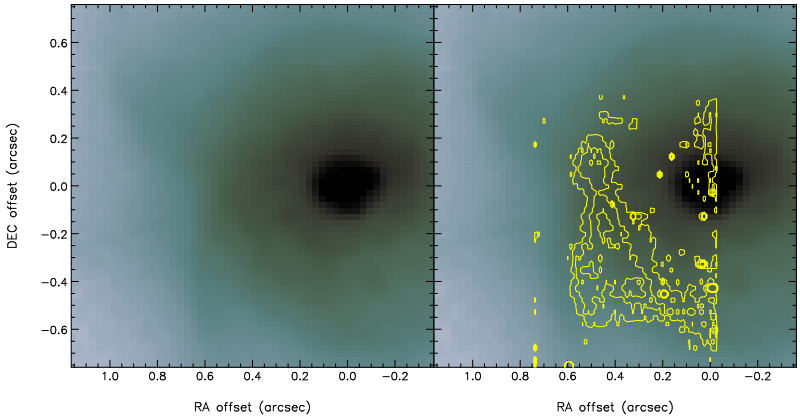


(c) The comparison of the HST image and the 1-0 S(1) emission observed with SINFONI at high resolution.

Figure 7.3: The comparison of the HST images and the 1-0 S(1) emission observed with integral field spectroscopy. The left hand panels in (a), (b) and (c) display the HST image between 12 and 21 mag arcsec$^{-1}$. The right hand panels display the HST image at the same values as the left hand panel, over-plotted with $H_2$ 1-0 S(1) emission in yellow contours at levels: (a) $1.0F^{-18}$ and 2.5 to $20.0F^{-18}$, separated by 2.5-$F^{-18}$; (b) 1.0 $F^{-18}$ and 2.5 to 20.0 $F^{-18}$, separated by 2.5-$F^{-18}$, and (c) 15.0 to 30.0 $F^{-18}$, separated by 5.0-$F^{-18}$.

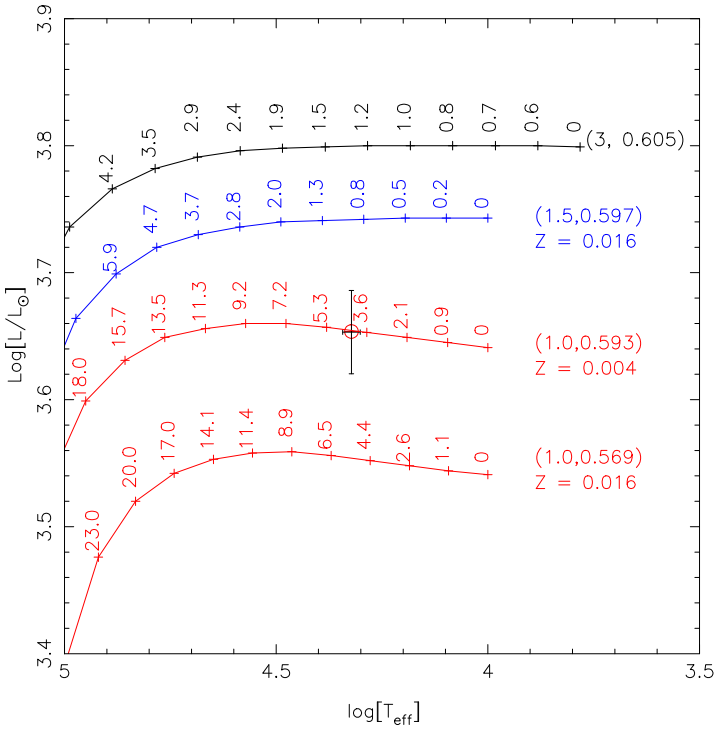


Figure 7.4: The plotted luminosity and effective temperature, with errors derived from chapter 5, of *IRAS* 19306+1407 placed on a HR diagram. The post-AGB evolution tracks from Blöcker (1995b) and Vassiliadis & Wood (1994b), where the former is highlighted by a thick black line and the latter by thin coloured lines. The initial and final mass are annotated within the parenthesis. The tracks from Vassiliadis & Wood (1994b) are marked with the metal abundance for each star. The annotated numbers above each point indicate time in $10^3$ years from their zero point age

## 7.2 *IRAS* 19306+1407's place in the evolutionary sequence

The central star is a B-type with an effective temperature of 21,000 K, using a Kurucz model[1] (see Chapter 5 Lowe & Gledhill 2007; Kelly & Hrivnak 2005). It has not started to significantly ionise its CSE, but Br$\gamma$ emission has been detected close to the central source. It has an estimated luminosity at 2.7 kpc of 4500±340 $L_{\odot}$. Figure 7.4 indicates the star's position on the HR diagram compared with four models from

[1] `http://kurucz.harvard.edu/grids.html`

Blöcker (1995b) and Vassiliadis & Wood (1994b). The models of Vassiliadis & Wood (1994b)[2] define the zero age of the post-AGB star once it has reached a temperature of $10^4$ K. Blöcker (1995b)[3] define the zero age of a post-AGB star when the mass loss has decreased significantly. The two models have a different treatment of the mass loss and cannot be directly compared; in addition, the metallicity in the models by Blöcker (1995b) is greater, with a value of $Z = 0.021$, than Vassiliadis & Wood (1994a). *IRAS* 19306+1407 settles on the evolutionary track for a 1 $M_{\odot}$ star with a metallicity of $Z = 0.004$ and an estimated age of $3.6 \times 10^3$ years (Vassiliadis & Wood 1994b). The predicted final mass is $\sim$0.6 $M_{\odot}$. The Hydrogen-burning models provide better fitting evolutionary tracks than the Helium-burning models. Siódmiak et al. (2008) classify *IRAS* 19306+1407's morphology as SOLE. They estimate the final masses of SOLE type post-AGB stars, to be around $\sim 0.6$ $M_{\odot}$, but retain the caveat that higher mass progenitors may be possible.

In Chapter 5 the predicted post-AGB age was 400 years, which assumes an expansion speed of the CSE equal to 15 km $s^{-1}$. It is assumed that the estimated expansion speed of CSE is constant. In addition, the distance is estimated using an extinction to distance relationship. The evolution time from Blöcker (1995b) and Vassiliadis & Wood (1994b) assumes spherical mass loss for a single star, in the case of *IRAS* 19306+1407, the mass loss is not spherical. Therefore the evolution time from Blöcker (1995b) and Vassiliadis & Wood (1994b) is not directly comparable to *IRAS* 19306+1407. It is also possible that *IRAS* 19306+1407 is rapidly evolving. The position on the HR diagram suggests that this post-AGB star is not yet a PN, since its temperature is between the maximum and minimum temperature for a AGB and PN star of $\sim 3200$ K and $\sim 30,000$ K, respectively. This is supported by the fact that the central star has not started to ionise the CSE, but is starting to fluoresce the $H_2$. García-Hernández et al. (2002) shows the fluorescence excitation occurs when

[2]The model results are available from an online catalogue Vassiliadis & Wood (1994a)
[3]The model results are available from an online catalogue Blöcker (1995a)

the star is on the verge of ionising its CSE; therefore, it is expected that a post-AGB object should fluoresce its CSE before transiting to the PN stage. Davis et al. (2003) show fluorescence is detected in post-AGB, YPN and PN objects. Suárez, Gómez, & Morata (2007) did not detect any water maser emission. In addition, Luciano Cerrigone (private communication) did not detect any 12.8 μm NeII emission from their Spitzer spectroscopy and did not detect *IRAS* 19306+1407 in radio continuum, which *'confirms it as a not yet ionized (or very low excitation) object.'* However, the radio free-free emission could be optical thick at the observed frequency.

### 7.2.1 Using $H_2$ and Br$\gamma$ emission as an evolutionary marker

Cox et al. (1997) investigated is AFGL 2688 and NGC 7027 and detected extended $H_2$ emission. These two objects are characterised as a post-AGB and a YPN, and each central illumination source has an effective temperature of 6500 K and 200,000 K, respectively. AFGL 2688 has no Br$\gamma$ emission and NGC 7027 has extended Br-$\gamma$ emission associated with the $H_2$ emission. Cox et al. (1997) showed that AFGL 2688 is too cool to ionise its CSE and the $H_2$ is excited by shocks. In the case of NGC 7027, the $H_2$ is excited by UV photons and the atomic hydrogen is photo-ionised. *IRAS* 19306+1407's central illumination source has an effective temperature of 21,000 K, with extend $H_2$ and unresolved Br$\gamma$ emission. The $H_2$ in the CSE shows a mixture of fluorescence and shocks. When considering the $H_2$, Br$\gamma$ and effective temperature of the central illumination source of *IRAS* 19306+1407, AFGL 2688 and NGC 7027, suggests that *IRAS* 19306+1407 is a post-AGB object and not quite a YPN.

Davis et al. (2003) investigated 11 evolved stars, which included PPNe, YPNe and PNe with spectral types ranging from G to B and white dwarfs, using single slit *K*-band spectroscopy. In cases of a resolved CSE, the spectrograph's slit was aligned to morphological features. The slit was aligned east-west if the science target was

unresolved or its morphology was unknown. The authors measured $H_2$, HeI and Br$\gamma$ emission lines, produced 1-0 S(1)/2-1 S(1), 1-0 S(1)/3-2 S(3), 1-0 S(1)/Br$\gamma$ and 1-0 S(1)/HeI, and modelled the calculated CDRs using bow shocks with a contribution from fluorescence. The F- and G-type PPN have low levels of fluorescence, ranging from 2 to 30 per cent, whilst the B- and O-type PPNe/YPNe have fluorescence levels of 10 to 44 percent. The fluorescence varies from 0 to 60 per cent for the PNe. The F- and G-type PPNe show either no Br$\gamma$ and HeI emission or unresolved Br$\gamma$ emission. The B- and O-type PPNe/young PNe show Br$\gamma$ and HeI emission. The slit aligned to the major axis of M 1-92 and it has extend Br$\gamma$, but no HeI emission. *IRAS* 18062+2410 and *IRAS* 21282+5050 [4] has Br$\gamma$ emission in the centre of the slit; however, the slit was positioned east-west in both cases. *IRAS* 21282+5050 is elongated to the north-northwest to south-southeast with respect to $H_2$ and Br$\gamma$ (Davis et al. 2005; Lowe & Gledhill, in preparation); therefore, Davis et al. (2003) did not place the slit along the major axis of the nebula and did not resolve the extended emission. There is no published image of the CSE for *IRAS* 18062+2410. The PNe all have white dwarf central stars (except NGC 6302 that has an additional G2 component) and all show extended Br$\gamma$ and HeI emission. *IRAS* 19306+1407 has no detected HeI emission, similar to M 1-92, but its Br$\gamma$ emission is not extended. In Davis et al. (2003) show that *IRAS* 17150-3224 has Br$\gamma$ emission close to the position of the central star; however, in a later paper by Kelly & Hrivnak (2005) and Davis et al. (2005) shows Br$\gamma$ in absorption. *IRAS* 19306+1407 is not as evolved as the B- and O-type PPNe, YPNe and PNe in the sample provided by Davis et al. (2003), but it is certain that it is more evolved than the F- and G-type PPNe.

Kelly & Hrivnak (2005) investigated a range of post-AGB objects using single slit *K*-band spectroscopy, where the slit is aligned east-west, for G to B spectral types. They found that the B spectral types showed a mixture of fluorescence and

[4]Davis et al. (2003) state a spectral type of WC 11, but Crowther, De Marco, & Barlow (1998) determine a O9–O9.5 spectral type.

thermal excitation, except *IRAS* 20462+3416, which was wholly fluorescent. However, the estimate of the level of fluorescence is based solely on the 1-0 S(1)/2-1 S(1) ratio. In Chapter 6 the level of fluorescence, with respect to shocks, was estimated from the 1-0 S(1)/2-1 S(1) ratio and the calculated CDR values, determined from the $H_2$ fluxes stated in Kelly & Hrivnak (2005). It was found that the line ratio gives a greater value for the level of fluorescence than the CDR method.

There have been a few in-depth studies of individual B-type post-AGB stars, which have revealed extended $H_2$ emission. For example: *IRAS* 16594-4656 (van de Steene & van Hoof 2003; van de Steene et al. 2008), *IRAS* 22023+5249 (Volk et al. 2004; Kelly & Hrivnak 2005) and IRAS 19343+2926 (M 1-92) (Bujarrabal et al. 1998)).

*IRAS* 16594-4656 has a B7 spectral type central illumination source. Van de Steene & van Hoof (2003) conducted single slit spectroscopy and detected $H_2$, atomic hydrogen and [FeII] emission, which is thought to arise from C- or J-shocks. In the subsequent paper, van de Steene et al. (2008), 1-0 S(1), 2-1 S(1), [FeII] and Pa$\beta$ emission was observed at higher spectral and spatial resolution using multiple position angles. The authors indicate that the $H_2$ emission originates in a shell structure undergoing slow shocks and the atomic emission from faster shocks close to the central source. *IRAS* 19306+1407 shows a similar separation in the $H_2$ and atomic hydrogen emission, with the former in the CSE and the latter close to the central illumination source. However, van de Steene & van Hoof (2003) and van de Steene et al. (2008) only compare the 1-0 S(1)/2-1 S(1) ratio with planer shocks models from Le Bourlot et al. (2002) and Wilgenbus et al. (2000), and do not consider a contribution from fluorescence. Additional $H_2$ emission lines are needed, corresponding to higher ro-vibrational energy levels, to determine the geometry and type of shocks, and the level of fluorescence, using the $r_{21}$ versus $r_{23}$ and CDR methods,

*IRAS* 22023+5249 is classified as a B-type PPN and shows slightly extended emission in narrow band 1-0 S(1) image (Volk et al. 2004) and a rich $H_2$ spectrum (Kelly & Hrivnak 2005). In the later paper, the fluorescence contribution is 60 per cent, which is higher than in *IRAS* 19306+1407. I have re-evaluated re-evaluated the level of fluorescence by fitting the shock and fluorescence models, detailed in Chapter 6, to the stated $H_2$ fluxes in Kelly & Hrivnak (2005). The best-fitting model is a J-bow shock model (J2) with a density of $10^3$ cm$^{-3}$ and pre-shock velocity of 30 km s$^{-1}$, with a 32 per cent contribution from fluorescence. It is possible that *IRAS* 22023+5249 is more evolved than *IRAS* 19306+1407; however, more observations, of the $H_2$, atomic hydrogen and [FeII] are needed for *IRAS* 22023+5249 to determine the locations of the shocks and the spectral type.

M 1-92 shows extended $H_2$, H$\alpha$, [OI], [SII] and [OIII] emission which is produced by the fast post-AGB wind interacting with the older AGB envelope (Bujarrabal et al. 1998). The extended H$\alpha$ emission indicates it is more evolved that *IRAS* 19306+1407. Unfortunately, there have not been any high resolution imaging follow up studies. Extended [FeII] emission has been observed in Davis et al. (2005).

*IRAS* 19306+1407 is important to further the understanding of the transition from the post-AGB to the PN stage, because it shows a mixture of emission common to PPNe and YPNe. It shows spatially unresolved Br$\gamma$ emission, similar to some F/G and B type PPNe (e.g. *IRAS* 17423-1755 Davis et al. 2005), but not extended as in the more evolved YPNe and PNe. There is no detected HeI emission in *IRAS* 19306+1407, which is present in YPNe and PNe. The $H_2$ shows a mixture of fluorescence and shocks, which is similar to the level detected in PPNe. *IRAS* 19306+1407 is a post-AGB object and is on the verge of becoming a YPNe. As the central source of *IRAS* 19306+1407 evolves and increases in temperature, it will begin to photo-ionise the CSE, giving rise to extended Br$\gamma$ emission. In addition, HeI emission may 'switch on' and become extended. This object warrants further

observation to measure the changes in atomic and $H_2$ emission, and to detect [FeII].

## 7.3 Morphology of *IRAS* 19306+1407

*IRAS* 19306+1407 can be described as a bipolar nebula with a faint outer halo. It has a waist in the optical images that is due to extinction by an equatorially enhanced dusty torus, whose symmetry axis is not perpendicular to that of the bipolar lobes. It has been demonstrated that the polarised emission can be modelled with a Generalised Interacting Stellar Winds (GISW) model with a density distribution described by Kahn & West (1985).

It seems likely that a collimated outflow formed the bipolar lobes, which are visible in the *HST* images. The velocity of the $H_2$ emission increases towards the end of the lobes. There are no detected $H_2$ caps[5], which indicate that *IRAS* 19306+1407 is not a closed bubble. The lobes, tails and equatorial regions show evidence for shocked $H_2$, and also have a contribution of fluorescence. The superposition of the bright arcs in the $H_2$ and the shoulders in polarised flux, indicate that the enhanced mass loss is being shocked. The axis defined by the enhanced mass loss is not perpendicular to the bipolar lobes and this indicates that there may have been a recent change in the outflow axis.

### 7.3.1 Shaping mechanisms

The post-AGB stars' CSEs are shaped by collimated winds produced by magnetic fields, binary interactions, fast rotating stars, or a mixture of these mechanisms (for a review see Balick & Frank 2002). García-Segura et al. (2005) present a compelling argument for magnetic shaping in post-AGB stars, in which the toroidal magnetic field strength at the stellar surface varies from 0.1 to 5 G. They suggest that the magnetic fields are produced by a dynamo effect of differential rotation of stellar core with respect to the CSE, but do not explicitly state how the magnetic field in

[5]An example of $H_2$ caps can been seen in *IRAS* 17150-3224 (Hrivnak et al. 2006)

their models is generated or maintained. The magnetic field strength for the C-bow shocks, obtained from the shock modelling in Chapter 6, ranged from 0.02 to 1.28 mG, which is lower than those required to shape the nebula.

Dijkstra & Speck (2006) address the formation of the axisymmetric wind originating from a rotating AGB star. However, the model has two conditions: (1) the AGB star is rotating with sufficient angular momentum at the start of the AGB stage, and (2) the angular momentum is conserved. They do discuss the validity of these assumptions and suggest the momentum lost by the stellar wind could *'in principle be replaced by a low-mass companion star.'* Their results show that an equator-to-pole density ratio of $< 2.5$ is generated at the end of the AGB for a stellar mass of up to 3.5 $M_{\odot}$. To reproduce the equator-to-pole ratio for *IRAS* 19306+1407, using the Dijkstra & Speck (2006) model, requires a star to have a mass of $\sim 5$ $M_{\odot}$, which is significantly higher than the mass estimate from Vassiliadis & Wood (1994b) and Blöcker (1995b).

Soker & Rappoport (2001) discuss relatively close binaries with eccentric orbits and low period binary systems with circular or eccentric orbits, in which 25 and 35–50 per cent of elliptical and bipolar PNe, respectively, can be explained by these binary interactions. Soker (2001) estimates that 5 to 20 per cent of all PNe are formed from wide binaries, in which the secondary does not tidally distort the primary mass-losing star. The material ejected from the AGB star is swept up into a disc, around the secondary and creates a collimated wind, which in turn creates two jets and forms either an elliptical or bipolar morphology. Bipolar PNe with narrow waists are formed if the binary stars undergo tidal interaction or experiences Roche lobe overflow (Soker & Rappaport 2000). The effect of binary interactions to produce bipolar PNe is not strictly limited to stellar mass companions, but can include brown dwarfs or planets (Soker 2002). Nordhaus & Blackman (2006) investigate the evolution of an evolved star with a low mass companion ($< 0.3$ $M_{\odot}$) within

a common envelope and present three formation mechanisms for PPNe, which are an equatorial outflow, a possible dynamo-driven bipolar outflow and a disc, created from the shredded remains of the secondary, that drives a bipolar jet. Nordhaus et al. (2007) investigate the dynamo-driven outflow for a high mass–low mass binary system and for an isolated star, in which they suggest that binary interaction is more likely than an isolated star to produce PPNe. Soker (2006b) states that the observed PNe shapes cannot be produced solely from magnetic fields generated from a single star, and that binary interactions will dominate the shaping process. He also states that the detected magnetic fields are small local fields within the CSE. If a single star cannot produce the conditions for axisymmetric outflow then binary interaction must be considered.

Moe & De Marco (2006) and Soker (2006a) provide a population synthesis of PNe created from single and binary stars. The total estimated number of possible PNe is significantly greater than that observed. They suggest that the current population of visible PNe can be only explained if they originate from binary progenitors. This idea is reinforced by Soker & Subag (2005), who state that there is a hidden population of spherical PNe. They also state that some elliptical and bipolar PNe result from binary interactions with planets or more massive companions.

It is clear that there is still some debate on the underlying mechanisms that form and shape PPNe and the subsequent PNe stage. In the case of *IRAS* 19306+1407, the shaping of the CSE by magnetic fields is very attractive; however, the observations presented in this thesis cannot differentiate between the shaping mechanism driven by a single AGB star or that of a binary system. Future observations to differentiate between these mechanisms are discussed in section 7.4.

### 7.3.2 The 'twist'

The equatorial features, which are defined as shoulders and bright arcs in scattered light and $H_2$ emission, respectively, are not perpendicular to the bipolar lobes seen in the *HST* images. In addition, the 1-0 S(1) emission in the UIST+IFU and medium resolution SINFONI images show elongated contours to the northeast and southwest (Figs. 7.3a & b). This can be clearly seen in the false colour images (Fig. 7.1 left & centre). It is suspected that this 'twist' marks a change in the outflow direction. Two knot features have been detected at the end of the 'twist', in the medium resolution SINFONI images, and have the same level of fluorescence (21 per cent) with a shock velocity range of 26-28 km $s^{-1}$. The northern lobe shows similar fluorescence and shock velocity to the knots contained within the lobe, whilst the southern lobe has a greater level of fluorescence (39 per cent) and a shock velocity of 13 km $s^{-1}$. The comparison of the southern lobe to both knots suggests that there is faster outflow highlighted by the 'twist'. Upon inspection of the extracted regions (Fig. 6.21), the northern lobe overlaps part of the 'twist' feature and therefore any emission from the north lobe is contaminated.

Ramos-Larios, Guerrero & Miranda (2008) investigate NGC 6881 and its $H_2$, [NII], H$\alpha$ and Br$\gamma$ emission. It is more evolved than *IRAS* 19306+1407 because it shows ionised lobes in H$\alpha$ and Br$\gamma$. Their 1-0 S(1) emission shows that the inner region has a point-symmetric morphology, whilst the atomic emission is an axisymmetric bipolar nebula. They conclude that the $H_2$ emission, arising from the inner region, implies that the final evolution of the PN was the *'ejection of episodic fast collimated outflows with changing directions that interacted with the dense circumstellar envelope.'* Similar point symmetric structures in $H_2$ have been observed in NGC 6537 (Davis et al. 2003), K 4-55 and He 2-437 (Guerrero et al. 2000). In *IRAS* 19306+1407 the 'twist' is formed by the change in the outflow occurring after the formation of the bipolar lobes, or by a precessing outflow that is

carving out the bipolar lobes from the older AGB CSE.

### 7.3.3 The flocculent arc

The high resolution SINFONI image shows a flocculent structure in the bright south-east arc and indicates that the bright arcs consist of a series of clumps. The line ratios measured in these clumps show that shocks are exciting the $H_2$ (Chapter 6), which strongly suggests that a fast-wind is eroding the equatorial bright arcs into clumps. Similar structures have been seen in the lobes of AFGL 618 in H$\alpha$ (Cox et al. 2003) and in $H_2$ in *IRAS* 17150-3224 (Hrivnak et al. 2006). $H_2$ clumps in an equatorial region have been previously observed in CRL 2688 by Sahai et al. (1998). The CO observations of M 1-16 and HD 56126 in Sahai et al. (1994) and Meixner et al. (2004), respectively, suggest a clumpy molecular envelope. In evolved PNe, (e.g. Helix and Ring Nebula) clumpy $H_2$ knots have been detected (e.g. Speck et al. 2003; Matsuura et al. 2007); however, these clumpy regions are excited by UV photons or part of an ionisation front (Speck et al. 2003; Henney et al. 2007). The high resolution SINFONI observations of the bright southeast arc show that a fast-wind is shocking the $H_2$ in the equatorial torus, which would evolve and erode in the PNe stage. High resolution imaging polarimetry is required to investigate if circumstellar dust is coincident with the $H_2$ emission in the form of clumps.

## 7.4 Summary

The combination of near-IR polarimetry and IFS, with supporting archived *HST* images and sub-mm photometry, in conjunction with ALS, DART and $H_2$ shock models, have uncovered the properties of the central source and its surrounding CSE. The final critical data reduction stages, inspection and information extraction was carried out by a custom built IDL package called FUS.

The central source is consistent with a B1-type star with a radius of $3.8 \pm 0.6$ $R_{\odot}$, luminosity of $4500 \pm 340$ $L_{\odot}$ at a distance of $2.7 \pm 0.1$ kpc. Br$\gamma$ emission originates from or close to the central source and is produced by a fast J-shock or heated atomic gas.

The CSE consists of O-rich sub-micrometre dust grains, with a range in temperature from $130 \pm 30$ to $40 \pm 20$ K at the inner and outer radius, respectively, with inner and outer radii of $1.9 \pm 0.1 \times 10^{14}$ and $2.7 \pm 0.1 \times 10^{15}$ m. The CSE became detached $400 \pm 10$ years ago and the mass loss lasted $5700 \pm 160$ years, assuming a constant AGB outflow speed of 15 km $s^{-1}$. The dust mass and total mass of the CSE is $8.9 \pm 5 \times 10^{-4}$ and $1.8 \pm 1.0 \times 10^{-1}$ $M_{\odot}$, assuming a gas-to-dust ratio of 200. The mass loss rate was $3.4 \pm 2.1 \times 10^{-5}$ $M_{\odot}$ $year^{-1}$.

$H_2$ has been detected throughout the CSE and it is located in bright arcs and in the bipolar lobes. The velocity of the $H_2$ is greatest at the end of the lobes. The $r_{21}$ and $r_{32}$ ratios were used as a diagnostic and determined that $H_2$ was excited by bow shaped shocks. The $H_2$ emission does not arise from a dense fluoresced gas or planar shocks. The rotational and vibrational temperatures could not be wholly explained by bow shocks. The CDR values were fitted by combining C- or J-bow shock and fluorescence models. A contribution of fluorescence was observed throughout the CSE, which ranged from 5–77 per cent. The majority of shocks in the CSE can be described by a C-bow shock model with a magnetic field strength of

0.02 to 1.28 mG. The equatorial regions showed the greatest proportion of shocks, whilst the lobes showed a lower proportional of shocks. The polarimetry and IFS highlight a 'twist' feature, which could be due to an episodic jet undergoing a recent change in the outflow direction.

The sub-arcsecond IFS observations have resolved a flocculent structure in the southeast bright arc. This arc consists of several clumps, which have been interpreted as a fast-wind eroding an equatorial torus, which could form into the $H_2$ knots seen in other evolved PNe.

The combination of these observations and models have effectively constrained the spectral type, stellar radius, luminosity and distance, chemistry, dust grain properties, geometry, age, mass loss, excitation mechanism and evolutionary state of the post-AGB star and its surrounding CSE. However, the underlying shaping mechanism could not be constrained.

## 7.5 Future work

The combination of near infrared polarimetry and integral field spectroscopy is a powerful tool for uncovering the properties of post-AGB stars. It has shown that *IRAS* 19306+1407 is a post-AGB object that is on the verge of photo-ionising its CSE. The shaping of the CSE could be caused by the onset of collimated winds resulting from binary interaction or magnetic fields. A small number of binary systems have been detected in post-AGB objects and PNe (e.g. Bond, Liller, & Mannery 1978; Pollacco & Bell 1997). The primary method of detecting binary systems is based on the photometric variation caused by eclipse, irradiation or ellipsoidal effects. However, this technique is limited to close binary systems with periods that are less than 1 to 2 weeks (De Marco, Hillwig, & Smith 2008). Binary (or higher multiple) systems with longer periods can be detected with the radial velocity techniques; however, stellar winds and pulsations can introduce radial velocity shifts into the observations, which can mask the obital periods (e.g. Sorensen & Pollacco 2004; De Marco et al. 2004; Afšar & Bond 2005). De Marco et al. (2008) suggest that observations of intrinsically fainter stars will be less likely to have these effects in the radial velocity measurements. Van Winckel has investigated post-AGB objects that show an infrared dust excess, which is a possible signature of a binary system (e.g van Winckel, Waelkens, & Waters 2000; van Winckel 2001; van Winckel, Maas, & Lloyd-Evans 2004; van Winckel et al. 2006; van Winckel 2007). This infrared emission arises from a circumbinary keplerian dusty disc, which is heated from the binary stars. The candidate post-AGB objects are followed up by a radial velocity study and their circumbinary dusty discs by mid-IR interferometry (van Winckel et al. 2008). A working group called Planetary Nebula Binaries[6] (PlaN-B̈), was formed at the Asymmetric Planetary Nebula IV conference, to combine photometric and radial velocity surveys to detect close binaries. The combination of these surveys could

[6] http://www.noao.edu/wiyn/planb

measure the binary fraction for PNe and provide constraints for theoretical models.

A possible technique to detect binaries is to use spectro-astrometry (Bailey 1998; Brannigan et al. 2006). This method has primarily been used on young stellar objects and can obtain spatial resolution upto 1 mas. The technique uses four long slit positions at high spectral resolution and measures the spatial position of an emission line, such as H$\alpha$. The spectro-astrometric signature is dependent on the origin of the emission.

The molecular envelope can be investigated further by using Échelle spectroscopy of the 1-0 S(1) line. This would enable us to resolve the separation of the cavity walls in velocity. Such a technique has been used to produce a three dimensional representation of the cavity walls in *IRAS* 16594-4656 (van de Steene et al. 2008). Additional IFS in the *J*-band and optical wavelengths can uncover emission from forbidden transitions, such as [FeII] and [NII] and atomic recombination lines, such as H$\alpha$. The [FeII] can be a signature of J-type shocks (see McCoey et al. 2004, and references therein) which can be used as an extra measure of the extinction.

The major uncertainty of determining the inner radii and luminosity of post-AGB stars is the derived distance. The space mission GAIA[7] will measure the distance of 1 billion stars in the galaxy to a distance of $\sim$ 8.5 kpc. It will be able determine the distances to many post-AGB stars within our galaxy, for which presently the distances are either unknown or assumed for a chosen luminosity.

The sub-mm SCUBA observations in this thesis, highlight that colder parts of the CSE can constrain the outer radius. The successor instrument, SCUBA-2, is currently being installed and commissioned on the JCMT. This instrument has an increased sensitivity, approximately by a factor of 3 (Mark Thompson, Private communication), and larger arrays, which would be able to obtain sensitive flux measurements. The future Atacama Large Millimetre Array (ALMA) will revolu-

[7] `http://gaia.esa.int/science-e/www/area/index.cfm?fareaid=26`

tionise observations in the sub-mm. The predicted spatial resolution of 0.1 arcsec is possible with interferometry (Emerson & Baars 2000). In addition, the possibility of detecting polarised emission from cold dust grains, aligned with the magnetic field, would help to determine if magnetic fields are the dominant shaping mechanism in post-AGB stars, PPNe and PNe.

# Glossary

This chapter details commonly used acronyms and abbreviations. The letters that form the acronyms are highlighted in a boldface and upper-case font.

Term used and explanation.

| | |
|---|---|
| ACS | **A**dvanced **C**amera for **S**urveys |
| AGB | **A**symmtotic **G**iant **B**ranch. |
| ALS | **A**xisymmetric **L**ight **S**cattering |
| AO | **A**daptive **O**ptics |
| C | **C**arbon |
| CCD | **C**harge **C**ouple **D**evice |
| CDR | **C**olumn **D**ensity **R**atio. |
| CGS4 | **C**ooled **G**rating **S**pectrometer. |
| CONICA | **CO**ude **N**ear **I**nfrared **C**amer**A** |
| CSE | **C**ircum**S**tellar **E**nvelope |
| CSO | **C**altech **S**ub-millimetre **O**bservatory |
| DART | **D**usty **A**xisymmetric **R**adiative **T**ransfer |
| ESO | **E**uropean **S**outhern **O**bservatory. |
| DUPLEX | **DU**st-**P**rominent **L**ongitudinally **EX**tended |
| Far-IR | **FAR-I**nfra**R**ed. |
| FOV | **F**ield **O**f **V**iew. |
| FUS | **F**itting **U**tillity for **S**INFONI. |

| | |
|---|---|
| FUV | **F**ar **U**ltra**V**iolet |
| GISW | **G**eneral **I**nteracting **S**tellar **W**ind |
| H | **H**ydrogen |
| HI | Atomic Hydrogen. |
| HII | Ionised Hydrogen. |
| $H_2$ | Molecular Hydrogen. |
| He | **H**elium |
| HRC | **H**igh **R**esolution **C**hannel |
| *HST* | ***H**ubble **S**pace **T**elescope* |
| IDL | **I**nteractive **D**ata **L**anguage |
| IFS | **I**ntegral **Field S**pectroscopy. |
| IFU | **I**ntegral **F**ield **U**nit. |
| $IP_J$ | *J*-band polarised flux |
| $IP_K$ | *K*-band polarised flux |
| IR | **I**nfra**R**ed. |
| *IRAS* | ***I**nfra**R**ed **A**stronomical **S**atellite* |
| IRPOL2 | **I**nfra**R**ed **POL**arimetry waveplate. |
| ISAAC | **I**nfrared **S**pectrometer **A**nd **A**rray **C**amera. |
| *ISO* | ***I**nfrared **S**pace **O**bservatory* |
| ISW | **I**nteracting **S**tellar **W**ind |
| JCMT | **J**ames **C**lerk **M**axwell **T**elescope |
| LGS | **L**aser **G**uide **S**tar |
| LOS | **L**ine **O**f **S**ight |
| LSR | **L**ocal **S**tandard of **R**est |
| LTE | **L**ocal **T**hermal **E**quilibrium. |
| MFP | **M**ean **F**ree **P**ath |
| MICHELLE | **M**id-**I**nfrared e**CHELLE** spectrograph |

| | |
|---|---|
| Mid-IR | **MID-I**nfra**R**ed |
| NACO | **NA**OS **CO**NICA. |
| NASO | **N**asmyth **A**daptive **O**ptics **S**ystem |
| Near-IR | **NEAR-I**nfra**R**ed |
| NGS | **N**atural **G**uide **S**tar |
| NICMOS3 | **N**ear **I**nfra**R**ed **C**amera and **M**ulti-**O**bject **S**pectrometer 3 |
| NTT | **N**ew **T**echnology **T**elescope. |
| O | **O**xygen |
| ONFR | **O**n-**T**he-**F**ly **R**eprocessing of *HST* data |
| OPR | **O**tho-**P**ara **R**atio |
| PAH | **P**olycyclic **A**romatic **H**ydrocarbon |
| PDR | **P**hoto**D**issociation **R**egion |
| PN(e) | **P**lanetary **N**ebula(e). |
| PPN(e) | **P**roto-**P**lanetary **N**ebula(e). |
| PSF | **P**oint **S**pread **F**unction |
| QUIRC | **QU**ick **I**nfra**R**ed **C**amera |
| SCUBA | **S**ub-millimetre **C**ommon **U**ser **B**olometer **A**rray |
| SINFONI | **S**pectrograph for **IN**tegral **F**ield **O**bservations in the **N**ear **I**nfrared. |
| SofI | **S**on **of I**SAAC. |
| SOLE | **S**tar-**O**bvious **L**ow-level-**E**longated |
| Spaxel | **SP**ectr**A**l pi**XEL**. A pixel coordinate given in $x$ and $y$ for a IFS data cube that contains a spectrum in the $\lambda$ direction. |
| SPIPE | **S**INFONI **PIPE**line |
| UFTI | **U**KIRT **F**ast **T**rack **I**mager. |
| UIR | **U**nidentified **I**nfra**R**ed |
| UIST | **U**KIRT 1-5 micron **I**mager **S**pec**t**rometer. |

| | |
|---|---|
| UKIRT | **U**nited **K**ingdom **I**nfra**R**ed **T**elescope. |
| UT1 | **U**nitary **T**elescope one. |
| UT4 | **U**nitary **T**elescope four. |
| UV | **U**ltra**V**iolet |
| VLT | **V**ery **L**arge **T**elescope. |
| YPN(e) | **Y**oung **P**lanetary **N**ebula(e). |

# References


Afšar M., Bond H. E., 2005, MmSAI, 76, 608

Allamandola L.J., Tielens A. G. G. M., Barker J. R., 1989, ApJS, 71, 733

Allard E. L., Peletier R. F., Knapen J. H., 2005, ApJ, 633, 25

Allard E. L., Knapen J. H., Peletier R. F., Sarzi M., 2006, MNRAS, 371, 1087

Arquilla R., Leahy D. A., Kwok S., 1986, MNRAS, 220, 125

Bailey J., 1998, MNRAS 301, 161

Bains I., Gledhill T. M., Yates J. A., Richards A. M. S., 2003, MNRAS, 338, 287

Bains I., Richards A. M. S., Gledhill T. M., Yates J. A., 2004, MNRAS, 354, 529

Balick B., 1987, AJ, 94, 671

Balick B., Frank A., 2002, ARA&A, 40, 439

Berry D. S., Gledhill T. M., 2003, Starlink User Note 223, available from `http://www.starlink.ac.uk`

Black J. H., van Dishoeck E. F., 1987, ApJ, 322, 412

Blackman E. G., Frank A., Markiel J. A., Thomas J. H., Van Horn H. M., 2001, Nature, 409, 485

Blackman E. G., Frank A., Welch C., 2001, ApJ, 564, 288

Blackman E. G., Nordhaus J. T., 2007, arXiv, 708, arXiv:0708.4199, for the proceedings of "Asymmetric Planetary Nebuale IV," R. L. M. Corradi, A. Manchado, N. Soker eds

Blöcker T., 1995, VizieR Online Data Catalog, 329, 90755

Blöcker T., 1995, A&A, 299, 755

Bohren C. F., Huffman D. R., 1983, Absorption and Scattering of Light by Small Particles, Wiley.

Bond H. E., Liller W., Mannery E. J., 1978, ApJ, 223, 252

Bonnet H. et al., 2004, The ESO Messenger, 117, 17.

Brand J., Blitz L., 1993, A&A, 275, 67

Brand P. W. J. L., Moorhouse A., Burton M. G., Geballe T. R., Bird M., Wade R., 1988, ApJ, 334, 103

Brannigan E., Takami M., Chrysostomou A., Bailey J., 2006, MNRAS, 367, 315

Bujarrabal V., Alcolea J., Sahai R., Zamorano J., Zijlstra A. A., 1998, A&A, 331, 361

Bujarrabal V., Castro-Carrizo A., Alcolea J., Sánchez Contreras C., 2001, A&A, 377, 868

Burton M. G., Haas M. R., 1997, A&A, 327, 309

Burton M. G., Hollenbach D. J., Tielens A. G. G. M., 1989, Infrared Spectroscopy in Astronomy, 22nd ESLAB Symposium, ed. Kaldeich B., p141

Burton M. G., Brand P. W. J. L., Gaballe T. R., Webster A. S., 1989, MNRAS, 236, 409

Burton M. G., Hollenbach D. J., Tielens A. G. G. M., 1990, ApJ, 365, 620

Burton M. G., Hollenbach D. J., Tielens A. G. G. M., 1992, ApJ, 399, 563

Cappellari M., Copin Y., 2003, MNRAS, 342, 345

Cardelli J. A, Clayton G. C., Mathis J. S., 1989, ApJ, 345, 245

Chrysostomou A., 1993, PhD Thesis

Chrysostomou A., Brand P. W. J. L., Burton M. G., Moorhouse A., 1993, MNRAS, 265, 329

Cohen M., Van Winkel H., Bond H. E., Gull T. R., 2004, AJ, 127, 2362

Cox P., et al., 1997, A&A, 321, 907

Cox P., et al., 1998, ApJ, 495, 23

Cox P., Huggins P. J., Maillard J. P., Muthu C., Bachiller R., Forveille T., 2003, ApJ, 586, 87

Crowther P. A., De Marco O., Barlow M. J., 1998, MNRAS, 296, 367

Dabrowski I., 1984, CaJPh, 62, 1639

Davis C. J., Smith M. D., Stern L., Kerr T. H., Chiar, J. E., 2003, MNRAS, 344, 262

Davis C. J., Smith M. D., Gledhill T. M., Varricatt W. P., 2005, MNRAS 360, 104

Dayal A., Hoffmann W. F., Beiging J. H., Hora J. L., Deutsch L. K., Fazio G. G., 1998, ApJ, 492, 603

De Marco O., Bond H. E., Harmer D., Fleming A. J., 2004, ApJ, 602, 93

De Marco O., Hillwig T. C., Smith A. J., 2008, arXiv, 804, arXiv:0804.2436, Accepted for publication in the Astronomical Journal

Dijkstra C., Speck A. K., 2006, ApJ, 651, 288

Dobrinčić M., Villaver E., Guerrero M. A., Manchado A., 2008, AJ, 135, 2199

Dougados C., Rouan D., Lacombe F., Forveille T., Tiphene D., 1990, A&A, 227, 437

Draine B. T., 1980, ApJ, 241, 1021

Draine B. T., Bertoldi F., 1996, ApJ, 468, 269

Draine B. T., Roberge W. G., Dalgarno A., 1983, ApJ, 264, 485

Dumas C., 2007, approved Kaufer A., released Hainaut O., Very Large Telescope SINFONI user manual, VLT-MAN-ESO-14700-3517, version 80, `http://www.eso.org/instruments/sinfoni/doc/`

Efstathiou A., Rowan-Robinson M., 1990, MNRAS, 245, 275

Egan M.P. et al., 2003, The Midcourse Space Experiment Point Source Catalog Version 2.3

Eisenhauer F. et al., 2003, SPIE 4841, 1548

Eislöffel J., Simth M. D., Davis C. J., 2000, A&A, 359, 1147

Emerson D., Baars J., 2000, ALMA project book, Engineering Specifications, chapter 2.2

Exter K. M., Christensen L., 2005, AIPC, 804, 24

Fernandes A. J. L., Brand P. W. J. L., Burton M. G., 1997, MNRAS, 290, 216

Frank A., De Marco O., Blackman E., Balick B., 2007, arXiv, 712, arXiv:0712.2004, for the proceedings of "Asymmetric Planetary Nebuale IV," R. L. M. Corradi, A. Manchado, N. Soker eds

García-Hernández D. A., Manchado A., García-Lario P., Domínguez-Tagle C., Conway G. M., Prada F., 2002, A&A, 387, 955

García-Lario P., Manchado A., Pych W., Pottasch S. R., 1997, ApJS, 126, 479

García-Segura G., Langer N., Różyczka M., Franco J., 1999, ApJ, 517, 767

García-Segura G., López J. A., Franco J., 2005, ApJ, 618, 919

Gardiner T. A., Frank A., 2001, ApJ, 557, 250

Gawryszczak A. J., Mikołajewska J., Różyczka M., 2002, A&A, 385, 205

Guerrero M. A., Manchado A., 1998, ApJ, 508, 262

Guerrero M. A., Villaver E., Manchado A., Garcia-Lario P., Prada F., 2000, ApJS, 127, 125

Gledhill T. M., 2005, MNRAS, 356, 883

Gledhill T. M., Takami M., 2001, MNRAS, 328, 266

Gledhill T. M., Yates J. A., 2003, MNRAS, 343, 880

Gledhill T. M., Chrysostomou A., Hough J. H., Yates J. A., 2001, MNRAS, 322, 321

Gledhill T. M., Bains I., Yates J. A., 2002, MNRAS, 322, 55

Habing H. J., 1968, Bull. Astr. Inst. Netherlands, 19, 421

Habing H. J., Blommaert J. A. D. L., 1993, IAUS, 155, 243

He L., Whittet D. C. B., Kilkenny D., Spencer Jones J. H., 1995, ApJS, 101, 335

Henney W. J., Williams R. J. R., Ferland G. J., Shaw G., O'Dell C. R., 2007, ApJ, 671, 137

Heras A. M., Hony S., 2005, A&A, 439, 171

Herwig F., 2005, ARA&A, 43, 435

Hodge T. M., Kraemer K. E., Price S. D., Walker H. J., 2004, ApJS, 151, 229

Hollenbach D., McKee C. F., 1989, ApJ, 342, 306

Hollenbach D., Natta A., 1995, ApJ, 455, 133

Hollenbach D. J., Shull J. M., 1977, ApJ, 216, 419

Hora J. L., Latter W. B., Smith H. A., Marengo M., 2006, ApJ, 652, 426

Hrivnak B. J., Volk K., Kwok S., 2000, ApJ, 535, 275

Hrivnak B. J., Kelly D. M., Su K. Y. L., Kwok S., Sahai R., 2006, ApJ, 650, 237

Hummer D. G., Storey P. J., 1987, MNRAS, 224, 801

Hurwitz M., 1998, ApJ, 500, 67

Joint *IRAS* Science working group, Infrared Astronomical Satellite Catalogs, 1988. The Point Source Catalog, version 2.0, NASA RP-1190

Joshi Y. C., 2005, MNRAS, 362, 1259

Kahn F. D., West K. A., 1985, MNRAS, 212, 837

Kastner J. H., Weintraub D. A., Gatley I., Merrill K. M., Probst R. G., 1996, ApJ, 462, 777

Kelly D. M., Hrivnak B. J., 2005, ApJ, 629, 1040

Kelly D. M., Hrivnak B. J., Kwok S., Hinkle K., 2004, in Meixner M., Kastner J., Balick B., Soker N., eds, ASP Conf. Ser. 313, Asymmetric Planetary Nebulae III, Astron. Soc. Pac., San Fransico, p. 343

Kissler-Patig M., Szeifert T., 2005, The Very Large Telescope SINFONI user manual, VLT-MAN-ESO-14700-3517, Issue 1.3

Kwok S., 1993, ARA&A, 31, 63

Kwok S., 2000, The origin and evolution of planetary nebulae, eds. King A., Lin D., Maran S., Pringle J., Ward M., Cambridge University Press, p192

Kwok S., 2004, Nature, 430, 985

Kwok S., Purton C. R., Fitzgerald P. M, 1978, ApJ, 219, 125

Kwok S., Volk K., Bidelman W. P., 1997, ApJS, 112, 557

Latter W. B., Kelly D. M., Hora J. L., Deutsch L., K., 1995, ApJS, 100, 159

Latter W. B., Dayal A., Bieging J. H., Meakin C., Hora J. L., Kelly D. M., Tielens A. G. G. M., 2000, ApJ, 539, 783

Le Bourlot J., Pineau des Forêts G., Flower D. R., Cabrit S., 2002, MNRAS, 332, 985

Likkel L., 1989, ApJ, 344, 350

Likkel L., Forveille T., Omont A., Morris M., 1991, A&A, 246, 153

Lowe K. T. E., Gledhill T. M., 2005, in Adamson A., Aspin C., Davis C. J., Fujiyoshi T., eds, ASP Conf. Ser. Vol. 343, Astronomical Polarimetry: Current Status and Future Directions, Astron. Soc. Pac., San Fransico, p282

Lowe K. T. E., Gledhill T. M., 2006, IAUS, 234, 451

Lowe K. T. E., Gledhill T. M., 2007, MNRAS, 374, 176

Markwardt C., 2006, Markwardt IDL Library, http://cow.physics.wisc.edu/∼craigm/idl/idl.html

Mastrodemos N., Morris M., 1998, ApJ, 497, 303

Matsuura M. et al., 2004, ApJ, 604, 791

Matsuura M., Speck A. K., Smith M. D., Zijlstra A. A., Viti S., Lowe K. T. E., Redman M., Wareing C. J., Lagadec E., 2007, MNRAS, 382, 1447

McCoey C., Giannini T., Flower D. R., Caratti o Garatti A., 2004, MNRAS, 353, 813

Meixner M. et al., 1993, ApJ, 411, 266

Meixner M., Ueta T., Bobrowski M., Speck A., 2002, ApJ, 571, 936

Meixner M., Zalucha A., Ueta T., Fong D., Justtanont K., 2004, ApJ, 614, 371

Meixner M., McCullough P., Hartman J., Son M., Speck A., 2005, ApJ, 130, 1784

Ménard F., 1989, PhD thesis, Univ. Montreal

Mie G., 1908, Annalen der Physik, 330, 377

Moe M., De Marco O., 2006, ApJ, 650, 916

Moffat A. P. J., 1969, A&A, 3, 455

Molster F. J., Waters L. B. F. M., Tielens A. G. G. M., Barlow M. J., 2002, A&A, 382, 184

Monet D. G. et al., 2003, AJ, 125, 984

Monreal-Ibero A., Roth M. M., Schönberner D., Steffen M., Böhm P., 2005, ApJ, 628, 139

Murakawa K., Nakashima J., Ohnaka K., Deguchi S., 2007, A&A, 470, 957

Neri R., Kahane C., Lucas R., Bujarrabal V., Loup C., 1998, A&AS, 130, 1

Nordhaus J., Blackman E. G., 2006, MNRAS, 370, 2004

Nordhaus J., Blackman E. G., Frank A., 2007, MNRAS, 376, 599

Omont A., Loup C., Forveille T., te Lintel Hekkert P., Habing H., Sivagnanam P., 1993, A&A, 267, 515

Ossenkopf V., Henning Th., Mathis J. S., 1992, A&A, 261, 567

Ott T., 2005, QFITSVIEW, `http://www.mpe.mpg.de/~ott/QFitsView`, Max Planck Society for the Advancement of Science

Pégourié B., 1988, A&A, 194, 335

Pickles A. J., 1998, PASP, 110, 863

Pollacco D. L., Bell S. A., 1997, MNRAS, 284, 32

Preibisch Th., Ossenkopf V., Yorke H. W., Henning Th., 1993, A&A, 279, 577

Ramos-Larios G., Guerrero M. A., Miranda L. F., 2008, AJ, 135, 1441

Ramsay Howatt S.K. et al., 1998, SPIE, 3354, 456

Richter M. J., Graham J. R., Wright G. S., 1995, ApJ, 454, 277

Rudy R. J., Lynch D. K., Mazuk S., Puetter, R. C., Dearborn D. S. P., 2001, AJ, 121, 362

Sabin L., Zijlstra A. A., Greaves J. S., 2007, MNRAS, 376, 378

Sahai R., 2004, ASPC, 313, 141

Sahai R., Contreras C. S., 2004, in Meixner M., Kastner J., Balick B., Soker N., eds, ASP Conf. Ser. 313, Asymmetric Planetary Nebulae III, Astron. Soc. Pac., San Fransico, p. 32

Sahai R., Wootten A., Schwarz H. E., Wild W., 1994, ApJ, 428, 237

Sahai R., Hines D. C., Kastner J. H., Weintraub D. A., Trauger J. T., Rieke M. J., Thompson R. I., Schneider G., 1998, ApJ, 492, 163

Sahai R. et al., 1998, ApJ, 493, 301

Sahai R., Sánchez Contreras C., Morris M., 2005, ApJ, 620, 948

Sahai R., Young K., Patel N. A., Sánchez Contreras C., Morris M., 2006, ApJ, 653, 1241

Sahai R., Morris M., Sánchez Contreras C., Claussen M., 2007, AJ, 134, 2200

Sandin C., Schönberner D., Roth M. M., Steffen M., Monreal-Ibero A., Böhm P., Tripphahn U., 2006, IAUS, 234, 501

Santander-García M., Corradi R. L. M., Mampaso A., 2005, AIPC, 804, 179

Santander-García M., Corradi R. L. M., Whitelock P. A., Munari U., Mampaso A., Marang F., Boffi F., Livio M., 2007, A&A, 465, 481

Schlegel D. J., Finkbeiner D. P., Davis M., 1998, ApJ, 500, 525

Schönberner D., 1983, ApJ, 272, 708

Sharp R. G., Reilly N. J., Kable S. H., Schmidt T. W., 2006, ApJ, 639, 194

Siódmiak N., Meixner M., Ueta T., Sugerman B. E. K., Van de Steene G. C., Szczerba R., 2008, ApJ, 677, 382

Smith M. D., 1994, MNRAS, 266, 238

Smith M. D., Brand P. W. J. L., 1990a, MNRAS, 242, 495

Smith M. D., Brand P. W. J. L., 1990b, MNRAS, 243, 498

Smith M. D., Brand P. W. J. L., 1990c, MNRAS, 244, 384

Smith M. S., Brand P., Moorhouse A., 1991, MNRAS, 248, 451

Smith M. S., Davis C. J., Lioure A., 1997, A&A, 327, 1206

Soker N., 2001, ApJ, 558, 157

Soker N., 2002, MNRAS, 330, 481

Soker N., 2006a, ApJ, 645, 57

Soker N., 2006b, PASP, 118, 260

Soker N., Rappaport S., 2000, ApJ, 538, 241

Soker N., Rappaport S., 2001, ApJ, 557, 256

Soker N., Subag E., 2005, AJ, 130, 2717

Sorensen P., Pollacco D., 2004, ASPC, 313, 515

Speck A. K., Meixner M., Jacoby G. H., Knezek P. M., 2003, PASP, 115, 170

Sternberg A., Dalgarno A., 1989, ApJ, 338, 197

Su K. Y. L., Hrivnak B. J., Kwok S, Sahai R., 2003, AJ, 126, 848

Suárez O., Gómez J. F., Morata O., 2007, A&A, 467, 1085

Tsamis Y. G., Walsh J. R., Péquignot D., Barlow M. J., Danziger I. J., Liu X.-W., 2008, MNRAS, 386, 22

Turner J., Kirby-Docken K., Dalgarno A., 1977, ApJS, 35, 281

Ueta T., Meixner M., Bobrowsky M., 2000, ApJ, 528, 861

Ueta T., Meixner M., Moser D. E., Pyzowski L. A., Davis J. S., 2003, AJ, 125, 2227

Ueta T., Murakawa K., Meixner M., 2005, AJ, 129, 1625

Vassiliadis E., Wood P. R., 1994a, yCat, 209, 20125

Vassiliadis E., Wood P. R., 1994b, ApJS, 92, 125

van de Steene G. C., van Hoof P. A. M., 2003, A&A, 406, 773

van de Steene G. C., Ueta T., van Hoof P. A. M., Reyniers M., Ginsburg A. G., 2008, A&A, 480, 775

van der Veen W. E. C. J., Habing H. J., Geballe, T. R., 1989, A&A, 226, 108

van Winckel H., 2001, Ap&SS, 275, 159

van Winckel H., 2003, ARA&A, 41, 391

van Winckel H., 2007, BaltA, 16, 112

van Winckel H., Waelkens C., Waters L. B. F. M., 2000, IAUS, 177, 285

van Winckel H., Maas T., Lloyd-Evans T., 2004, ASPC, 313, 536

van Winckel H., Lloyd Evans T., Reyniers M., Deroo P., Gielen C., 2006, MmSAI, 77, 943

van Winckel H., Deroo P., Gielen C., Reyniers M., van Aarle E., Vidal E., 2008, AIPC, 1001, 349

Volk K., Hrivnak B. J., Kowk S., 2004, ApJ, 616, 1181

Wilgenbus D., Cabrit S., Pineau des Forêts G., Flower D. R., 2000, A&A, 356, 1010

Zhang C. Y., Kwok S., 1998, ApJS, 117, 341

# Appendix A

# IDL code.

## A.1 fitndfcube.pro – an IDL fitting program for UKIRT IFS cubes.

```
PRO fitndfcube
;This program fits emission lines to UKIRT IFU data, in the K-band.
; Author Krispian Lowe.

!P.MULTI = 0

set_plot, 'X'                    ;Setting the display to X windows

dummyalert = dialog_message("Please select your NDF IFS cube please: " $
             , /information)
                                 ;Alerts the user what to put in.

cubefile = dialog_pickfile(/read,filter='*.sdf')
                                 ;Pop-up dialogue box to select the NDF
                                 ;cube file.

cube = read_ndf(cubefile,0.0)    ;Reads the NDF data cube in.

cubesize = size(cube,/dimensions)
                                 ;Determines the datacubes name

loadct, 13                       ;Loading the colour table for X windows

device, retain=2, set_character_size=[10,12]
                                 ;Setting device information.
```

```
image = fltarr(cubesize[0],cubesize[1])
                                ;Creating an image array which has the
                                ;spatial dimensions of the IFS cube.

;A long FOR loop. This is the best way I can write this part of code.

for j = 0,  cubesize[1]-1 do begin
    for i = 0, cubesize[0]-1 do begin

        image[i,j] = total(cube[i,j,*])
                                ;Setting each pixel in the image
                                ;array to the sum (total) of the equivalent
                                ;spacial co-ordinate in the data cube.
    endfor
endfor

;tv, bytscl(frebin(image[0:cubesize[0]-1,0:cubesize[1]-1],512,512),min=0.0,max=1.0E-11)

dummyalert = dialog_message("Select the Wavelength data file (ascii format) ", /informat
                                ;Informing the user that a wavelength
                                ;table has to be supplied.
                                ;This can be obtained by using
                                ;FIGARO:ascout on a collapsed spectra
                                ;or extracting the lutmap for the
                                ;current frame, using KAPPA:wcsshow.

wavefile = dialog_pickfile(/read,filter='*.dat')
                                ;Reading the wave table file location
rdfloat, wavefile, lambda
                                ;Reading in the wave table.
                                ;It has to be a single column with no
                                ;tables headers/footers.

window, 0, ysize=512, xsize=2048;Setting the size of the display window

speccube = fltarr(cubesize[2])
                                ;Creating a spectrum array using the
                                ;cube dimensions

for i = 0, cubesize[2] -1 do begin

    speccube[i] = total(cube[*,*,i])
                                ;The summation of the data cube into a
                                ;1D spectrum
endfor
```

```
FMT = 'A, F'

readcol, '/local/home/klowe/data/IDL/custom_idl/LF_models/linelist.dat',F=FMT,
                                ;The line list for All visible lines
                                ;in the Near-IR.

lineid_plot, lambda,speccube,wline,text,LCHARSIZE=.7, $
    xmargin=[0,0],xstyle=1,ystyle=1,/ynozero,EXTEND=1
                                ;Plotting the spectrum out to X windows.

dummyalert = dialog_message("Select the emission line.", /information)
cursor, xcur, ycur, /data
                                ;The user selects
                                ;their emission line.

nearest0 = Min(Abs(wline - xcur), index)

print, "NEAREST FIVE LINES to the CHOSEN POSITION:"
print, "-----------------------------------"
print, '1: NEAREST: ', wline[index], " um  ", text[index], " by ", Abs(wline[i
print, '2: NEAREST: ', wline[index+1], " um  ", text[index+1], " by ", Abs(wli
print, '3: NEAREST: ', wline[index-1], " um  ", text[index-1], " by ", Abs(wli
print, '4: NEAREST: ', wline[index+2], " um  ", text[index+2], " by ", Abs(wli
print, '5: NEAREST: ', wline[index-2], " um  ", text[index-2], " by ", Abs(wli

xcur1 = [xcur]
ycur1 = [ycur]
                                ;Translating the cursor positions
                                ;into a nice variable.
oplot, float(xcur1), float(ycur1), color=100, psym=1
                                ;Plots the centre position on the image

check2 = where(lambda le xcur)
check3 = where(lambda ge xcur)
                                ;Finding out which array element is
                                ;nearest the cursor.

ilow   = fix(max(check2)-10)
ihigh  = fix(min(check3)+10)
                                ;+10 and -10 the cursors position.

print, ihigh, ilow
                                ;Printing out those values to the screen.
```

```
if ihigh gt 1023 then begin

    ihigh = 1023                ;If the +10 value is greater than 10 then
                                ;the value will be reduced to the maximum value.
endif

X = fltarr(ihigh-ilow + 1)      ;Setting up an 1-D array
                                ;with small number

;print, X1, fix(min(check3)+10), fix(max(check2)-10)

for ip = 0, (ihigh - ilow) do begin

    X[ip] = fix(ip) + ilow      ;fix converts the value to an integer.
                                ;Shifting the X array to the right
                                ;position in the 1D spectrum array
endfor

start   = [1.4D-17, fix(max(check2)), 1.D, 1.D-12]
                                ;The starting values are:
                                ;Continuum: 1.4x10\^-17     ::P(0)
                                ;The starting point is
                                ;the point you
                                ;clicked (check2)          ::P(1)
                                ;Sigma of one pixel        ::P(2)
                                ;With an Area of  !x10\^-12 ::P(3)

exp     = ' P(0) + GAUSS1(X,P(1:3))'
                                ;A flat continuum with a gaussian on
                                ;top.

areaarray    = fltarr( cubesize[0], cubesize[1] )
                                ;The area under the gaussian fit (2D
                                ;array)
centrearr    = fltarr( cubesize[0], cubesize[1] )
                                ;The central pixel value of the
                                ;gaussian fit (2D array)
writeerror   = fltarr( 4 )
                                ;The error array (1D array)
areaarrayerr = fltarr( cubesize[0], cubesize[1] )
                                ;The error in the area (2D array)
centrearrerr = fltarr( cubesize[0], cubesize[1] )
                                ;The error in the mean value (2D array)
sigmaarr     = fltarr( cubesize[0], cubesize[1] )
                                ;The width of the line
```

```
sigmaarrerr  = fltarr( cubesize[0], cubesize[1] )
                                ;The error in the width
contarr      = fltarr( cubesize[0], cubesize[1] )
                                ;The continuum values
contarrerr   = fltarr( cubesize[0], cubesize[1] )
                                ;The error in the continuum.
areaarray[*,*] = 0.0            ;Zero the array
centrearr[*,*] = 0.0            ;Zero the array

pi = replicate({fixed:0, limited:[0,0], limits:[0.D,0.D]},4)
                                ;Creating the constrain parameter pi
                                ;for each fitting variable.

pi(1).limited(0) = 1            ;Activate the low mean constraint
pi(1).limited(1) = 1            ;Activate the high mean constraint
pi(1).limits(0)  = double(ilow + 8)
                                ;The lower limit is 8 bins greater
                                ;than the lower wavelength limit
pi(1).limits(1)  = double(ihigh - 8)
                                ; The higher limit is 8 bins lower
                                ; than the highest wavelength limit
if ihigh eq 1023 then begin

    pi(1).limits(1) = double(1023)
                                ;If your at the edge of the spectrum
                                ;then the upper limit is at the end of
                                ;the spectrum.
endif

pi(2).limited(1) = 1            ;The upper limit for the width of
                                ;the line is set
pi(2).limits(1)  = double(4.0)  ;The max width is 4 pixels
pi(3).limited(0) = 1            ;The lower area limit is set
pi(3).limits(0)  = 0.0>0.0      ;The lowest limit is zero and
                                ;has to be greater than zero

read, centwave, PROMPT="PLEASE enter the wavelength: "
                                ;You have to enter the rest wavelength
dummy = "dummy"

read, dummy, PROMPT="PLEASE enter a filename: "
                                ;You have to enter the File name Prefix

;This section selects a region of the continuum to estimate the errors
;in fitting.
```

```
print, "CLICK A FEATURELESS POINT ON THE CONTINUUM."

cursor, xcontit, ydummy, /data  ;obtaining the cursor position.
print,  xcontit

xcontit1 = [xcontit]
ydummy1  = [ydummy]

oplot, xcontit1, ydummy1, color=150, psym=1
                                ;Plots the central point you clicked.

checkxcon2 = where(lambda le xcontit)
checkxcon3 = where(lambda ge xcontit)
                                ;Finding the bin number nearest to the
                                ;chosen wavelength

ilowxcon   = fix(max(checkxcon2)-10)
ihighxcon  = fix(min(checkxcon3)+10)
                                ;Taking wavelength bin numbers +10 and
                                ;-10 from the initial point.

oplot,  [lambda[ilowxcon]], ydummy1, color=200, psym=2
oplot,  [lambda[ihighxcon]],ydummy1, color=200, psym=2
                                ;Plotting the range of the continuum.
;oplot, lambda[ilowxcon], ydummy

set_plot,'PS'                   ;Setting the plotting environment to Postscript.

epsname = dummy+"fits.eps"      ;setting the output name.

epsname = strcompress(epsname,/remove_all)
                                ;Removing all white spaces from the
                                ;file name.

device, /color,/inches, xsize=8.27,ysize=11.69,/encapsul,filename=epsname,bits=8
                                ;Setting the page size. I think it is
                                ;A4. (in inches).
!P.MULTI = [66, 6, 11]          ;Setting up how many images per page. 11 rows of 6 colum

count   = 1
counter = 1

error_cont_before = fltarr(cubesize[2],cubesize[2])
                                ;Setting the error array to zero.
```

```
for j = 0, cubesize[1] -1 do begin

    for i = 0, cubesize[0] -1 do begin
                                ;The for loops are setup for every
                                ;spatial pixel.
        if ( total(cube[i,j,0:cubesize[2]-1]) gt 0.0 ) then begin
                                ;If there is a x,y position that has
                                ;no flux detail it is not
                                ;considered. This is due to
                                ;UKIRT:UIST:IFU with a interesting
                                ;slit alignments.

            ;for ki = ilowxcon, ihighxcon do begin

            ;    for kip = ilowxcon,  ihighxcon do begin
                            ;        if  ( kip ne ki ) then begin
                            ;           error_cont_before[ki,kip] = abs(cube[i
            ;        endif
                            ;    endfor

            ;endfor
                                ;Above is the old method. It was slow
                                ;and cumbersome, below is a quicker method.

            error_cont = stddev(cube[i,j,ilowxcon:ihighxcon]>0.0)
                                ;This ignores any negative spikes,
                                ;which do occur as a artefact of the
                                ;scrunching and cube reforming method.

            spectra  = cube[i,j,*]
                                ;Extracting a spectra from the data cube
            spectra2 = spectra[ilow:ihigh]
                                ;Extracting the area we are interested in.
            result   =   $
MPFITEXPR(exp,X,spectra2,error_cont,start,/quiet,parinfo=pi,perror=writeerror)
                                ;This is the main fitting
                                ;algorithm. It fits our Gaussian,
                                ;exp, using a free X variable array,
                                ;to spectra 2.
                                ;The error_count is the error
                                ;values. Start gives the starting
                                ;points. /quiet removes all bumpf from
                                ;the terminal window. Parinfo
                                ;indicates that I have stated limits,
```

```
                    ;with the errors written out to writeerror.

contarr[i,j]      = result(0)
contarrerr[i,j]   = writeerror(0)
                    ;The continuum, contarr[i,j], is in
                    ;W m\^-2 um\^-1
                    ;The error is also in W m\^-2 um\^-1

                    ;The difference in wavelength is
                    ;2.279766377349270E-04

centrearr[i,j]    = (((lambda[0]+(result(1)*2.279766377349270E-04))$
                      -centwave)/centwave) * 3E5
                    ;Gives a velocity in km s\^-1
centrearrerr[i,j] = (writeerror(1)) * ((2.279766377349270E-04/centwave)* 3E5
                     ;The error in the wavelength.
sigmaarr[i,j]     = result(2) * 2.279766377349270E-04
                    ;The line widths in microns
sigmaarrerr[i,j]  = writeerror(2) * 2.279766377349270E-04
                    ;Error given in microns
areaarray[i,j]    = result(3) * 2.279766377349270E-04
                    ;The flux of the emission line (Area
                    ;under the gaussian. The units are in
                    ;W m\^-2 arcsec\^-2*
                    ;* -If the data is formatted for per arcsec\^2.
areaarrayerr[i,j] = writeerror(3) * 2.279766377349270E-04
                    ;Error for the emission line in W m\^-1 arcsec\^-2*
if areaarray[i,j] eq 0.0 then begin

    centrearr[i,j] = 0.0

endif

titlestring = strcompress(string(i+1)+"_"+string(j+1),/remove_all)

plot, lambda[ilow:ihigh], spectra[ilow:ihigh], color=0,$
  title=titlestring, xticks=2,yticks=2, xstyle=1, $
  ystyle=1

oplot, lambda[ilow:ihigh], result(0) + GAUSS1(X,result(1:3)), color=100
                    ;Plotting th fit out to the Postscript file.
count = count + 1

if count eq 67 then begin
```

```
                count = 1

                device, /close

                epsname = dummy+"fits"+string(counter)+".eps"

                epsname = strcompress(epsname,/remove_all)

                device, /color,/inches, xsize=8.27,ysize=11.69,/encapsul,$
                  filename=epsname,bits=8

                counter = counter + 1

            endif
        endif
    endfor
endfor

device, /close

!P.MULTI = 0

set_plot, 'X'                   ;Resetting the display to X

;Setting the file names:
filenameoutlineout = strcompress(dummy+"_line",/remove_all)
filenameoutcentout = strcompress(dummy+"_vel",/remove_all)
filenameoutsigmout = strcompress(dummy+"_sigma",/remove_all)
filenameoutcontout = strcompress(dummy+"_cont",/remove_all)

;writing out data to the data and variance arrays.
write_ndf, areaarray, filenameoutlineout, comp='data'
write_ndf, areaarrayerr, filenameoutlineout, comp='v'

write_ndf, centrearr, filenameoutcentout,comp='data'
write_ndf, centrearrerr, filenameoutcentout,comp='v'

write_ndf, sigmaarr, filenameoutsigmout, comp='data'
write_ndf, sigmaarrerr, filenameoutsigmout, comp='v'

write_ndf, contarr, filenameoutcontout, comp='data'
write_ndf, contarrerr, filenameoutcontout, comp='v'

;Outputting the sum of the cube. i.e. a white light image.
write_ndf, image*(lambda[1023] -lambda[0]), 'Sum_of_cube',  comp='data'
```

```
END
```

## A.2 linefitting.pro

```
;+
;-------------------------------------------------------------
; NAME:
;   LINEFITTING with modules:
;
;      ANALBENCH, LFIT, SINGLEFIT, GAUSSFITTING, SAVE_LINEFITS,
;      REPLOTLINEFIT, SAVE_SPEC, CORRECT, MOVEPOINT, SELECTED, INTERPOL,
;      REPLOTSTDSPEC, OPLOTMODEL, MODELLOAD, FLUX_CALIB, DO_FLUXC, NORMBB,
;      READTEMP, BBGEN, STD_DIV_BBNORM, OPENREDCUBE, OPENCUBE, SPECTRUMLOAD,
;      CHANGE_CUT99, CHANGE_CUT, INSPECT_CUBE,GET_SPECTRA, HELP, EXIT_GUI,
;      VERSION, SAVE_CUBE, SKEWBENCH and SKEWFIX.
; AUTHOR:
;
;    Krispian T. E. Lowe, University of Hertfordshire, College Lane,
;    Hatfield,AL10 9AB
;    klowe at herts ac uk or krispian_lowe at hotmail com
;
; PURPOSE:
;
;    This programs and collection of modules were designed to analyse
;    SINFONI data. It can be used to inspect data, correct the 'skew'
;    through the cube, flux calibrate, remove intrinsic spectral lines
;    in standard spectra and fit user specified lines.
;
;    The line fitting uses MPFIT and various other routines developed
;    by Craig B. Markwardt. The latest version of his code are
;    available at http://cow.physics.wisc.edu/~craigm/idl/idl.html
;    I am indebted to this versitile code and wish to give him a bit
;    thanks.
;
; USAGE:
;
;    It is very simple type in ".r Linefitting" to compile the code
;    and then type "linefitting", please remember to remove the quote
;    marks.
;    You need to set up a IDL path to the location of MPFIT (etc.) and
;    Astronomy IDL libraries. The Astronomet Libraries can be found at
;    http://idlastro.gsfc.nasa.gov/homepage.html
;
;    NOTE: Please do not run multiple operations of linefitting
;          because I have used common variables and it might do
;          something nasty. This program should not overwrite orignal
;          data qutomatically. That could only be achieved if the user
```

```
;          intensionally wished to do so. Even so I do not take any
;          responsibily if any loss of data does occur. I will do
;          everything in my power to fix any problems.
;;
; BUGS:
;
;    I have no doubt that there are lots and many. If you do find a
;    bug please e-mail me and I will fix it.
;
;    But there are not any really bad bugs.
;
; DESCRIPTION:
;
;    This is brief desciption of the code. Each module has it own
;    documentation.
;
;    The module tree flow below
;
;    LINEFITTNG
;        +-OPENCUBE
;        +-SPECTRUMLOAD
;        +-SAVE_CUBE
;        +-OPENREDCUBE
;        +-EXIT_GUI
;        +-SKEWBENCH
;        |     +-SKEWFIX
;        |     +-EXIT_GUI
;        +-ANALBENCH
;        |     +-EXIT_GUI
;        |     +-SAVE_SPEC
;        |     +-CORRECT
;        |     |   +-MODELLOAD
;        |     |   +-SAVE_SPEC
;        |     |   +-REPPLOTSTDSPEC
;        |     |   +-OPLOTMODEL
;        |     |   +-INTERPOL
;        |     |   +-MOVEPOINT
;        |     |   +-EXIT_GUI
;        |     +-LFIT
;        |     |   +-REPLOTLINEFIT
;        |     |   +-SAVE_LINEFITS
;        |     |   +-GAUSSFITTING
;        |     |   +-SINGLEFIT
;        |     +-BBGEN
;        |     |   +-READTEMP
```

```
;        |     |   +-EXIT_GUI
;        |     +-NORMBB
;        |     +-STD_DIV_BBNORM
;        |     +-FLUX_CALIB
;        |     |   +-DO_FLUXC
;        |     |   +-EXIT_GUI
;        |     +-SELECTED
;        +-HELP
;        +-VERSION
;        +-CHANGE_CUT99
;        +-CHANGE_CUT
;        +-GET_SPECTRA
;        +-INSPECT_CUBE
;
; FUTURE DEVELOPMENTS:
;
;    These are a few things that I might do later, if I have time.
;
;    1. Measure the skew effect with a standard observation and apply
;       that to an observation cube. This is because if sources are not
;       point source like.
;
;    2. Correct for extinction. I am talking about intrinsic
;       extinction. The ratio of the 1-0S(1) line and the 1-0Q(3) line
;       have the same ratio and it would be possible to correct for
;       extinction. This would only work for K-band data initially.
;
;    3. Customisation of the fitting procedure. I have hard coded some
;       constraints. These were made to implement a quick roll out of
;       the code.
;
;    4. Anything that is suggested by users of this code.
;
; +=+=+=+=+=+=+=+=+=+=+=+=+=+=+=+=+=+=+=+=+=+=+=+=+=+=+=
; Comment convention starts at 0 and markers out at 77
; This excludes discriptions of common variables and PRO
; +=+=+=+=+=+=+=+=+=+=+=+=+=+=+=+=+=+=+=+=+=+=+=+=+=+=+=
;
;---------------------------------------------------------------------------
PRO linefitting

common set_sinfoni_data, cubearray, stdspectrum, wavelength, cal_standard, cal
;      Cubearray    - The Main array for the Object SINFONI data it is
;                     displayed in the main display area.
;      stdspectrum  - This is the main standard spectra.
```

```
;      wavelength   - The main wavelength which is used.
;      cal_standard - Calibrated standard based on its catalogue flux.
;      cal_object   - The flux calibrated object, which is read into
;                     cube array.

common set_file_check,   cubeopen, specopen, reducedopen
;      cubeopen     - Has the raw object cube been opened? 1 = yes ; 0 = no
;      specopen     - Has the standard 1D spectrum been opened? 1 = yes ; 0 = no
;      reducedopen  - Has the reduced cube been opened? 1 = yes ; 0 =
;                     no

common set_drawing,      drawid, slidepos, drawid2
;      drawid   -  The draw ID of the main window
;      slidepos -  The value of the slider position
;      drawid2  -  The drawid of the wavelength information

common set_rescale,      high, low, pphigh, pplow, textmax, textmin
;      high    - The high scale value to display the cube in the main window
;      low     - The low scale value to display the cube in the main window
;      pphigh  - The high user value from the rescale image
;      pplow   - The low user value from the rescale image
;      textmax - The high user value widget
;      textmin - The low user value widget

common set_autocutm,     textac, labelam, labelas
;      textac  - The text widget for the autocut
;      labelam - setting the new mean widget
;      labelas - setting the new sigma widget

common set_sizes,        jmax, kmax, imax, cubearraysize
;      jmax          - The maximum array indice for X in the array cubearray
;      kmax          - The maximum array indice for Y in the array cubearray
;      imax          - The maximum array indice for LAMBDA in the array cubearray
;      cubearraysize - The true array size for cubearray

common set_slider,       slider1
;      The slider widget variable name

common set_group_par,    tlb
;      The master (Group leader) widget_base variable

common set_specget,      draw1
;      This is the variable which is redundant

!P.MULTI = 0
```

```
;set_plot, 'X'

cubeopen    = 0
specopen    = 0
reducedopen = 0
slidepos    = 970

jmax = 63
kmax = 63


arrayflat= dblarr(jmax+1,kmax+1)

for i = 0, jmax do begin

    for j = 0, kmax do begin

        arrayflat[i,j] = double(i)+double(j)

    endfor

endfor


meanflat   = mean(arrayflat)
stddevflat = stddev(arrayflat)

;This program is an interactive program that can fit any line.

;This first section launches a dialogue box!

;This is the Base of the widget!
tlb = widget_base(column=1,mbar=mbar,$
title="Welcome to Krispian's SINFONI line fitting program!",
 /tlb_size_events,frame=1)

;This is the menu bar.
filemenu = widget_button(mbar,value='File')
fileopt1 = widget_button(filemenu,value='Open Raw Data Cube',
 event_pro='opencube')
fileopt2 = widget_button(filemenu,value='Open Standard Spectra',
 event_pro='spectrumload')
fileopt5 = widget_button(filemenu,value='Save Data Cube',
 event_pro='save_cube',/separator)
```

```
fileopt3 = widget_button(filemenu,value='Open Flux Calibrated Cube',
event_pro='openredcube',/separator)
fileopt4 = widget_button(filemenu,value='Exit',/separator,
event_pro='exit_gui')

rebinbench = widget_button(mbar,value='Rebin Spatial scale')
rebinopt1  = widget_button(rebinbench,value='Open Rebin Toolbox...',
 event_pro='binup_widget')

skewbench = widget_button(mbar,value='Correct SINFONI skew')
analopt1  = widget_button(skewbench,value='Open Skew fix Bench...',
event_pro='skewbench')

analbench = widget_button(mbar,value='Analysis Bench')
analopt1  = widget_button(analbench,value='Open Bench...',
 event_pro='analbench')

compline  = widget_button(mbar,value='L.R. Maps')

linecomp  = widget_button(compline,value='Compare two images',
 event_pro='linecomp')
extinctc  = widget_button(compline,value='Correct for extinction',
 event_pro='extinct_cor')


helpmenu = widget_button(mbar,value='Help?')
helpopt1 = widget_button(helpmenu,value='Introduction',event_pro='help')
helpopt2 = widget_button(helpmenu,value='About this Program',
/separator,event_pro='version')

fbase = widget_base(tlb,row=1,frame=1)
fbasedetc = widget_base(column=1,frame=1,group_leader=tlb,
 title="The wavelength dimension.")


pphigh = strcompress(string(300))
pplow  = strcompress(string(0.0))

labelmax = widget_label(fbase,value="Max: ")
textmax  = widget_text(fbase,/editable,xsize=10,value=pphigh,
 event_pro='change_cut99')
labelmin = widget_label(fbase,value=" Min")
textmin  = widget_text(fbase,/editable,xsize=10,value=pplow,
event_pro='change_cut99')
applymm  = widget_button(fbase,value='APPLY',xsize=60,$
```

```
                          event_pro='change_cut99')
fbase2   = widget_base(tlb,row=3,frame=1)
labelac  = widget_label(fbase2,value="Auto-mean +/- N*sigma | N:")
textac   = widget_text(fbase2,/editable,xsize=10,value='1.0',
 event_pro='change_cut')
applyac  = widget_button(fbase2,value='Apply autocut',xsize=100,$
                          event_pro='change_cut')

automean  = string(mean(arrayflat[0:jmax,0:kmax]))
autosigma = string(stddev(arrayflat[0:jmax,0:kmax]))

labelbam  = widget_label(fbase2,value='Auto mean: ')
labelam   = widget_label(fbase2,value=automean)
labelbas  = widget_label(fbase2,value='Sigma: ')
labelas   = widget_label(fbase2,value=autosigma)

loadct, 13

device, retain=2, set_character_size=[10,12]

draw1 = widget_draw(tlb,xsize=512,ysize=512, event_pro='get_spectra',
/motion_events) ;Button_Events=1)

slider1 = widget_slider(tlb,value=790,min=0,max=2217,
title='The spectral cube number.',$
xsize=512,event_pro='inspect_cube',scroll=1,/drag)

draw2 = widget_draw(fbasedetc,ysize=256,xsize=512)

;create widgets
widget_control, tlb, /realize
widget_control, fbasedetc, /realize
widget_control, draw1, get_value=drawid

widget_control, draw2, get_value=drawid2
wset, drawid

tv, bytscl(frebin(arrayflat[0:jmax,0:kmax],512,512),
min=meanflat-stddevflat,max=meanflat+stddevflat)

xmanager, 'linefitting', tlb

END
```

# Appendix B

# Example fits from SINFONI

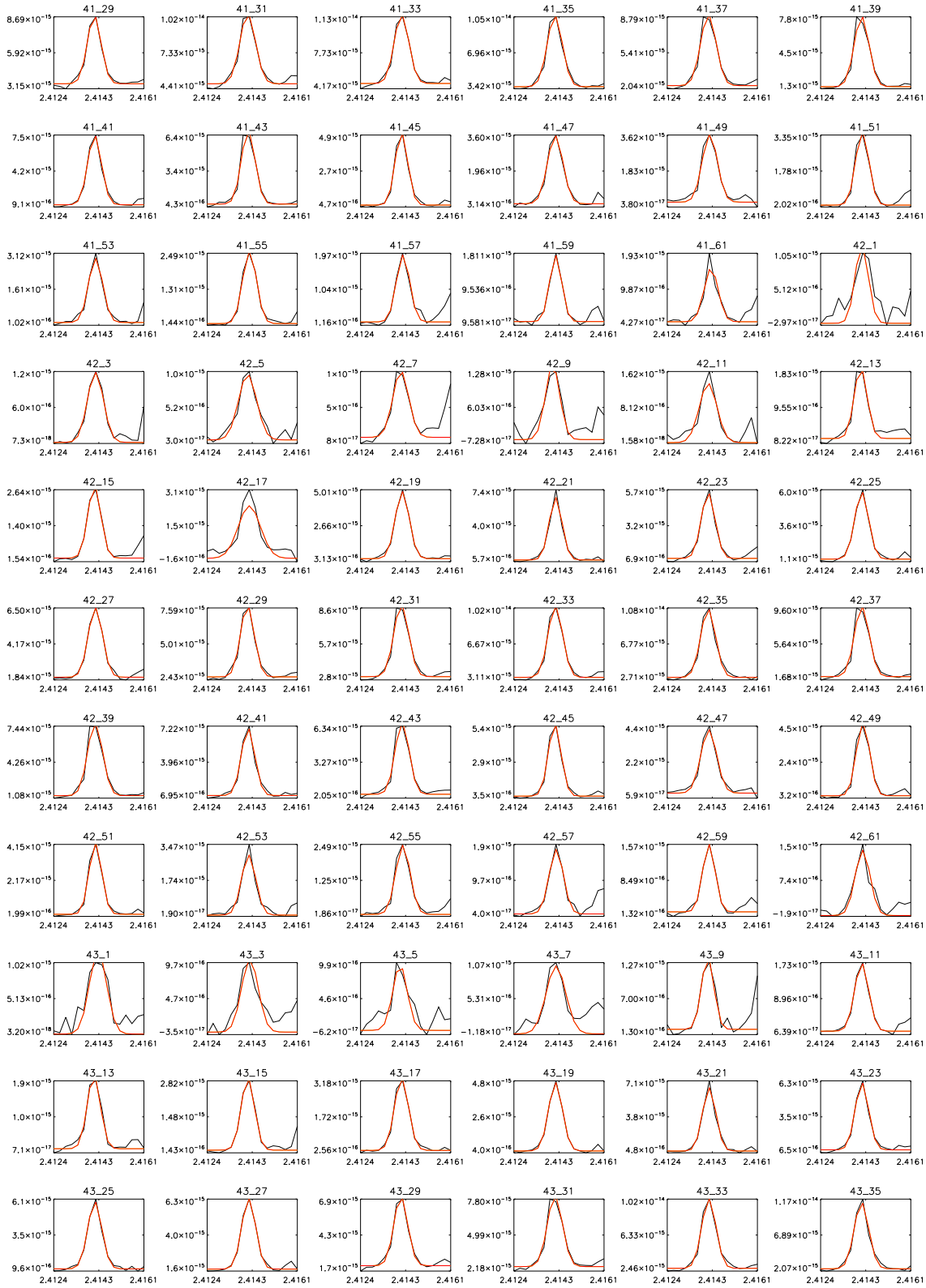


Figure B.1: Sample of SINFONI fits for one emission line for an entire data cube

# Appendix C

# Proton-Proton Chain and Triple-$\alpha$ Process

## C.1 Proton-Proton Chain

$$ {}^{1}_{1}\mathrm{H} + {}^{1}_{1}\mathrm{H} \rightarrow {}^{2}_{1}\mathrm{H} + \mathrm{e}^{+} + \nu_{\mathrm{e}} \tag{C.1} $$

$$ {}^{2}_{1}\mathrm{H} + {}^{1}_{1}\mathrm{H} \rightarrow {}^{3}_{2}\mathrm{He} + \gamma_{\mathrm{ray}} \tag{C.2} $$

$$ {}^{3}_{2}\mathrm{He} + {}^{3}_{2}\mathrm{He} \rightarrow {}^{4}_{2}\mathrm{He} + {}^{1}_{1}\mathrm{H} + {}^{1}_{1}\mathrm{H} \tag{C.3} $$

${}^{1}_{1}\mathrm{H}$ – Hydrogen; ${}^{2}_{1}\mathrm{H}$ – Deuterium; ${}^{3}_{2}\mathrm{He}$ – Helium-3; ${}^{4}_{2}\mathrm{He}$ – Helium-4; $\mathrm{e}^{+}$ – Positron; $\nu_{\mathrm{e}}$ – Electron Neutrino, and $\gamma_{\mathrm{ray}}$ – gamma ray.

## C.2 Triple Alpha Process

$$^{4}_{2}\mathrm{He} + ^{4}_{2}\mathrm{He} \rightleftharpoons ^{8}_{4}\mathrm{Be} + \gamma_{\mathrm{ray}} \tag{C.4}$$

$$^{8}_{4}\mathrm{Be} + ^{4}_{2}\mathrm{He} \rightleftharpoons ^{12}_{6}\mathrm{C}^{*} \tag{C.5}$$

$$^{12}_{6}\mathrm{C}^{*} \rightarrow ^{12}_{6}\mathrm{C} + \gamma_{\mathrm{ray}} \tag{C.6}$$

$$^{12}_{6}\mathrm{C} + ^{4}_{2}\mathrm{He} \rightarrow ^{16}_{8}\mathrm{O} + \gamma_{\mathrm{ray}} \quad \text{see note} \tag{C.7}$$

$^{4}_{2}$He – Helium-4; $^{8}_{4}$Be – Beryllium-8; $^{12}_{6}$C$^{*}$ – unstable Carbon-12; $^{12}_{6}$C – Carbon-12; $^{16}_{8}$O – Oxygen-16; $\gamma_{\mathrm{ray}}$ – gamma ray, and note – the production of Oxygen-16 is an additional step that is not part of the triple-$\alpha$ process.

## C.3 Carbon-Nitrogen-Oxygen cycle

$$^{12}_{6}\mathrm{C} + ^{1}_{1}\mathrm{H} \rightarrow ^{13}_{7}\mathrm{N} + \gamma_{\mathrm{ray}} \tag{C.8}$$

$$^{13}_{7}\mathrm{N}^{*} \rightarrow ^{13}_{6}\mathrm{C} + \mathrm{e}^{+} + \nu_{\mathrm{e}} \tag{C.9}$$

$$^{13}_{6}\mathrm{C} + ^{1}_{1}\mathrm{H} \rightarrow ^{14}_{7}\mathrm{N} + \gamma_{\mathrm{ray}} \tag{C.10}$$

$$^{14}_{7}\mathrm{N} + ^{1}_{1}\mathrm{H} \rightarrow ^{15}_{8}\mathrm{O} + \gamma_{\mathrm{ray}} \tag{C.11}$$

$$^{15}_{8}\mathrm{O}^{*} \rightarrow ^{15}_{7}\mathrm{N} + \mathrm{e}^{+} + \nu_{\mathrm{e}} \tag{C.12}$$

$$^{15}_{7}\mathrm{N} + ^{1}_{1}\mathrm{H} \rightarrow ^{12}_{6}\mathrm{C} + ^{4}_{2}\mathrm{He} \tag{C.13}$$

$^{1}_{1}$H – Hydrogen; $^{4}_{2}$He – Helium-4; $^{12}_{6}$C – Carbon-12; $^{13}_{6}$C – Carbon-13; $^{13}_{7}$N$^{*}$ – Unstable Nitrogen-13; $^{14}_{7}$N – Nitrogen-14; $^{15}_{7}$N – Nitrogen-15; $^{15}_{8}$O$^{*}$ – Unstable Oxygen-15; e$^{+}$ – Positron; $\nu_{\mathrm{e}}$ – Electron Neutrino, and $\gamma_{\mathrm{ray}}$ – gamma ray.